UNIVERSITY OF CALIFORNIA,
IRVINE

Self-Assembly of Peptide-Polymer Conjugates for the Formation of Functional Biomaterials via Molecular Dynamics Simulations

DISSERTATION

submitted in partial satisfaction of the requirements
for the degree of

DOCTOR OF PHILOSOPHY

in Chemical and Biochemical Engineering

by

Iris Wing Yin Fu

Dissertation Committee:
Professor Hung D. Nguyen, Chair
Professor Szu-Wen Wang
Professor Ray Luo

2015

DEDICATION

To my parents, who always encouraged me to take the first step,

and

To my love, me without you, that simply won't do

Table of Contents

LIST OF FIGURES

Page

LIST OF TABLES

Page

ACKNOWLEDGMENTS

I am thankful to my advisor, Professor Hung Nguyen, for his continuous guidance, and encouragement throughout this journey. Thanks for seeing potential in me and having the confidence in my ability to complete my PhD, even when I doubted myself. Thanks to the members of my qualifying and dissertation committee, Professor Szu-Wen Wang and Professor Ray Luo, for generously giving their time and expertise to better my work.

I would like to thank my labmates who made coming to work more enjoyable. Thanks Cade, partner-in-crime who is never further than a gchat or imessage away, for teaching me the basics of coding, helping me debug my code, and being a good soundboard to discuss ideas and simulations. It is reassuring to know that life won't be that much different after we graduate considering we have had more heart-to-heart, typing away with emoticons than IRL. I am still expecting you to share ridiculous memes and gifs. Thanks Quynh for reminding me that weekends are to be work-free and instead to be spent on foodie adventures, shopping, and doing stress-free 5K runs.

Thanks to all of my friends here at UCI, in particular, Vineet, Sophia, and Jessica. Vineet, thanks for sharing my love for Souplantation, maybe one day I'll feel the same way about Yogurtland. Twinsie, someday I will be less wildlife challenged and go camping but until then let's plan for a trip instead. Jessica, thanks for teaching me about baking and raw eggs in icing – our "NErDy OMg BeEr CoOKI" will always be a winner.

Thanks Ariel for always being there with words of encouragement as I ramble about all the things that happen inside my head. I am so blessed to have a friend like you in my life after all these years. Cheers. Thanks Erik for always believing in me and helping me get through so many hurdles so I can make it this far. Our promise is still on for the scooter.

Thanks Mom and Dad for your endless support and wish for my pursuit of happiness. Thanks for the sacrifices you have made to provide me with the resources, and opportunities I have today.

Finally, to Tim, thanks for always finding me.

This work would not have been possible without the financial support provided by the University of California, Irvine and the National Science Foundation Graduate Student Research Fellowship.

CURRICULUM VITAE

Iris Wing Yin Fu

EDUCATION

Doctor of Philosophy – Chemical and Biochemical Engineering **2015**
University of California, *Irvine, California*
Master of Science – Chemical and Biochemical Engineering **2011**
University of California, *Irvine, California*
Bachelor of Science – Chemical Engineering **2010**
University of California, *San Diego, California*

RESEARCH EXPERIENCE

Graduate Student Researcher 2010 - 2015
University of California, *Irvine, California*, Dissertation advisor: Professor Hung Nguyen

Computational Chemistry and Materials Science Summer Institute Fellow 2014
Lawrence Livermore National Laboratory, Livermore, California
Research advisor: Dr. Ed Lau

Undergraduate Student Researcher 2009
University of Washington, Research advisor: Professor Amy Shen

Undergraduate Student Researcher 2008
National Science Foundation Research Experiences for Undergraduates
Washington University in St. Louis, Research advisor: Professor Amy Shen

PUBLICATIONS

1) **I.W. Fu** and H.D. Nguyen. Sequence-Dependent Structural Stability of Self-Assembled Cylindrical Nanofibers by Peptide Amphiphiles. (Submitted, 2015)
2) C.B. Markegard, **I.W. Fu,** K.A. Reddy, H.D. Nguyen. Coarse-grained Simulation Study of Sequence Effects on DNA Hybridization in a Concentrated Environment. *J. Phys. Chem. B.* (2015), 119 (5): 1823-1834
3) **I.W. Fu,** C.B. Markegard, H.D. Nguyen. Solvent Effects on Kinetic Mechanisms of Self-Assembly by Peptide Amphiphiles via Molecular Dynamics Simulations. *Langmuir.* (2015), 31 (1): 315-324
4) Y. Cote*, **I.W. Fu*,** E.T. Dobson, J. Goldberger, H.D. Nguyen, J.K. Shen. Multi-scale modeling of pH-controlled self-assembly of nanofibers from peptide amphiphiles. *J. Phys. Chem. C*. (2014) **,**118 (29): 16272-16278. – *co-authors
5) B. Chu*, **I.W. Fu***, C.B. Markegard, S. Choi, H.D. Nguyen. The Tail of Two Peptide Amphiphiles: Effect of Conjugation on Folding. *Biomacromolecules*, (2014), 15 (9): 3313-3320. – *co-authors

6) **I.W. Fu,** C.B. Markegard, B. Chu, H.D. Nguyen. Role of Hydrophobicity on Self-Assembly by Peptide Amphiphiles via Molecular Dynamics Simulations. *Langmuir,* (2014), 30 (26) 7745-7754.
7) **I.W. Fu,** C.B. Markegard, B. Chu, H.D. Nguyen. The role of electrostatics and temperature on morphological transitions of hydrogel nanostructures self-assembled by peptide amphiphiles via molecular dynamics simulations. *Advanced Healthcare Materials,* (2013), 2: 1388–1400. – *Cover Article*

CONFERENCE ABSTRACTS

1) Sequence-Dependent Self-Assembly of Peptide Amphiphiles Via Molecular Simulations. I.W. Fu, C.B. Markegard, and H.D. Nguyen. AIChE National Meeting, November 2014, Atlanta, GA.
2) Invited Talk: Multi-Scale Modeling of the pH-Controlled Self-Assembly By Peptide Amphiphiles. I.W. Fu, and H.D. Nguyen. AIChE National Meeting, November 2014, Atlanta, GA.
3) Molecular Dynamics Simulations of Self-Assembly of Nonviral Gene Delivery Complexes by Pegylated Peptides and siRNA Molecules. I.W. Fu, S. Wong, J. Edson, C.B. Markegard, Y.J. Kwon, H.D. Nguyen. MRS National Meeting, April 2014, San Francisco, CA. – Poster Presentation
4) Stimuli-Responsive Self-Assembly of Hydrogel Nanostructures by Peptide Amphiles via Molecular Dynamics Simulations. I.W. Fu, C.B. Markegard, B. K. Chu, and H.D. Nguyen. MRS National Meeting, April 2014, San Francisco, CA.
5) Molecular Dynamics Simulations of Self-Assembly of Nonviral Gene Delivery Complexes By Pegylated Peptides and siRNA Molecules. I.W. Fu, S. Wong, J. Edson, C.B. Markegard, Y.J. Kwon, H.D. Nguyen. AIChE National Meeting, November 2013, San Francisco, CA.
6) Effect of Solvent on the Self-Assembly of Hydrogel Nanostructure from Peptide Amphiphiles. I.W. Fu, C.B. Markegard, and H.D. Nguyen. AIChE National Meeting, November 2012, Pittsburgh, PA.
7) Self-Assembly of Peptide Amphiphiles Into Hydrogel Via Multiscale Simulations. I.W. Fu, C.B. Markegard, and H.D. Nguyen. AIChE National Meeting, November 2012, Pittsburgh, PA.
8) Mechanistic Kinetics of Hydrogen Self-Assembly by Peptide Amphiphiles via Multiscale Simulations. . I.W. Fu, C.B. Markegard, and H.D. Nguyen. UC Systemwide Bioengineering Symposium, June 2012, Berkeley, CA.
9) Self-Assembly of Peptide Amphiphiles Into Hydrogel Via Multiscale Simulations. I.W. Fu, C.B. Markegard, and H.D. Nguyen. Gordon Research Conference: Peptide Folding Dynamics , January 2012, Ventura, CA. – Poster Presentation
10) Self-Assembly of Peptide Amphiphiles Into Hydrogel Via Multiscale Simulations. I.W. Fu, C.B. Markegard, and H.D. Nguyen. AIChE National Meeting, October 2011, Minneapolis, MN.

ABSTRACT OF THE DISSERTATION

Self-Assembly of Peptide-Polymer Conjugates for the Formation of Functional Biomaterials via Molecular Dynamics Simulations

By

Iris Wing Yin Fu

Doctor of Philosophy in Chemical and Biochemical Engineering

University of California, Irvine, 2015

Professor Hung D. Nguyen, Chair

Peptide-polymer conjugates are versatile molecular building blocks that can self-assemble into well-defined nanostructures with customizable biofunctionality and tunable physical properties for a wide range of biomedical applications. In this dissertation, two structural analogues of peptide-polymer conjugates are discussed: peptide amphiphiles and block copolymers with the difference between their respective domains tailored for specific applications. Self-assembly process of these peptide-polymer conjugates into different nanostructure morphologies is examined via molecular dynamics simulations using our recently developed integrated simulation package, called BioModi (Biomolecular Multiscale Models at UC Irvine). This simulation package consists of coarse-grained models that mimic realistic molecules and molecular interactions of amino acids, nucleic acids, and polymers, yet are simplified enough to allow molecular simulation of large systems over long time scales.

For peptide amphiphiles, emphasis is placed on achieving a fine balance between the two distinct hydrophobic and hydrophilic domains to attain a supramolecular

architecture that can serve as a biomimetic hydrogel scaffold for tissue engineering. The role of different environmental factors (e.g. temperature, pH, solvent) on the self-assembly behavior of peptide amphiphiles is elucidated in detail. Our simulations show that under optimal conditions, spontaneously self-assembly results in the formation of cylindrical nanofibers that can switch into spherical micelles in response to a small pH range as similarly observed by *in vitro* experiments. Moreover, phase diagrams are constructed to identify morphological transitions, and unique self-assembly kinetic mechanisms are characterized. Chemical modification of the peptide amphiphile sequence is investigated and contrasting structural characteristics are observed to correlate with differences in mechanical behavior of the resulting gel.

For block copolymers, the inherent design utilizes a cationic polypeptide conjugated to a synthetic polymer that promotes favorable electrostatic interactions with nucleic acid fragments upon the formation of a polyionic complex as an effective gene carrier. Efficient complexation of block polymers with siRNA is determined via molecular dynamics simulations to be a function of the length of the polymer and the charge density of the system.

Implementation of our newly developed coarse-grained models, BioModi, and insight gained from our simulations will provide key parameters to advance computer-aided design and development of innovative smart biomaterials.

CHAPTER 1 Introduction

1.1 Motivation

Molecular self-assembly is a spontaneous process that facilitates construction of well-defined, hierarchical structures. The formation of these supramolecular assemblies by peptide-polymer conjugates is held together primarily through non-covalent interactions such as hydrogen bonds, electrostatic and hydrophobic interactions.[1-3] Peptide-polymer conjugates have been exploited as advantageous molecular level building blocks due to their inherent biofunctional properties. Through the incorporation of both peptide motifs and synthetic polymer, this combination yields a hybrid system that serves to broaden nanostructure formation for multifaceted applications including but not limited to: protein therapeutics, drug delivery, gene delivery, and tissue engineering.[4,5] Although the ability for peptide-polymer conjugates to form a range of diverse nanostructures has been attributed to its chemical structure[6,7] or its dynamic response to the external environment[8-10] (i.e. pH, ion concentration, solvent, temperature, etc.), the current understanding of the underlying molecular pathway for self-assembly remains limited. Predominant approach has relied on the expertise or experience of experimentalists but through the use of computational aided design, the large design space can be explored in a more time manageable manner. With aims to develop these biomaterials for targeted therapeutic applications, molecular dynamics simulations are performed to provide a clearer understanding of the role of external environment and choice of specific chemical sequence in order to attain

nanostructures with desired structural design, morphological response, and biological functionality.

1.2 Use of peptide amphiphiles as molecular level building blocks for tissue engineering scaffolds

The loss or failure of an organ or tissue remains a tremendous health problem although viable treatment options such as surgical reconstruction, drug therapy, and use of synthetic prostheses and/or mechanical devices can be implemented.[11,12] However, each of these therapies is not a comparable substitute for the innate organ or tissue since they can neither restore full functionality nor guarantee an improved survival with the possibility of only serving as a temporizing measure. With the growing needs of organs and tissues transplant, the shortage of available donors is of concern.[13,14] In 2014, according to OPTN (Organ Procurement and Transplantation Network) an estimated 14,400 donors, living and deceased, donated an organ whereas over 123,000 candidates were on the waitlist for an organ (e.g. kidney, liver, pancreas, heart, lung, intestine). The vast shortages of donors have spurred recent advances in tissue engineering, specifically in the design of artificial scaffolds.[15]

Both the structure and the dynamic interactions of the extracellular matrix with surrounding cells have been shown to influence cell-fate behavior and function.[16-18] Consequently, aims to develop and create tissues that can be integrated within the body are of significant consideration in the design of artificial scaffolds for clinical applications. Essential features would be to have a definitive spatial structure that allows and guides the formation of new tissues, encourage desirable interactions between cells and the scaffold

to promote specific functionality, and most importantly to be biocompatible to minimize immunological responses and/or toxicity (**Figure 1.1**).[19,20]

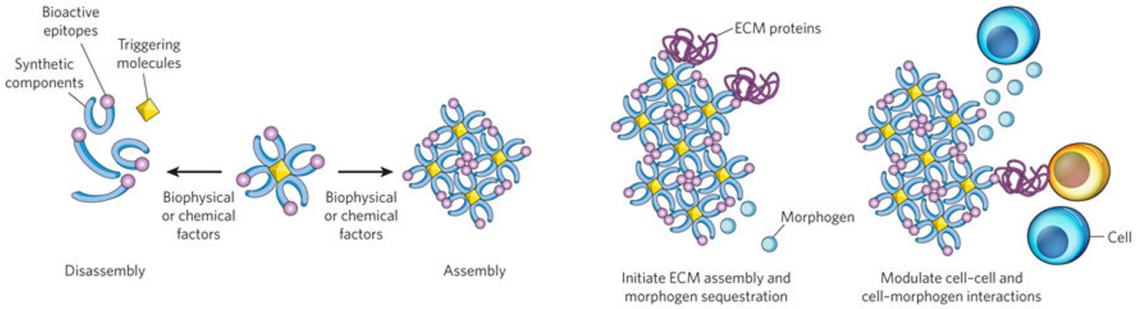

Figure 1.1 Schematic of a self-assembled extracellular matrix mimic by peptide-polymer conjugates. The crosslinked structure is designed to be biocompatible and biodegradable upon biophysical or chemical factors. In order to ensure viable tissue generation, the structure should also be designed to facilitate diffusion of nutrients as governed by the interactions within the interfiber network. Image taken from Huebsch and Mooney.[21]

Hydrogels are attractive biomaterials to serve as an extracellular matrix mimic because of its inherent 3D network structure that can absorb large amounts of water in an aqueous environment by swelling extensively without the polymer dissolving which is most resemblant of natural soft tissues.[22,23] The unique characteristic of hydrogels to have a 3D network further improves upon simple 2D models by better representing the intricate cellular microenvironment. The versatility of having flexible building blocks including natural, synthetic, or a combination of the above (i.e. hybrid) for polymer choices, enables the precise manipulation of the resulting scaffold's chemical, physical, and mechanical properties.

Natural polymer-based hydrogels comprised of polynucleotides, polypeptides, and polysaccharides have been widely used as scaffolding materials.[23,24] Derived from either mammalian protein or algae-based sources, these biomaterial such as collagen, hyaluronic acid, alginate, and chitosan are effective as extracellular matrices mimics because they

contain existing cell-signaling domain in addition to their inherent biocompatibility.[25] However, there has been a gradual transition toward the use of synthetic / biohybrid polymers due to unfavorable drawbacks including immunogenicity, weak mechanical strength, and complex structural aspects.[10,26] Even though chemical modification such as purification treatments can reduce the possibility of having antigenic determinants or use of crosslinking may improve mechanical properties, natural polymers are still limited by having a complex structure that is difficult to undergo these modifications.

Biohybrid synthetic polymer-based hydrogels offer an advantage in comparison to natural polymer-based hydrogels by maintaining levels of biocompatibility yet offering enhanced functionality, and efficiency. By design, biohybrid synthetic polymers maintain the ability to spontaneously self-assemble into hierarchical structures similar to native biological systems such as lipid bilayers or organized nucleic acids as genetic information carriers.[27] Preservation of this process allows for the precise "bottom-up" approach to fabricate novel materials. Biofunctional and mechanical properties of these materials can be carefully tuned through chemical modification and/or response to external stimuli.

A specific class of these synthetic hydrogel-forming polymer-based building blocks is peptide amphiphiles that shares structural similarities to surfactant molecules and other self-assembling peptides including hybrid block copolymers[28-30] and peptide-polymer conjugates[31,32]. The hydrophobic domain can be comprised of single or multiple hydrocarbon chains covalently attached to a charged polypeptide sequence as the hydrophilic domain with built-in biofunctionality.[33,34] Alternatively, the two domains can be simplified to be a uniform polypeptide sequence[35,36] or further complicated with the added specification of spacers[37,38] or difference in molecular geometry[39,40]. The structural

flexibility incorporated in the inherent design of these molecules have marketed the resulting nanoassemblies derived from PA molecules to be advantageous candidates in drug delivery[41,42] and tissue engineering applications[43-46]. Integration of a polymer tail with polypeptides enables a collaborative environment in which the polymer tail yields minimal toxicity and added stability complemented by the polypeptide to facilitate tunable attributes through specific sets of structural and chemical functionality.[2,47]

1.3 Development of Block Copolymers for siRNA Delivery

Block copolymers are structurally designed to overcome challenges associated with common non-viral vectors such as liposomes, polymers and polymer-lipid hybrids.[48] In general, there are a wide variety of cationic polymers that can form self-assembled nanostructures with genetic material including poly(L-lysine) (PLL), poly(ethyleneimine) (PEI) and poly(amido amine) (PAMAM).[49,50] The nanostructures' arrangement adopts a configuration in which the cationic polymer is positioned on the surface with a charge-neutralized inner core comprised of the polymer and the nucleic acid fragments. While this arrangement is beneficial for traversing the cellular membrane, it also facilitates non-specific association to form large aggregates with charged serum proteins resulting in rapid clearance. Instead, these structures can be modified to incorporate a biocompatible polymer such as hydrophilic polyethylene glycol (PEG) to form stable nanostructures of smaller sizes.[51] Combination of a PEGylated block copolymer with poly(L-lysine) results in a "core-shell" structure with the outer layer as steric stabilization to shield the genetic material that is complexed with the cationic peptide (**Figure 1.2**).[52]

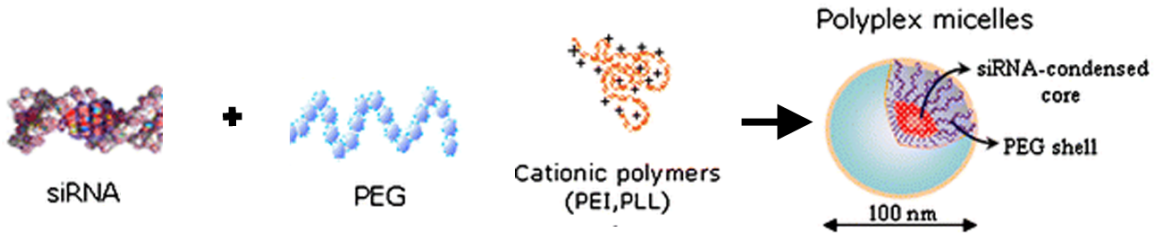

Figure 1.2. Adapted schematic representation taken from Jeong et al.,[51] of polyion complex formation with siRNA and PEG-PLL conjugate . A core-shell model is shown with the siRNA and PLL located in the core and the PEG is on the surface.

1.4 Implementation of Molecular Dynamics Simulations to Examine Self-Assembly Processes of Peptide-Polymer Conjugates

Experimental work has contributed tremendously to the advancement of scientific research but limitations are inevitable with respect to understanding the properties of molecular behavior and their interactions due to the spatial and temporal resolution.[53] Computer simulations act as a liaison connecting theoretical and experimental work. It provides an efficient means to simulate and investigate systems that are difficult or otherwise impossible. Molecular dynamics (MD) simulations are one of the techniques that have been advantageous in examining biomolecular systems. Fundamentally, Newton's equations of motion is integrated forward in time to simulate the dynamics of the system of atoms or molecules.[54] In contrast to experimental aspects, precise details of a particle's motion can be characterized as a function of time, providing a means to identify pathways or to discern the dynamic features of a process.[55,56]

Different models are implemented in conjunction with molecular dynamics depending on the level of resolution that they can represent. All-atomistic (AA) models developed have been able to represent atoms as individual sites with a one-to-one mapping.[57] Interactions between these atoms are represented by continuous potentials with terms

describing bond stretches, bond angles, torsional rotations, and non-bonded interactions. While this model has been previously limited to small systems of a few hundred of molecules, recent advances of computational model has now been able to examine more computationally complex systems including explicitly solvated proteins.[58] However, with interest to examine large macromolecular aggregates and processes such as molecular rearrangement that occurs on larger timescales, the feasibility of atomistic simulations is limited. For atomistic models, with an integration of 2 fs time step while solving Newton's equation of motion, the extent of the trajectory is limited to 1 μs to about 100 ns which can study stability of preformed structures but has difficulty with protein folding or protein aggregation.[59] Development of coarse-grained (CG) models offers an united-atoms approach by reducing the complexity of the system through the representation of multiple atoms or groups as a single entity. In combination with the use of implicit solvent and simplification of potentials, the overall computational cost is greatly reduced to allow for larger timescale simulations.[60] The use of coarse-grained models as opposed to atomistic models are not to be thought of to replace one another.[61] Instead, information from atomistic models is used to obtain parameters for coarse-grained potentials providing accuracy for data obtained without being limited by computational speed.

Aside from the use of a simplified model to reduce the degree of freedom in a modeled system to increase computational speed, the transition from traditional, continuous molecular dynamics, to discrete, or discontinuous molecular dynamics (DMD) can be a practical alternative.[62] As briefly described above, traditional molecular dynamics is a method to simulate the particles' motion in a system through integration of Newton's equation of motion. Continuous potentials are used and the algorithm updates the particles

coordinates and velocity at fixed time steps whereas with DMD, the potentials are simplified and are represented as discontinuous step-functions. The velocity of a particle remains constant until a collision event is encountered and the next collision event is calculated under laws of conservation. Consequently, DMD is a technique that offer a much faster algorithm to simulate large biomacromoleuclar systems.[63]

In this work, self-assembly of peptide amphiphiles and block copolymers is examined using a newly developed coarse-grained model, ePRIME, which is an extended version of the original PRIME model.[64-66] Modifications have been made such that ePRIME can accommodate all 20 naturally occurring amino acids by accounting for the size, hydrophobicity, and charge of each sidechain type using well-established experimental and modeling parameters.[67,68] The ePRIME model is designed to contain sufficient genuine biological character to represent real amino acids and polymers while being simple enough to be computationally tractable.[65] This model has been shown to examine spontaneous self-assembly processes starting from random initial configurations without a predetermined structure eliminating any conformational biases. By modeling the necessary interactions involved between peptide and polymer species including steric, directional hydrogen bond, hydrophobic, electrostatic interactions, this model is able to further examine secondary structure formation as a function of the trajectory. The use of ePRIME with a discontinuous molecular dynamics (DMD) algorithm, a fast alternative to standard molecular dynamics, further enables the simulation of very large systems. The current ePRIME model has been further developed into BioModi (Biomolecular Multiscale Models at UC Irvine) to incorporate and adequately model the biological behavior of nucleic acids and polyethylene glycol units to examine the complexation behavior of block copolymers with siRNA. siRNA

is modeled with sequence specificity instead of a simple flexible polymer to account for sequence-dependent interactions (e.g. base-stacking, electrostatic interactions, solvent-induced interactions). Physiologically relevant behavior is captured from performing atomistic simulations to determine the dynamics of individual PEGylated-polypeptide and double stranded siRNA molecules.

1.5 Structure of the Dissertation

The general goal of this dissertation aims to determine the factors that influence the thermodynamics and kinetics of peptide-polymer conjugates self-assembly. In particular, we employ our newly developed coarse-grained model, ePRIME, and perform molecular dynamics simulations to examine the underlying principles for the formation of different nanostructures. This dissertation begins by introducing our coarse-grained model, ePRIME, and comparing its performance to atomistic model for single molecules of peptide amphiphiles (Chapter 2). Cylindrical nanofibers are observed to form from large spontaneous self-assembly event of 800 peptide amphiphiles. The role of modifying the electrostatic interaction (i.e., pH and ion concentration) between charged side chain groups, and the effect of changing temperature is found to yield a broad array of nanostructures. In Chapter 3, the formation of cylindrical nanofibers is examined in-depth with the use of an all-atom constant pH molecular dynamics in conjunction with our coarse-grained ePRIME model. The implementation of both of these models provides a multiresolution perspective of the pH-dependent self-assembly of nanofibers and indicates our coarse-grained model is a valid candidate for computer-aided design and discovery of novel biomaterials.

In Chapter 4, the role of hydrophobicity on self-assembly by peptide amphiphiles is examined to provide an intuition with respect to selecting particular polymer type or solvent choice. Phase diagrams are constructed to illustrate optimal conditions at which cylindrical nanofibers can be formed. To further examine the underlying kinetic pathway as a function of the external stimuli, Chapter 5 presents a detailed quantitative analysis to characterize the multistep process for the formation of these nanostructures. Aside from looking at the effect of external stimuli, the effect of changing the peptide sequence is also examined using two sequences that share the same chemical composition but different placement of hydrophobic residues with respect to the polymer tail. In Chapter 6, single molecule peptide amphiphiles are studied in-depth to examine the intramoleuclar interactions between the hydrophobic and hydrophilic domains of the molecule and its effect on the subsequent peptide folding. Chapter 7 provides further studies of these two sequences in large self-assembly events indicating that the single molecule behavior influences nanostructure formation and the resulting stability and mechanical behavior of the nanostructure.

In Chapter 8, ePRIME is further developed into BioModi by extending to model polyethylene glycol (PEG) monomer chain and nucleic acids. The model is built to evaluate the feasibility and validity of the coarse-grained model for a heterogeneous system. Complexation of siRNA with PEGylated polymer is observed and the parameters that influence the size and distribution of the aggregates are determined. Finally, the conclusions of this dissertation are summarized in Chapter 9, and some directions for future research are presented.

1.6 References

1. Ulijn, R. V. & Smith, A. M. Designing peptide based nanomaterials. *Chem. Soc. Rev.* **37,** 664 (2008).
2. Cavalli, S., Albericio, F. & Kros, A. Amphiphilic peptides and their cross-disciplinary role as building blocks for nanoscience. *Chem. Soc. Rev.* **39,** 241 (2009).
3. Hamley, I. W. Self-assembly of amphiphilic peptides. *Soft Matter* **7,** 4122 (2011).
4. Shu, J. Y., Panganiban, B. & Xu, T. Peptide-Polymer Conjugates: From Fundamental Science to Application. *Annu. Rev. Phys. Chem.* **64,** 631–657 (2013).
5. Sohdi, A., Campbell, D. & Topham, P. Polymer-peptide conjugate hydrogels: towards controlled drug delivery. *Chiang Mai journal of science* (2012).
6. Xu, X.-D., Jin, Y., Liu, Y., Zhang, X.-Z. & Zhuo, R.-X. Self-assembly behavior of peptide amphiphiles (PAs) with different length of hydrophobic alkyl tails. *Colloids and Surfaces B: Biointerfaces* **81,** 329–335 (2010).
7. Greenfield, M. A., Hoffman, J. R., Olvera de la Cruz, M. & Stupp, S. I. Tunable Mechanics of Peptide Nanofiber Gels. *Langmuir* **26,** 3641–3647 (2010).
8. Zhou, X.-R., Ge, R. & Luo, S.-Z. Self-assembly of pH and calcium dual-responsive peptide-amphiphilic hydrogel. *J. Pept. Sci.* **19,** 737–744 (2013).
9. Ahn, S.-K., Kasi, R. M., Kim, S.-C., Sharma, N. & Zhou, Y. Stimuli-responsive polymer gels. *Soft Matter* **4,** 1151 (2008).
10. Ahmed, E. M. Hydrogel: preparation, characterization, and applications. *Journal of Advanced Research* (2013). doi:10.1016/j.jare.2013.07.006
11. Kim, B.-S. & Mooney, D. J. Development of biocompatible synthetic extracellular matrices for tissue engineering. *Trends in biotechnology* **16,** 224–230 (1998).
12. Shapiro, J. M. & Oyen, M. L. Hydrogel Composite Materials for Tissue Engineering Scaffolds. *JOM* **65,** 505–516 (2013).
13. Stock, U. A. & Vacanti, J. P. Tissue engineering: current state and prospects. *Annual review of medicine* **52,** 443–451 (2001).
14. Niklason, L. E. & Langer, R. Prospects for organ and tissue replacement. *JAMA: the journal of the American Medical Association* **285,** 573–576 (2001).
15. Geckil, H., Xu, F., Zhang, X., Moon, S. & Demirci, U. Engineering hydrogels as extracellular matrix mimics. *Nanomedicine* **5,** 469–484 (2010).
16. Engler, A. J., Sen, S., Sweeney, H. L. & Discher, D. E. Matrix Elasticity Directs Stem Cell Lineage Specification. *Cell* **126,** 677–689 (2006).
17. Benoit, D. S. W., Schwartz, M. P., Durney, A. R. & Anseth, K. S. Small functional groups for controlled differentiation of hydrogel-encapsulated human mesenchymal stem cells. *Nat Mater* **7,** 816–823 (2008).
18. Discher, D. E. Tissue Cells Feel and Respond to the Stiffness of Their Substrate. *Science* **310,** 1139–1143 (2005).
19. El-Sherbiny, I. M. & Yacoub, M. H. Hydrogel scaffolds for tissue engineering: Progress and challenges. *Global Cardiology Science and Practice* (2013). doi:10.2217/nnm.10.12
20. Liu, C., Xia, Z. & Czernuszka, J. T. Design and Development of Three-Dimensional Scaffolds for Tissue Engineering. *Chemical Engineering Research and Design* **85,** 1051–1064 (2007).
21. Huebsch, N. & Mooney, D. J. Inspiration and application in the evolution of biomaterials. *Nature* **462,** 426–432 (2009).
22. Papavasiliou, G., Sokic, S. & Turturro, M. Synthetic PEG Hydrogels as Extracellular Matrix Mimics for Tissue Engineering Applications. (2012).
23. Zhu, J. & Marchant, R. E. Design properties of hydrogel tissue-engineering scaffolds. *Expert Rev Med Dev* **8,** 607–626 (2011).
24. Vermonden, T., Censi, R. & Hennink, W. E. Hydrogels for Protein Delivery. *Chem. Rev.* **112,** 2853–2888 (2012).
25. Peppas, N. A., Hilt, J. Z., Khademhosseini, A. & Langer, R. Hydrogels in Biology and Medicine: From Molecular Principles to Bionanotechnology. *Adv. Mater.* **18,** 1345–1360 (2006).
26. Hong, Y. *et al.* Mechanical properties and in vivo behavior of a biodegradable synthetic polymer microfiber–extracellular matrix hydrogel biohybrid scaffold. *Biomaterials* **32,** 3387–3394 (2011).

27. Zhao, X. *et al.* Molecular self-assembly and applications of designer peptide amphiphiles. *Chem. Soc. Rev.* **39,** 3480 (2010).
28. Rösler, A., Vandermeulen, G. & Klok, H. A. Advanced drug delivery devices via self-assembly of amphiphilic block copolymers. *Advanced Drug Delivery Reviews* **53,** 95–108 (2001).
29. Xiong, X.-B., Falamarzian, A., Garg, S. M. & Lavasanifar, A. Engineering of amphiphilic block copolymers for polymeric micellar drug and gene delivery. *Journal of Controlled Release* **155,** 248–261 (2011).
30. Loh, W. Block copolymer micelles. *Encyclopedia of surface and colloid science* 802–813 (2002).
31. Shu, J. Y., Tan, C., DeGrado, W. F. & Xu, T. New Design of Helix Bundle Peptide−Polymer Conjugates. *Biomacromolecules* **9,** 2111–2117 (2008).
32. Collier, J. H. & Messersmith, P. B. Self-Assembling Polymer–Peptide Conjugates: Nanostructural Tailoring. *Adv. Mater.* **16,** 907–910 (2004).
33. Hartgerink, J. D. Self-Assembly and Mineralization of Peptide-Amphiphile Nanofibers. *Science* **294,** 1684–1688 (2001).
34. Cui, H., Webber, M. J. & Stupp, S. I. Self-assembly of peptide amphiphiles: From molecules to nanostructures to biomaterials. *Biopolymers* **94,** 1–18 (2010).
35. Saiani, A. *et al.* Self-assembly and gelation properties of α-helix versusβ-sheet forming peptides. *Soft Matter* **5,** 193 (2008).
36. Zhang, S. Fabrication of novel biomaterials through molecular self-assembly. *Nat Biotechnol* **21,** 1171–1178 (2003).
37. Löwik, D. W., Ayres, L., Smeenk, J. M. & Van Hest, J. C. Synthesis of Bio-Inspired Hybrid Polymers Using Peptide Synthesis and Protein Engineering. *Advances in Polymer Science* **202,** 19–52 (2006).
38. Missirlis, D. *et al.* Effect of the Peptide Secondary Structure on the Peptide Amphiphile Supramolecular Structure and Interactions. *Langmuir* **27,** 6163–6170 (2011).
39. Gröhn, F., Klein, K. & Brand, S. Facile Route to Supramolecular Structures: Self-Assembly of Dendrimers and Naphthalene Dicarboxylic Acids. *Chem. Eur. J.* **14,** 6866–6869 (2008).
40. Storrie, H. *et al.* Supramolecular crafting of cell adhesion. *Biomaterials* **28,** 4608–4618 (2007).
41. Matson, J. B., Newcomb, C. J., Bitton, R. & Stupp, S. I. Nanostructure-templated control of drug release from peptide amphiphile nanofiber gels. *Soft Matter* **8,** 3586–3595 (2012).
42. Ghosh, A. *et al.* Fine-Tuning the pH Trigger of Self-Assembly. *J. Am. Chem. Soc.* **134,** 3647–3650 (2012).
43. Toksoz, S., Mammadov, R., Tekinay, A. B. & Guler, M. O. Electrostatic effects on nanofiber formation of self-assembling peptide amphiphiles. *Journal of Colloid And Interface Science* **356,** 131–137 (2011).
44. Dagdas, Y. S., Tombuloglu, A., Tekinay, A. B., Dana, A. & Guler, M. O. Interfiber interactions alter the stiffness of gels formed by supramolecular self-assembled nanofibers. *Soft Matter* **7,** 3524–3532 (2011).
45. Haines-Butterick, L. *et al.* Controlling hydrogelation kinetics by peptide design for three-dimensional encapsulation and injectable delivery of cells. *Proceedings of the National Academy of Sciences* **104,** 7791–7796 (2007).
46. Schneider, J. P. *et al.* Responsive Hydrogels from the Intramolecular Folding and Self-Assembly of a Designed Peptide. *J. Am. Chem. Soc.* **124,** 15030–15037 (2002).
47. Klok, H.-A. Biological-synthetic hybrid block copolymers: Combining the best from two worlds. *J. Polym. Sci. A Polym. Chem.* **43,** 1–17 (2004).
48. Han, S.-O., Mahato, R. I., Sung, Y. K. & Kim, S. W. Development of Biomaterials for Gene Therapy. *Molecular Therapy* **2,** 302–317 (2000).
49. Park, T., Jeong, J. & Kim, S. Current status of polymeric gene delivery systems ☆ . *Advanced Drug Delivery Reviews* **58,** 467–486 (2006).
50. Parekh, H. S. The advance of dendrimers-a versatile targeting platform for gene/drug delivery. *Current pharmaceutical design* **13,** 2837–2850 (2007).
51. Jeong, J. H., Park, T. G. & Kim, S. H. Self-Assembled and Nanostructured siRNA Delivery Systems. *Pharm Res* **28,** 2072–2085 (2011).
52. Katakura, H. *et al.* Improvement of retroviral vectors by coating with poly(ethylene glycol)-poly(L-lysine) block copolymer(PEG-PLL). *J. Gene Med.* **6,** 471–477 (2004).
53. Allen, M. P. Introduction to molecular dynamics simulation. *Computational Soft Matter: From Synthetic Polymers to Proteins* **23,** 1–28 (2004).
54. Saunders, M. G. & Voth, G. A. Coarse-Graining Methods for Computational Biology. *Annu. Rev. Biophys.* **42,** 73–93 (2013).

55. Karplus, M. & Petsko, G. A. Molecular dynamics simulations in biology. *Nature* **347,** 631–639 (1990).
56. Karplus, M. & McCammon, J. A. Molecular dynamics simulations of biomolecules. *Nature Structural & Molecular Biology* **9,** 646–652 (2002).
57. MacKerell, A. D., Jr *et al.* All-atom empirical potential for molecular modeling and dynamics studies of proteins. *J. Phys. Chem. B* **102,** 3586–3616 (1998).
58. Norberg, J. & Nilsson, L. Advances in biomolecular simulations: methodology and recent applications. *Quarterly reviews of biophysics* **36,** 257–306 (2003).
59. Wei, G., Mousseau, N. & Derreumaux, P. Computational simulations of the early steps of protein aggregation. *Prion* (2007).
60. Morriss-Andrews, A. & Shea, J.-E. Computational Studies of Protein Aggregation: Methods and Applications. *Annu. Rev. Phys. Chem.* **66,** 643–666 (2015).
61. Cranford, S. & Buehler, M. J. Coarse-Graining Parameterization and Multiscale Simulation of Hierarchical Systems. Part I: Theory and Model Formulation. (2010).
62. Buldyrev, S. V. Application of discrete molecular dynamics to protein folding and aggregation. 97–131 (2008).
63. Alder, B. J. & Wainwright, T. E. Studies in molecular dynamics. I. General method. *J. Chem. Phys.* **31,** 459 (1959).
64. Voegler Smith, A. & Hall, C. K. α-Helix formation: Discontinuous molecular dynamics on an intermediate-resolution protein model. *Proteins: Structure, Function, and Bioinformatics* **44,** 344–360 (2001).
65. Nguyen, H. D. & Hall, C. K. Molecular dynamics simulations of spontaneous fibril formation by random-coil peptides. *Proceedings of the National Academy of Sciences* **101,** 16180–16185 (2004).
66. Nguyen, H. D., Marchut, A. J. & Hall, C. K. Solvent effects on the conformational transition of a model polyalanine peptide. *Protein Science* **13,** 2909–2924 (2004).
67. Wesson, L. & Eisenberg, D. Atomic solvation parameters applied to molecular dynamics of proteins in solution. *Protein Science* **1,** 227–235 (1992).
68. Wallqvist, A. & Ullner, M. A simplified amino acid potential for use in structure predictions of proteins. *Proteins: Structure, Function, and Bioinformatics* **18,** 267–280 (1994).

CHAPTER 2 The Role of Electrostatics and Temperature on Morphological Transition of Hydrogel Nanostructures Self-Assembled by Peptide Amphiphiles via Molecular Dynamics Simulations

2.1 Abstract

Smart biomaterials that are self-assembled from peptide amphiphiles (PA) are known to undergo morphological transitions in response to specific physiological stimuli. The design of such customizable hydrogels is of significant interest due to their potential applications in tissue engineering, biomedical imaging, and drug delivery. Using a novel coarse-grained peptide/polymer model, which has been validated by comparison of equilibrium conformations from atomistic simulations, we have performed large-scale molecular dynamics simulations to examine the spontaneous self-assembly process. Starting from random configurations, these simulations result in the formation of nanostructures of various sizes and shapes as a function of the electrostatics and temperature. At optimal conditions, the self-assembly mechanism for the formation of cylindrical nanofibers is deciphered involving a series of steps: (1) PA molecules quickly undergo micellization whose driving force is the hydrophobic interactions between alkyl tails; (2) neighboring peptide residues within a micelle engage in a slow ordering process that leads to the formation of β-sheets exposing the hydrophobic core; (3) spherical micelles merge together through an end-to-end mechanism to form cylindrical nanofibers that exhibit high structural fidelity to the proposed structure based on experimental data. As the temperature and electrostatics vary, PA molecules undergo alternative kinetic mechanisms, resulting in the formation of a wide spectrum of nanostructures. A phase

diagram in the electrostatics-temperature plane is constructed delineating regions of morphological transitions in response to external stimuli.

2.2 Introduction

Hydrogels are versatile biomaterials with many potential applications in drug delivery, diagnostic medicine, tissue engineering, and design of bio-inspired nanomaterials.[1-5] They are characterized by three-dimensional polymer-related networks capable of absorbing a significant amount of fluid[1,2,5,6] and have physiological stimuli-responsive properties that can influence the resulting network structure and/or mechanical strength for tailored purposes.[1,2,5-10] Emerging interest has been focused on the molecular-level self-assembly of a specific class of molecules called peptide amphiphiles (PA), which consists of a hydrophobic alkyl tai, an amino acid sequence that drives secondary and tertiary conformations, and a hydrophilic head group of a few amino acids for bioactive signaling.[11-15] Experiments have shown that assemblies by PAs exhibit excellent biocompatibility and desired functionality in a physiological environment.[16-20] Moreover, through structural analysis on PA molecules that self-assemble into fibrous morphology as observed in cryo-TEM experiments, a model structure described as a cylindrical nanoscale fiber has been proposed by Stupp and co-workers.[12,13] Furthermore, critical factors influencing the self-assembly of such nanostructures have been identified as chemical structure, molecular geometry, intermolecular interactions (e.g. hydrophobic, hydrogen bonding, and electrostatic interactions) and the solvent condition.[21,22] The size, shape, interfacial curvature, and mechanical properties of the resulting assemblies reflect a delicate interplay of these important factors.[16,23-25] However, the current understanding of

the mechanism wherein peptide amphiphiles assemble into certain shapes at different solvent environments and the exact nature of how PA molecules arrange within those nanostructures are not fully elucidated.

The contributions from theoretical and simulation perspectives on PA assembly are invaluable, especially the works by Schatz, Ratner, and colleagues who examined the role of geometric packing and structural stability.[26,27] However, relevant atomic-resolution simulation studies of the whole self-assembly process are difficult due to the large system sizes required and the long timescales involved.[28,29]. For example, Lee, Stupp et al., performed an atomistic molecular dynamics (MD) simulation on a system of 144 peptide amphiphiles that were arranged in a cylindrical configuration as an initial structure.[29] After 40ns, the structure remained stable and secondary structure analysis signified the presence of both α-helical and β-sheet content. Although the results are comparable to experimental findings[12,13] by capturing the detailed interactions and distinctive structural motifs that comprise of a cylindrical nanofiber, the mechanism by which this structure is formed cannot be extracted since the simulation started from a cylindrical template. Consequently, most simulation studies capable of examining the whole self-assembly process have been limited to using simplified models.[30-33] For instance, Velichko et al., used a coarse-grained model to perform Monte Carlo simulations providing a molecular perspective between the structure and simulation conditions of the system.[32] By varying the strength of the hydrophobic attraction and the hydrogen bond, their model was able to capture important aspects of PA self-assembly by delineating a phase diagram with distinct morphologies. However, electrostatic interactions and peptide specificity were not included; such an omission could alter the phase diagram. Recently, Lee, Cho et al.,[33]

performed coarse-grained MD simulations on a system containing 140 PA molecules solvated in an aqueous environment for 16μs using the MARTINI force field.[34] They observe that the PA molecules self-assemble into micelles, which subsequently merge into a fiber. Water molecules are excluded from the hydrophobic core of the fiber and majority of peptides is exposed to aqueous environment. However, since the MARTINI force field[34] requires that the secondary structure of a peptide to be predetermined and fixed during the simulation, it was unfeasible to examine the role of solvent condition on the time-dependent formation of hydrogen bonds and secondary structures, which is known to play an important role in the self-assembly of nanostructures.[35]

To investigate the kinetics and thermodynamics of spontaneous PA self-assembly without predetermined secondary structures, we use our newly-developed coarse-grained (CG) model called ePRIME (see Supporting Information), which is an extended version of the original PRIME model.[36-38] We have modified this model to accommodate all 20 amino acids by accounting for the size, hydrophobicity, and charge of each sidechain type using well-established experimental and modeling parameters.[39,40] The ePRIME model contains enough genuine biological character to mimic real amino acids and polymers, yet is simple enough to be computationally tractable.[37] When coupled with a Discontinuous Molecular Dynamics (DMD) algorithm,[41] a fast alternative to standard molecular dynamics, our model allows us to simulate very large systems. This in turn enables us to probe the fundamental physics underlying self-assembly by exploring nanostructures of various morphologies under specific solution conditions (pH or ionic strength, and temperature).

In this work, we simulate the spontaneous formation of nanostructures including cylindrical nanofibers as a function of the electrostatics and temperature. The model

peptide amphiphile chosen for this study is a hydrophobic alkyl 16-mer tail covalently conjugated to a peptide sequence, which is comprised of valine, alanine, and glutamic acid, $V_3A_3E_3$, as shown in **Figure 2.1a**. It is one of the sequences systematically designed by Pashuck et al., who investigated the placement and position of valine and alanine on the mechanical properties of the resulting nanofiber gels.[42] Two types of simulations are performed: one type is on a single molecule for validation and the other type is on a multiple-molecule system to examine self-assembly (see Supporting Information). As a proof-of-concept study to validate our CG model, the results from single-molecule replica-exchange simulations using ePRIME are contrasted with those from atomistic NAMD[43] simulations using the CHARMM 27 force field.[44-46] Here the comparisons focus on (1) the detailed interactions between the alkyl tail and peptide segment and (2) the equilibrium structure of the peptide segment at different temperatures. To investigate the self-assembly of PA chains, constant temperature simulations on a system containing 800 PA molecules are performed at a high concentration of c = 85mM over a range of temperatures (T^* = 0.08 – 0.15 in reduced units) beginning from an initial random conformation. To examine the effect of ionic concentration and pH, the repulsive strength (ε_{ES}) of the electrostatic interactions between charged glutamic acids are varied systematically by increasing its value relative to the strength of a hydrogen bond (ε_{HB}). In this case, differing kinetic mechanisms responsible for the formation of a variety of self-assembled nanostructures are deciphered. Structural characterization of the self-assembled aggregates allows the construction of a phase diagram to delineate a wide range of morphological nanostructures that are formed at different environmental conditions. The results of this study aim to provide a fundamental understanding of the role of

electrostatics and temperature on the self-assembly of PA molecules for the design of smart bio-inspired hydrogel materials.

2.3 Results and Discussions

2.3.1 Equilibrium conformations of single PA molecule are similar from coarse-grained and atomistic simulations

As a proof-of-concept to validate the use of our coarse-grained ePRIME model, replica-exchange simulations were performed using both atomistic NAMD[43] and ePRIME models to examine the effect of temperature on the equilibrium structure of the chosen PA molecule. For both simulations, 16 replicas corresponding to 16 temperatures are selected to encompass a wide range of temperatures to observe the formation of entire spectrum of secondary structures. Snapshots of the PA molecule over a range of reduced temperatures (T* = 0.07 – 0.17) using the ePRIME model are shown in **Figure 2.1b**. At the lowest temperature of T* = 0.07, the peptide folds into an α-helical conformation. Comparing this structure at T* = 0.07 (**Figure 2.1b**) to the final conformation obtained at T = 260K from the NAMD replica-exchange simulation (**Figure 2.1c**) shows a high resemblance in the folded conformation of the peptide segment and the interactions between the alkyl tail and the peptide segment from the coarse-grained and all-atom simulations. In both simulations, the alkyl tail does not disrupt the folding process of the peptide segment to form secondary structure at low temperatures. Once the peptide segment folds into an α-helical conformation, favorable hydrophobic interactions are present between the flexible hydrophobic tail and the sidechains of the corresponding hydrophobic residues. In particular, weak hydrophobic interactions are predominantly between the alkyl tail and

valine residues since the valine sidechains are more hydrophobic than the alanine and glutamic sidechains.

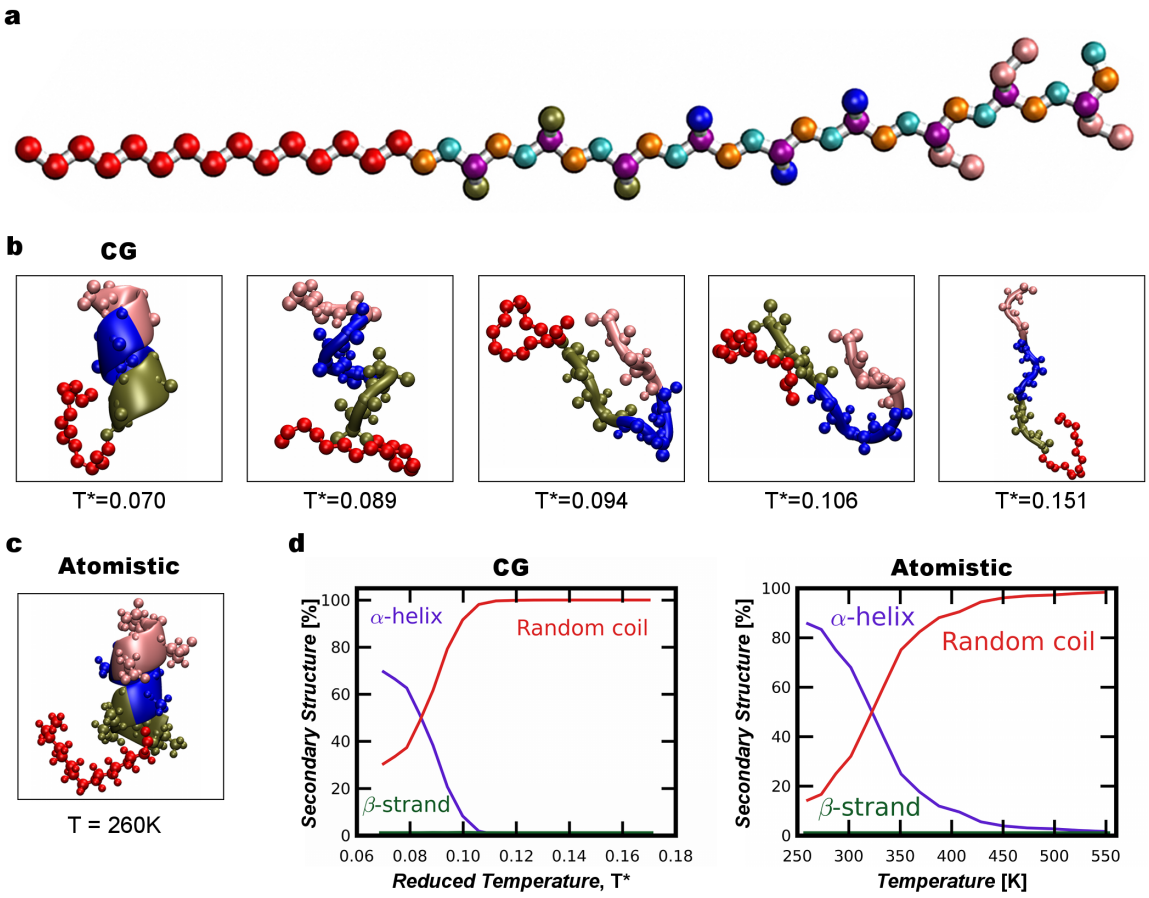

Figure 2.1. (a) Geometry of our coarse-grained (CG) model, ePRIME, for the studied PA molecule, $C_{16}H_{31}O$-$Val_3Ala_3Glu_3$, representing united groups of atoms as spheres: alkyl group (red); valine sidechain (green), alanine sidechain (blue), glutamic acid sidechain (pink), and backbone atoms (NH, CαH, and CO as cyan, purple and orange, respectively). The united atoms are not shown full size for ease of viewing. (b) Snapshots of equilibrium structures of the PA molecule at different reduced temperatures from ePRIME replica-exchange simulation. The color scheme is: hydrophobic alkyl tail (red), valine (green), alanine (blue), glutamic acid (pink), consistent for all subsequent figures. (c) Equilibrium PA structure obtained from NAMD replica-exchange temperature simulation at T = 260K. (d) Plot of the percentage of secondary structure formation as a function of temperature obtained from replica-exchange simulations for 16 temperatures using coarse-grained ePRIME and atomistic NAMD. The temperature range for ePRIME is T* = 0.07 – 0.17 and for NAMD is T = 260 – 550K. Data shown is taken from the average of the last 10% of equilibrium data and standard deviation is calculated to be ±20%.

Equilibrium results obtained from replica-exchange simulations using either our coarse-grained or all-atom models produce similar structures over a wide range of temperatures as shown in **Figure 2.1d**, which plots the percentages of secondary

structures created by the peptide segment as a function of temperature. At low temperatures, α-helical morphologies are the primary conformations while random coil structures are less prevalent. As the temperature increases to higher values than the melting temperature at T* = 0.085 that corresponds to ~320K, an inverse relationship is observed such that the predominant morphology is random coil. Interestingly, β-strand characteristics are minimal even at moderate temperatures because (1) the peptide containing nine residues is too short to form a complete β-hairpin, and (2) high number of hydrophobic interactions especially between the alkyl tail and the peptide segment are more favorable than just a few hydrogen bonds. Since the peptide segment is relatively short containing just nine residues, it folds and unfolds rapidly producing a large standard deviation error of about 20% in the structural data. Nevertheless, the results plotted in **Figure 2.1d** show similar trends such as the morphological transitions between equilibrium conformations throughout the whole range of selected temperatures. This indicates that our coarse-grained model of the chosen PA molecule has a remarkable ability to predict not only the secondary structure created by the peptide segment as a function of temperature but also the interactions between the alkyl tail and the peptide segment.

2.3.2 Self-assembly of PA molecules is spontaneous to form supramolecular aggregates starting from a random configuration

Self-assembly of PA chains to form supramolecular aggregates is observed spontaneously in molecular dynamics simulations of large systems containing 800 isolated PA molecules starting as random coils. Beginning from an unseeded random conformation, multiple aggregates are formed over the course of simulation at a moderate temperature

(T* = 0.11) and weak electrostatic interaction strength ($\varepsilon_{ES} = 100\%\varepsilon_{HB}$), The main driving force for self-assembly is the hydrophobic interactions between the alkyl tails, which bring PA molecules together to create large aggregates. The arrangement of these PA molecules within each aggregate consists of the alkyl tails residing in the interior with the peptide residues covering the exterior of the aggregate. Upon arriving at an aggregated state, the peptide segments stay away from one another due to repulsive electrostatic interactions between the charged sidechains of glutamic acids. Gradually, each peptide segment starts to form hydrogen bonds between neighboring molecules, thus leading to the emergence of secondary structure motifs within the aggregate. The final morphologies of self-assembled nanostructures at this above-mentioned condition are mostly cylindrical micelles (whose average number per simulation is 3 ± 2) and spherical micelles (whose average number per simulation is 30 ± 4). Typical cylindrical micelles comprise of 30-49 PA molecules and spherical micelles are comprised of 13-18 PA molecules. Cylindrical micelles that have elongated attributes with a significant amount of β-sheets are identified as cylindrical nanofibers as shown in **Figure 2.2a**.

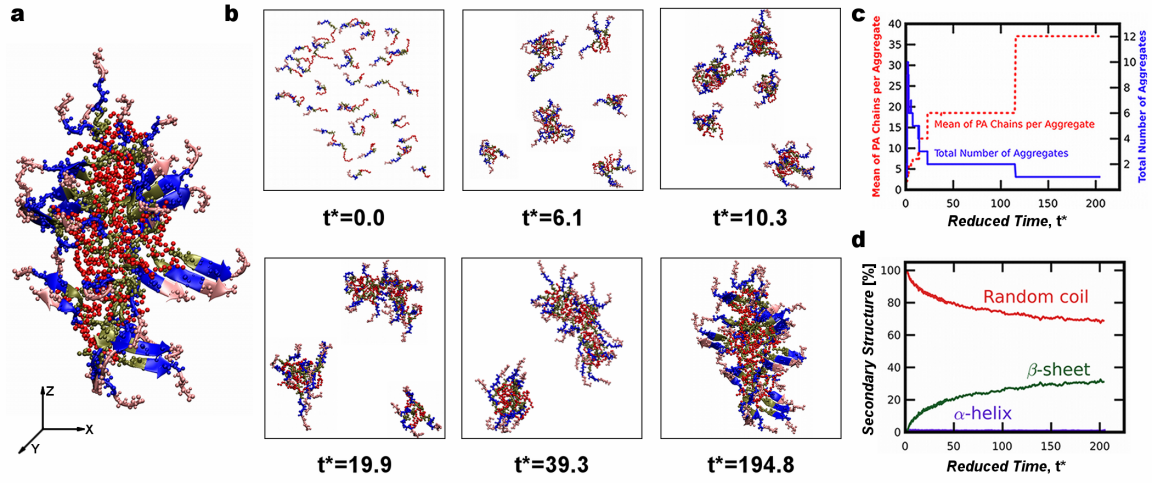

Figure 2.2. (a) A typical self-assembled cylindrical nanofiber observed from a simulation at a moderate temperature (T* = 0.11) and weak electrostatic interaction strength (ε_{ES} = 100% ε_{HB}); the fiber axis is along the length of hydrophobic core in the z-direction. (b) Self-assembly process of PA molecules to form a cylindrical nanofiber starting from a random configuration shown through time-dependent snapshots. For ease of viewing, only PA molecules involved in the self-assembly of a chosen cylindrical nanofiber are shown since the whole simulation system contains 800 PA molecules. (c) For the cylindrical nanofiber shown in (a), the average number of PA molecules per aggregate and total number of aggregates as a function of reduced time are plotted. (d) Plot of the percentages of secondary structures of the PA molecules involved in the self-assembly of the cylindrical nanofiber shown in (a) as a function of reduced time.

2.3.3 Formation of cylindrical nanofibers is preceded by multiple merging events involving spherical micelles

A kinetic mechanism, which is responsible for the formation of cylindrical nanofibers, is deciphered based on the results from 10 simulations at a moderate temperature (T* = 0.11) and weak electrostatic interaction strength (ε_{ES} = 100%ε_{HB}). It involves a series of steps: (1) simultaneous formation of multiple spherical micelles driven by hydrophobic interactions between alkyl tails, and (2) micelle-merging events prompted by the exposure of the hydrophobic core due to the change in the architecture of the spherical micelles that ultimately leads to the fabrication of one continuous rod-shaped nanostructure. **Figure 2.2b** depicts such a mechanism through time-dependent snapshots by capturing the self-assembly process of a cylindrical nanofiber containing 37 PA molecules that were selected for ease-of-viewing from the 800-PA system. Initially, each system is raised to a high temperature of T* = 5.0 briefly to ensure that all PA molecules are indiscriminately dispersed as random coils to minimize any bias that might potentially be added to the simulation. Next, the system is reduced to a specified temperature of T* = 0.11 that remains constant throughout each MD simulation to begin a production run (t* = 0.0).

Immediately following the production run, groups of 5–7 PA random coils condense into multiple small micelles spontaneously by forming hydrophobic interactions between neighboring alkyl tails (t* = 6.1). Since the electrostatic repulsion between charged

residues are located at the periphery of each micelle, peptide segments adopt a disperse arrangement to minimize the charge-charge repulsion through the creation of a spherical micelle with the residues distributed uniformly on the surface. Due to the kinetic energy, spherical micelles continue to collide with one another and gradually over time collapse together to form a larger elongated unit via a micelle-merging step, thereby reducing the total number of aggregates as seen at t* = 10.3. This micelle-merging event can be attributed to the presence of exposed hydrophobic regions of the alkyl tails on spherical micelles provided that the initial aggregate sizes are relatively small. In other words, spherical micelles merge together by forming more hydrophobic interactions at the micelle-micelle interface between exposed hydrophobic domains on two micelles.

Over the course of simulation, the elongated structure continues to add one more micelle at t* = 19.9 and another at t* = 39.3. Upon undergoing multiple successive micelle-merging events, the resulting self-assembled structure is shown at t* = 194.8 containing a total of 37 PA molecules. The final nanostructure is similar to the cylindrical nanofiber model that has been proposed by Stupp and coworkers[12,13] (see Subsection 2.3.5).

The kinetic mechanism involving micelle-merging events is quantitatively shown in **Figure 2.2c**, which plots the average number of PA molecules per aggregate and the number of aggregates as a function of reduced time. This plot indicates that the average number of PA molecules per aggregate increases while the total number of aggregates decreases in a step-wise manner. At distinct points of time (t* = 39.3 and 115.0), a step-function is characterized by the decrease in the total number of aggregates whereas the average number of PA molecules increases until the formation of one final aggregate is reached. Such successive micelle-merging events are typical in all simulations at moderate

temperatures and weak electrostatic interaction strengths allowing spherical micelles to merge together to form large cylindrical nanofibers.

2.3.4 High frequency of micelle-merging events is correlated to an ordering process by the peptides on the surface of spherical micelles through the formation of β-sheets

Hydrophobic interactions by the alkyl groups are responsible for the formation of small spherical micelles causing the alkyl groups to locate in the interior core and the peptide segments to reside on the surface. Since each peptide segment contains three negatively charged residues of glutamic acid, those charges are uniformly distributed along the surface of spherical micelles to minimize the number of charge-charge repulsions between neighboring PA molecules. Once in an aggregated state, peptide residues start forming intermolecular hydrogen bonds resulting in the creation of β-sheets. As a result, the peptide segments on the surface are no longer uniformly distributed; instead, such an ordering process of β-sheet formation creates segregation wherein isolated β-sheets expose the hydrophobic core to the surface. These micelles subsequently merge together at the exposed location through hydrophobic interactions by the alkyl groups. This information can be extracted from **Figure 2.2c** and **Figure 2.2d**, which plots the percentage of secondary structure formation by the PA molecules that eventually form the cylindrical nanofiber as a function of time. Over a short period of just t* = 20 time units initially, the number of aggregates reduced quickly from 10 to 2 while the percentage of β-sheet structure is already half of the final value of 30% at t* ~ 200. After this early stage (t* > 20), the peptides within the self-assembled cylindrical nanofiber undergo a slow reorganization process until the end of simulation by increasing the percentage of β-sheet

structure from 15% to 30%. As a result of such a structural reordering process, random coil conformations decrease as the nanostructure stabilizes towards the end of simulation to reach equilibrium. In other words, the sharp increase in β-sheet formation during the early stage of the self-assembly process corresponds to the high frequency of micelle-merging events. This correlation indicates the formation of β-sheets thereby facilitating the exposure of hydrophobic regions so micelle-merging events can take place.

2.3.5 Similarity between coarse-grained PA self-assembled structure and experimental morphology and all-atom molecular dynamics simulation

The self-assembled cylindrical nanofiber structures from the ePRIME model show high fidelity to the proposed model structure by Stupp and coworkers.[12,13] Using cryo-TEM, they performed structural characterization of nanofibers by examining the result of positive-stain TEM that preferentially stains for acidic groups. Since the image showed two concentric circles with the outer circle darker compared to the inner circle, it was hypothesized that the charged residues from the peptide sequence were on the surface of the cylindrical nanofiber whereas the core is composed of the hydrophobic alkyl tail. FTIR spectroscopy data further indicated the presence of secondary structure elements such as α-helices and β-sheets. A typical oblong structure observed from our simulations (at a moderate temperature simulation of $T^* = 0.11$ and weak electrostatic interaction strength of $\varepsilon_{ES} = 100\%\ \varepsilon_{HB}$) as shown in **Figure 2.2a** parallels the model structure of a cylindrical nanofiber proposed from experiments by presenting its fiber axis (i.e., vertical axis) that is longer in comparison to its horizontal axis. Moreover, in accordance with experimental data, peptide residues are distributed at the surface of the nanostructure exhibiting β–

sheet conformations with the core of the structure populated by hydrophobic alkyl tails. These tails are intertwined and entangled to maximize the number of favorable hydrophobic interactions due to their relative structural flexibility as compared to the peptide segments. This arrangement can be attributed to the following reasons: (1) alkyl tails can only interact with one another via hydrophobic interactions that are non-isotropic in nature; (2) the entropic cost to arrange themselves in an absolutely ordered fashion is prohibitively high.

The morphology of our cylindrical nanofiber structures compares reasonably well with the all-atom simulation results by Lee, Stupp et al.[29] They performed an explicit solvent atomistic molecular dynamics simulation for 40ns starting from a structure that was built by arranging 144 PA molecules (whose peptide sequence is SLSLAAAEIKVAV) into a cylindrical nanofiber model as proposed Stupp and coworkers.[12,13] Lee, Stupp et al., characterized the distribution of water molecules inside the fiber and found that water molecules solvate around the peptide portion without penetrating into the alkyl tails during the simulation.[29] This agrees with spectroscopic measurements by Tovar et al., who used a hydrophobic probe attached to various locations on a different IKVAV-bearing PA molecule PA molecule (peptide sequence: AAAAGGGEIKVAV) and found that the peptide shell is well solvated.[47] Although the solvent is not explicitly modeled in our simulations, most peptide segments of our cylindrical structures are significantly exposed to the surroundings whereas the interior portion is relatively shielded. This can be seen in a snapshot of the full structure shown in **Figure 2.2a**. However, the alkyl portion of our cylindrical structure has a high degree of porosity as shown in **Figure 2.3a** indicating that the alkyl tails are not closely packed with one another. Instead, many valine residues

position themselves in the interior among the alkyl tails as seen in **Figure 2.3b**, which shows all alkyl tails and valine residues of the cylindrical nanofiber. Due to the bulkiness and strong hydrophobicity of the valine sidechains as compared to any other chemical groups available in this system, favorable hydrophobic interactions with the alkyl tails can be formed. Therefore, the interior core is closely packed and shielded from the surrounding since many valine residues, which adopt random coil conformations, intertwine with the alkyl tails. Since it is uncertain to speculate that the hydrophobic residues peripheral to the alkyl tail are buried within the hydrophobic core based on the spectroscopic experiments by Tovar et al.,[47] comparison with their results is inconclusive. However, it is of certainty to state that our results regarding the hydrophobic core are in contrast with the observation by Lee, Stupp et al., who found that only the alkyl portion is closely packed.[28] This can be attributed mainly to the difference in our choice of the peptide sequence (VVVAAAEEE) and to some degree their simulation setups. Because the initial configuration in the atomistic simulation by Lee, Stupp et al., is a densely-packed cylindrical nanofiber structure,[29] PA molecules especially the interior segments are perhaps too confined to undergo any dynamics after just 40ns for the hydrophobic residues at the interior to form interactions and intertwine with the alkyl tails on neighboring molecules. Moreover, the secondary structures were fixed in the coarse-grained simulations by Lee, Cho et al., which could deter the formation of hydrophobic interactions between the first few peptide residues and the alkyl tails.[33] In comparison, our simulations are started from random configurations so the PA molecules have the freedom to undergo the whole self-assembly process before arriving at the lowest energy state. In this case, it is more favorable for the valine residues to form hydrophobic interactions with the alkyl tails than hydrogen bonds with neighboring

peptide segments; thus those residues become random coils. In light of our results, experimental work using this selected peptide sequence of VVVAAAEEE may see a more dramatic shift in peak intensity of spectroscopic measurements due to the incorporation of strongly hydrophobic residues that are peripheral to the alkyl tail in order to extend the notion of a minimal void space within the interior of the self-assembled structure.

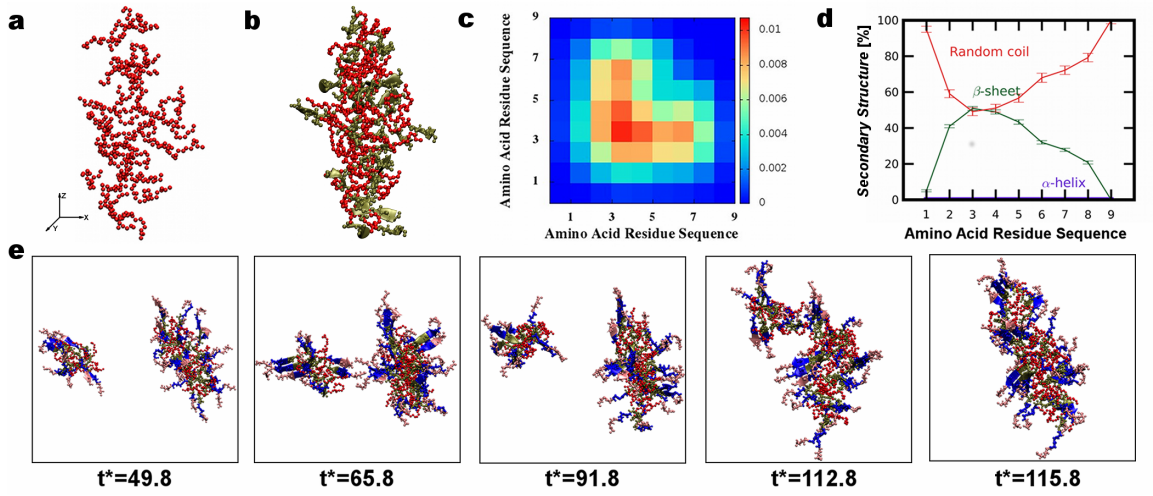

Figure 2.3. (a) Hydrophobic core of a cylindrical nanofiber (**Figure 2.2a**) comprised of alkyl tails from a simulation at a moderate temperature (T* = 0.11) and weak electrostatic interaction strength (ε_{ES} = 100% ε_{HB}) shown with the fiber axis along the z-direction and (b) Hydrophobic core of the same cylindrical nanofiber comprised of alkyl tails and valine residues. (c) The probability for each peptide residue to form a hydrogen bond with another residue on a neighboring peptide is shown. The amino acid residue sequence of $V_3A_3E_3$ corresponds to numbers 1-9 respectively. (d) The percentages of secondary structures corresponding to the amino acid residue are shown. (e) Time-dependent snapshots show the last self-assembly step involving a micelle-merging event between two micelles to form the cylindrical nanofiber as shown in **Figure 2.2b**. For (c) and (d), data is taken from the average of the last 10% of equilibrium data for 10 independent simulations performed at the same conditions shown in **Figure 2.2**.

The arrangement of the peptides forming β-sheets within our cylindrical nanofibers is relatively disordered in such a way that each peptide is shifted by a few residues compared to its neighbors. Such a misalignment among the peptides within β–sheets at the surface can be seen in **Figure 2.3c**, which is a contour plot representing the probability that a residue forms a hydrogen bond with any residues on a neighboring peptide. This plot

indicates that that the position of the sidechains of the peptide sequence contributes to the misalignment of the hydrogen bond formation. Specifically, hydrophobic residues 3 and 4, corresponding to valine and alanine respectively, are primarily responsible for the formation of β-sheets as seen in **Figure 2.3d**, which shows the probability of each residue forming a particular secondary structure motif. In other words, the residues that are positioned further away from charged glutamic acid residues and to the alkyl tails contribute to the large percentage of β-sheet formation. In contrast, the valine residues at positions 1 and 2 adopt mostly random-coil conformations because they are buried within the interior forming hydrophobic interactions with the alkyl tails. Similarly, the three glutamic acid residues at positions 7 - 9 adopt random coil conformations due to the electrostatic repulsion between the charges on their sidechains.

2.3.6 Formation of a cylindrical nanofiber involves micelle-merging events through an "end-to-end" mechanism due to electrostatic repulsions

The growth of cylindrical nanofibers is unidirectional allowing additional spherical micelles to add onto the cylindrical structure only through its ends (top and bottom positions along the z-direction of the structure shown in **Figure 2.2a**). For example, the final micelle-merging event of the self-assembly process observed in the simulation shown in **Figure 2.2b** occurs at the ends of the cylindrical micelle as opposed to any other location. **Figure 2.3e** renders detailed snapshots at sequential times preceding the resulting self-assembled structure from the same simulation as depicted in **Figure 2.2a**. Initially, two micelles are present (t* =49.8 in **Figure 2.3e**) with the right cylindrical one slightly larger in size (27 PA chains) than the left spherical micelle (10 PA chains). The

micelle on the left interacts with the micelle on the right at multiple instances yet the final merging event of a non-spherical assembly does not occur for a long time. At t* = 65.8, the two micelles are within close contact with the left spherical micelle approaching the right cylindrical micelle on the side only to be dispersed away at t* = 91.8. Next, as a second attempt, the spherical micelle traversed to the top of the cylindrical micelle (t* = 112.8) to which it finally succeeds in a micelle-merging event (t* = 115.8). From these interactions, we hypothesize that micelle-merging events occur via an "end-to-end" growing mechanism.

The morphological transition from a spherical to a cylindrical nanostructure can be attributed to minimizing the electrostatic repulsion between PA chains while maximizing hydrophobic interactions between the alkyl tails that drive micelle-merging events. The first merging event involves two spherical micelles meeting at any location where hydrophobic regions are exposed to the surface. This event creates the first oblong micelle; subsequent micelle-merging events are significantly different due to the positions of the charged residues. As a spherical micelle merges onto the cylindrical micelle during the self-assembly process, the oblong micelle is not only larger in size, but also is comprised of more charged residues. To accommodate more PA molecules, a spherical to non-spherical assembly transition is exhibited at t* = 115.8 in **Figure 2.3e** arriving at a self-assembled structure that is cylindrical with a large percentage of β –sheet formation. With efforts to minimize the electrostatic repulsion, charged residues are positioned on the surface, but due to geometry restriction, the total charge on the fiber axis is significantly greater than the other. This provides an explanation as to why the spherical micelle on the left is seen to interact with the cylindrical micelle on the right at multiple instances. Significant electrostatic repulsion on the side of the cylindrical micelle prevents the spherical micelle

to merge onto the cylindrical micelle. However, at the optimal placement of these two micelles, noticeably at the "end" of the micelles, a micelle-merging event occurs due to the presence of lesser electrostatic repulsions.

2.3.7 Increasing the strength of the electrostatic interaction between charged residues results in a cylindrical to spherical morphological transition

Repulsive electrostatic interactions play an important role in determining the morphology of the self-assembled nanostructures as seen in **Figure 2.4a**, which shows snapshots of large aggregates observed at the end of the simulations at increasing electrostatic interaction strengths and the same moderate temperature (T* = 0.11). Self-assembled nanostructures display a hydrophobic core comprised of alkyl tails and the surface aligned with charged residues. When the strength of the electrostatic repulsion is weak or moderately strong (i.e., $50\%\varepsilon_{HB} \leq \varepsilon_{ES} \leq 300\%\varepsilon_{HB}$), cylindrical nanofibers as described previously in **Figures 2.2** and **2.3** are the prevalent species. Over this particular range of electrostatic repulsion strengths, the amount of β-sheet varies slightly as shown in **Figure 2.4b**, which plots the percentages of secondary structure elements (α-helix, β-sheet, random coil) as a function of the electrostatic interaction strength. The percentage of β-sheet is at the highest quantity of ~35% when the strength of electrostatic repulsion is relatively weak at a value of $\varepsilon_{ES} = 50\%\varepsilon_{HB}$; it drops to ~25% when the when the strength of electrostatic repulsion is relatively strong at a value of $\varepsilon_{ES} = 300\%\varepsilon_{HB}$. Such a range of β-sheet amounts observed in our simulations for cylindrical nanofibers is in good agreement with previous CD spectra experiments by Niece et al.,[48] who found the β-sheet population of IKVAV-bearing PAs is ~25 ± 20% even though our peptide of a completely different

sequence. They also determined the α-helix population of IKVAV-bearing PAs showing a broad range from less than 10% to ~80%. Although the α-helix population is minimal from our simulations at this moderate temperature of T* = 0.11, lowering the temperature to T* = 0.09 increases the α-helix population to ~8% without disrupting the cylindrical nanofiber morphology of self-assembled nanostructures as shown in **Figure 2.6a** and **Figure 2.6b**, and discussed in Subsection 2.3.9.

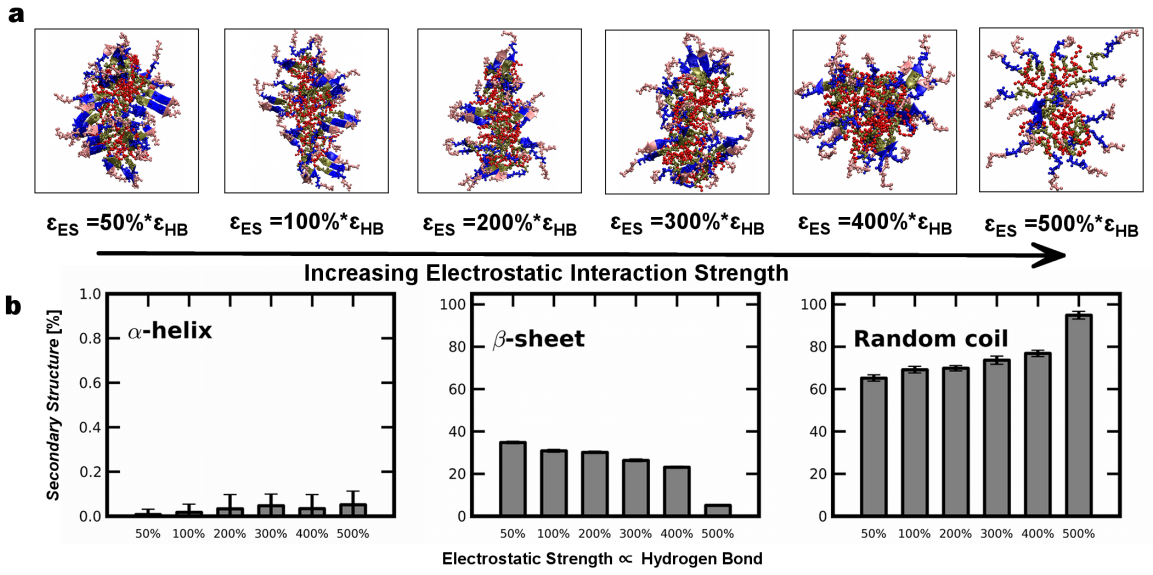

Figure 2.4. (a) Snapshots of representative self-assembled structures observed from simulations at increasing electrostatic repulsion strength between charged residues showcasing a spherical to cylindrical transition. (b) Comparison of secondary structure elements (α-helix, β-sheet, random coil) as a function of the electrostatic interaction strength that is varied relative to the strength of a hydrogen bond. All simulations are conducted at the same moderate temperature of T* = 0.11.

The morphology of self-assembled supramolecular aggregates undergoes a sharp transition as a function of the strength of the electrostatic repulsion. A shift from cylindrical nanofibers to spherical micelles occurs when the strength of the electrostatic repulsion increases significantly above the strength of hydrogen bond (i.e., ε_{ES} > 300%ε_{HB}). Interestingly, the spherical micelles at ε_{ES} = 400%ε_{HB} is quite distinctive from those at

higher electrostatic repulsion strengths (e.g., ε_{ES} = 500%ε_{HB}). The amount of β-sheet decreases significantly from almost 25% at ε_{ES} = 400%ε_{HB} to about 5% at ε_{ES} = 500%ε_{HB}; inversely, the amounts of random coils considerably increase. This suggests when electrostatic repulsion strengths are strong, charged residues are positioned uniformly around the surface maximizing the distance between charged residues and prohibiting additional interactions with PA molecules on other micelles.

The morphological transition observed for supramolecular aggregates as a function of the electrostatic interaction strength is analogous to experimental results that have examined the effects of pH and ionic concentration. Xu et al., examined a series of peptide amphiphiles with different length of hydrophobic alkyl tails at different pH conditions.[49] The nanofibers self-assembled from PAs with relatively short hydrophobic alkyl tail at an acidic pH convert into spherical micelles upon a pH increase due to electrostatic repulsion between the headgroups from deprotonation of the peptide charges. For the system containing relatively long hydrophobic alkyl tails, a high number of hydrophobic interactions can tolerate the electrostatic repulsion, thus maintaining the nanofibers regardless of the changing pH. Toksoz et al., investigated the effect of charged groups on the peptides on nanofiber formation, which was triggered upon neutralization of the charged residues by pH change or addition of either electrolyte or biomacromolecules.[50] For PA molecules that do not undergo charge neutralization, no nanofiber structure was observed, resulting in the formation of a viscous solution in contrast to a gel. Ghosh et al., demonstrated that certain self-assembling PA molecules can exhibit a pH-triggered reversible assembly mechanism switching between single molecules, spherical micelles, and nanofibers through the precise control of several tenths of a pH unit.[51] They observed a

shift from cylindrical nanofibers to spherical micelles occurring at a pH value of ~6.0, which corresponds to our strength of the electrostatic repulsion that is significantly above the strength of hydrogen bond (i.e., $\varepsilon_{ES} > 300\%\varepsilon_{HB}$). This qualitative correlation indicates that our results can provide a framework in elucidating the governing principles underlying PA self-assembly and explaining existing trends observed in characterizing PA aggregation.

2.3.8 Micelle-merging events are not observed at strong electrostatic interactions

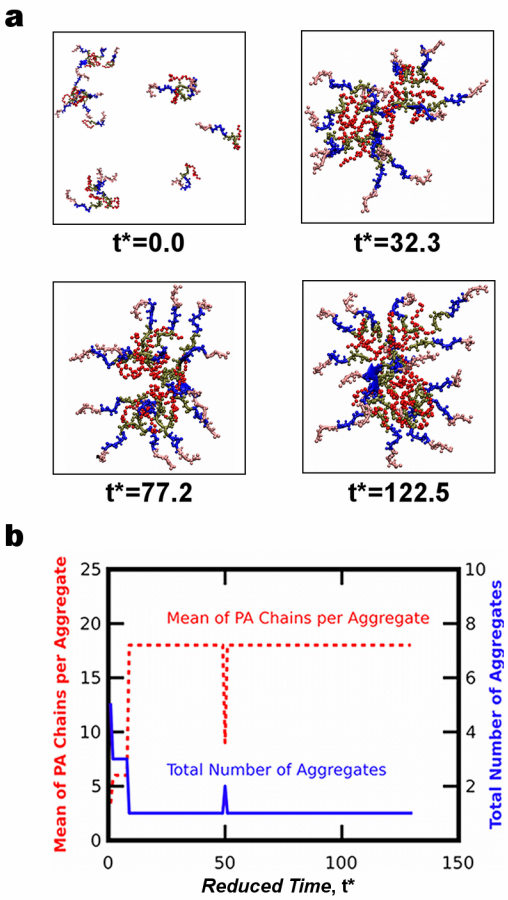

Figure 2.5. (a) Snapshots of the self-assembly process at strong electrostatic repulsion (ε_{ES} = 500% ε_{HB}) and a moderate temperature (T* = 0.11) as a function of reduced time units. (b) Corresponding plot of the average size of an aggregate characterized by the number of chains and the total number of aggregates as a function of time.

Contrasting with the weak conditions described earlier, an alternative mechanism is involved at highly repulsive electrostatics as shown in **Figure 2.5a** through time-dependent snapshots of the self-assembly process when the electrostatic interaction strength is significantly stronger than a hydrogen bond (ε_{ES} = 500%ε_{HB}) and moderate temperature (T* = 0.11). Due to strong charge-charge repulsion, intermolecular hydrogen bonds favoring the formation of β-sheets are near impossible between neighboring peptides. Once micelles are formed, charged residues are distributed uniformly along the surface of each micelle inhibiting interactions with the nearby micelles. Therefore, these micelles become spherical and persist as isolated aggregates throughout each simulation. Such a mechanism of self-assembly is quantitatively seen in **Figure 2.5b**, which plots the average aggregate size increasing and the number of aggregates decreasing over a brief period of time to form a spherical micelle. This indicates that the chosen spherical micelle containing 18 PA molecules remains relatively stable over a long period of time with the absence of multiple micelle-merging events. The size of such spherical nanostructures is much less than cylindrical nanofibers that are formed through multiple merging events involving many spherical micelles when the electrostatic repulsion is weaker as shown in **Figure 2.2**.

2.3.9 At low temperatures, spherical micelles with both α-helical and β-sheet structures are observed

Temperature plays an important role during the folding and self-assembly process of PA molecules at various PA concentrations. As shown in **Figure 2.1b**, a single PA molecule at an extremely diluted concentration folds into an α-helical conformation at low temperatures (T* = 0.07). At moderate temperatures (T* ≥ 0.09), the α-helical

conformation unravels; however, weak interactions between the hydrophobic alkyl tail and valine residues are still present. As the temperature increases further, the PA molecule adopts to more extended conformations ($T^* \geq 0.13$). This behavior carries over to the system at high PA concentrations as decreasing the temperature from $T^* = 0.11$ to $T^* = 0.08$ shifts the cylindrical nanofibers to predominant spherical micelles with occasional rod-like structures. Interestingly, the spherical micelle structure observed at $T^* = 0.08$ shows the presence of α-helical conformation in addition to β-sheet as shown in **Figure 2.6a**. Indeed, the amount of α-helical conformations and β-sheet are highly dependent upon the temperature as shown in **Figure 2.6b**. The optimal β-sheet formation occurs at intermediate temperatures of $T^* = 0.10 - 0.11$ which corresponds to the temperature at which the α-helix reaches complete unfolding (**Figure 2.1d**). The optimal α-helix formation occurs around $T^* = 0.08 - 0.09$, which is of the temperature range where a single PA molecule folds into an α-helical structure.

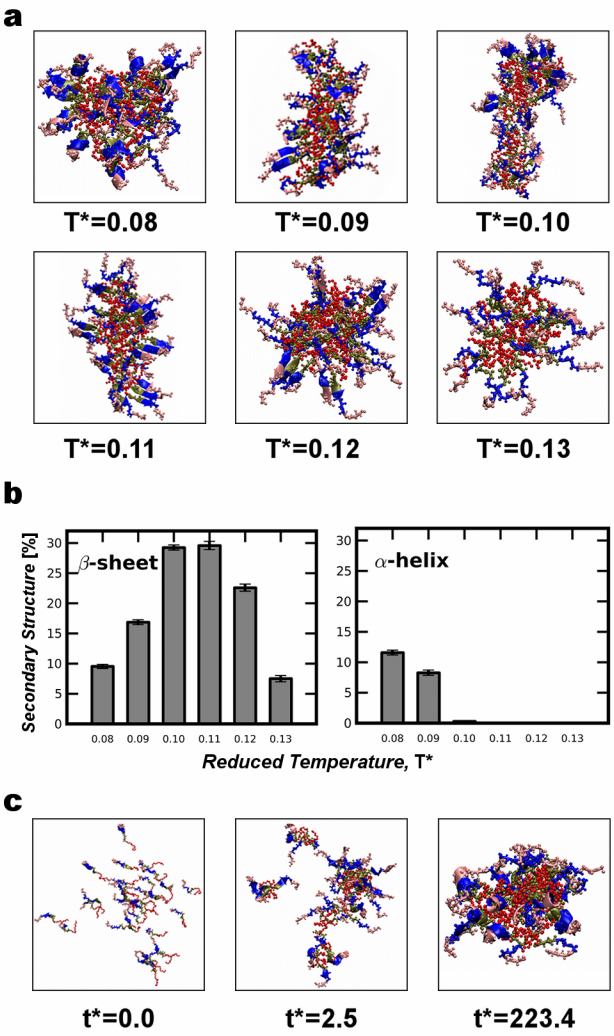

Figure 2.6. (a) Snapshots of representative self-assembled structures observed from simulations of increasing temperatures and weak electrostatic interaction strength (ε_{ES} = 100% ε_{HB}). (b) Plots of the percentage of β-sheet and α-helical structures as function of the temperature; the data are averaged from the last 10% of all simulations at equilibrium. (c) Time-dependent snapshots of the self-assembly process for the formation of a spherical micelle at a low temperature of T* = 0.08 exhibiting predominantly α-helical and some β-sheet structures.

The mechanism of forming spherical micelles with α-helical conformations at a low temperature of T* = 0.08 is unique in the sense that secondary structure elements are formed prior to a condensation step as shown in **Figure 2.6c**, which shows time-dependent snapshots of the self-assembly process for the formation of a spherical micelle. Single PA molecules exhibiting extended conformations swiftly form hydrogen bonds (i.e.,

intramolecular to create α-helices) followed by the formation of a spherical micelle at low temperatures. This is in contrast to the mechanism responsible of forming cylindrical nanofiber structures at higher temperatures wherein condensation into an aggregate precedes the formation of hydrogen bonds (i.e., intermolecular to create β-sheet). The presence of α-helical structures, which are distributed evenly on the surface, prevents micelle growth and elongation due to steric interactions and electrostatic repulsions.

Increasing the temperature beyond T* = 0.11 shifts the cylindrical nanofibers to spherical micelles as shown in **Figure 2.6a**. Spherical micelle structures are also observed at T* = 0.13 but lack the presence of secondary structure as indicated by the quantitative results plotted in **Figure 2.6b**. In this case, the kinetic energy at a high temperature prevents non-isotropic hydrogen bonds from forming yet still allows isotropic hydrophobic interactions to occur to form micelles. A further increase in the temperature prevents micelles from self-assembly; thus all PA molecules are random coils at high temperatures (i.e., T* > 0.13).

2.3.10 Electrostatics-temperature phase diagram of self-assembled nanostructures

In this study, we investigate the effect of temperature on the self-assembly of PA chains by performing MD simulations on a system containing 800-PA molecules at a high concentration of c = 85mM over a wide range of temperature. Moreover, we examine the role of ionic concentration and pH on self-assembly by varying the repulsive strength (ε_{ES}) of the electrostatic interactions between charged glutamic acids systematically relative to the strength of a hydrogen bond (ε_{HB}). The results from these simulations are summarized

as a phase diagram shown in **Figure 2.7**, which delineates the regions where distinct structures are stable as a function of the temperature and electrostatic interaction strength.

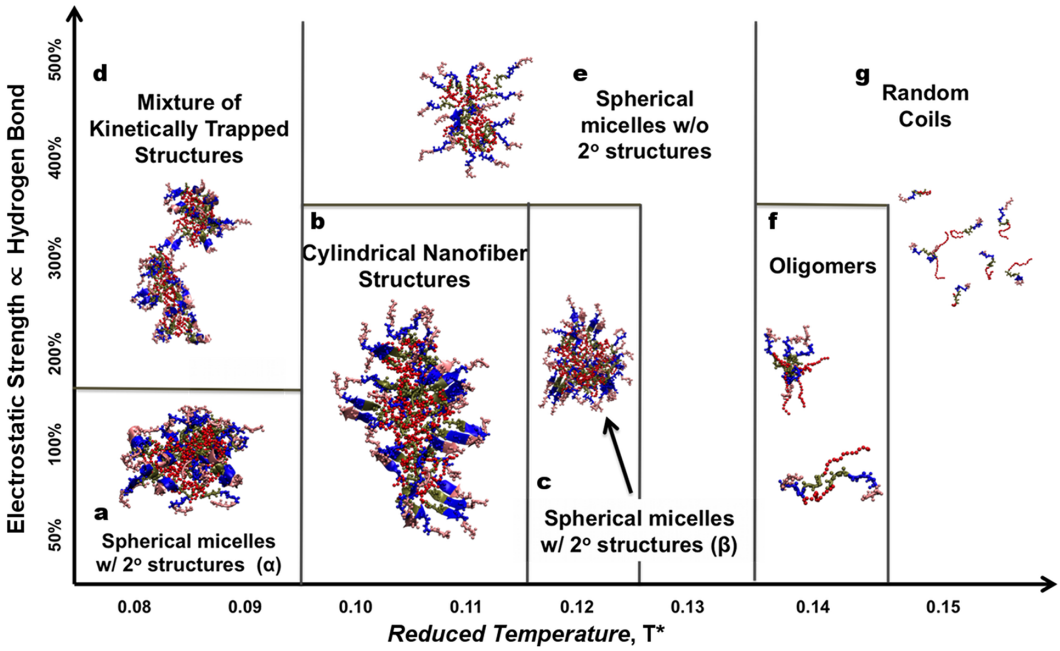

Figure 2.7. Phase diagram obtained from simulation results at various electrostatic interaction strengths and temperatures. Defined regions are marked indicating the different morphologies exhibited including: (a) spherical micelles with predominantly α-helices; (b) cylindrical nanofiber structures; (c) spherical micelles with only β-sheets; (d) mixture of kinetically trapped amorphous aggregates; (e) spherical micelles without secondary structure elements; (f) oligomers; (g) random coils.

When the charge-charge repulsion is weak at a low temperature, the high propensity for PA molecules to form intramolecular interactions result primarily in spherical-like structures that are comprised of mostly α-helices in addition to β-sheets (**Figure 2.7a**). With an increase in temperature, predominant spherical micelles containing α-helices and β-sheets transition into cylindrical nanofibers that have prevalent β-sheets located on the surface (**Figure 2.7b**). Further increasing in temperature drives a second morphological transition from cylindrical nanofibers to spherical micelles with only β-sheets (**Figure 2.7c**). At sufficiently high temperatures, spherical micelles are still present;

however, they lose secondary structures as the peptide segments unravel into random coils (**Figure 2.7e**). At extreme temperatures, small aggregates or oligomers exist (**Figure 2.7f**). Increasing the temperature further prevents PA molecules to form aggregates; in this case, PA molecules exist as random coils (**Figure 2.7g**).

When the electrostatic repulsion is strong at low temperatures, a mixture of kinetically trapped structures is observed (**Figure 2.7d**). Initially, PA molecules quickly self-assemble into small aggregates; however, the charges of glutamic acids are not only on the surface but also in the interior to avoid strong electrostatic repulsions. Therefore, a few PA molecules are able to organize themselves in an opposite orientation to form small aggregates with alkyl tails exposed on the surface and peptide segments located in the structure's interior. Thus by definition, these structures are strictly not micelles. Resulting structures are due to favorable interactions between alkyl tails of neighboring aggregates in addition to contributions by occasional peptide segments that protrude further away from the hydrophobic core to facilitate hydrogen bond formation across different aggregates. Due to low kinetic energy present in the system, just a few favorable hydrophobic interactions or hydrogen bonds can hold these aggregates together and maintain their stability. These interactions serve as strong linkers between multiple aggregates that undergo minimal structural rearrangement resulting in the formation of large kinetically trapped amorphous aggregates. While the morphology is ill-defined, these structures exhibit a significant number of α-helices (~10%) and β-sheets (~13%). They are different than those at the same low temperature but weaker electrostatic repulsions (**Figure 2.7a**), wherein every PA molecule within a micelle organizes themselves in the same orientation (alkyl tails in the interior while peptide segments on the surface forming

both α-helices and β-sheets) without linkers between multiple micelles. At higher temperatures and strong electrostatic strength, small spherical micelles without secondary structure elements are observed (**Figure 2.7e**). Charge-charge repulsion results in the uniform distribution of the charges reducing the ability of proximal peptide residues to form β-sheet structures. Increasing the temperature further destabilizes hydrophobic interactions, which results in the formation of oligomers (**Figure 2.7f**) and extended conformations (**Figure 2.7g**).

The phase diagram obtained by the results of our simulation captures a similar range of morphological structures observed in the Monte Carlo simulations by Velichko et al.;[32] however, our phase diagram expands further from their schematic phase diagram due to our inclusion of additional relevant interactions and realistic representation of the model PA molecule. First, through the use of the ePRIME model, peptide specificity is incorporated extending beyond the general chemical structure representation to describe the hydrophobic interaction between the sidechains of the hydrophobic residues and the alkyl tails. Second, specification of the twenty natural amino acids further accounts for the electrostatic interaction between charged residues to examine the different encompassing factors on the self-assembly process of PA molecules. Third, our model can accommodate the formation of secondary structures such as α-helices and β-sheets depending upon the peptide sequence. Therefore, our simulations are able to assemble a wider range of structures than those observed by Velichko et al.[32] For example, spherical micelles seen in our simulations contain both α-helical and β-sheet structures as well as those without secondary structure elements.

2.4 Conclusions

By using our newly-developed coarse-grained model of peptides and polymers called ePRIME, which is coupled with the very fast DMD technique, we have been able to examine spontaneous self-assembly of a large system of 800 PA molecules starting from a random configuration. Our model of peptide amphiphiles accounts for important molecular interactions such as steric interactions, hydrogen bonding, hydrophobic interactions, and electrostatic interactions, allowing MD simulations to capture the essential aspects of the self-assembly process of PA molecules. The molecular self-assembly process of PA molecules is found to be dependent upon the external stimuli such as the temperature and pH / ionic concentration. Resulting self-assembled nanostructures exhibit a wide range of morphologies including spherical, non-spherical, cylindrical fibers, amorphous structures with or without the presence of secondary structure elements, small oligomers, and single molecules with extended conformations as shown in a phase diagram in **Figure 2.7**. The ability for PA molecules to undergo morphological transitions in response to external stimuli offers versatility for applications in drug delivery, tissue engineering, and nanotechnology.

At appropriate conditions, random PA molecules are observed to self-assemble into large cylindrical nanofiber structures exhibiting the following morphological properties: (1) the peptide segments are on the surface encapsulating the alkyl tails which reside at the interior; (2) the micelles have a rod-like or cylindrical shape; and (3) a relatively high number of peptide residues exhibit β-sheet conformations contributed by valine and alanine residues whereas glutamic acid residues adopt random coil conformations. These simulation-observed properties are in agreement with experimental results extracted by

Stupp and coworkers.[12,13] Moreover, our simulation results offer similar structural details as compared those from a previous all-atom simulation study.[29]

Our simulation results can provide insights into a kinetic mechanism that is responsible for self-assembly of large cylindrical nanofiber structures. At a moderate temperature and weak electrostatic interactions, the formation of multiple spherical micelles precedes the self-assembly of cylindrical nanofiber nanostructure (**Figure 2.8a**). Spherical micelles can undergo multiple micelle-merging events to form cylindrical nanofibers by forming hydrophobic interactions between exposed hydrophobic regions. The presence of exposed hydrophobic domains on spherical micelles is facilitated by the formation of inter-molecular hydrogen bonds between neighboring peptide segments to create β-sheets. As peptide segments move closer to form β-sheets, this process segregates groups of peptides from one another thus exposing the hydrophobic alkyl tails to the exterior. The unidirectional transformation of spherical micelles into a cylindrical nanofiber as opposed to multi-directional transformation of spherical micelles into an amorphous aggregate is attributed to (1) the lessened amount of charge-charge repulsion on the ends of the structure and (2) accommodation of the number of increasing PA chains and maximizing the number of hydrophobic interactions between the alkyl tails.

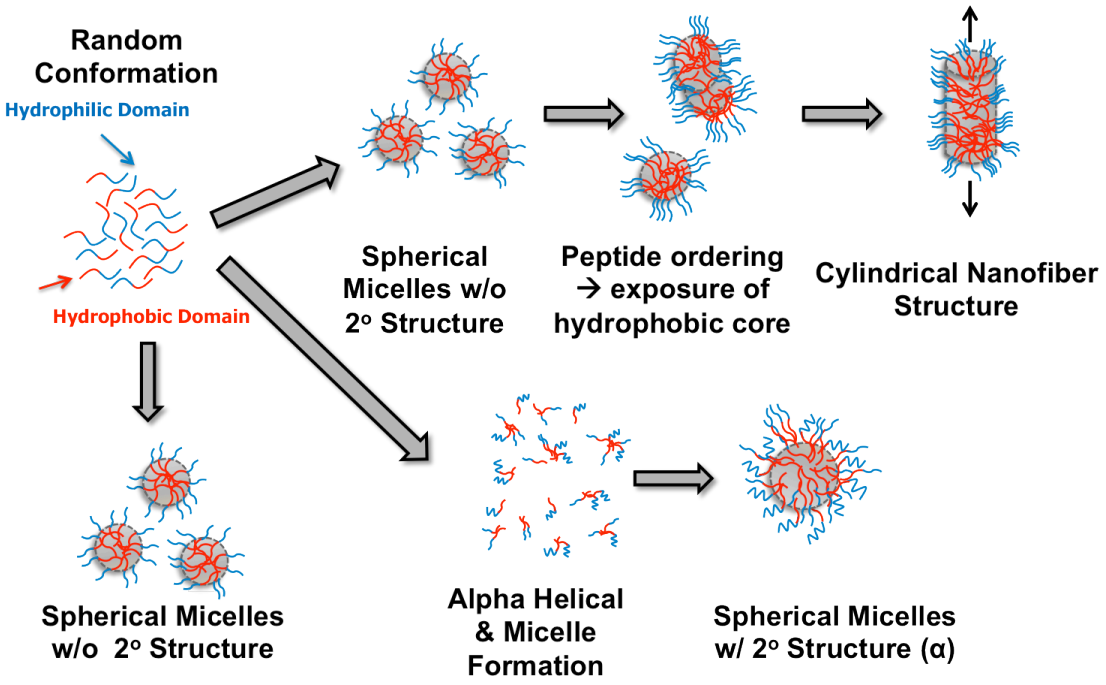

Figure 2.8. Schematic diagram of three kinetic mechanisms proposed by simulation results. (a) At moderate temperatures (T* = 0.10 - 0.11) and weak electrostatic interaction strength (ε_{ES} = 100% ε_{HB}), cylindrical nanofibers are formed. (b) At moderate temperatures, weak hydrophobic interaction strength, and strong electrostatic interaction strength (ε_{ES} > 300% ε_{HB}), spherical micelles are formed with the absence of secondary structures. (c) At low temperatures (T* = 0.08 - 0.09), mild hydrophobic interaction strength, and weak electrostatic interaction strength, spherical micelles with secondary structures (predominantly α-helices) are stable.

The kinetic mechanism of PA self-assembly involving micelle-merging events has also been observed recently via coarse-grained simulations by Lee, Cho et al.[33] who employed the MARTINI CG model.[34] They observed that PA molecules self-assemble into micelles, each of which is composed of 30 – 50 PA molecules; subsequently, these micelles merge forming a cylindrical fiber at a moderate temperature of T = 330K. They found that peptides are exposed to the fiber surface and the hydrophobic tails are aggregated inside the fiber, but the hydrophobic core exhibits some discontinuities along the fiber axis. To observe self-assembly of PA molecules into a fiber with a continuous hydrophobic core, they performed MD simulations at a much higher temperature, which allows the system to

access a relaxed configuration. In comparison, our typical spherical micelles are comprised of only 13-18 PA molecules and our cylindrical nanofibers that are self-assembled at a moderate temperature exhibit a continuous hydrophobic core. These differences might be attributed to the fact the secondary structure of a peptide was predetermined and fixed during their simulations; therefore, those PA molecules are relatively rigid.[33] In contrast, PA molecules in our simulations started out as flexible random coils, which can undergo an ordering process by forming β-sheet structures exposing the hydrophobic interior for micelle-merging events. Moreover, conformational conversion from random coils into β-sheets within a micelle is reminiscent of the amyloid fibril formation process in which amorphous oligomers transform into ordered fibril structures as was first shown by Serio et al.,[52] in a yeast prion protein Sup35 system and has been confirmed by many experiments and computer simulations in various amyloidogenic proteins systems.[37,53-57]

Two additional self-assembly mechanisms have been characterized to examine the effect of the electrostatic interaction strength and temperature on the self-assembly of nanostructures as shown through a schematic diagram in **Figure 2.8b** and **Figure 2.8c**. At a moderate temperature and strong electrostatic interactions, peptides experience significant charge-charge repulsion preventing them from forming intermolecular hydrogen bonds and thus β-sheets. Consequently, successive micelle-merging events are not observed; instead, spherical micelles without secondary structure elements are the predominant morphology (**Figure 2.8b**). When the temperature is low and electrostatic interaction strength is weak, intramolecular hydrogen bonding is immediately favorable resulting in the formation of α-helices that assemble into a spherical micelle as a stable structure, which also contains a small amount of β-sheets (**Figure 2.8c**).

It is hoped that our results as summarized in a phase diagram (**Figure 2.7**) will provide experimentalists some guidance in locating the temperature and electrostatics at which to conduct in-vitro self-assembly experiments to seek or avoid the formation of certain nanostructures. In our simulations, variables for experimental conditions are expressed in reduced quantities to provide a qualitative frame of reference. While a direct correspondence to experimental or physiological values is difficult, correlation at a reference condition can be established by identifying the melting temperature at which a PA molecule exhibits equal percentage of α-helical and random coil structures as shown in Figure 1d from all-atom and coarse-grained simulations; i.e., our melting temperature is T*=0.085 which corresponds to ~320K. Morphological transitions at higher or lower temperatures compared to the melting temperature are meant for a qualitative interpretation. Similarly, correlation between experimental pH (or ionic strength) values with our electrostatic interaction strengths can be obtained in a qualitative manner using our transition value (i.e., $\varepsilon_{ES} = 300\%\varepsilon_{HB}$) as a reference condition.

From the work described, it is important to note a number of limitations regarding our model and analysis. Inherently, the model is coarse-grained using a simplified representation of the PA molecule. Moreover, an implicit solvent model is used with the absence of water and salt ions resulting in an approximation of the force field of the solvent but this is instead exchanged for the increase in computational tractability and performance. Furthermore, hydrophobic interactions are modeled independent of temperature, which is a simplification of the known models of temperature-dependent hydrophobicity.[58,59] Despite these limitations, our model allows us to conduct large-scale molecular-dynamics simulations to observe a wide range of nanostructures and

morphological transitions that are dependent upon the ionic strength and temperature. Comparison of the observed nanostructures with both experimental and all-atom simulations have shown to exhibit a high degree of structural resemblance indicating the lengths at which interactions are modeled and accounted are of biological relevance. Ongoing research in our group is aimed at using this method to study the effects of varying the peptide sequence, peptide concentration and hydrophobic interaction strength on the formation of interesting nanostructures in different environments. These studies can provide a template to guide experimental efforts in identifying critical interactions that are possessed by a chosen PA molecule and affected by external environmental conditions in forming self-assembled structures. We hope to extend our current simulations to aid in the design and development of bio-inspired materials for the fields of drug delivery, diagnostic medicine, tissue engineering, and regenerative medicine.

2.5 Acknowledgements

This work was originally published in Advanced Healthcare Materials, 2013 © Wiley-VCH. Co-authors include Cade B Markegard, Brian K Chu, and Hung D Nguyen. We are grateful to Wonpil Im (U. Kansas) for assistance on parameterization of PA molecules in CHARMM. HDN acknowledges financial support from UC Irvine. IWF acknowledges support from a Graduate Research Fellowship from the National Science Foundation (DGE-0808392). This work used the Extreme Science and Engineering Discovery Environment (XSEDE), which is supported by National Science Foundation grant number OCI-1053575. We are also thankful for the computational resources provided by the GreenPlanet network and Broadcom Distributed Unified Cluster at UC Irvine.

2.6 Supporting Information

The model peptide amphiphile (PA) sequence is comprised of a sixteen-carbon alkyl tail covalently conjugated to nine residues of valine, alanine, and glutamic acids ($C_{16}H_{31}O$-$Val_3Ala_3Glu_3$), which was chosen based on previous experimental work by Pashuck et al.[42] Each PA molecule is represented using ePRIME, an extension of PRIME,[36-38] Protein Intermediate Resolution Model, accounting for all twenty natural amino acids. For the peptide segment, the backbone atoms (NH, $C_\alpha H$, and CO) of each amino acid residue are represented by three spheres. The model for the sidechains of each amino acid is adopted from the scheme originally developed by Wallqvist and Ullner.[40] In this case, all amino acid side chains, except glycine, are represented with at least one sphere. Short side chains are represented as one sphere while long side chains are represented as two spheres (the parameters of selected amino acids and the alkyl group are shown in **Table 2.1**). The size of a sidechain sphere is derived from the solvent accessible area, which was obtained by Eisenberg and coworkers.[39] The single-sphere sidechains are used for Ala, Val, Pro, Thr, Ser, Asn and Asp. The longer sidechains are subdivided into two hydrophobic spheres for the purely hydrophobic residues Leu, Ile, Phe, Tyr, Trp, Met and Cys. Amphiphilic sidechains such as Arg, Lys, Glu, Gln, and His are modeled with a hydrophobic first sphere and a hydrophilic second sphere. Each first sphere of the sidechain is connected to the CαH atom through a bond whose equilibrium distance corresponds to an average separation between CαH atom and the center of mass of the atoms represented by first side chain sphere. For the tail, each alkyl group, $-CH_2-$, is represented as single sphere, which is

connected to another alkyl group or the peptide segment through a bond whose equilibrium distance and fluctuation are extracted from available atomistic parameters. Each PA molecule $C_{16}H_{31}O$-$Val_3Ala_3Glu_3$ is represented by 55 united-atom spheres as shown in **Figure 2.1a**.

The solvent is modeled implicitly; its effect is factored into the energy function as a potential of mean force averaged over the solvent degrees of freedom. In other words, the effect of solvent is wholly incorporated into the effective residue-residue potential that is based on the hydrophobicity of each sidechain. This potential is essentially a measure of the free energy of transfer of amino acids from water to octanol as obtained by Eisenberg and coworkers.[39] In this case, the potential form was taken to be either a square-well potential, which approximates an attractive Lennard-Jones potential for purely hydrophobic side chains like alanine, or a square-shoulder potential, which approximates a repulsive form of the Lennard-Jones potential for purely hydrophilic side chains like aspartate. The interaction strength between two sidechain spheres is $\varepsilon_{HP,ij} = R * (\Delta G_i + \Delta G_j)$ where ΔG is the free energy of transfer of amino acids from water to octanol[39] and R is a measure of the strength of the hydrophobic/hydrophilic interaction (ε_{HP}). The value of this ratio R is an indication of the type of solvent used, a lower value is for apolar solvent while a high value is for a non-polar solvent. In this study, the value of R is fixed at R=1/3 for all simulations. Since the alkyl groups of the polymeric tail are non-polar, they are also allowed to form hydrophobic interactions with polymeric tail of other chains or non-polar sidechains of the peptide segment. Hydrogen bonding between amide hydrogen atoms and carbonyl oxygen atoms is represented by a directionally dependent square-well attraction of strength ε_{HB}=12 kJ/mol between NH and CO united atoms. Since the sidechains of Lys,

Arg, His, Glu, Asp are charged, the electrostatic contributions between two those charged sidechain groups are treated at the level of Debye-Huckel theory. The effective electrostatic interaction is implemented using a triple attractive/repulsive square well potential with a long interaction range of 12Å. Such interaction can be represented as a qq'/ ε_dr term where ε_d is the dielectric constant using three-step square-well or shoulder-well potentials. For simplicity, the maximum strength (ε_{ES}) of an electrostatic repulsion between two charges on the glutamic acids is $\varepsilon_{ES} = I^*\varepsilon_{HB}$ relative to that of the hydrogen bond, ε_{HB}, where I is a measure of the solvent condition that is affected by changing ionic concentration or pH.

Table 2.1. The ePRIME model: parameters of all united-atom spheres representing the studied peptide amphiphile molecule: $C_{16}H_{31}O$-$Val_3Ala_3Glu_3$.

Name	**Atoms**	**Hydropathy**	**Radius (Å)**	$\boldsymbol{\Delta G}$ **(kJ/mol)**	**Charge**
Backbone	-C_αH-	None	1.85	0.00	None
Backbone	-NH	None	1.65	0.00	None
Backbone	-CO	None	2.00	0.00	None
Ala sidechain	-CH_3	Hydrophobic	1.77	1.76	None
Val Sidechain	-$CH(CH_3)_2$	Hydrophobic	2.07	6.95	None
Glu Sidechain 1	-CH_2-	Hydrophobic	1.5	1.36	None
Glu Sidechain 2	-CH_2-COO-	Hydrophilic	2.5	-2.73	Negative
Alkyl	-CH_2-	Hydrophobic	1.5	1.36	None

Simulations are performed by using the DMD simulation algorithm,[41] a variant on standard molecular dynamics that is applicable to systems of molecules interacting via discontinuous potentials, e.g., hard-sphere, and square-well potentials. Unlike soft potentials such as the Lennard-Jones potential, discontinuous potentials exert forces only when particles collide, enabling the exact (as opposed to numerical) solution of the collision dynamics. DMD simulations proceed by locating the next collision, advancing the system to that collision, and then calculating the collision dynamics. For details on DMD simulations, see papers by Alder and Wainwright[41] and Smith, Hall, and Freeman[60].

Simulations are performed in the canonical ensemble with periodic boundary conditions imposed to eliminate artifacts due to box walls. Constant temperature is achieved by implementing the Andersen thermostat method.[61] In this case, all beads are subjected to random, infrequent collisions with ghost particles whose velocities are chosen randomly from a Maxwell Boltzmann distribution centered at the system temperature. Simulation temperature is expressed in terms of the reduced temperature, $T^* = k_BT/\varepsilon_{HB}$, where k_B is Boltzmann's constant, and T is the temperature. Reduced time is defined to be $t^*=t/\sigma(k_BT/m)^{1/2}$, where t is the simulation time, and σ and m are the average bead diameter and mass, respectively.

For the self-assembly simulations, starting from a random coil configuration, 800 PA molecules were placed in a cubic box with periodic boundary dimensions of 250 Å x 250 Å x 250 Å. The system containing 44,000 particles at a PA concentration of c = 85 mM. Each simulation was heated at high temperature (T^* = 5.0) to reach an un-biased initial configuration, and then quickly cooled to the temperature of interest, T^* = 0.08-0.15, for a constant-temperature production run until equilibration. To examine the effect of ionic concentration or pH on self-assembly, each simulation was conduct at an electrostatic repulsion strength of $\varepsilon_{ES} = I^*\varepsilon_{HB}$ relative to that of the hydrogen bond, ε_{HB}, where I is 50%, 100%, 200%, 300% and 500%. At each condition of the middle range of temperature and electrostatic repulsion strength, 10 independent simulations were conducted because of the stochastic nature of self-assembly. At each condition of the extreme ends of temperature and electrostatic repulsion strength, only three independent simulations were conducted since variability in the data is relatively low.

Quantitative results in this paper are averages of the last 10% of simulation data with error bars taken from the standard deviation. The secondary structures are defined through the implementation of STRIDE[62] including: α-helix, 3_{10}-helix, π-helix, β-strand/sheet (extended conformation), turn, bridge, isolated bridge, and random coil. However, we only focus on α-helix, β-strand/sheet, and random coil that also incorporate turn structures. An aggregate is defined if each peptide in a group of PA molecules has at least two interpeptide hydrogen bonds or four hydrophobic interactions with a neighboring PA molecule in the same group.

For model validation, a replica-exchange simulation conducted for a single PA chain on a system containing 16 replicas distributed over a broad interval of temperature ranging from $T^* = 0.07$ to a high temperature at which each peptide is a random coil ($T^* = 0.17$). Each replica system is simulated at a different temperature T in the canonical ensemble using the DMD method. The number of replicas and the distribution of temperatures are chosen to ensure that (1), there is a free random walk in temperature space, which means that every replica has the same probability of being switched to a neighboring temperature; (2), the number of replicas and hence temperatures sampled must be high enough to ensure that the probability of each replica being switched to a neighboring temperature is >10%; and (3), the highest temperature sampled must be high enough to prevent the system from becoming trapped in a local energy minimum. These requirements are the same as those stated by Sugita and Okamoto.[63] Exchange attempts occur every $t^* = 5.0$ reduced time units. This corresponds to a replica-exchange attempt after ~6,000,000 collisions at each temperature. 29,700 replica-exchange attempts are made before equilibrium is reached. The criteria for equilibrium is that the ensemble

average of the system's total potential energy, which is collected at the end of each DMD run, should vary by no more than 2.5% during the second half of all DMD runs at each temperature. Once equilibrium is reached, the data collection phase begins in which 3300 extra replica-exchange attempts are made.

All-atom replica-exchange simulation is also performed using NAMD[43] for a single PA chain to serve as a validation of our coarse-grained model. The simulation has 16 replicas over a wide range of temperature ranging from T = 260K to T = 550K using the CHARMM 27 force field.[64,65] A replica-exchange attempt is made at every 2000 steps, which corresponds to 4ps for each temperature and an approximate 85,000 replica-exchange attempts were made. Energy analyses are calculated using the last 10% of the simulation data with error bars corresponding to the standard deviation.

2.7 References

1. Drury, J. L. & Mooney, D. J. Hydrogels for tissue engineering: scaffold design variables and applications. *Biomaterials* **24,** 4337–4351 (2003).
2. Peppas, N. A., Hilt, J. Z., Khademhosseini, A. & Langer, R. Hydrogels in Biology and Medicine: From Molecular Principles to Bionanotechnology. *Adv. Mater.* **18,** 1345–1360 (2006).
3. Chow, D., Nunalee, M. L., Lim, D. W., Simnick, A. J. & Chilkoti, A. Peptide-based biopolymers in biomedicine and biotechnology. *Materials Science and Engineering: R: Reports* **62,** 125–155 (2008).
4. Anderson, J. M., Andukuri, A., Lim, D. J. & Jun, H.-W. Modulating the Gelation Properties of Self-Assembling Peptide Amphiphiles. *ACS Nano* **3,** 3447–3454 (2009).
5. Vermonden, T., Censi, R. & Hennink, W. E. Hydrogels for Protein Delivery. *Chem. Rev.* **112,** 2853–2888 (2012).
6. Lee, K. Y. & Mooney, D. J. Hydrogels for Tissue Engineering. *Chem. Rev.* **101,** 1869–1880 (2001).
7. Khademhosseini, A. & Langer, R. Microengineered hydrogels for tissue engineering. *Biomaterials* **28,** 5087–5092 (2007).
8. Branco, M. C. & Schneider, J. P. Self-assembling materials for therapeutic delivery. *Acta Biomaterialia* **5,** 817–831 (2009).
9. Cavalli, S., Albericio, F. & Kros, A. Amphiphilic peptides and their cross-disciplinary role as building blocks for nanoscience. *Chem. Soc. Rev.* **39,** 241 (2009).
10. Gupta, P., Vermani, K. & Garg, S. Hydrogels: from controlled release to pH-responsive drug delivery. *Drug discovery today* **7,** 569–579 (2002).
11. Yu, Y.-C. *et al.* Structure and Dynamics of Peptide–Amphiphiles Incorporating Triple-Helical Proteinlike Molecular Architecture †. *Biochemistry* **38,** 1659–1668 (1999).
12. Hartgerink, J. D. Self-Assembly and Mineralization of Peptide-Amphiphile Nanofibers. *Science* **294,** 1684–1688 (2001).
13. Hartgerink, J. D., Beniash, E. & Stupp, S. I. Peptide-amphiphile nanofibers: A versatile scaffold for the preparation of self-assembling materials. *Proceedings of the National Academy of Sciences* **99,** 5133–

5138 (2002).
14. Cui, H., Webber, M. J. & Stupp, S. I. Self-assembly of peptide amphiphiles: From molecules to nanostructures to biomaterials. *Biopolymers* **94,** 1–18 (2010).
15. Luo, J. & Tong, Y. W. Self-assembly of collagen-mimetic peptide amphiphiles into biofunctional nanofiber. *ACS Nano* **5,** 7739–7747 (2011).
16. Qiu, Y. & Park, K. Environment-sensitive hydrogels for drug delivery. *Advanced Drug Delivery Reviews* **53,** 321–339 (2001).
17. Ozbas, B., Kretsinger, J., Rajagopal, K., Schneider, J. P. & Pochan, D. J. Salt-Triggered Peptide Folding and Consequent Self-Assembly into Hydrogels with Tunable Modulus. *Macromolecules* **37,** 7331–7337 (2004).
18. Klok, H.-A. Biological-synthetic hybrid block copolymers: Combining the best from two worlds. *J. Polym. Sci. A Polym. Chem.* **43,** 1–17 (2004).
19. Dai, H. *et al.* A Temperature-Responsive Copolymer Hydrogel in Controlled Drug Delivery. *Macromolecules* **39,** 6584–6589 (2006).
20. Ahn, S.-K., Kasi, R. M., Kim, S.-C., Sharma, N. & Zhou, Y. Stimuli-responsive polymer gels. *Soft Matter* **4,** 1151 (2008).
21. Stendahl, J. C., Rao, M. S., Guler, M. O. & Stupp, S. I. Intermolecular Forces in the Self-Assembly of Peptide Amphiphile Nanofibers. *Adv. Funct. Mater.* **16,** 499–508 (2006).
22. Jiang, H., Guler, M. O. & Stupp, S. I. The internal structure of self-assembled peptide amphiphiles nanofibers. *Soft Matter* **3,** 454 (2007).
23. Beebe, D. J. *et al.* Functional hydrogel structures for autonomous flow control inside microfluidic channels. *Nature* **404,** 588–590 (2000).
24. Champion, J. A., Katare, Y. K. & Mitragotri, S. Particle shape: A new design parameter for micro- and nanoscale drug delivery carriers. *Journal of Controlled Release* **121,** 3–9 (2007).
25. Doshi, N. & Mitragotri, S. Macrophages Recognize Size and Shape of Their Targets. *PLoS ONE* **5,** e10051 (2010).
26. Tsonchev, S., Schatz, G. C. & Ratner, M. A. Hydrophobically-Driven Self-Assembly: A Geometric Packing Analysis. *Nano Lett.* **3,** 623–626 (2003).
27. Tsonchev, S., Troisi, A., Schatz, G. C. & Ratner, M. A. On the Structure and Stability of Self-Assembled Zwitterionic Peptide Amphiphiles: A Theoretical Study. **4,** 427–431 (2004).
28. Tsonchev, S., Troisi, A., Schatz, G. C. & Ratner, M. A. All-Atom Numerical Studies of Self-Assembly of Zwitterionic Peptide Amphiphiles. *J. Phys. Chem. B* **108,** 15278–15284 (2004).
29. Lee, O.-S., Stupp, S. I. & Schatz, G. C. Atomistic Molecular Dynamics Simulations of Peptide Amphiphile Self-Assembly into Cylindrical Nanofibers. *J. Am. Chem. Soc.* **133,** 3677–3683 (2011).
30. Tsonchev, S., Schatz, G. C. & Ratner, M. A. Electrostatically-Directed Self-Assembly of Cylindrical Peptide Amphiphile Nanostructures. *J. Phys. Chem. B* **108,** 8817–8822 (2004).
31. Tsonchev, S., Niece, K. L., Schatz, G. C., Ratner, M. A. & Stupp, S. I. Phase Diagram for Assembly of Biologically-Active Peptide Amphiphiles †. *J. Phys. Chem. B* **112,** 441–447 (2008).
32. Velichko, Y. S., Stupp, S. I. & la Cruz, de, M. O. Molecular Simulation Study of Peptide Amphiphile Self-Assembly. *J. Phys. Chem. B* **112,** 2326–2334 (2008).
33. Lee, O.-S., Cho, V. & Schatz, G. C. Modeling the Self-Assembly of Peptide Amphiphiles into Fibers Using Coarse-Grained Molecular Dynamics. *Nano Lett.* **12,** 4907–4913 (2012).
34. Monticelli, L. *et al.* The MARTINI Coarse-Grained Force Field: Extension to Proteins. *J. Chem. Theory Comput.* **4,** 819–834 (2008).
35. Paramonov, S. E., Jun, H.-W. & Hartgerink, J. D. Self-Assembly of Peptide–Amphiphile Nanofibers: The Roles of Hydrogen Bonding and Amphiphilic Packing. *J. Am. Chem. Soc.* **128,** 7291–7298 (2006).
36. Voegler Smith, A. & Hall, C. K. α-Helix formation: Discontinuous molecular dynamics on an intermediate-resolution protein model. *Proteins: Structure, Function, and Bioinformatics* **44,** 344–360 (2001).
37. Nguyen, H. D. & Hall, C. K. Molecular dynamics simulations of spontaneous fibril formation by random-coil peptides. *Proceedings of the National Academy of Sciences* **101,** 16180–16185 (2004).
38. Nguyen, H. D., Marchut, A. J. & Hall, C. K. Solvent effects on the conformational transition of a model polyalanine peptide. *Protein Science* **13,** 2909–2924 (2004).
39. Wesson, L. & Eisenberg, D. Atomic solvation parameters applied to molecular dynamics of proteins in solution. *Protein Science* **1,** 227–235 (1992).

40. Wallqvist, A. & Ullner, M. A simplified amino acid potential for use in structure predictions of proteins. *Proteins: Structure, Function, and Bioinformatics* **18,** 267–280 (1994).
41. Alder, B. J. & Wainwright, T. E. Studies in molecular dynamics. I. General method. *J. Chem. Phys.* **31,** 459 (1959).
42. Pashuck, E. T., Cui, H. & Stupp, S. I. Tuning Supramolecular Rigidity of Peptide Fibers through Molecular Structure. *J. Am. Chem. Soc.* **132,** 6041–6046 (2010).
43. Phillips, J. C. *et al.* Scalable molecular dynamics with NAMD. *J. Comput. Chem.* **26,** 1781–1802 (2005).
44. MacKerell, A. D., Jr *et al.* All-atom empirical potential for molecular modeling and dynamics studies of proteins. *J. Phys. Chem. B* **102,** 3586–3616 (1998).
45. Mackerell, A. D., Jr., Feig, M. & Brooks, C. L., III. Extending the treatment of backbone energetics in protein force fields: Limitations of gas-phase quantum mechanics in reproducing protein conformational distributions in molecular dynamics simulations. *J. Comput. Chem.* **25,** 1400–1415 (2004).
46. Brooks, B. R. *et al.* CHARMM: The biomolecular simulation program. *J. Comput. Chem.* **30,** 1545–1614 (2009).
47. Tovar, J. D., Claussen, R. C. & Stupp, S. I. Probing the Interior of Peptide Amphiphile Supramolecular Aggregates. *J. Am. Chem. Soc.* **127,** 7337–7345 (2005).
48. Niece, K. L. *et al.* Modification of gelation kinetics in bioactive peptide amphiphiles. *Biomaterials* **29,** 4501–4509 (2008).
49. Xu, X.-D., Jin, Y., Liu, Y., Zhang, X.-Z. & Zhuo, R.-X. Self-assembly behavior of peptide amphiphiles (PAs) with different length of hydrophobic alkyl tails. *Colloids and Surfaces B: Biointerfaces* **81,** 329–335 (2010).
50. Toksoz, S., Mammadov, R., Tekinay, A. B. & Guler, M. O. Electrostatic effects on nanofiber formation of self-assembling peptide amphiphiles. *Journal of Colloid And Interface Science* **356,** 131–137 (2011).
51. Ghosh, A. *et al.* Fine-Tuning the pH Trigger of Self-Assembly. *J. Am. Chem. Soc.* **134,** 3647–3650 (2012).
52. Serio, T. R. *et al.* Nucleated conformational conversion and the replication of conformational information by a prion determinant. *Science* **289,** 1317–1321 (2000).
53. Soreghan, B., Kosmoski, J. & Glabe, C. Surfactant properties of Alzheimer's A beta peptides and the mechanism of amyloid aggregation. *Journal of Biological Chemistry* **269,** 28551–28554 (1994).
54. Khurana, R. *et al.* Partially Folded Intermediates as Critical Precursors of Light Chain Amyloid Fibrils and Amorphous Aggregates †. *Biochemistry* **40,** 3525–3535 (2001).
55. Lee, J., Culyba, E. K., Powers, E. T. & Kelly, J. W. amyloid-b forms fibrils by nucleated conformational conversion of oligomers. *Nature Chemical Biology* 1–8 (2011). doi:10.1038/nchembio.624
56. Thakur, A. K. *et al.* Polyglutamine disruption of the huntingtin exon 1 N terminus triggers a complex aggregation mechanism. *Nat Struct Mol Biol* **16,** 380–389 (2009).
57. Auer, S., Trovato, A. & Vendruscolo, M. A Condensation-Ordering Mechanism in Nanoparticle-Catalyzed Peptide Aggregation. *PLoS Comput Biol* **5,** e1000458 (2009).
58. Dill, K. A., Alonso, D. O. V. & Hutchinson, K. Thermal stabilities of globular proteins. *Biochemistry* **28,** 5439–5449 (1989).
59. Shimizu, S. & Chan, H. S. Temperature dependence of hydrophobic interactions: A mean force perspective, effects of water density, and nonadditivity of thermodynamic signatures. *J. Chem. Phys.* **113,** 4683–4700 (2000).
60. Smith, S. W., Hall, C. K. & Freeman, B. D. Molecular dynamics for polymeric fluids using discontinuous potentials. *J Comput Phys* **134,** 16–30 (1997).
61. Andersen, H. C. Molecular dynamics simulations at constant pressure and/or temperature. *J. Chem. Phys.* **72,** 2384 (1980).
62. Frishman, D. & Argos, P. Knowledge-based protein secondary structure assignment. *Proteins: Structure, Function, and Bioinformatics* **23,** 566–579 (1995).
63. Sugita, Y. & Okamoto, Y. Replica-exchange molecular dynamics method for protein folding. *Chemical Physics Letters* **314,** 141–151 (1999).
64. Foloppe, N. & MacKerell, A. D., Jr. All-atom empirical force field for nucleic acids: I. Parameter optimization based on small molecule and condensed phase macromolecular target data. *J. Comput. Chem.* **21,** 86–104 (2000).
65. MacKerell, A. D., Jr & Banavali, N. K. All-atom empirical force field for nucleic acids: II. Application to molecular dynamics simulations of DNA and RNA in solution. *J. Comput. Chem.* **21,** 105–120 (2000).

CHAPTER 3 Mechanism of the pH-Controlled Self-Assembly of Nanofibers from Peptide Amphiphiles

3.1 Abstract

Stimuli-responsive, self-assembling nanomaterials hold a great promise to revolutionize medicine and technology. However, current discovery is slow and often serendipitous. Here we report a multiscale modeling study to elucidate the pH-controlled self-assembly of nanofibers from the peptide amphiphiles, palmitoyl-I-A_3E_4-NH_2. The coarse-grained simulations revealed the formation of random-coil based spherical micelles at strong electrostatic repulsion. However, at weak or no electrostatic repulsion, the micelles merge into a nanofiber driven by the β-sheet formation between the peptide segments. The all-atom constant pH molecular dynamics revealed a cooperative transition between random coil and β-sheet in the pH range 6–7, matching the CD data. Interestingly, although the bulk pK_a is more than one unit below the transition pH, consistent with the titration data, the highest pK_a's coincide with the transition pH, suggesting that the latter may be tuned by modulating the pK_a's of a few solvent-buried Glu side chains. Together, these data offer, to our best knowledge, the first multiresolution and quantitative view of the pH-dependent self-assembly of nanofibers. The novel protocols and insights gained are expected to advance the computer-aided design and discovery of pH-responsive nanomaterials.

3.2 Introduction

Peptide amphiphiles (PAs) are peptides with a terminal group covalently linked to a long hydrophobic chain. Over the past decade, biocompatible PAs have attracted much

attention as building blocks of nanomaterials due to the ability to self-assemble into supramolecular structures at specific solution conditions relevant for biomedical and biotechnological applications (see a recent review[1] and references therein). Using TEM, FTIR, and other techniques, Stupp and co-workers showed that PAs self-assemble into nanofibers[2] upon a change in the external stimuli such as solution pH and ionic concentrations and that the morphology, surface chemistry, and potential bioactivity of the nanomaterials can be controlled by the selection of amino acid sequence or the modification of the alkyl tail.[3] This pioneering work set the stage for designing PA-based nanomaterials with desired properties to target specific applications.[4]

Of particular interest to us are the PAs that can form nanocarriers for delivery of therapeutic or imaging agents in response to endogenous stimuli such as a drop in pH at tumor site.[5] Toward this end, Goldberger and co-workers designed a series of PAs that can self-assemble into nanofibers when the solution pH is decreased from the normal physiological condition 7.4 to 6.6, the mild acidic condition found in the microenvironment of malignant tumor tissues.[6] The PAs used are the charged polypeptides palmitoylated at the N-terminus, CH_3-$(CH_2)_{14}$CO-NH-X-Ala_3-Glu_4-CO-NH_2, where X is a hydrophobic residue, such as Ile, Phe, Val, or Tyr, with a varying propensity for β-sheet formation. The Glu residues are present to allow pH response. CD and TEM experiments revealed that, at high pH, PAs at low concentrations are in random-coil states while PAs at high concentrations form micelles. Goldberger and co-workers also conducted titration experiments, which showed that the bulk pK_a of the nanofibers remains at 4.7, while the self-assembly transition pH decreases from 6.6 to 6.0, when Ile is substituted by Tyr. Thus, they concluded that the transition pH is not dependent on the pK_a of the Glu side chains but

rather on the β propensity of the X residue. The transition pH is shifted lower because Tyr has a lower beta propensity than Ile.[7] Below we will refer to the sequence of the PA with X being Ile as PA1.

In order to systematically design PAs that can self-assemble into nanomaterials at specified pH conditions with desired properties, it is desirable to learn the detailed mechanism of the pH-induced self-assembly process and to make quantitative prediction of the transition pH. Using the standard all-atom molecular dynamics (MD) as well as various coarse-grained Monte Carlo and MD simulations, studies led by Stupp, Ratner, and de la Cruz groups have provided valuable insights into the structural and kinetic aspects of the PA self-assembly.[8-11] However, there are two limitations of these studies. First, the secondary structure change that accompanies the nanofiber formation cannot be described by the coarse-grained models used. And importantly, the pH-dependent mechanism of the self-assembly cannot be studied by the standard all-atom MD simulations.

Here we present a multiscale MD study to elucidate the pH-dependent kinetic and thermodynamic aspects of the nanofiber self-assembly from the aforementioned PA synthesized in the Goldberger lab.[6] The kinetic details will be qualitatively mapped out using discrete molecular dynamics with the Protein Intermediate Resolution model (PRIME)[12-14] that was originally developed by the Hall group and recently extended by Nguyen and co-workers (ePRIME).[15] The mechanism of the pH-dependence will be quantitatively uncovered by studying the unfolding of a tetrameric β-sheet model using the recently developed all-atom version[16] of the continuous constant pH molecular dynamics (CpHMD) technique[17,18] with the pH-based replica-exchange protocol.[19] The CG simulations showed that the PAs self-assemble into micelles, which merge into an elongated nanofiber

driven by the β-sheet formation at low pH conditions. The all-atom CpHMD simulations revealed a cooperative transition from β-sheet to random coil and were able to determine the bulk pK_a as well as individual pK_a's of Glu side chains, both of which are in quantitative agreement with the experiment. Surprisingly, the data showed that the transition pH is determined by the deprotonation of the central Glu residues. The combined coarse-grained and all-atom simulation data offer, to our best knowledge, the first multiresolution and quantitative view of the pH-dependent mechanism of PA self-assembly.

3.3 Simulation Methods

3.3.1 Coarse-Grained Discontinuous Molecular Dynamics Simulations

The self-assembly process was simulated using the discontinuous molecular dynamics[20] with our newly developed coarse-grained model ePRIME for the representation of the PA molecule, CH_3-$(CH_2)_{14}$CO-Ile-Ala_3-Glu_4-CO-NH_2.[15] ePRIME is an extension of the original PRIME model, in which each amino acid residue is represented by four beads, three of which represent the backbone while a single bead represents the side chain.[12-14] The ePRIME model offers representations for all 20 amino acid side chains by taking into account size, hydrophobicity, and charge using well-established experimental data and modeling parameters.[21,22] The discontinuous molecular dynamics (MD) is orders of magnitude faster than regular molecular dynamics because the forces are modeled by hard-sphere or square-well potentials. Solvent effect is included implicitly as a potential of mean force in the energy function. Hydrogen bonding between the backbone amide and

carbonyl groups is represented by a directionally square-well attraction potential of the magnitude ε_{HB}, which serves as a reference strength for other types of interactions.

The self-assembly simulations were initiated from a configuration in which 800 PA molecules were randomly placed in a cubic box with periodic boundary dimensions of 250 Å × 250 Å × 250 Å. The system contained 42 400 particles representing a PA concentration of 85 mM. Each simulation was heated at high temperature (reduce temperature of 5.0) to reach an unbiased initial configuration and then quickly cooled to the temperature of interest (reduced temperature of 0.08–0.15), for a constant-temperature production run until equilibration. To mimic the effect of pH, each simulation was conducted at an electrostatic repulsion strength of 0%, 200%, 400%, and 600%, relative to that of the hydrogen bond, $\varepsilon_{ES}/\varepsilon_{HB}$. Each simulation was independently repeated ten times to ensure statistical significance. Quantitative results in this paper are the averages of the last 10% of simulation data with error bars taken from the standard deviation. The secondary structures were defined through the implementation of STRIDE.[23] Here we focused on α-helix, β-strand or β-sheet, and random coil that also contains turn. An aggregate is defined if each peptide in a group of PA molecules has at least two interpeptide hydrogen bonds or four hydrophobic interactions with a neighboring PA molecule in the same group.

3.3.2 All-Atom Constant pH Molecular Dynamics Simulations

The initial structure of the tetrameric β-sheet of PA1 was built with PyMOL[24] in which the four PA1 peptides were placed in a well-defined parallel β-sheet conformation with protonated Glu side chains. The β-sheet was immersed in a cubic box of 4296 water molecules, keeping a minimal distance of 9 Å between the solute and each face of the box. The system was then subjected to energy minimization prior to a 100 ns standard

molecular dynamics (MD) run with fixed protonation states using the GROMACS package.[25] The CHARMM C36 force field was used to represent the proteins,[26] and the modified TIP3P model was used for water.[27] The MD run was performed with periodic boundary conditions at constant temperature, pressure, and fixed protonation states. The temperature was maintained at 298 K using the Nosé–Hoover thermostat,[28,29] while the pressure was maintained at 1 atm using the Parrinello–Rahman barostat.[30] The LINCS algorithm[31] was used to constrain all bonds containing hydrogen atoms, allowing an integration time step of 2 fs. The coordinates were saved every 2 ps. The particle-mesh-Ewald method[32,33] was used for the calculation of electrostatic interactions, and a cutoff of 12 Å was used for the calculation of van der Waals interactions. If not specified, the default setting was used for all other input parameters.

Final snapshots of the PA1 tetramer were extracted from the above simulations to initiate the all-atom, pH-based replica-exchange (REX)[16] continuous constant pH MD (CpHMD)[17,18] using an in-house modified version of the CHARMM package (c37b1).[34] The same force fields as in the GROMACS simulations were used. The tetramer was resolvated in a cubic box filled with 5013 TIP3P water molecules. Sixteen co-ions were added to level the total charge,[16] while 16 sodium ions were added for neutralizing the system. No additional salt ions were added to avoid the possible convergence issue related to the insufficient sampling of salt ions. In the pH-based REX protocol,[19] 24 replicas were placed in the range of pH 3–11 with an interval of 0.5 pH units. The exchange of pH was attempted every 250 steps or 0.5 ps between replicas adjacent in the pH ladder. Additional replicas were added in order to achieve an exchange ratio of at least 15% at all pH conditions. Each pH replica underwent 12 ns molecular dynamics at constant temperature, pressure, and

pH. The temperature was 298 K using the Hoover thermostat,[29] while the pressure was maintained at 1 atm using the Langevin piston pressure coupling algorithm.[35] The SHAKE algorithm was applied to all the hydrogen bonds and angles to allowed a time step of 2 fs, and the coordinates were saved every 0.5 ps. The electrostatic interactions were calculated using the generalized reaction field method with a cutoff of 14 Å. The same cutoff distance was used in the calculation of van der Waals interactions. The REX all-atom CpHMD was repeated once by starting from a different set of initial velocities.

Following our previous work,[18] the protonated and unprotonated forms of a titratable side chain are defined as the states with λ value below 0.1 and above 0.9, respectively. After each replica-exchange attempt, the λ values of all Glu's were recorded. The unprotonated fractions were calculated for individual Glu's as well as by taking into account all 16 Glu's. Fitting the former data at different the pH values to the generalized Henderson–Hasselbalch equation gives the microscopic pK_a's, while fitting the latter data gives the macroscopic or bulk pK_a of the β-sheet. The data from the last 2 ns (per replica) was used for analysis and pK_a calculations.

3.4 Results and Discussions

3.4.1 Kinetic Mechanism of the Self-Assembly Process

Discrete molecular dynamics with the ePRIME model[15] was applied to study the self-assembly process of 800 PA1 molecules (CH_3-$(CH_2)_{14}$CO-NH-I-A_3-E_4-CO-NH_2) that were randomly distributed in the simulation box at the beginning. To mimic the varying degree of ionization of the EEEE-stretch under different pH conditions, the strength of the electrostatic repulsion between the peptide segments was varied, relative to that of a

hydrogen bond, i.e., $\varepsilon_{ES}/\varepsilon_{HB}$. Driven by hydrophobic forces, small spherical micelles were quickly formed, burying the alkyl groups in the interior and exposing the peptide segments on the surface (**Figure 3.1**). However, the next sequence of kinetic steps was determined by the strength of the electrostatic repulsion between the EEEE-stretches. When the electrostatic repulsion is strong, i.e., $\varepsilon_{ES}/\varepsilon_{HB} \geq 200\%$, representing the high pH conditions, under which some or all of the Glu side chains were deprotonated or charged, the micelles remain in the spherical arrangement with the peptide segments uniformly distributed along the surface to minimize repulsion between neighboring EEEE-stretches (**Figure 3.1A**).

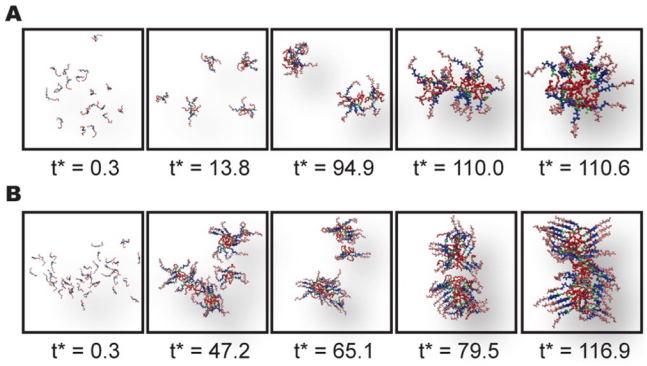

Figure 3.1. Snapshots of the self-assembly process of PA1 molecules as a function of CG simulation time (in reduced time units). (A) A spherical micelle without β-sheet content is formed at a strong electrostatic repulsion (200% εHB). (B) A cylindrical nanofiber with β-sheet content is formed at zero electrostatic repulsion. PA1 molecules are colored as follows: alkyl tail in red, isoleucine in green, alanine in blue, and glutamic acid in pink.

By contrast, in the absence of electrostatic repulsion, representing the low pH conditions, under which the Glu side chains are fully protonated or neutral, hydrogen bonds started to form between the backbone amide and carbonyl groups of the adjacent peptide segments, leading to the formation of β-sheets (**Figure 3.1B**). As a result, the peptide segments on the surface of the micelle were no longer uniformly distributed, creating segregation that facilitates the exposure of hydrophobic alkyl groups to the

surface. These micelles subsequently merged at the exposed locations through hydrophobic interactions between the alkyl groups. Thus, the early stage of the nanofiber self-assembly was characterized by the sharp increase in the β-sheet content, which accompanies the highly frequent events of micelle merging. Therefore, a kinetic mechanism for the formation of nanofibers is deciphered, involving the following steps: (1) simultaneous formation of multiple spherical micelles driven by hydrophobic interactions between alkyl tails and (2) micelle-merging events prompted by the exposure of the hydrophobic core due to the change in the architecture of the spherical micelles that ultimately leads to the fabrication of one continuous rod-shaped nanostructure. The latter supports the notion that β-sheet promotes fiber formation based on the existing experimental data.[36]

3.4.2 Structural Details of the Self-Assembled Nanofiber in Agreement with Experiment

The in silico observation that PA1 molecules self-assemble into spherical micelles and a rod-shaped nanofiber at conditions of high and low electrostatic repulsion, respectively, is in agreement with the CD and TEM data of Goldberger lab, which showed the formation of spherical micelles at high pH and nanofibers at low pH when the PA concentrations were high (corresponding to the simulation condition).[6] The in silico observation of β-sheet formation in the nanofiber and not in the micelles also agrees with the aforementioned CD data[6] as well as the earlier studies of Stupp and co-workers using FTIR[2] and CD experiments.[4] The rod-shaped nanofiber with exposed peptide segments and buried alkyl tails observed in the simulation is consistent with the model proposed by Stupp and co-workers over a decade ago based on cryo-TEM imaging and staining, which

showed PA molecules forming cylindrical nanofiber with the charged amino acids on the surface and alkyl tails buried in the core.[2]

3.4.3 Electrostatic Repulsion Controls the Micelle-to-Nanofiber Transition

Since the intermolecular electrostatic repulsion between the charged Glu side chains favors the formation of micelle, while the backbone hydrogen bonding between peptide segments drives the distortion and subsequent merging of spherical micelles leading to the formation of nanofiber, weakening electrostatic repulsion would shift the equilibrium from micelle to nanofiber. The latter corresponds to a decrease in the degree of ionization of Glu side chains and therefore mimics the condition of lowering pH. In fact, the coarse-grained simulations resulted in a nanofiber when the electrostatic repulsion strength is below 200% relative to the hydrogen bonding ($\varepsilon_{ES}/\varepsilon_{HB}$) (**Figure 3.2A**). In the absence of electrostatic repulsion (all Glu side chains are neutral), the self-assembled nanofiber contains a β-sheet content of almost 35% (**Figure 3.2A**). As the relative electrostatic repulsion strength is at or above 200%, β-sheet content drops below 5% (**Figure 3.2A**). The typical size of a β-sheet in the cylindrical nanofiber fluctuates between two and four (**Figure 3.2B**). The range of β-sheet content observed in our simulation is in good agreement with the CD data by Stupp and co-workers, who showed the β-sheet population of IKVAV-bearing PAs to be 25 ± 20%.[4] The electrostatic repulsion strength at the micelle-to-fiber transition for PA1 is lower than but consistent with that for the palmitoyl-$V_3A_3E_3$ molecules ($\varepsilon_{ES}/\varepsilon_{HB} \leq 300–400\%$) from our previous work,[15] likely due to the fact that the latter sequence has one fewer charged residue and two extra hydrophobic residues as compared to PA1.

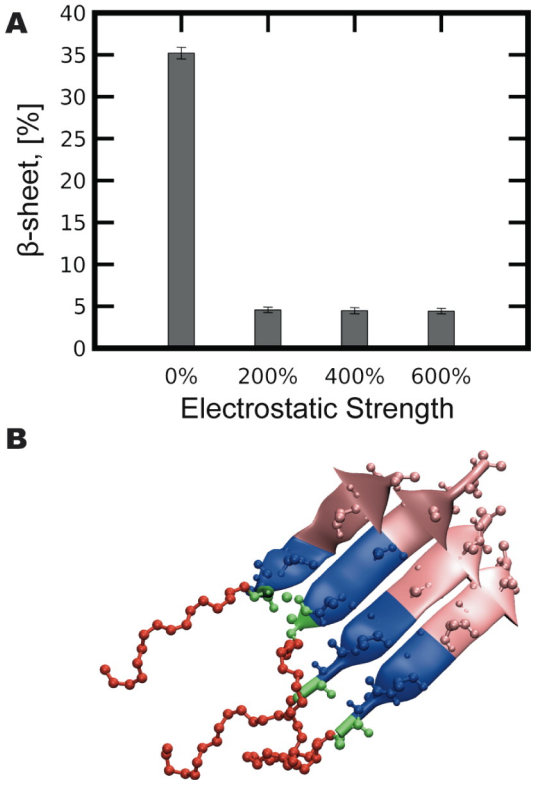

Figure 3.2. A. β-sheet content at varying strength of electrostatic repulsion in the CG simulation. B. Snapshot of a typical β-sheet in the CG simulation.

3.4.4 Establishing a Tetrameric β-Sheet Model for the All-Atom CpHMD Simulations

The coarse-grained simulations have established the pH-induced β-sheet formation as the hallmark and driving force for the creation of nanofibers. To understand the details of the pH-dependent transition between the random coil (as present in micelle) and β-sheet (nanofiber), we employed the all-atom continuous constant pH molecular dynamics (CpHMD) simulations with the pH replica-exchange sampling protocol. To make the study amenable to the current computational capability, we focused on the pH-dependent stability of a minimal β-sheet model comprising four PA1 peptides (NH_2-IAAAEEEE-CO-NH_2), consistent with the observed sheet size in the CG simulation (**Figure 3.2**). The alkyl

tails were omitted as they do not contain ionizable residues and as such do not influence the pH dependence. The tetramer was prebuilt with four parallel β-strands, and all Glu were protonated to represent the least electrostatic repulsion, which is the most favorable condition for the formation of the β-sheet based nanofiber. The tetramer was then subjected to the standard all-atom MD simulations with fixed protonation states to verify stability and establish the starting structure as well as control for the subsequent pH-dependent simulations. Indeed, within 100 ns, the PA1 tetramer remained stable with a well-defined β-sheet along the Glu sequences. A snapshot for the tetramer is shown in **Figure 3.3**.

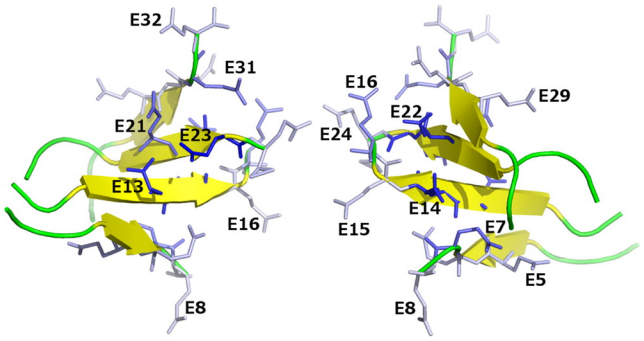

Figure 3.3. Snapshot of the PA1 tetramer obtained from the 100 ns standard MD simulation with all Glu side chains fully protonated. Two views (related by a 180° rotation) are presented. The Glu side chains are highlighted in blue stick representation. The shade of blue (white to blue) corresponds to the pK_a value (0 to 8). The pK_a values are extracted from an explicit-solvent CpHMD simulation (see **Figure 3.5**).

3.4.5 Tetrameric β-Sheet that Undergoes a pH-Dependent Unfolding Transition

We next performed the all-atom replica-exchange (REX) CpHMD simulations[16] on the PA1 tetramer starting from the structures extracted from the aforementioned standard MD simulations. Two independent runs of REX CpHMD simulations were performed. Each run of simulations included pH replicas in the pH range 3–10. Simulation of each replica

lasted 12 ns per replica. More details are given in Simulation Methods. The discussion below will focus on simulation run 1. **Figure 3.4a** shows the residue-based β-sheet content. At pH 3, the β-sheet is most stable and spans residues 2–7 (AAAEEE) in the monomer. As pH is increased to 6.5, the β-sheet is shortened to residues 4–6 (AEEE). As pH is increased further to 8, the β content reduces to below 20% in those regions, indicating that the tetramer is nearly unfolded. It is worthwhile to notice that the β-sheet is less stable in the two edge monomers as compared to the central ones, as a result of solvent exposure.

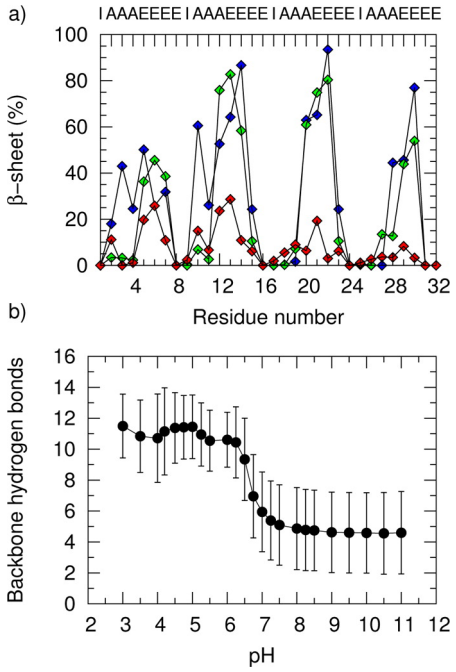

Figure 3.4. pH-dependent β-sheet content of the PA1 tetramer. (a) Residue-based β-sheet content calculated as the percentage residence time of a residue in the β-sheet conformation (assigned using the DSSP algorithm[37]). Blue, green, and red represent pH 3, 6.5, and 8, respectively. The four monomers correspond to residues 1–8, 9–16, 17–24, and 25–32, respectively. (b) Total number of backbone hydrogen bonds as a function of pH. Data points are the averages while the error bars represent the standard deviation. Data from the last 2 ns of the all-atom CpHMD simulation run 2 were used.

To quantitatively characterize the pH-dependent unfolding transition, we calculated the total number of backbone hydrogen bonds for each snapshot (**Figure 3.4b**). At low pH conditions, pH 3–6, there are on average 11 backbone hydrogen bonds, corresponding to a

β-sheet content of 26%, in good agreement with the coarse-grained data (35%, see **Figure 3.2**). At high pH conditions, pH 7.5–11, the average number of hydrogen bonds is 4.5, in agreement with the β-content found for individual residues (**Figure 3.4a**). Interestingly, a sharp drop in the number of hydrogen bonds occurs in a narrow pH range of 6–7, indicating that the β-sheet starts to unfold at pH 6 and the unfolding is complete at pH 7. The latter is in a quantitative agreement with the CD data, indicating that at 10 μM the PA1 molecules undergo a random-coil to β-sheet transition in the pH range pH 6.8–6.0 with an estimated transition pH of 6.6.[6] To verify convergence, a second set of replica-exchange CpHMD simulations was performed starting from a different velocity seed. The resulting transition pH region remains the same.

3.4.6 pK_a Values for the Glu's in the Central Strands Determine the Transition pH

To further understand the pH-dependent β-sheet formation, we examine the calculated pK_a values of individual Glu side chains in the PA1 tetramer and their degree of ionization (also known as unprotonated fractions) at different pH values. The individual pK_a's range from 4.2 to 6.6 with most of them shifted up from the model value of 4.4, giving an average pK_a of 5.4 (**Figure 3.5a**), which is 0.7 units higher than the measured average pK_a of the PA1 solution based on acid-based titration.[6] We note the second set of simulations gave an average pK_a of 5.2. The pK_a up-shifts are due to the intermolecular electrostatic repulsion between the ionized Glu's on the adjacent β-strands. The pK_a shifts are more pronounced for Glu's in the central strands (residues 13–16 and 21–24) as compared to those in the edge strands (residues 5–8 and 29–32), because the central Glu's are shielded from solvent, as evident from the significantly smaller solvent accessible

surface area of the carboxylic groups in the protonated form as compared to those of the edge residues (data not shown). Thus, the wide spread in the individual pK_a's is a result of different local environment of Glu side chains, which can be visualized by projecting the pK_a values onto the initial structure of the PA1 tetramer (**Figure 3.3**). It can be seen that the lowest pK_a values are from those Glu side chains in the edge strands pointing out to solvent, while the highest pK_a's are from those Glu side chains in the two central strands that are in a confined configuration (**Figure 3.3**). Interestingly, the Glu side chains in the edge strands, which have a relatively higher pK_a value (see n = 7 and 31), point inside the tetramer and interact with the Glu's in the central strands (**Figure 3.3**).

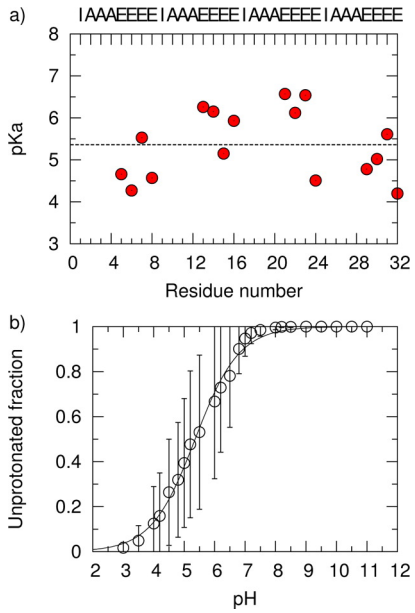

Figure 3.5. Titration of Glu residues in the PA1 tetrameric β-sheet. (a) Calculated pK_a values of the individual Glu side chains. The black dashed line indicates an average pK_a of 5.4. (b) The unprotonated fraction averaged over all the Glu's of the PA1 tetramer as a function of pH. The curve represents the fitting to the generalized Henderson–Hasselbalch equation. The obtained bulk pK_a is 5.4 with a Hill coefficient of 0.6. The error bars correspond to the standard deviation among the unprotonated fractions of all the Glu's.

Structure analysis revealed that, at low pH conditions, the carboxylic groups of the Glu's in the central β-strands form hydrogen bonds, which disappear at high pH conditions

(data not shown). These hydrogen bonds stabilize the β-sheet as well as the protonated state. Thus, in addition to intermolecular charge–charge repulsion, hydrogen bonding is another contributor to the pK_a upshift for the central Glu's. Interestingly, intermolecular hydrogen bonding between carboxylic side chains and the effect on the pK_a shift have also been suggested for fatty acids in the premicellar aggregates based on experimental data[38] and recently confirmed by simulation.[39]

Related to the large variation in the pK_a's is the varying degree of ionization of the individual Glu's at a specific pH (**Figure 3.5b**). The variation is particularly large in the pH region where the unfolding of the β-sheet occurs. For example, at pH 6, the degree of ionization for individual Glu's can be as low as 30% and as high as 100% (error bars in **Figure 3.5b**). Similar effects of interpeptide electrostatic repulsion leading to a wide range of pK_a values have been suggested for the β-sheet self-assembly of small peptides containing Glu and Arg residues.[40] It is reasonable to hypothesize that the tetramer β-sheet unfolds when all the Glu side chains become ionized. Indeed, above pH 7, when the unfolding transition is complete (**Figure 3.4**), the Glu's are at least 95% ionized including those in the two central strands (**Figure 3.5b**). By contrast, at pH 6, when the β-sheet starts to unfold, the Glu's in the two edge strands are completed ionized, while those in the two central strands become ionized by at least 30%. The average ionization is about 65%. Thus, these data suggest that, to completely unfold the β-sheet, all Glu's need to be ionized. Since Glu's of the central strands ionize at much higher pH than those of the edge strands, their pK_a's determine the transition pH. The average degree of ionization (unprotonated fraction) over all the Glu's as a function of pH can be fit to the Hill equation, giving an average or bulk pK_a of 5.4 (**Figure 3.5b**), in agreement with the one obtained by averaging

the individual pK_a's (**Figure 3.5a**). The Hill coefficient is 0.6 (**Figure 3.5b**), indicating a high degree of anticooperativity due to electrostatic repulsion between the charged Glu side chains.

3.5 Conclusions

In this study we employed the state-of-the-art coarse-grained (CG) and all-atom molecular dynamics simulations to elucidate the kinetic and thermodynamic mechanisms of the pH-dependent self-assembly of PA1 molecules. The CG simulations revealed that the PA1 molecules initially aggregate to form multiple spherical micelles with the palmitoyl tails buried in the micellar core and the PA1 peptides in the random-coil state exposed to solvent. When the electrostatic repulsion between the peptide segments is weak, corresponding to the low pH conditions when the Glu side chains are (mainly) neutral, interpeptide hydrogen bonds begin to form, which perturbs the spherical shape of the micelle, leading to the exposure of hydrophobic regions. The latter drives the micelles to merge, ultimately leading to the formation of one continuous rod-shaped nanofiber with the PA1 peptides aligned in a β-sheet configuration. The kinetic pathway to nanofiber driven by the β-sheet formation is in agreement with existing experimental work.[2,4,6]

To investigate the pH-dependent thermodynamic aspect, conformational dynamics of a PA1 tetrameric β-sheet model was studied using the all-atom CpHMD simulations. On the basis of the number of backbone hydrogen bonds, the unfolding of the β-sheet occurs between pH 6 and pH 7 with the transition midpoint at about pH 6.5. Remarkably, the individual pK_a's of the Glu's in the tetramer vary widely, and the calculated average or bulk pK_a is 5.3 (5.4 and 5.2 in two independent runs). The Glu's of the edge strands are generally

solvent exposed and have pK_a's close to the model value of 4.4. By contrast, the Glu's of the central strands, especially those three next to Ala, are shielded from solvent and have pK_a's that are shifted to 6–6.6. Together, these data suggest that ionization of the three Glu's next to Ala in the central peptides induces unfolding of the β-sheet. Their pK_a's determine the pH condition for the transition from nanofiber to micelle. The cooperative unfolding transition of PA1 β-sheet is reminiscent of the pH-dependent phase behavior of self-assembling peptides containing Glu's, for which the ionization of single Glu was suggested to be responsible.[40]

Finally, we remark on the caveats of the simulations. In the coarse-grained simulations, the PA concentration (85 mM) was more than 3 orders of magnitude higher than the experimental condition (10 μM). Therefore, alternative kinetic pathways such as the direct formation of nanofiber from single PA molecules can not be studied as it would require orders of magnitude longer simulation time which is currently not feasible. In the all-atom simulations, since only counterions and no additional salt ions were included (to avoid the potential convergence problem due to limited sampling of ions), the ionic strength was lower than that in experiment (150 mM).[6] We suggest that this is a major cause for the calculated average pK_a to be about 0.6 units higher than the measured value, as lower ionic strength leads to the overestimation of electrostatic repulsion which increases the pK_a's. Another limitation of the all-atom simulation is that the concentration effect is not accounted for due to the nature of the unfolding simulation. However, despite these limitations, the data show that the combined coarse-grained and all-atom constant pH molecular dynamics simulations present an attractive strategy that may be used to guide the design and discovery of pH-responsive nanomaterials.

3.6 Acknowledgements

This work was originally published in Journal of Physical Chemistry C, 2014 © American Chemical Society. Co-authors include Yoann Cote, Eric T. Dobson, Joshua E. Goldberger, Hung D. Nguyen, and Jana K. Shen. Y.C. and J.K.S. acknowledge National Institutes of Health (R01 GM098818) for funding. I.W.F. acknowledges support from a Graduate Research Fellowship from the National Science Foundation (DGE-1321846). This work used the Extreme Science and Engineering Discovery Environment (XSEDE), which is supported by National Science Foundation grant number OCI-1053575. H.D.N. is also thankful for the computational resources provided by the GreenPlanet and High Performance Computing cluster at UCI.

3.7 References

1. Cui, H., Webber, M. J. & Stupp, S. I. Self-assembly of peptide amphiphiles: From molecules to nanostructures to biomaterials. *Biopolymers* **94,** 1–18 (2010).
2. Hartgerink, J. D. Self-Assembly and Mineralization of Peptide-Amphiphile Nanofibers. *Science* **294,** 1684–1688 (2001).
3. Hartgerink, J. D., Beniash, E. & Stupp, S. I. Peptide-amphiphile nanofibers: A versatile scaffold for the preparation of self-assembling materials. *Proceedings of the National Academy of Sciences* **99,** 5133–5138 (2002).
4. Niece, K. L. *et al.* Modification of gelation kinetics in bioactive peptide amphiphiles. *Biomaterials* **29,** 4501–4509 (2008).
5. Mura, S., Nicolas, J. & Couvreur, P. Stimuli-responsive nanocarriers for drug delivery. *Nat Mater* **12,** 991–1003 (2013).
6. Ghosh, A. *et al.* Fine-Tuning the pH Trigger of Self-Assembly. *J. Am. Chem. Soc.* **134,** 3647–3650 (2012).
7. Kim, C. A. & Berg, J. M. Thermodynamic β-sheet propensities measured using a zinc-finger host peptide. (1993).
8. Tsonchev, S., Schatz, G. C. & Ratner, M. A. Electrostatically-Directed Self-Assembly of Cylindrical Peptide Amphiphile Nanostructures. *J. Phys. Chem. B* **108,** 8817–8822 (2004).
9. Velichko, Y. S., Stupp, S. I. & la Cruz, de, M. O. Molecular Simulation Study of Peptide Amphiphile Self-Assembly. *J. Phys. Chem. B* **112,** 2326–2334 (2008).
10. Lee, O.-S., Stupp, S. I. & Schatz, G. C. Atomistic Molecular Dynamics Simulations of Peptide Amphiphile Self-Assembly into Cylindrical Nanofibers. *J. Am. Chem. Soc.* **133,** 3677–3683 (2011).
11. Lee, O.-S., Cho, V. & Schatz, G. C. Modeling the Self-Assembly of Peptide Amphiphiles into Fibers Using Coarse-Grained Molecular Dynamics. *Nano Lett.* **12,** 4907–4913 (2012).
12. Voegler Smith, A. & Hall, C. K. α-Helix formation: Discontinuous molecular dynamics on an intermediate-resolution protein model. *Proteins: Structure, Function, and Bioinformatics* **44,** 344–360 (2001).

13. Nguyen, H. D., Marchut, A. J. & Hall, C. K. Solvent effects on the conformational transition of a model polyalanine peptide. *Protein Science* **13,** 2909–2924 (2004).
14. Nguyen, H. D. & Hall, C. K. Molecular dynamics simulations of spontaneous fibril formation by random-coil peptides. *Proceedings of the National Academy of Sciences* **101,** 16180–16185 (2004).
15. Fu, I. W., Markegard, C. B., Chu, B. K. & Nguyen, H. D. The Role of Electrostatics and Temperature on Morphological Transitions of Hydrogel Nanostructures Self-Assembled by Peptide Amphiphiles Via Molecular Dynamics Simulations. *Advanced Healthcare Materials* **2,** 1388–1400 (2013).
16. Wallace, J. A. & Shen, J. K. Charge-leveling and proper treatment of long-range electrostatics in all-atom molecular dynamics at constant pH. *J. Chem. Phys.* **137,** 184105 (2012).
17. Lee, M. S., Salsbury, F. R., Jr. & Brooks, C. L., III. Constant-pH molecular dynamics using continuous titration coordinates. *Proteins: Structure, Function, and Bioinformatics* **56,** 738–752 (2004).
18. Khandogin, J. & Brooks, C. L. Constant pH Molecular Dynamics with Proton Tautomerism. *Biophysical Journal* **89,** 141–157 (2005).
19. Wallace, J. A. & Shen, J. K. Continuous Constant pH Molecular Dynamics in Explicit Solvent with pH-Based Replica Exchange. *J. Chem. Theory Comput.* **7,** 2617–2629 (2011).
20. Alder, B. J. & Wainwright, T. E. Studies in molecular dynamics. I. General method. *J. Chem. Phys.* **31,** 459 (1959).
21. Wesson, L. & Eisenberg, D. Atomic solvation parameters applied to molecular dynamics of proteins in solution. *Protein Science* **1,** 227–235 (1992).
22. Wallqvist, A. & Ullner, M. A simplified amino acid potential for use in structure predictions of proteins. *Proteins: Structure, Function, and Bioinformatics* **18,** 267–280 (1994).
23. Frishman, D. & Argos, P. Knowledge-based protein secondary structure assignment. *Proteins: Structure, Function, and Bioinformatics* **23,** 566–579 (1995).
24. deLano, W. L. The PyMOL molecular graphics system, version 1.7. http:// sourceforge.net/projects/pymol/.

.

25. Pronk, S. *et al.* GROMACS 4.5: a high-throughput and highly parallel open source molecular simulation toolkit. *Bioinformatics* **29,** 845–854 (2013).
26. Best, R. B. *et al.* Optimization of the Additive CHARMM All-Atom Protein Force Field Targeting Improved Sampling of the Backbone ϕ, ψ and Side-Chain χ1 and χ2 Dihedral Angles. *J. Chem. Theory Comput.* **8,** 3257–3273 (2012).
27. Jorgensen, W. L., Chandrasekhar, J., Madura, J. D., Impey, R. W. & Klein, M. L. Comparison of simple potential functions for simulating liquid water. *J. Chem. Phys.* **79,** 926 (1983).
28. NOSE, S. A Molecular-Dynamics Method for Simulations in the Canonical Ensemble. *Molecular Physics* **52,** 255–268 (1984).
29. Hoover, W. G. Canonical Dynamics - Equilibrium Phase-Space Distributions. *Physical Review A* **31,** 1695–1697 (1985).
30. Parrinello, M. Polymorphic transitions in single crystals: A new molecular dynamics method. *J. Appl. Phys.* **52,** 7182 (1981).
31. Hess, B., Bekker, H., Berendsen, H. & Fraaije, J. LINCS: A linear constraint solver for molecular simulations. *J. Comput. Chem.* **18,** 1463–1472 (1997).
32. Darden, T., York, D. & Pedersen, L. Particle mesh Ewald: An N· log (N) method for Ewald sums in large systems. *J. Chem. Phys.* (1993).
33. Essmann, U. *et al.* A Smooth Particle Mesh Ewald Method. *Journal of Chemical Physics* **103,** 8577–8593 (1995).
34. Brooks, B. R. *et al.* CHARMM: The biomolecular simulation program. *J. Comput. Chem.* **30,** 1545–1614 (2009).
35. Feller, S. E., Zhang, Y., Pastor, R. W. & Brooks, B. R. Constant pressure molecular dynamics simulation: The Langevin piston method. *J. Chem. Phys.* **103,** 4613 (1995).
36. Goldberger, J. E., Berns, E. J., Bitton, R., Newcomb, C. J. & Stupp, S. I. Electrostatic control of bioactivity. *Angewandte Chemie (International ed. in English)* **50,** 6292–6295 (2011).
37. Kabsch, W., Kabsch, W., Sander, C. & Sander, C. Dictionary of protein secondary structure: pattern recognition of hydrogen-bonded and geometrical features. *Biopolymers* **22,** 2577–2637 (1983).
38. Kanicky, J. R. & Shah, D. O. Effect of Premicellar Aggregation on the p Kaof Fatty Acid Soap Solutions. *Langmuir* **19,** 2034–2038 (2003).

39. Morrow, B. H., Koenig, P. H. & Shen, J. K. Self-Assembly and Bilayer–Micelle Transition of Fatty Acids Studied by Replica-Exchange Constant pH Molecular Dynamics. *Langmuir* **29,** 14823–14830 (2013).
40. Aggeli, A. *et al.* pH as a Trigger of Peptide β-Sheet Self-Assembly and Reversible Switching between Nematic and Isotropic Phases. *J. Am. Chem. Soc.* **125,** 9619–9628 (2003).

CHAPTER 4 The Role of Hydrophobicity on Self-Assembly by Peptide Amphiphiles via Molecular Dynamics Simulations

4.1 Abstract

Using a novel coarse-grained model, large-scale molecular dynamics simulations are performed to examine self-assembly of 800 peptide amphiphiles (sequence: palmitoyl-$V_3A_3E_3$). Under suitable physiological conditions, these molecules readily assemble into nanofibers leading to hydrogel construction as observed in experiments. Our simulations capture this spontaneous self-assembly process, including the formation of secondary structure, to identify morphological transitions of distinctive nanostructures. As the hydrophobic interaction strength is increased, progression from open networks of secondary structures towards closed cylindrical nanostructures containing either β-sheets or random coils are observed. Moreover, temperature effects are also determined to play an important role in regulating the formation of secondary structures within those nanostructures. These understandings of the molecular interactions involved and the role of environmental factors on hydrogel formation provide useful insight for the development of innovative smart biomaterials for biomedical applications.

4.2 Introduction

Macromolecular self-assembly of amphiphilic peptide-based polymers have been shown to form well-defined supramolecular architectures that can be exploited for the fabrication of nanomaterials with tunable chemical and physical properties,[1,2] prompting recent advancement in diverse fields such as drug delivery, tissue engineering, medical imaging and regenerative medicine.[3-5] Peptide amphiphiles (PA) belong to a subset of these

amphiphilic peptide-based polymers that spontaneously assemble into stimuli-responsive hydrogels, which can mimic the natural extracellular three-dimensional matrix environment with minimal immunogenic responses for therapeutic applications.[6,7] The structural design of PAs parallels prior established peptide-based systems[8] through integration of an alkyl tail that provides added mechanical control while retaining a polypeptide chain with desirable bioactive properties in terms of pharmacokinetics and degradability.[5,9-11] The presence of hydrophilic and hydrophobic regions of a typical PA molecule provides a local domain by which weak, non-covalent interactions (e.g. electrostatic, hydrophobic, hydrogen bonding, and van der Waals)[5,8,12] facilitate molecular self-assembly in such a delicate manner that the balance between these interactions can largely influence the morphology of the resulting nanostructures.[13-15]

Current research efforts focus on elucidating the interrelationship between the microscopic structural properties and macroscopic material characteristics to aid in the development of a versatile system that exhibits appropriate and suitable functional, structural, and mechanical properties.[16,17] This is accomplished by changing the strength of the intermolecular forces and controlling the ability of PA molecules to form hydrophobic interactions in addition to other types of interactions. The effect of hydrophobicity on PA assembly is primarily through modification of the alkyl tail and/or peptide sequence.[10,18,19] For example, truncating or shortening the alkyl tail deters formation of a nanofiber network whereas stabilized ordered structures are observed at an optimal moderate alkyl tail length of 16 carbons. In addition, the role of the hydrophobic effect has been further examined with amphiphilic peptides through substitution of individual amino acids[20,21]. On one hand, addition of a few hydrophobic residues can significantly affect secondary

structure formation by either having predominant α-helical or β-sheet elements resulting in different supramolecular properties such as ordering and packing of the aggregate assemblies[20]. On the other hand, by interchanging a strong hydrophobic residue with a less hydrophobic residue, intermolecular hydrogen bonding becomes more favorable extending the different types of nanostructures to include nanotube and globular micelle in addition to nanofiber.[21] Computationally, the effect of hydrophobicity has been examined by Velichko *et al*. who used a simplified model to perform Monte Carlo simulations[14]. However, their simplified model was unable to capture the formation of a variety of secondary structures, electrostatic interaction and peptide specificity.

Previously, we examined the role of electrostatic interactions on self-assembly behavior of a model PA molecule, palmitoyl-$V_3A_3E_3$ (comprised of a hydrophobic alkyl 16-mer tail that is covalently conjugated to a peptide segment of valine, alanine, and glutamic acids)[19,22] using our coarse-grained (CG) peptide-polymer model, ePRIME.[23] The model is an extension of the Protein Intermediate Resolution Model called PRIME[24] by accounting for all twenty natural amino acids. It captures fundamental biological character to mimic realistic molecular interactions based on amino acids and polymers, yet is simplified enough for the simulation of large systems over relatively long time scales. Such large-scale molecular dynamics simulations are capable of capturing spontaneous formation of secondary structures during the self-assembly process by PA molecules starting from a random configuration.

This approach is in contrast to the MARTINI[25] model used by Lee *et al*., who performed MD simulations on a similar PA system in which the amount of secondary structures was predetermined in advance and fixed throughout the simulation.[26] We

showed that as the strength of the electrostatic interaction increases between charged residues, a morphological transition from cylindrical nanofibers to spherical micelles was observed in agreement with experimental results on the effects of pH and ionic concentrations.[18,27,28] Moreover, our cylindrical nanofiber structures share high fidelity to the proposed structure by Stupp and coworkers[9] based on cryo-TEM and FTIR spectroscopy data and the atomistic model from simulations performed by Schatz and coworkers.[29]

In this study, we investigate the role of hydrophobic interactions on the self-assembly behavior of the model PA molecules by systematically modifying the strength, ε_{HP}, of the hydrophobic interactions between both domains of the model PA sequence. The pairwise strength, $\varepsilon_{HP}=R(\Delta G_i+\Delta G_j)$, is modulated by a scale factor, R, where R ranges from 1/8 to 1.3 and ΔG is the free energy of transferring each amino acid or chemical group from water to octanol.[30,31] This scale factor, R, is an inclusive parameter that is analogous to selecting a particular polymer type. Using the alkyl tail as a reference with R=1/3, a higher value of R corresponds to a strongly hydrophobic polymeric tail (e.g., polystyrene)[32] whereas a lower value of R corresponds to a more hydrophilic polymeric tail (e.g., poly(ethylene glycol)).[33] In addition, the hydrophobicity scale factor R can be considered as a degree of conjugation corresponding to the length of the alkyl tail. Alternatively, this R parameter can be interpreted as the degree of hydrophobicity between the polymeric tail and nonpolar peptide residues that is governed by the particular solvent choice. In this case, high values of R correspond to polar solvent (or by adding polar cosolutes) whereas low values of R are associated with nonpolar solvent (or by adding nonpolar cosolutes).[34] By performing molecular dynamics simulations at different values of R, we hope to provide

a detailed perspective in identifying the transition points between changes in morphology of self-assembled nanostructures and characterizing additional structures that may not be as easily isolated in experimental work.

To provide a frame of reference, replica-exchange simulations are first performed on a single molecule of palmitoyl-$V_3A_3E_3$ using ePRIME[23] to demonstrate the effect of hydrophobicity on secondary structure formation. A comparison is then made with the secondary structures observed from atomistic simulations using the CHARMM27[35,36] force field in NAMD[37] as a form of validation for our coarse-grained model. From the behaviors learned in single molecule simulations, we extend our study to a large-scale system containing 800 PA molecules in random coil conformations as the initial configuration at a PA concentration of 85 mM for molecular dynamics simulations. Self-assembled nanostructures are characterized as a function of hydrophobic interaction strength to identify morphological transitions. Since hydrophobicity is dependent of the temperature,[38,39] the effect of temperature on the structural aspect of the assembly is also discussed at different hydrophobic interaction strengths. Modification of both of these variables (i.e., hydrophobic interaction strength and temperature) together allows investigation of their influence on the formation of shape-specific nanostructures and provides a customizable platform for achieving distinctive nanoassemblies.

4.3 Methods

The model peptide amphiphile (PA) sequence is palmitoyl-$Val_3Ala_3Glu_3$, which was chosen based on previous experimental work by Pashuck *et al.*[19] Each PA molecule is represented using ePRIME[23], an extension of the Protein Intermediate Resolution Model

(PRIME),[24] by accounting for all twenty natural amino acids. For the peptide segment, the backbone atoms (NH, $C_\alpha H$, and CO) of each amino acid residue are represented by three spheres. The model for the side chains of each amino acid is adopted from the scheme originally developed by Wallqvist and Ullner.[40] In this case, all amino acid side chains, except glycine, are represented with at least one sphere. Short side chains are represented as one sphere while long side chains are represented as two spheres. The size of a side-chain sphere is derived from the solvent accessible area, which was obtained by Eisenberg and coworkers.[30] For the polymeric tail, each monomeric group is represented as single sphere whose bond distance and fluctuation are extracted from available atomistic parameters.[23]

The solvent is modeled implicitly by factoring its effect into the energy function as a potential of mean force averaged over the solvent degrees of freedom. In other words, the effect of solvent is wholly incorporated into the effective residue-residue potential that is based on the hydrophobicity of each side chain. In this case, the potential form is taken to be either a square-well potential, which approximates an attractive Lennard-Jones potential for purely hydrophobic side chain or polymeric group, or a square-shoulder potential, which approximates a repulsive form of the Lennard-Jones potential for purely hydrophilic side chain or polymeric group. The interaction strength between two groups is $\varepsilon_{HP} = R(\Delta G_i + \Delta G_j)$ where ΔG is the free energy of transferring each group from water to octanol[30,31] and R is a measure of the strength of the hydrophobic interaction ranging from 1/8, to 1.3. In addition, hydrogen bonding between amide hydrogen atoms and carbonyl oxygen atoms is represented by a directionally dependent square-well attraction of strength ε_{HB}=12 kJ/mol between NH and CO united atoms. Moreover, electrostatic

interactions, which are treated at the level of Debye-Huckel theory, are implemented using three-step square-well or shoulder-well potentials with a 12 Å cutoff. In this study, the strength of an electrostatic repulsion between two charges on the glutamic acids, ε_{ES}, is the same as that of the hydrogen bond, ε_{HB}, as it is the optimal condition where cylindrical nanofibers were observed in our previous study.[23]

Simulations are performed by using the DMD (discontinuous molecular dynamics) simulation algorithm[41], a variant on standard molecular dynamics that is applicable to systems of molecules interacting via discontinuous potentials, e.g., hard-sphere, and square-well potentials. Unlike soft potentials such as the Lennard-Jones potential, discontinuous potentials exert forces only when particles collide, enabling the exact (as opposed to numerical) solution of the collision dynamics. DMD simulations proceed by locating the next collision, advancing the system to that collision, and then calculating the collision dynamics. Simulations are performed in the canonical ensemble with periodic boundary conditions imposed to eliminate artifacts due to box walls. Constant temperature is achieved by implementing the Andersen thermostat method[42]. In this case, all beads are subjected to random, infrequent collisions with ghost particles whose velocities are chosen randomly from a Maxwell Boltzmann distribution centered at the system temperature. Simulation temperature is expressed in terms of the reduced temperature, $T^* = k_BT/\varepsilon_{HB}$, where k_B is Boltzmann's constant, and T is the temperature. Reduced time is defined to be $t^*=t/\sigma(k_BT/m)^{1/2}$, where t is the simulation time, and σ and m are the average bead diameter and mass, respectively.

For the self-assembly simulations, starting from a random coil configuration, 800 PA molecules were placed in a cubic box with periodic boundary dimensions of 250 Å x 250 Å

x 250 Å. The system containing 44,000 particles at a PA concentration of c = 85 mm. Each simulation was heated at high temperature (T^* = 5.0) to reach an un-biased initial configuration, and then quickly cooled to the temperature of interest, T^* = 0.08-0.15, for a constant-temperature production run until equilibration. The criteria for equilibrium is that each simulation was conducted for a long period of time until the ensemble averages of the system's total potential energy varied by no more than 2.5% during the last three-quarters of each simulation run. To examine the effect of hydrophobicity on self-assembly, each simulation was conduct at a hydrophobicity scale factor, R, ranging from 1/8 to 1.3. At each condition of the middle range of temperature and hydrophobicity strength, 10 independent simulations were conducted because of the stochastic nature of self-assembly. At each condition of the extreme ends of temperature and hydrophobicity strength, only three independent simulations were conducted since variability in the data is relatively low. Quantitative results in this paper are averages of the last 10% of simulation data with error bars taken from the standard deviation.

The secondary structures are defined through the implementation of STRIDE[43] including: α-helix, 3_{10}-helix, π-helix, β-strand/sheet (extended conformation), turn, bridge, isolated bridge, and random coil. However, we only focus on α-helix, β-strand/sheet, and random coil that also contains turn. An aggregate is defined if each PA molecule in a cluster has at least two interpeptide hydrogen bonds or four hydrophobic interactions with a neighboring PA molecule in the same group.

For model validation, five replica-exchange simulations at different hydrophobicity scale R values were conducted for a single PA chain. Each simulation contains 16 replicas distributed over a broad interval of temperature ranging from T^* = 0.07 to T^* = 0.17.

Exchange attempts occur every $t^* = 5.0$ reduced time units. This corresponds to a replica-exchange attempt after ~6,000,000 collisions at each temperature. Approximately 29,700 replica-exchange attempts are made before equilibrium is reached. The criteria for equilibrium is that the ensemble average of the system's total potential energy, which is collected at the end of each DMD run, should vary by no more than 2.5% during the second half of all DMD runs at each temperature. Once equilibrium is reached, the data collection phase begins in which 3300 extra replica-exchange attempts are made.

All-atom replica-exchange simulation is also performed using NAMD[37] for a single PA chain to serve as a validation of our coarse-grained model. The simulation has 16 replicas over a wide range of temperature ranging from T = 260K to T = 550K using the CHARMM 27 forcefield[35,36]. A replica-exchange attempt is made at every 2000 steps, which corresponds to 4ps for each temperature and an approximate 30,000 replica-exchange attempts were made.

4.4 Results and Discussions

4.4.1 Increasing the strength of hydrophobic interactions between polymeric tail and peptide segment hinders secondary structure formation

Conformational behavior of a single PA molecule is observed to be a function of the hydrophobic interaction strength by performing replica exchange molecular dynamics (REMD) simulations[44] (consisting of 16 replicas distributed over a range of temperature T* = 0.07 – 0.17 in reduced values) using our ePRIME model.[23] Representative equilibrium conformations from the lowest temperature at 5 different hydrophobic interaction strengths (R) are shown in **Figure 4.1A**. At weak hydrophobicity (R=1/8), the peptide

segment folds into α-helical conformations while the polymeric tail is positioned away from the peptide segment as indicated by few number of hydrophobic interactions (**Figure 4.1B)**. As the hydrophobic interaction strength is increased to R = 1/2, the polymeric tail bends in the middle to form hydrophobic interactions with nonpolar residues, especially proximal valines. The peptide segment is seemingly unperturbed by the polymeric tail as it remains in an α-helical conformation. However, further increase of the hydrophobic interaction strength to R = 1.0 causes both the peptide segment and the polymeric tail to collapse into a condensed structure that is no longer resemblant of a hierarchical folded structure.

Predominant conformations exhibited by single PA molecules are α-helical and random coil structures as a function of the temperature as shown by the percentage of secondary structures for 5 different hydrophobic interaction strengths (**Figures 3.1C-D**). (Increasing values of R from weak to strong hydrophobic interaction strength correspond to the color scale from black to red shown in **Figure 4.1A.** Standard deviation is considerably large at about 20% but this is an inherent byproduct of short peptides that exhibit a high degree of structural flexibility). At low temperatures and weak hydrophobic interaction strength, α-helical structures are prevalent with minimal random coil structures. However, a transition towards random coil structures is observed as the temperature increases above the melting temperature, which is observed at T* = 0.085. The effects of temperature can be attributed to the available kinetic energy within the system. At high temperatures, the kinetic energy disrupts the ability for residues to form stable interactions as opposed to at lower temperatures. Across all conditions, minimal amount of β-strand is observed since the chosen peptide sequence is relatively short

containing six strong helix-forming residues (alanines and glutamic acids) and just three β-strand-forming residues (valines). This agrees with the predictive models by Chou *et al.*[45] and Levitt and workers[46] based on their statistical analysis on a large library of globular proteins found in nature.

At weak to moderate hydrophobic interaction strengths, R ≤ 1/2, the overall trend of conformations observed from CG simulations across a broad range of temperature shows agreement with the data from atomistic simulation using an alkyl chain for the polymeric tail (shown in inset). Moreover, equilibrium structures from both CG and atomistic simulations (not shown) produce a high degree of similarity of conformations by the peptide segment and the interactions between the polymeric tail and the peptide segment.

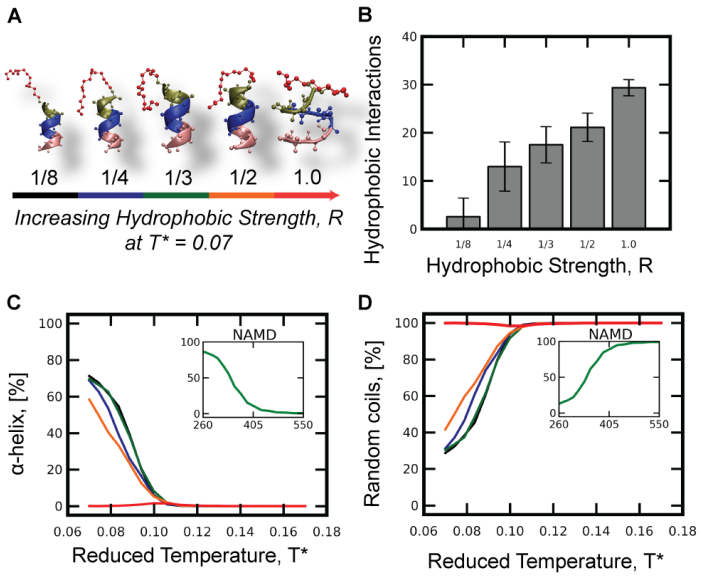

Figure 4.1. (A) Snapshots of equilibrium conformations for a single PA molecule is shown at T*=0.07 for 5 different R values. Color scheme for the molecule by using VMD[47]: hydrophobic polymeric tail (red), valine (green), alanine (blue), and glutamic acid (pink). (B) The number of hydrophobic interactions between the polymeric tail and the peptide side chains as a function of R at T*=0.07. The percentage of (C) α-helical and (D) random coil structures as a function of temperature over a range of R values using coarse-grained ePRIME. Inset graph provides validation data obtained from atomistic simulation. All data shown is taken from the average of the last 10% of equilibrium data.

4.4.2 Varying the hydrophobic interaction strength results in the formation of distinctive nanostructures

Starting from an initial random configuration, 800 isolated PA molecules were observed to spontaneously self-assemble into supramolecular aggregates at a moderate temperature of T* = 0.11 for a wide range of hydrophobic interaction strengths. The nanostructures can be classified as either open- or closed- structures due to the arrangement of the hydrophobic core that is comprised primarily of polymeric tails (**Figure 4.2A**). At weak hydrophobic interaction strength (R = 1/6), the position of the polymeric tails with respect to each other lack a coherent structure as compared to stronger hydrophobic strengths (R > 1/6) in which the polymeric tails form an enclosed core.The preference to form a network can be attributed to the electrostatic repulsion between charged glutamic acid residues. Weak hydrophobic interaction strength allows the electrostatic repulsion to be more effective, which promotes the formation of an extended structure to minimize charge-charge repulsion. As the hydrophobic interaction strength increases, the electrostatic repulsion between charged glutamic acid residues becomes less dominant, allowing PA molecules to condense into micelles. This transition in the overall architecture of nanostructures from scattered to condensed states suggests that the porosity and swelling-ratio of hydrogels can be controlled by varying the effective hydrophobicity of self-assembling PA molecules for drug-release applications.[48,49]

The degree of scattered or condensed disposition of a nanostructure with respect to the intermolecular interaction strengths can be determined by calculating the average solvent accessible surface area (SASA) restricted to only the polymeric tail (**Figure 4.2B**). At weak hydrophobic interaction strength of R = 1/6, SASA values are almost twice as large

in contrast with moderate and strong hydrophobic interaction strengths. The absence of an enclosed hydrophobic core at R = 1/6 exposes both the hydrophobic polymeric tails and peptide segments to nearby solvent molecules. In contrast, at stronger hydrophobic interaction strength, R > 1/6, the arrangement of the polymeric tails is sequestered away from the surrounding solvent by a protective barrier that is created by the peptide residues, which enclose the polymeric tails and reduce possible solvent penetration. This implies that the formation of compact structures, due to the increase in hydrophobic interaction strength, is possible by pulling the polymeric tail and hydrophobic amino acids towards the central axis and condensing each PA molecule.

To investigate the internal organization of self-assembled nanostructures, the average radius of gyration, R_g, of each peptide segment is calculated for the large-scale system and was found to be an inverse linear relationship to the hydrophobic interaction strength (**Figure 4.2C**). The R_g value for the open-network of β-sheets at R = 1/6 is relatively larger than for closed structures at stronger hydrophobic strengths. Isolating a prototypical single molecule conformation in the aggregate at each of the transitioning point shows pronounced progression, from an extended to a compacted conformation that is correlated to the number of favorable intermolecular interactions that aids in condensing the entire nanostructure. The inverse proportional relationship between radius of gyration and hydrophobic interaction strength observed from our simulations corresponds well with previous studies, which demonstrated that compact aggregated assemblies are correlated with significant hydrophobic character of individual PA molecules.[21,50]

4.4.3 Formation of secondary structures by individual PA molecules governs morphological transitions of aggregated assemblies

The presence of secondary structure elements provides insight into macroscopic material properties. Specifically, selective peptide sequences that can form β-sheet due to intermolecular hydrogen bonding have been correlated with an increase in hydrogel mechanical properties such as robustness, stiffness, and density.[19,51-54] Since the mechanical properties of hydrogels acting as synthetic extracellular matrix can affect cell adhesion and cell differentiation, such correlation can be used as a parameter to customize biomaterials for tailored biomedical applications.[55] Therefore, it is important to examine the formation of secondary structure of the peptide segment of individual PA molecules within different nanostructures as a function of the hydrophobic interaction strength.

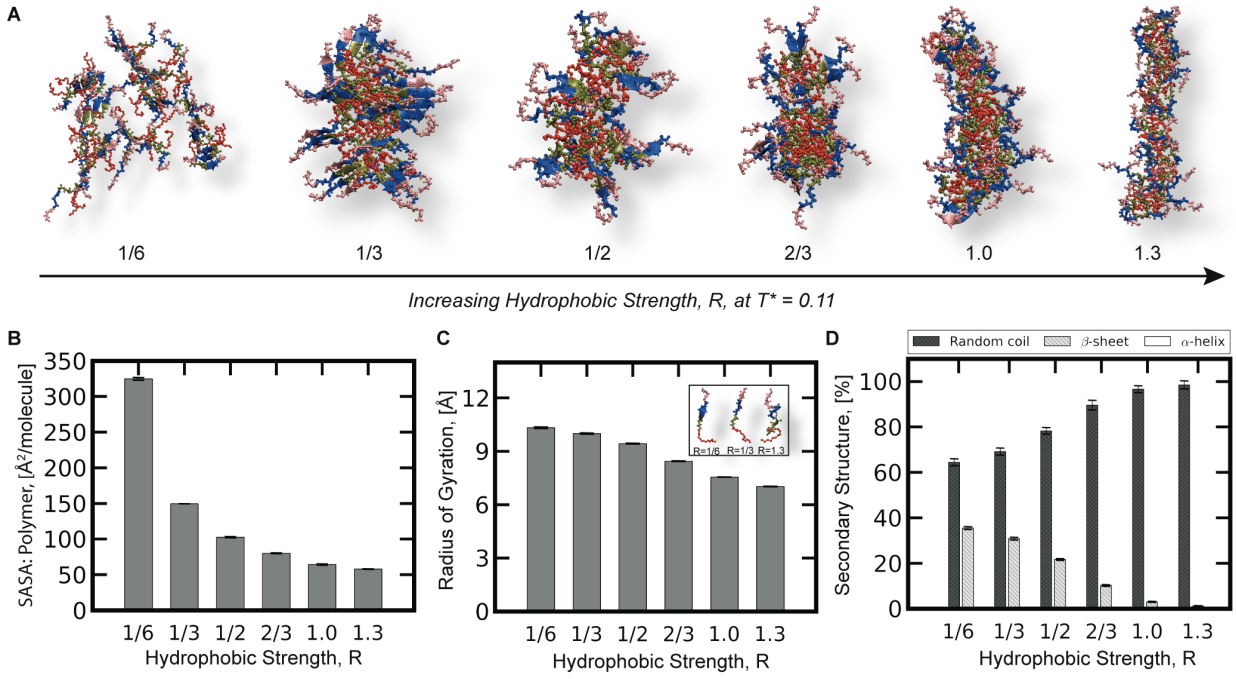

Figure 4.2. (A) Distinctive nanostructures (e.g. network of β-sheets, cylindrical nanofibers, and cylindrical micelles) at equilibrium are shown. (B) Average solvent accessible surface area restricted to the polymeric

tail implemented in VMD,[47] using a probe of 1.4Å radius, (C) average radius of gyration, and (D) secondary structure formations as a function of hydrophobic interaction strength are plotted at a moderate temperature of T* = 0.11. Inset in plot (C) shows representative single molecule conformation extracted from self-assembled aggregates at weak, moderate and strong hydrophobic interaction strength.

For a broad distribution of hydrophobic interaction strengths at a constant moderate temperature of T* = 0.11, β-sheets and random coil are the predominant secondary structure elements (**Figure 4.2D**). Since the chosen temperature is higher than the melting temperature at T*=0.085 of a single molecule (**Figure 4.1C**), minimal α-helical structures are seen (**Figure 4.2D**). Instead, β-conformations that are absent in a single molecule system are now observed for a large-scale system. With multiple PA molecules present nearby in a concentrated system, peptide residues are able to form favorable intermolecular hydrogen bonds and arrange themselves into β-sheets. The propensity to form the most β-sheet content is when the hydrophobic interaction strength is weak at R = 1/6. Interestingly, characterization of open networks indicates that the contribution of intermolecular hydrogen bonds is to act as an adhesive to hold multiple β-sheets together and thus support the overall architecture. This type of self-assembled nanostructures is therefore described as an open-network of β-sheets.

Calculation of the secondary structure formation at moderate and strong hydrophobic interaction strengths can differentiate rod-like structures into cylindrical nanofibers, which exhibit β-sheet content, and cylindrical micelles, which exhibit random-coil content. At a moderate hydrophobic interaction strength, $1/3 \leq R < 2/3$, the percentage of β-sheet content ranges between 10% to 30%. Such a range of β-sheet amounts observed in our simulations for cylindrical nanofibers is in good agreement with previous experiments and simulations.[26,29,56,57] Moreover, our cylindrical nanofibers share high

fidelity to the proposed structure by Stupp and coworkers[9] based on cryo-TEM and FTIR spectroscopy data and the atomistic model from simulations performed by Schatz and coworkers.[29] These cylindrical nanofibers would create robust hydrogels as suggested by the correlation between fibrous gels and high mechanical properties based on experimental observations.[19,51-54] At strong hydrophobic interaction strength, $2/3 \leq R \leq 1.3$, the percentage of random coil is much larger than those at moderate and weak hydrophobicity. The absence of β-sheets can be attributed to the increase in favorable hydrophobic interactions between polymeric tail and peptide residues or between peptide residues. This interferes with formation of intermolecular hydrogen bonds and β-sheets, causing each PA molecule to collapse into a condensed conformation as previously discussed.

The hydrophobic core of cylindrical nanostructures is not only comprised of the polymeric tail but also of the nearby hydrophobic residues depending upon the hydrophobic interaction strength. Examination of the cylindrical nanofibers containing approximately the same number of PAs at moderate hydrophobic interaction strength ($R = 1/3$) (**Figure 4.3A**) indicates that only some valine residues position themselves within the interior exhibiting significant random coil conformations (the first valine residue at position 1 in **Figure 4.3B**). Instead, the majority of nonpolar peptide residues 2 to 6 contribute to the formation of β-sheets through favorable intermolecular hydrogen bonds (**Figure 4.3B**). In contrast, at strong hydrophobic interaction strength ($R = 1.3$), significant hydrophobic interactions between the polymeric and nonpolar peptide residues withdraw these residues into the interior of cylindrical micelles (**Figure 4.3C**) and prevent the peptide residues from β-sheet formation, resulting in the presence of random coil

conformations for all residues (**Figure 4.3D**). For both cases, the three glutamic acid residues at positions 7 - 9 adopt random coil conformations due to the electrostatic repulsion between charged side chains.

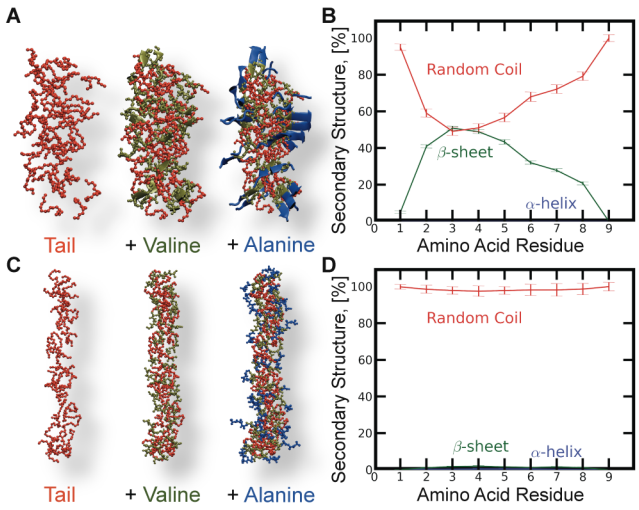

Figure 4.3. Representative structures (at a moderate temperature of T* = 0.11) shown to highlight the composition of hydrophobic core of cylindrical nanostructures containing polymeric tails (red), valines (green), alanines (blue) and the secondary structure as a function of sequence at (A-B) moderate, and (C-D) strong hydrophobic interaction strength. Valines are at position 1-3, alanines at 4-6, and glutamic acids at 7-9.

It is interesting that even though more nonpolar residues are in the interior hydrophobic core at strong hydrophobic interaction strength (R=1.3) than those at weak hydrophobic interaction strength (R=1/3), cylindrical nanostructures at R=1.3 are smaller in diameter than those at R=1/3 (full structures are shown in **Figure 4.2A**). If one could also correlate the hydrophobic interaction strength (R) as the overall hydrophobic character of a particular PA sequence of choice, these results provide a suggestion for future studies wherein replacing alanines with more nonpolar peptide residues might transform thick nanofibers containing β-sheets into slender micelles containing random coils. This is plausible since a previous simulation work[26] demonstrated that replacing β-

sheet-forming peptides residues with random-coil-forming residues using the MARTINI[25] model still results in the assembly of cylindrical micelles (without β-sheet content). Moreover, the formation of one-dimensional cylindrical nanostructures containing no β-sheet but high α-helical content has been experimentally observed using a PA mimetic molecule that incorporates glucagon-like peptide-1.[58] Furthermore, detecting the fiber thickness at the nanometer scale is feasible using AFM and TEM as demonstrated by Xu *et al*.,[59] who showed that increase in the hydrophobic region from A_6K to A_9K causes a substantial reduction in the diameter by 5nm of long nanofibers.

4.4.4 At strong hydrophobic interaction strength, temperature affects the presence of peptide residues within the hydrophobic core of cylindrical micelles

When the hydrophobic interaction strength is strong, hydrophobic interaction becomes a dominant driving force compared to hydrogen bonding and electrostatic interaction. However, temperature also plays a significant role in the self-assembly of PA molecules into cylindrical micelles (**Figure 4.4A**). At low temperatures, T* = 0.08 – 0.09, the discontinuity of the hydrophobic core is a result of the presence of nonpolar peptide residues (i.e., valine and alanine) that are located between sections of polymeric tails. The mechanism that is responsible for forming these nanostructures (**Figure 4.7**) involves condensation of small and spherical micelles, which tend to aggregate together in a kinetically trapped state. This causes the formation of nanostructures with 'branched' morphology at low temperatures. When the temperature increases, the ratio of peptide residues to polymer tail that comprise of the hydrophobic core slowly approaches zero. This yields un-branched cylindrical micelles with continuous hydrophobic cores.

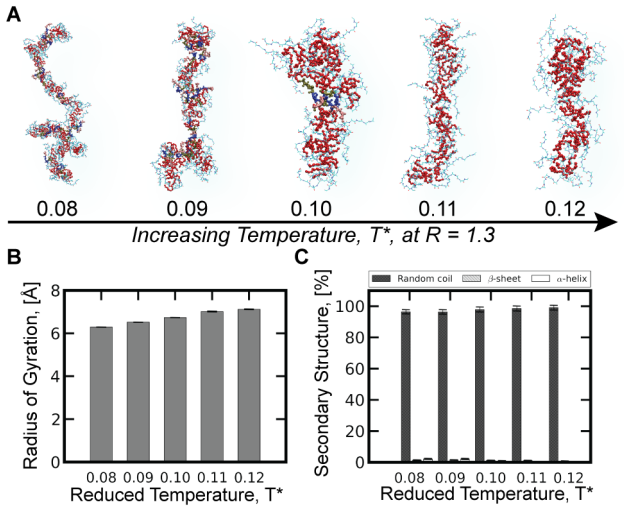

Figure 4.4. At strong hydrophobic interaction strength of R = 1.3: (A) arrangement of the polymeric tails (red) within the hydrophobic core is shown to emphasize the discontinuity within the central axis of the representative equilibrium supramolecular aggregates; the (B) average radius of gyration; and (C) secondary structure as a function of temperature.

The extent of discontinuity present in the hydrophobic core of cylindrical micelles as a function of the temperature is the outcome of the competition between intra- and intermolecular interactions. At low temperatures, each PA molecule collapsed into a condensed conformation by forming intramolecular hydrophobic interactions before forming intermolecular interactions with neighboring molecules. In contrast, at higher temperatures, T* > 0.10, each PA molecule has extra kinetic energy to freely explore the conformational space and form intermolecular interactions with neighboring molecules without forming intramolecular interactions with itself. These PA molecules can overcome the kinetically trapped state by re-orienting themselves into extended conformations (**Figure 4.4B**) such that the polymeric tails are in the interior and peptides residues are on the surface. This allows them to assemble into more energetically favorable structures. Regardless of the adopted conformation by the individual PA molecules as either compact

or extended as a function of temperature, minimal amounts of α-helices and β-sheets are present; instead, random coil is the predominant conformation.

4.4.5 At weak hydrophobic interaction strength, temperature affects the formation of secondary structures of open networks

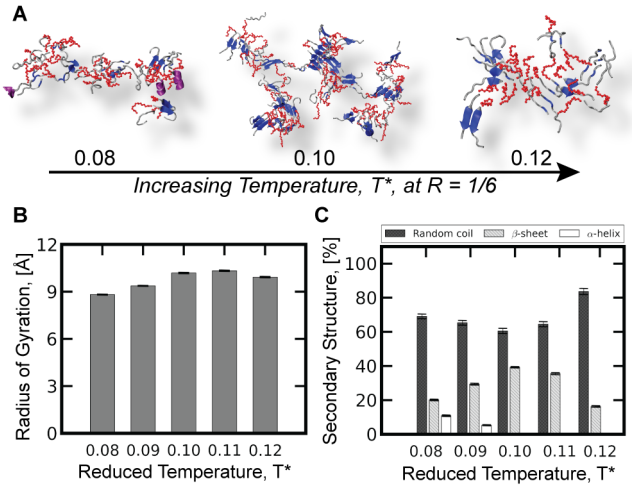

Figure 4.5. At weak hydrophobic strength of R = 1/6: (A) representative nanostructures are shown emphasizing the formation of β-sheets (blue) and α-helices (purple); (B) average radius of gyration; and (C) secondary structure as a function of temperature.

At a weak hydrophobic interaction strength of R = 1/6, hydrophobic interactions are not as dominant of a driving force compared to hydrogen bonding. Therefore, hydrogen bonding yields the formation of open networks that contain relatively large amounts of α-helices and β-sheets (**Figure 4.5A**). Moreover, with respect to the individual peptide conformation, calculation of the radius of gyration (**Figure 4.5B**) indicates the formation of compact structures of α-helices at lower temperatures compared to extended structures of β-sheets at higher temperatures. This is confirmed by the amount of secondary structures as a function of the temperature (**Figure 4.5C**). At low temperatures, T* = 0.08 – 0.09, a

significant percentage of α-helical structures is observed, which can be attributed to favorable intramolecular hydrogen bonds between peptide residues within the same molecule. As the temperature increases, T* = 0.10 – 0.11, α-helical structures becomes less prevalent since the molecule can undergo multiple structural rearrangement resulting in the disruption of intramolecular hydrogen bonds and shift towards the formation of intermolecular hydrogen bonds and thus β-sheets. At higher temperatures, T* ≥ 0.12, the architecture of aggregates maintains an open-network with the absence of an enclosed hydrophobic core, however, there is a sharp decrease in α-helical and β-sheet formation. Instead, a large amount of random coil structures are evident due to increased flexibility of the PA molecules at high temperatures.

Increasing the temperature from 0.08 to higher values enhances the structural order of PAs by increasing the amount of β-sheet and decreasing α-helices as seen in **Figure 4.5C**. Such temperature-dependent formation of α-helices in a highly concentrated environment is reflective of the single-molecule behavior as shown in **Figure 4.1C**. As a single molecule at the start of simulation, PAs prefer to form α-helices especially at low temperatures of T* = 0.08 – 0.09. However, when there are neighboring molecules nearby, they can form intermolecular interactions and thus result in β-sheets. When the temperature increases beyond the melting point (which is at 0.085 as seen in **Figure 4.1C**), the amount of α-helices decreases; inversely, β-sheets increase significantly. This conformational transition from α-helices at low temperatures to β-sheets at high temperatures is also seen in amyloid fibril formation systems involving amyloidogenic peptides.[60]

4.4.6 Hydrophobic-temperature phase diagram delineating PA morphological transitions

The introduction of a scale factor, R, representing the effective hydrophobic interaction strength has allowed us to examine the choice of polymeric tail and to some degree both the sequence dependence and aqueous medium on the spontaneous self-assembly of PA molecules. The results from large-scale CG MD simulations are summarized as a phase diagram shown in **Figure 4.6** with regions denoted with characteristic nanostructures that are stable for the associated hydrophobic interaction strength and temperature.

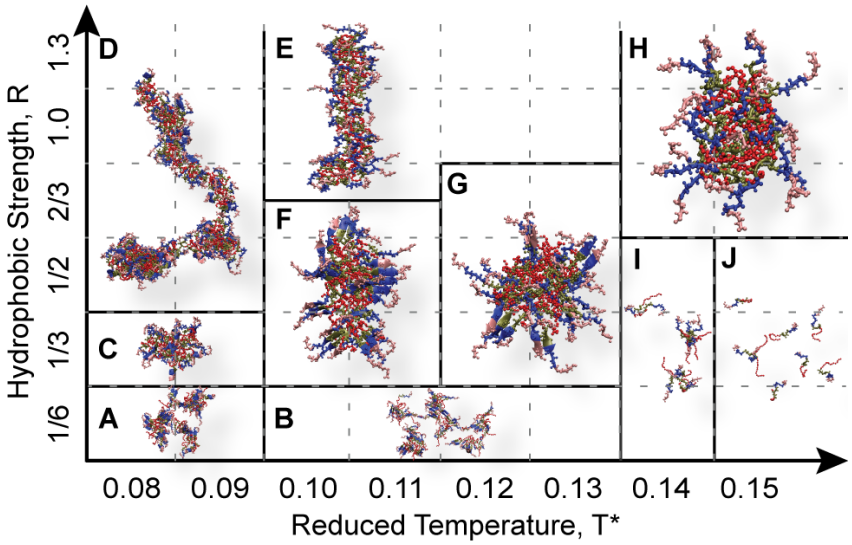

Figure 4.6. Phase diagram of representative equilibrium structures as function of hydrophobic interaction strength and temperature: (A) network of α-helical and β-sheets; (B) network of β-sheets; (c) spherical micelles with α-helical and β-sheets; (D) cylindrical micelles stabilized by contiguous core of polymeric tails and peptide residues; (E) cylindrical micelles stabilized by contiguous core of polymeric tails; (F) cylindrical nanofiber structures; (G) spherical micelles with only β-sheets; (H) spherical micelles with minimal secondary structure elements; (I) oligomers; (J) random coils.

At weak hydrophobic interaction strength and low temperatures, the available kinetic energy is low within the system. Therefore, PA molecules are driven to form

intramolecular interactions primarily in the formation of α-helical structures with intermittent β-sheets (**Figure 4.6A**). As the temperature increases, a transition from α-helical to more prevalent β-sheet structures is observed since PA molecules tend to form more favorable intermolecular hydrogen bonds (**Figure 4.6B**). The morphology of these nanostructures can be generalized as an open-network of either predominantly α-helices or β-sheets. Weak hydrophobic interaction strength allows the electrostatic repulsion between charged glutamic acids to be dominant, which promotes the formation of an extended structure to minimize charge-charge repulsion.

As the hydrophobic interaction strength increases at low temperature, a structural shift from open- to closed- structures is observed with the emergence of an enclosed hydrophobic core primarily due to the arrangement of the polymeric tails. To maximize favorable hydrophobic interactions, nonpolar residues are essentially sequestered from the surrounding solvent forming small spherical micelles (**Figure 4.6C**). When charge-charge repulsion is weakened by an increase in hydrophobic interaction strength, spherical micelles can merge together to form larger continuous rod-like structures. At strong hydrophobic interaction strength, subtle differences lies within the rod-like nanostructure. The hydrophobic core of branched nanostructures at low temperatures is comprised of both the polymeric tail and hydrophobic peptide residues (**Figure 4.6D**). At higher temperatures, structural rearrangement yields the polymeric tail as the only element within the hydrophobic core (**Figure 4.6E**).

For moderate hydrophobic interaction strength and moderate temperature, a cylindrical nanofiber structure is observed with the formation of β-sheets aligning the surface while maintaining a hydrophobic core (**Figure 4.6F**). However, as the temperature

increases, rod-like structures are no longer formed. Instead, unstable interactions break such nanostructures into smaller spherical micelles; however, large percentage of β-sheets remains (**Figure 4.6G**). At sufficiently high temperatures and strong hydrophobic strength, spherical micelles are formed from initial hydrophobic collapse but minimal secondary structures are observed (**Figure 4.6H**). For weak hydrophobic interaction strength and high temperatures, small aggregates or oligomers (**Figure 4.6I)** and random coils (**Figure 4.6J**) are the primary species as large aggregates cease to form.

The nanostructures observed from our CG model can be broadly compared to the work of Velichko *et al*.[14], who examined the interplay of hydrogen bonding and hydrophobic forces on PA self-assembly (the strength of their hydrogen bond is inversely proportional to our reduced temperature). For example, free molecules observed at low hydrophobic attraction and hydrogen bonding correlate with the oligomers and random coil that we see at high temperatures. At strong hydrophobic interaction and low temperature, spherical micelles are observed for both CG models. In general, our simulations observe a similar range of basic morphologies, which serves as a good validation for our CG model. However, since our model can accommodate the formation of secondary structure and accounts for hydrophobic interactions between polymeric tail and nonpolar residues, our simulations are able to assemble a wider range of structures such as open networks containing both α-helices and β-sheets in addition to cylindrical micelles containing disrupted and continuous hydrophobic cores.

The effect of hydrophobicity on PA self-assembly is remarkably different than the effect of electrostatics as previously studied[23]. At moderate temperatures, instead of the progression from open networks of secondary structures towards closed cylindrical

nanostructures containing β-sheets and then random coils as the strength of hydrophobic interactions is increased, cylindrical nanofibers shift to spherical micelles when the electrostatic repulsion between the charged groups on glutamic acids becomes strong. Moreover, when such electrostatic repulsion is weak, spherical-like structures that are comprised of both α-helices β-sheets at low temperatures transition into cylindrical nanofibers containing prevalent β-sheets on the surface at moderate temperatures. Further increase in temperature drives a second morphological transition from cylindrical nanofibers to spherical micelles with only β-sheets. At sufficiently high temperatures, spherical micelles are still present; however, they lose secondary structures as the peptide segments unravel into random coils. At higher temperatures, small aggregates or oligomers exist. Increasing the temperature further prevents PA molecules to form aggregates; in this case, PA molecules exist as random coils. Furthermore, when the electrostatic repulsion is strong at low temperatures, a mixture of kinetically trapped amorphous structures, which is observed at low temperatures, transitions into small spherical micelles without secondary structure elements at moderate temperatures. Increasing the temperature further destabilizes attractive interactions, which results in the formation of oligomers and extended conformations.

4.5 Conclusions

Implementation of our recently developed peptide/polymer coarse-grained model, ePRIME,[23,24] coupled with a fast MD algorithm,[41] has allowed us to understand the spontaneous self-assembly behavior of peptide amphiphiles. In this study, we examined the effective effects of either modifying the polymeric tail, peptide sequence, or aqueous

medium, and temperature for both single molecule and large-scale concentrated system of PA molecules. By altering the corresponding model parameters, hydrophobic interaction strength and temperature, a wide range of distinctive nanostructures are formed that are reflective of the single molecule behavior. At a constant moderate temperature, β-sheet-rich cylindrical nanofiber structures, which share high similarity to previous experiments[9,56] and simulations[26,29,57], transition into either open networks containing β-sheets or cylindrical micelles containing random coils as a function of hydrophobic interaction strength. Although such morphological transitions have not been observed on amphiphilic polymer-peptide conjugates, experimental works on amphiphilic peptides[21,59] have shown structural transitions between lamellar sheets, fibers, worm-like micelles, and short rods as the number of hydrophobic peptide residues increases[59]. Moreover, temperature also governs the morphology of self-assembled aggregates via the formation of secondary structures. The interplay between these two variables is documented in the form of a phase diagram to identify nanostructures with specific traits.

Structural characterization for each of the nanostructures is measured in terms of the solvent accessible surface area, secondary structure formation, and the radius of gyration. The solvent accessible surface area enables differentiation between open- and closed- structures. Calculation of the secondary structure formation allows further classification between cylindrical structures that contain β-sheets (nanofibers) or random coils (micelles), which provides an intuition about the corresponding bulk material properties such that large amount of β-sheets correlate with stiffer materials.[19,51-54] The packing density and/or porosity of the nanostructure can also be extrapolated by calculating the radius of gyration that essentially describes the internal arrangement of the

self-assembled PA molecules.[50] Through these analysis methods, we hope to establish appropriate and adequate benchmarks for the design of biomaterials using these molecular level building blocks.

Our results as summarized in a phase diagram can provide experimentalists some guidance in using appropriate temperature and polymeric tail to conduct *in-vitro* self-assembly experiments to seek or avoid the formation of certain nanostructures. In our simulations, variables for experimental conditions are expressed in reduced quantities to provide a qualitative frame of reference. While a direct correspondence to experimental or physiological values is difficult, correlation at a reference condition can be established by identifying the melting temperature at which a PA molecule exhibits equal percentage of α-helical and random coil structures as shown in **Figure 4.1C-D** from all-atom and coarse-grained simulations; i.e., our melting temperature is T*=0.085 which corresponds to ~320K. Morphological transitions at higher or lower temperatures compared to the melting temperature are meant for a qualitative interpretation. Similarly, correlation between polymeric types with our hydrophobic interaction strengths can be obtained in a qualitative manner by using our hydrophobic parameter R at 1/3 as a reference condition for the alkyl tail. These simulation insights on the effect of hydrophobicity, along with those on the effect of electrostatics[23], are valuable in aiding the design and development of bio-inspired materials for the fields of drug delivery, diagnostic medicine, tissue engineering, and regenerative medicine.

4.6 Acknowledgements

This work was originally published in Langmuir, 2014 © American Chemical Society. Co-authors include Cade B Markegard, Brian K Chu, and Hung D Nguyen. HDN acknowledges financial support from UC Irvine. IWF acknowledges support from a Graduate Research Fellowship from the National Science Foundation (DGE-1321846). This work used the Extreme Science and Engineering Discovery Environment (XSEDE), which is supported by National Science Foundation grant number OCI-1053575. We are also thankful for the computational resources provided by the GreenPlanet and High Performance Computing cluster at UCI.

4.7 Supplementary Information

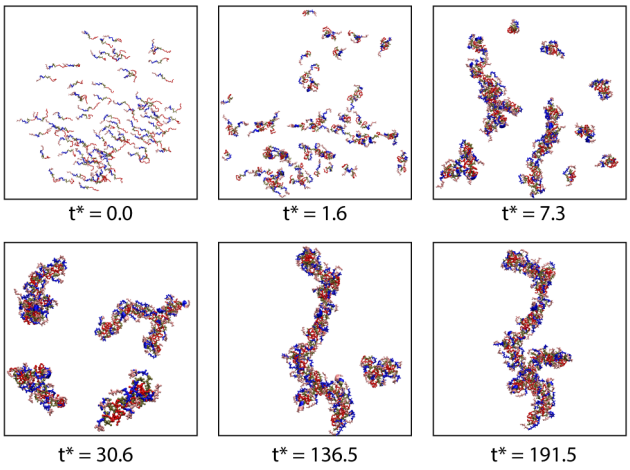

Figure 4.7. Snapshots of PAs as a function of time (t*, in reduced time units) showing the formation of a cylindrical micelle with discontinuity in its hydrophobic core at T*=0.08 and R = 1.3.

4.8 References

1. Duncan, R. The dawning era of polymer therapeutics. *Nat Rev Drug Discov* **2,** 347–360 (2003).
2. Löwik, D. W., Ayres, L., Smeenk, J. M. & Van Hest, J. C. Synthesis of Bio-Inspired Hybrid Polymers Using Peptide Synthesis and Protein Engineering. 19–52 (2006). doi:10.1007/12_081
3. Chow, D., Nunalee, M. L., Lim, D. W., Simnick, A. J. & Chilkoti, A. Peptide-based biopolymers in biomedicine and biotechnology. *Materials Science and Engineering: R: Reports* **62,** 125–155 (2008).
4. Nicodemus, G. D. & Bryant, S. J. Cell Encapsulation in Biodegradable Hydrogels for Tissue Engineering

Applications. *Tissue Engineering Part B: Reviews* **14,** 149–165 (2008).
5. Cui, H., Webber, M. J. & Stupp, S. I. Self-assembly of peptide amphiphiles: From molecules to nanostructures to biomaterials. *Biopolymers* **94,** 1–18 (2010).
6. Storrie, H. *et al.* Supramolecular crafting of cell adhesion. *Biomaterials* **28,** 4608–4618 (2007).
7. Collier, J. H., Rudra, J. S., Gasiorowski, J. Z. & Jung, J. P. Multi-component extracellular matrices based on peptide self-assembly. *Chem. Soc. Rev.* **39,** 3413 (2010).
8. Zhang, S., Marini, D. M., Hwang, W. & Santoso, S. Design of nanostructured biological materials through self-assembly of peptides and proteins. *Current Opinion in Chemical Biology* **6,** 865–871 (2002).
9. Hartgerink, J. D. Self-Assembly and Mineralization of Peptide-Amphiphile Nanofibers. *Science* **294,** 1684–1688 (2001).
10. Hartgerink, J. D., Beniash, E. & Stupp, S. I. Peptide-amphiphile nanofibers: A versatile scaffold for the preparation of self-assembling materials. *Proceedings of the National Academy of Sciences* **99,** 5133–5138 (2002).
11. Klok, H.-A. Biological-synthetic hybrid block copolymers: Combining the best from two worlds. *J. Polym. Sci. A Polym. Chem.* **43,** 1–17 (2004).
12. Trent, A., Marullo, R., Lin, B., Black, M. & Tirrell, M. Structural properties of soluble peptide amphiphile micelles. *Soft Matter* **7,** 9572–9582 (2011).
13. Meng, Q. *et al.* Tunable Self-Assembled Peptide Amphiphile Nanostructures. *Langmuir* **28,** 5017–5022 (2012).
14. Velichko, Y. S., Stupp, S. I. & la Cruz, de, M. O. Molecular Simulation Study of Peptide Amphiphile Self-Assembly. *J. Phys. Chem. B* **112,** 2326–2334 (2008).
15. Tsonchev, S., Schatz, G. C. & Ratner, M. A. Electrostatically-Directed Self-Assembly of Cylindrical Peptide Amphiphile Nanostructures. *J. Phys. Chem. B* **108,** 8817–8822 (2004).
16. Zhu, J. & Marchant, R. E. Design properties of hydrogel tissue-engineering scaffolds. *Expert Rev Med Dev* **8,** 607–626 (2011).
17. El-Sherbiny, I. M. & Yacoub, M. H. Hydrogel scaffolds for tissue engineering: Progress and challenges. *Nanomedicine* **2013,** 469–484 (2010).
18. Xu, X.-D., Jin, Y., Liu, Y., Zhang, X.-Z. & Zhuo, R.-X. Self-assembly behavior of peptide amphiphiles (PAs) with different length of hydrophobic alkyl tails. *Colloids and Surfaces B: Biointerfaces* **81,** 329–335 (2010).
19. Pashuck, E. T., Cui, H. & Stupp, S. I. Tuning Supramolecular Rigidity of Peptide Fibers through Molecular Structure. *J. Am. Chem. Soc.* **132,** 6041–6046 (2010).
20. Missirlis, D. *et al.* Effect of the Peptide Secondary Structure on the Peptide Amphiphile Supramolecular Structure and Interactions. *Langmuir* **27,** 6163–6170 (2011).
21. Han, S. *et al.* Self-Assembly of Short Peptide Amphiphiles: The Cooperative Effect of Hydrophobic Interaction and Hydrogen Bonding. *Chem. Eur. J.* **17,** 13095–13102 (2011).
22. Greenfield, M. A., Hoffman, J. R., Olvera de la Cruz, M. & Stupp, S. I. Tunable Mechanics of Peptide Nanofiber Gels. *Langmuir* **26,** 3641–3647 (2010).
23. Fu, I. W., Markegard, C. B. & Chu, B. K. The Role of Electrostatics and Temperature on Morphological Transitions of Hydrogel Nanostructures Self-Assembled by Peptide Amphiphiles Via Molecular …. *Advanced healthcare …* (2013). doi:10.1002/adhm.201200400
24. Nguyen, H. D., Marchut, A. J. & Hall, C. K. Solvent effects on the conformational transition of a model polyalanine peptide. *Protein Science* **13,** 2909–2924 (2004).
25. Monticelli, L. *et al.* The MARTINI Coarse-Grained Force Field: Extension to Proteins. *J. Chem. Theory Comput.* **4,** 819–834 (2008).
26. Lee, O.-S., Cho, V. & Schatz, G. C. Modeling the Self-Assembly of Peptide Amphiphiles into Fibers Using Coarse-Grained Molecular Dynamics. *Nano Lett.* **12,** 4907–4913 (2012).
27. Toksoz, S., Mammadov, R., Tekinay, A. B. & Guler, M. O. Electrostatic effects on nanofiber formation of self-assembling peptide amphiphiles. *Journal of Colloid And Interface Science* **356,** 131–137 (2011).
28. Ghosh, A. *et al.* Fine-Tuning the pH Trigger of Self-Assembly. *J. Am. Chem. Soc.* **134,** 3647–3650 (2012).
29. Lee, O.-S., Stupp, S. I. & Schatz, G. C. Atomistic Molecular Dynamics Simulations of Peptide Amphiphile Self-Assembly into Cylindrical Nanofibers. *J. Am. Chem. Soc.* **133,** 3677–3683 (2011).
30. Wesson, L. & Eisenberg, D. Atomic solvation parameters applied to molecular dynamics of proteins in solution. *Protein Science* **1,** 227–235 (1992).
31. Gu, W., Rahi, S. J. & Helms, V. Solvation Free Energies and Transfer Free Energies for Amino Acids from

Hydrophobic Solution to Water Solution from a Very Simple Residue Model. *J. Phys. Chem. B* **108,** 5806–5814 (2004).
32. Shu, J. Y. *et al.* Amphiphilic Peptide–Polymer Conjugates Based on the Coiled-Coil Helix Bundle. *Biomacromolecules* **11,** 1443–1452 (2010).
33. Jain, A. & Ashbaugh, H. S. Helix Stabilization of Poly(ethylene glycol)–Peptide Conjugates. *Biomacromolecules* **12,** 2729–2734 (2011).
34. Davis-Searles, P. R., Saunders, A. J., Erie, D. A., Winzor, D. J. & Pielak, G. J. Interpreting the effects of small uncharged solutes on protein-folding equilibria. *Annual Review of Biophysics and Biomolecular Structure* **30,** 271–306 (2001).
35. Foloppe, N. & MacKerell, A. D., Jr. All-atom empirical force field for nucleic acids: I. Parameter optimization based on small molecule and condensed phase macromolecular target data. *J. Comput. Chem.* **21,** 86–104 (2000).
36. MacKerell, A. D., Jr & Banavali, N. K. All-atom empirical force field for nucleic acids: II. Application to molecular dynamics simulations of DNA and RNA in solution. *J. Comput. Chem.* **21,** 105–120 (2000).
37. Phillips, J. C. *et al.* Scalable molecular dynamics with NAMD. *J. Comput. Chem.* **26,** 1781–1802 (2005).
38. Dill, K. A., Alonso, D. O. V. & Hutchinson, K. Thermal stabilities of globular proteins. *Biochemistry* **28,** 5439–5449 (1989).
39. Shimizu, S. & Chan, H. S. Temperature dependence of hydrophobic interactions: A mean force perspective, effects of water density, and nonadditivity of thermodynamic signatures. *J. Chem. Phys.* **113,** 4683–4700 (2000).
40. Wallqvist, A. & Ullner, M. A simplified amino acid potential for use in structure predictions of proteins. *Proteins: Structure, Function, and Bioinformatics* **18,** 267–280 (1994).
41. Alder, B. J. & Wainwright, T. E. Studies in molecular dynamics. I. General method. *J. Chem. Phys.* **31,** 459 (1959).
42. Andersen, H. C. Molecular dynamics simulations at constant pressure and/or temperature. *J. Chem. Phys.* **72,** 2384 (1980).
43. Frishman, D. & Argos, P. Knowledge-based protein secondary structure assignment. *Proteins: Structure, Function, and Bioinformatics* **23,** 566–579 (1995).
44. Sugita, Y. & Okamoto, Y. Replica-exchange molecular dynamics method for protein folding. *Chemical Physics Letters* **314,** 141–151 (1999).
45. Chou, P. Y. & Fasman, G. D. Prediction of protein conformation. *Biochemistry* **13,** 222–245 (1974).
46. Levitt, M. Conformational Preferences of Amino-Acids in Globular Proteins. *Biochemistry* **17,** 4277–4284 (1978).
47. Humphrey, W., Dalke, A. & Schulten, K. VMD: visual molecular dynamics. *Journal of molecular graphics* **14,** 33–38 (1996).
48. Hoffman, A. S. Applications of thermally reversible polymers and hydrogels in therapeutics and diagnostics. *Journal of Controlled Release* **6,** 297–305 (1987).
49. Fu, Y. & Kao, W. J. Drug release kinetics and transport mechanisms of non-degradable and degradable polymeric delivery systems. *Expert Opin. Drug Deliv.* **7,** 429–444 (2010).
50. Wiradharma, N., Tong, Y. W. & Yang, Y.-Y. Design and Evaluation of Peptide Amphiphiles with Different Hydrophobic Blocks for Simultaneous Delivery of Drugs and Genes. *Macromol. Rapid Commun.* **31,** 1212–1217 (2010).
51. Schneider, J. P. *et al.* Responsive Hydrogels from the Intramolecular Folding and Self-Assembly of a Designed Peptide. *J. Am. Chem. Soc.* **124,** 15030–15037 (2002).
52. Roberts, D., Rochas, C., Saiani, A. & Miller, A. F. Effect of Peptide and Guest Charge on the Structural, Mechanical and Release Properties of β-Sheet Forming Peptides. *Langmuir* **28,** 16196–16206 (2012).
53. Ozbas, B., Kretsinger, J., Rajagopal, K., Schneider, J. P. & Pochan, D. J. Salt-Triggered Peptide Folding and Consequent Self-Assembly into Hydrogels with Tunable Modulus. *Macromolecules* **37,** 7331–7337 (2004).
54. Dagdas, Y. S., Tombuloglu, A., Tekinay, A. B., Dana, A. & Guler, M. O. Interfiber interactions alter the stiffness of gels formed by supramolecular self-assembled nanofibers. *Soft Matter* **7,** 3524–3532 (2011).
55. Discher, D. E. Tissue Cells Feel and Respond to the Stiffness of Their Substrate. *Science* **310,** 1139–1143 (2005).
56. Niece, K. L. *et al.* Modification of gelation kinetics in bioactive peptide amphiphiles. *Biomaterials* **29,**

4501–4509 (2008).
57. Lee, O.-S., Liu, Y. & Schatz, G. C. Molecular dynamics simulation of β-sheet formation in self-assembled peptide amphiphile fibers. *Journal of Nanoparticle Research* **14,** 1–7 (2012).
58. Khan, S., Sur, S., Newcomb, C. J., Appelt, E. A. & Stupp, S. I. Acta Biomaterialia. *Acta Biomaterialia* **8,** 1685–1692 (2012).
59. Xu, H. *et al.* Hydrophobic-Region-Induced Transitions in Self-Assembled Peptide Nanostructures. *Langmuir* **25,** 4115–4123 (2008).
60. Nguyen, H. D. & Hall, C. K. Molecular dynamics simulations of spontaneous fibril formation by random-coil peptides. *Proceedings of the National Academy of Sciences* **101,** 16180–16185 (2004).

CHAPTER 5 Solvent Effects on Kinetic Mechanisms of Self-Assembly by Peptide Amphiphiles via Molecular Dynamics Simulations

5.1 Abstract

Peptide amphiphiles are known to form a variety of distinctive self-assembled nanostructures (including cylindrical nanofibers in hydrogels) dependent upon the solvent condition. Using a novel coarse-grained model, large-scale molecular dynamics simulations are performed on a system of 800 peptide amphiphiles (sequence: palmitoyl-$Val_3Ala_3Glu_3$) to elucidate kinetic mechanisms of molecular assembly as a function of the solvent condition. The assembly process is found to occur via a multi-step process with transient intermediates that ultimately leads to the stabilized nanostructures including open networks of β-sheets, cylindrical nanofibers and elongated micelles. Different kinetic mechanisms are compared in terms of peptide secondary structures, solvent accessible surface area, radius of gyration, relative shape anisotropy, intra/inter-molecular interactions and aggregate size dynamics to provide insightful information for the design of functional biomaterials.

5.2 Introduction

Peptide amphiphiles (PAs), which belong to a class of peptide-polymer conjugates,[1,2] contain a hydrophobic monoalkyl tail covalently attached to a hydrophilic peptide sequence including a bioactive segment.[3,4] These PA molecules exhibit excellent biocompatibility and possess dynamic stimuli-responsive properties presenting themselves as "smart" biomaterials.[5-9] Upon local environmental cues, PA molecules can readily self-assemble into a variety of distinctive nanostructures including high aspect ratio cylindrical nanofibers

containing alkyl tails residing in the interior with peptides on the surface.[4,10,11] The ability for PAs to self-assemble into a multifunctional system is particularly advantageous for biomedical applications such as targeted vehicles for imaging agent and drug delivery[12,13] or as artificial three-dimensional tissue scaffolds.[14-16]

PA nanostructure formation is heavily dependent on the balance between weak non-covalent interactions such as electrostatic, hydrophobic, and hydrogen bonding.[17-19] This balance can be tuned by sequence specificity and solvent condition. Sequence specificity can be used to promote either intra- or intermolecular interactions and drive specific secondary structure formation (i.e., α-helix, β-sheet).[20-22] Changes in the aqueous medium (e.g., pH, ion concentration, temperature) can also induce phase and morphological transitions of the system.[23] Modification of the chemical structure or solvent environment exemplifies the modular and customizable design of a PA by providing direct control over the resulting gel's viscoelastic behavior and related mechanical properties.[24,25] While examination of equilibrium structures of *static* morphologies provide leverage in biomaterial design with respect to composition and functionality, less emphasis has been placed on characterizing the *dynamic* self-assembly process by monitoring structural changes and identifying kinetically trapped structures.

Developing a biocompatible vehicle that can transform from one morphology to another in response to specific physiological stimuli could lead to a novel class of sensing, diagnostic, and therapeutic agents.[26-28] Focus on the design such peptide-based vehicles extend beyond the current subset of PAs and can provide the foundation for the exploration of increasingly complex amphiphilic peptides. Through rational design, several biocompatible building blocks have been identified and shown to be effective in biomedical

applications.[29-32] To target tumor-specific sites, supramolecular peptide-amphiphile systems consisting of hydrophilic poly-(L-lysine) dendrimer and hydrophobic poly-(L-leucine) demonstrated its viability as a smart nanovehicle upon pH-triggered disassembly.[29] Other successful approaches to designing drug delivery vehicles includes the use of multiple hydrophobic tails conjugated to a neuroprotective peptide sequence to favor non-lamellar architectures due to geometric means[30] and using enzymatic reactions to influence the resulting morphology of the amphiphilic polymer-peptides with different substrates.[31] For a different system, the strength of hydrogel can be tuned depending on the redox environment through the introduction of a cysteine residue.[32] While this class of molecules can be customized to be responsive to different stimuli, the ability to generalize comprehensive design principles from existing systems remains to be difficult due to a large number of poorly elucidated variables. By utilizing an elementary PA molecule containing only rudimentary properties, key factors that can promote or enhance self-assembly behavior can be better determined by reducing possible interfering elements.

Our current understanding of the underlying kinetic pathway for PA self-assembly remains limited. Extraction of kinetics information from *in vitro* experiments is difficult while *in silico* studies involving large-scale systems are computationally intensive. Nevertheless, previous simulation studies have shown that PA self-assembly is a multi-step process.[33] Performing coarse-grained molecular dynamics simulations using MARTINI force field,[34] Schatz and co-workers showed that initial association of the hydrophobic tails facilitates micelle development, which promotes formation of cylindrical nanofibers by merging micelles together.[35] Targeted molecular dynamics simulations and umbrella sampling techniques were further used to propose a more descriptive two-stage

mechanism: an initial stage with PA aggregation through contribution of both desolvation and head-tail conformation followed by a conformational disorder-to-order transition due to the interaction between peptide segments.[35,36] Detailed free-energy landscape suggests that the spherical micelle formation is strictly a transient state.[37] Instead, the prevalent transition from a disordered to an ordered state is exemplified by a pillar-like intermediate followed by the final development of a semifiber.

Recently, Nguyen and collaborators performed multiscale modeling study to elucidate the effect of electrostatics on PA self-assembly mechanism.[38,39] Coarse-grained simulations revealed that when the electrostatic repulsion between the charged groups on glutamic acids are strong, representing high pH conditions under which some or all of the Glu sidechains were deprotonated or charged, PA molecules quickly undergo micelle formation whose driving force is the hydrophobic interactions between alkyl tails. When the electrostatic repulsion between the charged groups on glutamic acids are weak, corresponding to the low pH conditions when Glu sidechains are mainly neutral, these micelles merge together leading to the formation of one continuous rod-shaped nanofiber in which PA peptides are aligned in multiple β-sheets. These cylindrical nanofibers exhibit high structural fidelity to the proposed structure based on experimental data.[10] To investigate the pH-dependent thermodynamics of the nanofiber formation, conformational dynamics of a PA tetrameric β-sheet model was studied via all-atom CpHMD simulations.[39] Based on the number of backbone hydrogen bonds, the unfolding of the β-sheet occurs between pH 6–7 with the transition midpoint at about pH 6.5, matching the CD data.[13] Moreover, pKa data of Glu residues suggest that ionization of the Glu residues in the central

peptides induces unfolding of the β-sheet; therefore, their pKa values determine the pH condition for the transition from nanofiber to micelle.[32]

In this work, we examine the role of solvent condition on self-assembly behavior of a model PA molecule, palmitoyl-$Val_3Ala_3Glu_3$ (comprised of a hydrophobic monoalkyl 16-mer tail that is covalently conjugated to a short peptide segment of valine, alanine, and glutamic acids)[40] by systematically modifying the strength, ε_{HP}, of the hydrophobic interactions between both domains of the model PA sequence using our coarse-grained (CG) peptide-polymer model, ePRIME.[38] The pairwise strength, $\varepsilon_{HP}=R(\Delta G_i+\Delta G_j)$, is modulated by a scale factor, R, where R ranges from 1/6 to 1.3 and ΔG is the free energy of transferring each amino acid or chemical group from water to octanol.[41,42] This scale factor, R, is an inclusive parameter that can be interpreted as the degree of hydrophobicity between non-polar groups (such as the alkyl tail and nonpolar peptide residues) and is governed by the particular solvent choice. For example, low values of R are associated with nonpolar solvent by either adding organic cosolutes or co-solvent such as hexafluoroisopropanol (HFIP).[43] In contrast, high values of R correspond to either polar solvent or by adding polar cosolutes.[44] Using aggregate dynamics analysis and examining the dynamic behavior of secondary structure formation, solvent accessible surface area, radius of gyration, relative shape anisotropy and intra-/intermolecular interactions, we examine self-assembly behavior of PA molecules at three representative hydrophobic interaction strengths that yield distinctive nanostructures.

5.3 Methods

A peptide amphiphile of sequence $C_{16}H_{31}O$-$V_3A_3E_9$ was chosen based on previous experimental work by Pashuck *et al*.[40] It contains triplets of valine, alanine, and glutamic acid with the first valine conjugated to the monoalkyl segment of sixteen hydrocarbons. This sequence is represented using a coarse grained model called ePRIME[38], an extension of the Protein Intermediate Resolution Model (PRIME),[45] by accounting for all twenty natural amino acids. The peptide backbone atoms are represented by three spheres for the amide, alpha carbon, and carbonyl groups (NH, $C_\alpha H$, and CO). Adapting a model by Wallqvist and Ullner,[46] the sidechains are represented with either one or two spheres based on the length of the side chain. The size of the side chain is derived from the experimentally determined solvent accessible obtained by Eisenberg and coworkers.[41] For the polymeric tail, each CH_2 group is represented as a single sphere whose bond distance and fluctuation are extracted from available atomistic parameters.[38]

For the system of interest, an implicit solvent model is implemented to reduce the system's size for tractable simulations that can still capture the underlying physics of the system. The solvent effect is incorporated into the effective residue-residue potential due to the hydrophobic or hydrophilic character of each peptide residue or alkyl group. Representation of this behavior is either through a square-well or square-shoulder potential that approximates an attractive or repulsive continuous potential, respectively. For example, square-well potential is used for attractive interactions between hydrophobic side chains and/or polymeric segments while square-shoulder potential is used for repulsive interactions between hydrophilic side chains or polymeric segments. The strength of the interaction between two groups is $\varepsilon_{HP} = R(\Delta G_i + \Delta G_j)$ where ΔG is the free energy of transferring each group from water to octanol[41,42] and R is a measure of the

strength of the hydrophobic interaction ranging from 1/8 to 1.3. From prior work examining the formation of distinctive equilibrium structures at a wide range of R values,[47] three values of R are chosen for this study to form a smaller subset: R = 1/6, 1/3, and 1.3. The focus on this smaller subset is to provide more in-depth details with respect to the molecular pathway while highlighting the extreme conditions at small and large values of R. Although at this stage of the model, R does not provide a direct correspondence with solvent selection, the range of R selected aims to provide a qualitative understanding that can be extrapolated by comparing and contrasting with the prototypical cylindrical nanofiber observed at the reference condition of R = 1/3.

Hydrogen bonding is represented by a directionally dependent square-well attraction of strength ε_{HB}=12 kJ/mol between NH and CO united atoms. Electrostatic interactions, which are treated at the level of Debye-Huckel theory, are implemented using three-step attractive square-well or repulsive shoulder-well potentials with a 12 Å cutoff. In this study, the strength of an electrostatic repulsion between two charges on the glutamic acids, ε_{ES}, is the same as that of the hydrogen bond, ε_{HB}, as it is the optimal condition where cylindrical nanofibers were observed in our previous study.[38]

In junction with the coarse grained representation of the system, discontinuous molecular dynamics (DMD) method is utilized to enable simulations of large system sizes and extended time scales. As an alternative to standard molecular dynamics, DMD models bonded and nonbonded interactions through discontinuous potentials, e.g., hard-sphere and square-well potentials. Unlike soft potentials such as the Lennard-Jones potential, discontinuous potentials exert forces only when particles collide, enabling the exact (as opposed to numerical) solution of the collision dynamics. DMD simulations proceed by

locating the next collision, advancing the system to that collision, and then calculating the collision dynamics. By reducing the interaction details that is needed by being an event-driven process as opposed to time-driven process, this type of simulation allows for greater time scales on large systems. Simulations are performed in the canonical ensemble (NVT) with periodic boundary conditions imposed to eliminate artifacts due to box walls. Constant temperature is achieved by implementing the Andersen thermostat method[48]. In this case, all beads are subjected to random, infrequent collisions with ghost particles whose velocities are chosen randomly from a Maxwell Boltzmann distribution centered at the system temperature. Simulation temperature is expressed in terms of the reduced temperature, $T^* = k_BT/\varepsilon_{HB}$, where k_B is Boltzmann's constant, and T is the temperature. Reduced time is defined to be $t^*=t/\sigma(k_BT/m)^{1/2}$, where t is the simulation time, and σ and m are the average bead diameter and mass, respectively. While the use of reduced quantities *in silico* pose difficulty in achieving an experimental analogue, qualitative correlations can be extracted. From earlier work examining single molecule behavior using both atomistic and coarse grained models,[47] a qualitative frame of reference can be identified correlating the melting temperature of T* = 0.085T to 320K.

The initial configuration of each simulation contains 800 PA molecules (44,000 particles) in a cubic box whose dimension is 250 Å. This initial configuration was randomized to remove any bias conformation by heating the system at a high temperature (T* = 5.0) for a short amount of time (<1% of production run) to mimic experimental conditions. Afterwards, the system was quickly quenched to T* = 0.11, which is the final temperature for the production run for 200 – 400 time units until reaching equilibrium. The criteria for equilibrium is that each simulation was conducted for a long period of time

until the ensemble averages of the system's total potential energy varied by no more than 2.5% during the last three-quarters of each simulation run. The sudden change in temperature should have negligible effects on the system properties as the randomization is used only for the purpose of removing any computational bias due to the technique of populating the system with PA molecules. From our previous study on the effects of temperature, we found that below and at the melting point of T* = 0.085, PAs formed kinetically trapped aggregates that are amorphous. At higher temperatures, T*=0.10-0.11, cylindrical nanofibers can be formed when R=1/3. Similarly, Schatz and coworkers[33] conducted their simulations observing the formation of nanofibers at 330K, which is slightly higher than the melting point. In this study, we varied the R parameter but kept the temperature constant at T*=0.11.

Analysis was performed on the data collected during the production period. At each hydrophobic interaction strength, quantitative results reported in this paper are computed from the averages of 10 independent simulations with error bars taken from the standard deviation. Calculation of the secondary structure within the system is through the implementation of STRIDE[49] including: α-helix, 3_{10}-helix, π-helix, β-strand/sheet (extended conformation), turn, bridge, isolated bridge, and random coil. However, we only focus on α-helix, β-strand/sheet, and random coil that also contains turn. To identify an aggregate formed during the trajectory of the simulation, individual PA molecules of a cluster must form at least two interpeptide hydrogen bonds or four hydrophobic interactions with a neighboring PA molecule in the same group.[50] This criterion ensures that an aggregate is defined by at least two or more chains that form enough stable interactions. Solvent

accessible surface area (SASA) is calculated in VMD[51] with the measure SASA module using a probe of 1.4Å radius.

Relative shape anisotropy (RSA) parameter was also calculated to provide a quantitative analysis of the variation in shape of the identified aggregates or assemblies. To do so, the radius of gyration tensor was first calculated to determine the eigenvalues (i.e., principal moments of inertia) via diagonalization of the 3 x 3 matrix in the Cartesian coordinates x, y, and z. This calculation provides a direct correspondence of the distribution of mass of the object as a function of the atom's position. From the diagonalization of the matrix, identified eigenvalues, with the listed criteria $\lambda_x^2 \leq \lambda_y^2 \leq \lambda_z^2$, can be related to determine radius of gyration, R_g, asphericity, b, acylindricity, c, as well as the RSA value using Equation (1). Further details of the calculation can be found in the provided references by Vymětal *et al.*,[52] and Dima *et al*.[53]

$$RSA = \frac{b^2+0.75*c^2}{R_g^4} = 1.5 * \frac{\left(\lambda_x^2\right)^2+\left(\lambda_y^2\right)^2+\left(\lambda_y^2\right)^2}{\left(\lambda_x^2+\lambda_y^2+\lambda_z^2\right)^2} - 0.5 \qquad \text{Eqn. 1}$$

RSA parameter calculated Equation (1) ranges between the values of 0 and 1. As the parameter approaches unity, RSA = 1, it indicates that the distribution of points of an object is representative of a line (e.g., rod-like structure). In contrast, as the parameter reaches zero, RSA = 0, the distribution of points of the aggregate resembles spherically symmetric conformation (e.g., spherical structure). In this case, only the carbon atoms of the aliphatic tail and C_α atoms of the peptide backbone are used. To avoid including misleading values obtained from single molecules and small oligomers, RSA values were calculated on aggregates that contain at least 5 or more PA chains. The RSA parameter at each time point

of the simulation is the average of multiple RSA values of different aggregates belonging to a particular supramolecular structure assembled at equilibrium.

5.4 Results and Discussions

Since this article builds upon our earlier work on self-assembly of peptide amphiphiles of the same sequence,[47] it is useful to briefly review those results that are pertinent to the discussion here. Previously, we investigated the role of hydrophobic interactions on the self-assembled nanostructures at equilibrium by systematically modifying the strength of the hydrophobic interactions between both domains of the model PA sequence as represented by a scale factor, *R*.[47] We found that systematic modification of the hydrophobic interaction strength led to the formation of three distinctive nanostructures with key structural differences (**Figure 5.1**). At a moderate hydrophobic interaction strength of R = 1/3, cylindrical nanofibers were formed. Cylindrical nanofiber is an elongated structure whose peptide residues are distributed at the surface exhibiting β–sheet conformations while the hydrophobic alkyl tails are populating at its core. These cylindrical nanofibers have no hemispherical cap in each end indicating that they can potential merger together at longer timescale of simulations. On one hand, reducing the hydrophobic strength to R=1/6 results in the formation of small β-sheets, which are connected together by both hydrophobic interactions and hydrogen bonds creating an open network. On the other hand, increasing the hydrophobic strength to R=1.3 results in the formation of closed elongated micelles that are smaller in diameter than that of cylindrical nanofibers. In this case, alkyl tails and peptide residues are intertwined together in the interior and the peptide segments exhibits only random-coil conformation without any β-

sheet elements. At the end of our simulations, aggregates of different sizes were formed containing up to 50 PA molecules with a polydisperse distribution of aggregate size. After an infinitely long time, these aggregates are expected to merge together to form one large structure. However, that would require multiple orders of magnitude more simulation times than the current computational methods can afford as also demonstrated by Schatz and co-workers,[33] who observed nanostructures of similar size as those seen from our simulations.

In this study, we performed kinetic analysis on self-assembly dynamics of those three distinctive nanostructures to provide a complementary understanding to the previous structural characterization[47] on equilibrium structures of static morphologies.

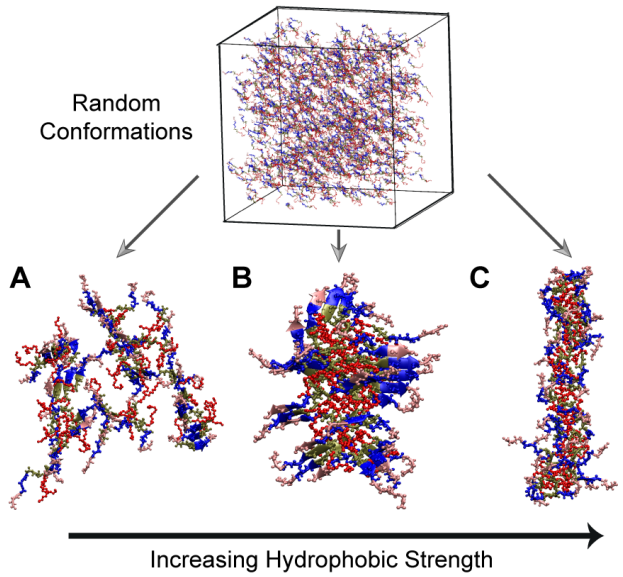

Figure 5.1. Distinctive equilibrium nanostructures such as (A) open network of β-sheets, (B) cylindrical nanofibers and (C) elongated micelles that are self-assembled from large-scale simulations containing 800 PAs as a function of hydrophobic interaction strength, *R*. Color scheme for the molecule by using VMD[51]: hydrophobic polymeric tail (red), valine (green), alanine (blue), and glutamic acid (pink).

5.4.1 Cylindrical Nanofibers at Moderate Hydrophobic Interaction Strength

Spontaneous self-assembly of PA molecules into a cylindrical nanofiber is observed through multiple successive stages from Figure 5.2, which shows time-dependent snapshots of 39 PA molecules selected from the 800-PA system for ease-of-viewing at a moderate hydrophobic interaction strength, R = 1/3. Beginning with a random initial conformation (t* = 0.0), isolated PA molecules are driven by hydrophobic collapse between alkyl tails and quickly condense into small aggregates (t* = 8.2). To maximize the number of favorable hydrophobic interactions, these aggregates merge together leading to the formation of small micellar structures (t* = 14.2). This multi-step process from small clusters gradually evolving in size into larger micelles shares similarity to previous CG MD studies that examined amphiphilic peptides of sequence $(AF)_6H_5K_{15}$[54,55] and nonionic surfactant pentaethylene glycol monododecyl ether.[56]

The alkyl tails are arranged in the interior of each spherical micelle forming an enclosed hydrophobic core that sequesters away from the solvent while hydrophilic residues are positioned on the surface serving as a protective shield (t* = 27.4). In particular, charged segments are uniformly distributed around each micelle to minimize the charge-charge repulsion (t* = 27.4). These micelles undergo a geometrical transition to yield an oblong structure (t*=59.2) and finally develop into a cylindrical nanofiber structure (t* = 313.2). This geometrical transition can be seen by examining the data on relative shape anisotropy (RSA) as a function of time in **Figure 5.3A**, which displays a transition from an average RSA value close to 0, which represents spherical micelles, to RSA value of ~0.30, which represents cylindrical nanofibers. This is in agreement with a

previous study, which examined nonionic surfactant pentaethylene glycol monododecyl ether and demonstrated a spherical-to-rod transition in the range of 0.0 – 0.1 based on the RSA parameter.[56]

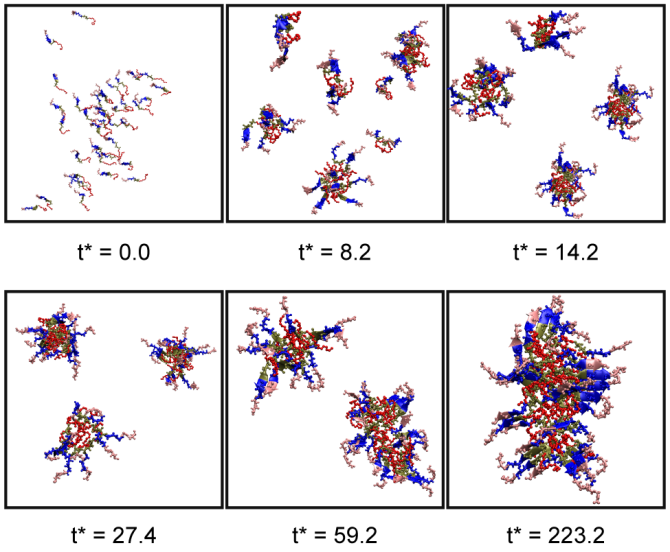

Figure 5.2. Time-dependent snapshots of the self-assembly process for the formation of a cylindrical nanofiber at moderate hydrophobic interaction strength, R = 1/3.

A quantitative representation of self-assembly is shown in **Figure 5.3B**, which plots the average number of PA molecules per aggregate and the total number of aggregates as a function of reduced time. This plot indicates that 10 aggregates (each contains about 5 PA molecules) are formed instantaneously as the simulation begins. These aggregates merge together as the average number of PA molecules per aggregate increases while the total number of aggregates decreases in a step-wise manner. Moreover, as the structure grows in size, its association with each incoming structure is reliably stable as indicated by few fluctuations of the aggregation kinetics data.

A typical cylindrical nanofiber grows through the addition of spherical micelles at its ends (**Figure 5.2**). At t*=59.2, after two micelles have merged together to form an oblong

structure; the spherical micelle on the left tries to merge with the oblong structure on the right via multiple times. When the micelle approaches the oblong structure along its side, it is unsuccessful due to electrostatic repulsion between charged GLU side chains on the surface of both structures. Since the density of GLU side chains on the side of oblong structure is higher than that on its ends, the spherical micelle is more successful merging at the ends of the oblong structure to minimize the electrostatic repulsion.

As the progression from a randomly dispersed assembly into a cylindrical nanofiber is observed, SASA values restricted to the polymeric tails are noticeably decreasing, which indicates that the alkyl tails are buried in the interior away from the solvent (**Figure 5.3C**). Moreover, the radius of gyration values increases slightly over time indicating each PA molecule adopts an extended conformation to avoid intramolecular interactions. This is reflected in the low values calculated for the average number of intramolecular hydrophobic interactions and hydrogen bonds as shown in **Figure 5.3D** when comparing to a significantly higher number of intermolecular interactions as discussed below.

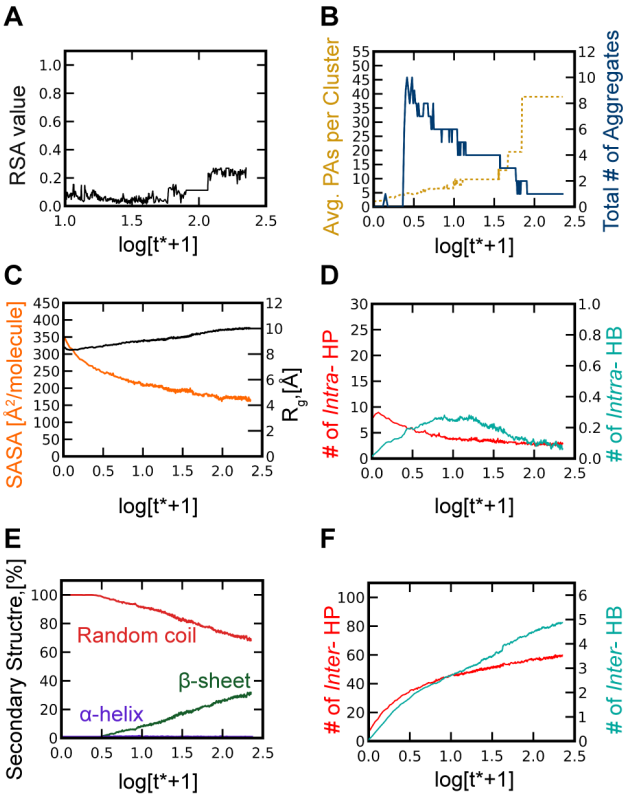

Figure 5.3. For the cylindrical nanofiber shown in **Figure 5.2**, time dependent data are plotted in a logarithmic scale for (A) Relative shape anisotropy value, (B) Average number of PA molecules per aggregate and total number of aggregates; (C) Average solvent accessible surface area restricted to the polymeric tail and the radius of gyration; (D) Number of intramolecular interactions per PA molecule (E) Secondary structure formation; (F) Number of intermolecular interactions per PA molecule. For plots (D) and (F), HP denotes hydrophobic interactions (red) and HB denotes hydrogen bonds (green).

The spherical-to-cylindrical transition can be attributed to the dynamic formation of secondary structure elements, β-sheets, between nearby peptide residues. As more PA molecules condense into micellar structures from an initial homogenous system, the formation of β-sheets steadily increases whereas random coil formation decreases (**Figure 5.3E**). Absence of α-helical structures is attributed to the temperature being higher than the melting temperature of PA molecules.[38,47] Ordering of the β-sheets increases the distance between groups of charged PA molecules due to the formation of intermolecular hydrogen bonds between nearby peptide residues. Consequently, regions of the enclosed hydrophobic core are exposed to the solvent; in this case, intermolecular hydrophobic

interactions between nearby micelles are promoted. Therefore, the formation of β-sheets facilitates merging of spherical micelles into oblong nanofibers.

By calculating the number of intermolecular hydrophobic interaction and hydrogen bonding as a function of time, the ratio between these two quantities can be used as a reference to differentiate between nanostructures. For the formation of cylindrical nanofibers, hydrophobic interactions either between alkyl-alkyl tails, alkyl-peptide, or peptide-peptide dominates over hydrogen bonding by an order of magnitude (**Figure 5.3F**). Since hydrophobic interactions are isotropic without angle dependence, direction-dependent hydrogen bonding is much less favorable. Further comparison of the weak and strong hydrophobic interaction strengths will be discussed below.

5.4.2 Open Networks of β-sheets at Weak Hydrophobic Interaction Strength

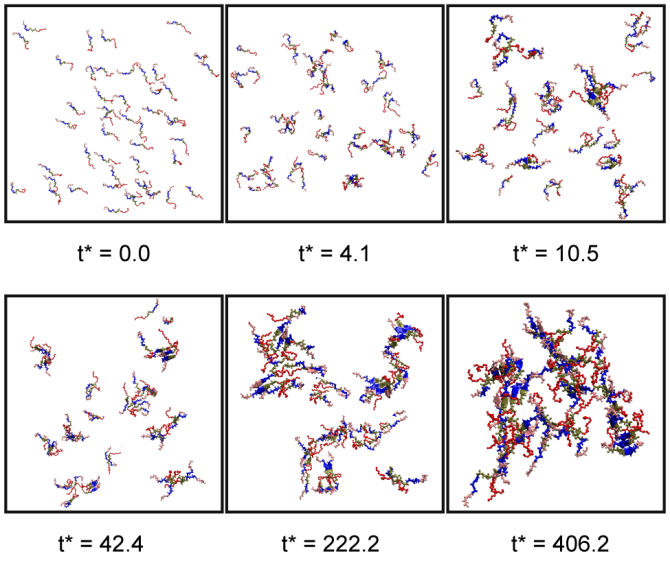

Figure 5.4. Time-dependent snapshots of the self-assembly process for the formation of a network of β-sheets at weak hydrophobic interaction strengths, R = 1/6.

At weak hydrophobic interaction strength, R = 1/6, spontaneous self-assembly of 800 PA molecules occurs to form open networks of β-sheets via a multi-step process (**Figure 5.4**). Following an initial random configuration, hydrophobic collapse is the driving force for the emergence of small aggregates, each of which contains 2-3 PA molecules (t*=4.1). These small aggregates grow in size by forming increasingly more favorable hydrophobic interactions. However, unlike the scenario at moderate hydrophobicity in which intermolecular hydrophobic interactions are predominant between alkyl tails, hydrophobic interactions are now also between alkyl tail and non-polar peptide side chains.

Over time, intermolecular hydrogen bonds slowly form between nearby peptide residues resulting in a gradual development of small β-sheets (t*=10.5). However, these β-sheets have no particular orientation since parallel and anti-parallel β-sheets exist across different aggregates in the system. A lack of preference for a particular direction thereby allows both hydrophobic interaction and hydrogen bonding to occur to connect multiple β-sheets together (t*=42.4). Consequently, larger aggregate structures are stitched together to maximize the number of favorable interactions (t*=222.2). Finally, large networks of β-sheets range widely in size from 23 to 48 PA molecules (t*=406.2). Our characterization of a network of β-sheets is in good agreement with a recent computational study performed by Mu and Yu on self-assembly by a short peptide containing six hydrophobic residues.[57] They found that weak hydrophobic interaction strength and moderate temperature produce single-layered β-sheets. These β-sheets are unable to collapse together to form a fibril structure without adequate hydrophobic interactions; instead, they predominantly increase in size by adding more peptide through hydrogen bonds to their β-sheet ends.

During self-assembly to form open networks of β-sheets, each growing structure never undergoes a structural transition as indicated by relatively small and constant values of the RSA parameter as shown in **Figure 5.5A**. Moreover, the formation of open networks is slow as seen from **Figure 5.5B**, which shows that the aggregate size gradually grows in size even though there are multiple merging opportunities. It takes more than 300 time units to reach an aggregate containing 48 PAs compared to 80 time units at moderate hydrophobicity (**Figure 3B**). In addition to encountering a barrier for rapid association, the system at weak hydrophobicity faces difficulty in attaining an equilibrium structure since minimal energy is required to disrupt the interaction. At the end of the simulation, the structure undergoes multiple rearrangements as shown by the fluctuation in both the average number of chains in that aggregate and the total number of aggregate of that particular assembly (**Figure 5.5B**).

At weak hydrophobicity, the SASA value decreases only slightly as a function of time (**Figure 5.5C**) indicating that the alkyl tails are quite exposed to the solvent. While small aggregates can be formed, further maturation into micellar structures is prevented; hence it lacks an enclosed hydrophobic core within the framework. The radius of gyration value (**Figure 5.5C**) of each PA molecule is comparable to the scenario by which cylindrical nanofibers are formed (**Figure 5.3C**) by increasing from its initial value as a random coil, indicating that PAs stretch out to preferentially form intermolecular instead of intramolecular interactions as indicated by their small numbers in **Figure 5.5D**.

The formation of secondary structure at weak hydrophobicity (**Figure 5.5E**) is similar to the condition at moderate hydrophobicity (**Figure 5.3E**). Comparable amount of β-sheets of about 35% at equilibrium is achieved without α-helical structures. However,

the rate of β-sheet formation is smaller as compared to the moderate hydrophobic interaction strength since the system takes a longer time for PAs to achieve stable aggregate structures.

The numbers of intermolecular hydrophobic interaction and hydrogen bonding shows that their ratio approaches almost unity as both of these interactions have the same order of magnitude (**Figure 5.5F**). Comparing this number to the formation of a cylindrical nanofiber (**Figure 5.3F**) indicates that with a decrease in hydrophobic interaction strength, the two domains of a PA molecule becomes much more flexible to yield alternative nanostructures besides the prototypical nanofibers.

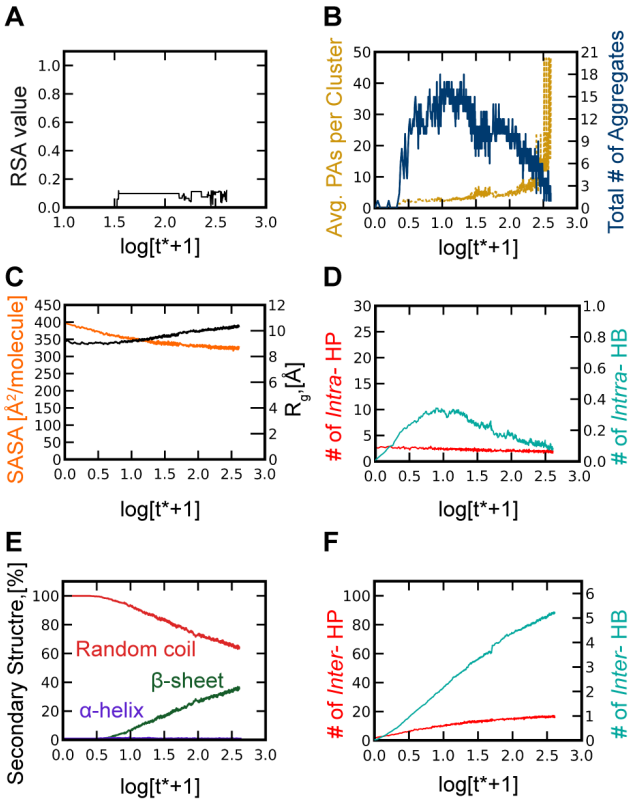

Figure 5.5. For the assembly shown in **Figure 4**, time dependent data are plotted in a logarithmic scale for (A) Relative shape anisotropy value, (B) Average number of PA molecules per aggregate and total number of aggregates; (C) Average solvent accessible surface area restricted to the polymeric tail and the radius of gyration; (D) Number of intramolecular interactions per PA molecule (E) Secondary structure formation; (F) Number of intermolecular interactions per PA molecule. For plots (D) and (F), HP denotes hydrophobic interactions (red) and HB denotes hydrogen bonds (green).

5.4.3 Elongated Micelles at Strong Hydrophobic Interaction Strength

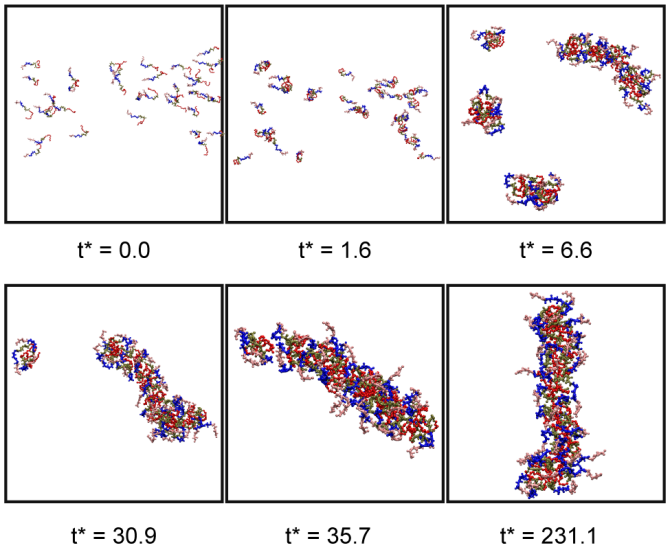

Figure 5.6. Time-dependent snapshots of the spontaneous self-assembly process are shown for strong hydrophobic interaction strengths, R = 1.3.

At strong hydrophobic interaction strength, R = 1.3, an elongated micelle is observed at equilibrium with minimal secondary structure elements (**Figure 5.6**). Similar to the self-assembly mechanism as described for the moderate and weak hydrophobic interaction strengths, hydrophobic collapse through the alkyl tails drives the formation of small aggregates of 2-4 PA molecules (t*=1.6) starting from an initial random configuration (t*=0.0). The next events involve the formation of moderately sized spherical micelles of 13-18 PA molecules that are driven by favorable hydrophobic interactions between alkyl tails (t*=6.6). Subsequent steps involve merging spherical micelles into an elongated structure that is significantly smaller in diameter than a cylindrical nanofiber observed at moderate hydrophobicity (**Figure 5.1**).

The transition from spherical micelles into an elongated structure can be quantitatively seen by examining the data on relative shape anisotropy as a function of

time in **Figure 5.7A**. This shows two major transitions from an average RSA value of 0.3, which represents small micelles, to RSA value of ~0.6, then ending at ~0.8, which represents large elongated micelles. The RSA values of elongated micelles at R=1.3 are significantly higher than those of cylindrical nanofibers at R=1/3. Since an elongated structure is remarkably smaller in diameter than a cylindrical nanofiber (**Figure 5.1**), its aspect ratio is skewed higher; therefore, RSA is also a good measurement of the cylindrical diameter. Reduction of the diameter of elongated structures without β-sheets is also observed in experimental work by Missirlis *et al.* on a PA molecule containing a 16-mer peptide. Upon insertion of four alanines between the alkyl tail and peptide, β-sheet formation is now allowed resulting in an extended PA conformation that contributes to a significant growth in diameter of cylindrical structures as well as their stability.[22]

Similar to the moderately hydrophobic condition, aggregates merge together in a step-wise manner as indicated by discrete increases of the average number of PA molecules per aggregate and decreases of the total number of aggregates in **Figure 5.7B.** This plot indicates that 10 aggregates (each contains about 2-3 PA molecules) are formed instantaneously as the simulation begins. As each structure grows, its association with each incoming structure is reliably stable as indicated by few fluctuations of the aggregation kinetics data.

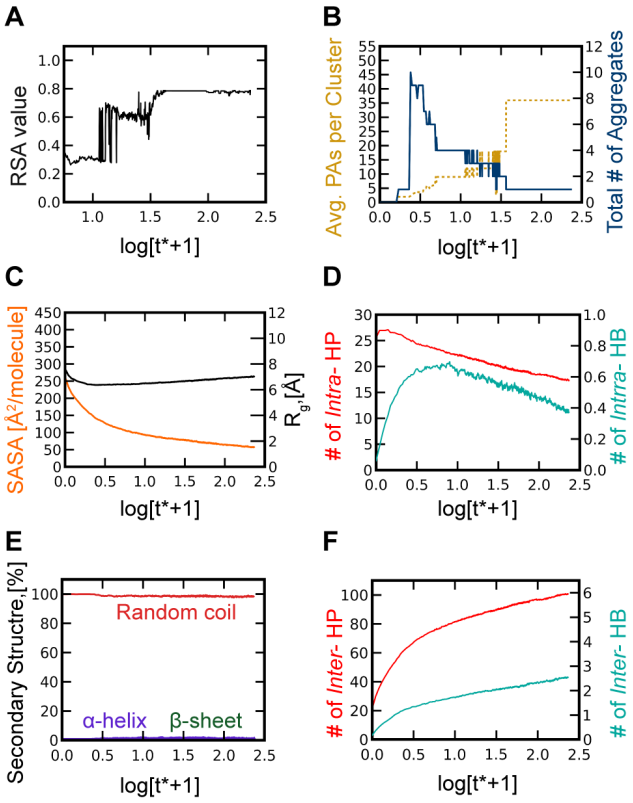

Figure 5.7. For the elongated micelle in **Figure 6**, time dependent data are plotted in a logarithmic scale for (A) Relative shape anisotropy value, (B) Average number of PA molecules per aggregate and total number of aggregates; (C) Average solvent accessible surface area restricted to the polymeric tail and the radius of gyration; (D) Number of intramolecular interactions per PA molecule (E) Secondary structure formation; (F) Number of intermolecular interactions per PA molecule. For plots (D) and (F), HP denotes hydrophobic interactions (red) and HB denotes hydrogen bonds (green).

Only the alkyl tails are buried in the hydrophobic core of cylindrical nanofibers at moderate hydrophobicity; in contrast, both alkyl tails and peptide resides are significantly buried in the interior of the final structures of elongated micelles at strong hydrophobicity. This can be seen by considerable decrease of SASA values shown in **Figure 5.7C** compared to the cases at moderate hydrophobicity (**Figure 5.5C**). Moreover, noticeable decrease in values of the radius of gyration is observed in **Figure 5.7C** indicating that each PA structure is more compact and condensed compared to extended conformations at weak and moderate hydrophobic interaction strengths.

A significant number of intra-molecular hydrophobic interactions (**Figure 5.7D**) are observed between alkyl tails and hydrophobic residues (e.g., valine and alanine) preventing the formation of intermolecular hydrogen bonds and contributing to a small amount of secondary structure (**Figure 5.7E**). Indeed all PA molecules exhibit random-coil conformations compared those cases at weak and moderate hydrophobic interaction strengths where 35% PAs exhibit β-sheet content. In contrast to the weak hydrophobicity but similar to the moderate hydrophobic condition, the two domains that comprise of a PA molecule serve differing roles. The hydrophobic alkyl tail along with the hydrophobic peptide residues are located at the core of the nanostructure to stabilize the core-shell structure while the hydrophilic residues frame the periphery. With the charged residues aligning on the surface of the structure, it acts as a guide to deter micelles from merging along the sides (t^*=30.9) and instead promotes merging at the ends of the nanostructure (t^*=35.7) where the repulsion strength is reduced. The final structure, which is varied in size between 30-39 PA molecules, is characterized as an elongated micelle that contains a continuous hydrophobic core (Figure 5.7B).

The number of intermolecular hydrophobic interactions exceedingly outnumbers the number of hydrogen bonds formed; therefore, the ratio between intermolecular hydrophobic interactions and hydrogen bonds approaches two orders of magnitude (**Figure 5.7F**). This indicates that PA molecules are intertwined together to accommodate the maximum number of hydrophobic interactions over hydrogen bonding. Since the hydrophobic interaction becomes significantly large, the effective strength of the electrostatic repulsion is somewhat diminished. Therefore, some charged residues are also buried in the interior rather than positioning on the surface of elongated micelles.

5.5 Conclusions

Employing our peptide/polymer coarse-grained model, ePRIME,[38,45] which is coupled with a fast MD algorithm,[58] large-scale simulations allowed us to understand the solvent effects on spontaneous self-assembly behavior of peptide amphiphiles. Even though the solvent condition is discussed throughout this manuscript in terms of the hydrophobicity scale factor R, this R factor could be interpreted as the character of each PA molecule. For instance, it represents a particular polymer type. Using the alkyl tail as a reference at R=1/3, a higher value of R corresponds to a strongly hydrophobic polymeric tail (e.g., polystyrene)[59] whereas a lower value of R corresponds to a more hydrophilic polymeric tail (e.g., poly(ethylene glycol)).[60] Alternatively, the hydrophobicity scale factor R can be considered as a degree of conjugation corresponding to the length of the alkyl tail.[61-63]

In this study, distinctive kinetic mechanisms are delineated dependent upon the solvent condition, which produces unique nanostructures at moderate temperatures as summarized in **Figure 5.8**. Multiple successive steps are necessary for the self-assembly process of PA molecules. At weak hydrophobic interaction strength, initial aggregates are formed due to both hydrophobic interactions and hydrogen bonding. These aggregates gradually grow in an arbitrary manner involving many directions into a structure whose PA molecules are arranged without particular order. This results in an open network containing β-sheets without a hydrophobic core (**Figure 5.8A**). Even though no PAs have been observed to form open β-sheet networks, short peptide sequences (without the alkyl tail) can form structures that are similar to our open β-sheet networks. For example,

Bowers and co-workers recently studied the aggregation process of six short peptides that are NNQQNY mutants: NVVVVY, NVVQIY, NVQVVY, NNVVNY, VIQVVY, and NNVVNV.[64] They found that only NVVVVY, due to its strong hydrophobic core, aggregates quickly into β-sheets, which in turn stack together and form long fibrils with a well-defined morphology at room temperature. Since the hydrophobicity of the peptide hydrophobic core of the other peptides is reduced, they can only form either β-sheets, short fibrils with poorly defined morphologies or amorphous aggregates; therefore, their peptide fibril-formation capability is weakened. Moreover, previous simulation studies showed that when hydrophobic interaction strength between non-polar sidechains of short peptides is weak, β-sheets remain as single layers without stacking into amyloid fibrils.[57] In our PA case, β-sheets also remain as single layers; however, they are interconnected due of the presence of the alkyl tails even when their hydrophobic interaction strength is weak.

As the hydrophobic interaction strength increases, the morphology transitions away from an open-structure to a closed-structure with the development of an enclosed hydrophobic core. While initial self-assembly involves hydrophobic interactions between alkyl tails as the main driving force, inter-peptide hydrogen bonding is not evident until the later stages. Spherical micelles are first observed with PA molecules arranging themselves to form a hydrophobic core to ensure a stable structure while maximizing the number of favorable interaction. The charged peptide segments are aligned on the periphery of the structure to minimize electrostatic repulsion. As hydrogen bonds between peptide segments form β-sheets and expose the hydrophobic core to the solvent, micelle-micelle interactions are promoted for the hydrophobic core to grow in size eventually developing into a cylindrical nanofiber that contains a large amount of β-sheets (**Figure 5.8B**).

Merging of spherical micelles into a cylindrical nanofiber is similarly observed by Lee *et al*. who performed MD simulations on a related PA system. However, our ePRIME model permits spontaneous formation of hydrogen bonds and secondary structures allowing observation of conformational changes over time. In contrast, Lee *et al*. used the MARTINI[34] model in which the amount of secondary structures was predetermined in advance and fixed throughout simulations.[33] Hydrogen bonding and β-sheet formation are known to play a critical role the self-assembly of PAs into nanofibers.[65] They also contribute to the rigidity of nanofibers as demonstrated by Stupp and co-workers who use EPR spectra of nitroxide spin probes to examine molecular motion within nanofiber structure.[66] They observed for a PA molecule that is able to form strong intermolecular interactions in an uninhibited manner, solid-like motion is detected as opposed to fluid-like dynamics for a system that is prohibited from β-sheet formation. Therefore, increased order in the system can be correlated to high propensity for β-sheet formation.

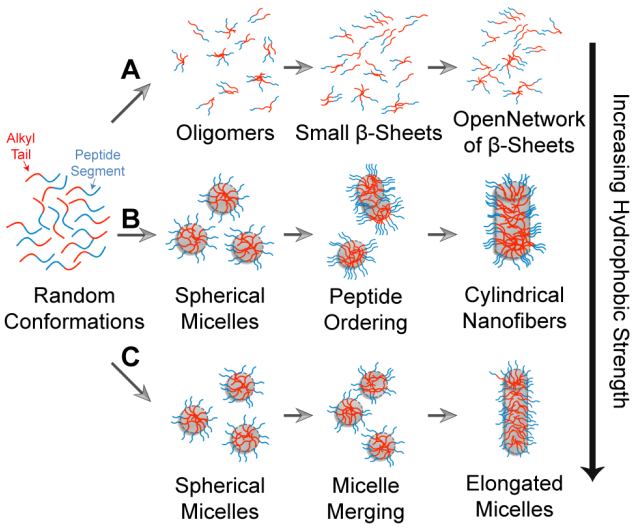

Figure 5.8. Schematic diagram of three kinetic mechanisms proposed by simulation results at a weak electrostatic interaction strength (ε_{ES} = 100%*ε_{HB}) and at moderate temperatures (T* = 0.11): (A) at weak hydrophobic interaction strength (R = 1/6), network of β-sheets are formed with the hydrophobic elements in the system exposed to solvent; (B) at moderate hydrophobic interaction strength (R = 1/3), cylindrical nanofibers are formed; (C) at strong hydrophobic interaction strength, peptide-peptide hydrophobic

interaction aids in the micelle-merging process resulting in elongated micelles with minimal secondary structure elements.

At strong hydrophobic interaction strength, minimal secondary structures are present yet rod-like structures can be constructed. Strong hydrophobic interaction strength inhibits the formation of hydrogen bonding between nearby peptide residues; therefore, all peptides exhibit random coil conformations without forming β-sheets. Alkyl tails and nonpolar peptide residues are now driving micellization followed by micelle-micelle merging events forming a contiguous hydrophobic core that leads to the development of an elongated structure (**Figure 5.8C**).

The nature by which the morphological and phase transitions can be correlated with its structure is notable because it provides a method for sensitive control. From experimental studies, mobility of suspended cells or proteins within a scaffold can be regulated by the strength of the interaction between self-assembled PA molecules.[67] By understanding the rate of formation or degradation of the biomimetic matrix, different controlled release mechanisms and related functionality can be attained. Recent experimental work by Stupp and co-workers showed that the formation of β-sheets is dependent upon the amount of hexafluoroisopropanol (HFIP), which is an organic co-solvent, in water.[43] They found when HFIP content is greater than 21 vol %, no β-sheets are formed since PA molecules are well solvated as isolated molecules in random coil conformations. This corresponds to the simulation condition when hydrophobic interaction strength, *R*, is zero. In this case, PA molecules are prohibited from forming intermolecular interactions and thus undergoing no self-assembly, as also observed in systems of short peptides.[57,68] Moreover, they examined assembly kinetics of the β-sheets using circular dichroism, which revealed an increasing rate upon decreasing the HFIP

content from 21 vol %.[43] This is also observed in our simulations that show that the rate of β-sheet formation is smaller at R=1/6 compared to that at R=1/3. However, our hydrophobicity condition at R=1.3 cannot be compared to their experimental results. This is an extreme case in which strong hydrophobic interactions due to the replacement of valine and alanine residues for stronger non-polar peptide residues such as isoleucine or the replacement of an alkyl tail for a polystyrene tail. In this case, strong hydrophobic interactions can still allow PAs to assemble into elongated micelles without the presence of β-sheets. Furthermore, Stupp and co-workers also demonstrated how preparation protocols of mixing HFIP and PA in water play an important role in regulating different outcomes of the PA assembly process including hysteresis that is involved in the formation of β-sheets.[43] The insights on the effect of such kinetics and hysteresis on PA assembly can be further elucidated in future computational studies to provide an efficient approach to select the optimum assembly pathway necessary for formation of supramolecular structures with targeted functions.

Considering the coarse-grained model used to simplify the atomistic details of a PA molecule, inherent limitations are present such as the resolution that can be attained with this methodology. Another limitation involves using an implicit solvent model. Although this approach significantly decreases the computational time by reducing the number of degrees of freedom via the absence of explicit solvent molecules, the force field of the solvent is therefore approximated. Moreover, the hydrophobic interactions within the system are assumed to be temperature independent, which is a simplification of the known models of temperature-dependent hydrophobicity.[69,70] However, despite these limitations, the data show that our coarse-grained model allows us to conduct large-scale molecular-

dynamics simulations to observe a wide range of nanostructures. This yields a qualitative understanding of the effects of solvent condition on self-assembly pathways involved in the formation of nanostructures that share structurally similarities to those observed from prior experimental and atomistic computational works.[10,71]

5.6 Acknowledgements

This work was originally published in Langmuir, 2014 © American Chemical Society. Co-authors include Cade B Markegard, and Hung D Nguyen. HDN acknowledges financial support from UC Irvine. IWF acknowledges support from a Graduate Research Fellowship from the National Science Foundation (DGE-1321846). This work used the Extreme Science and Engineering Discovery Environment (XSEDE), which is supported by National Science Foundation grant number OCI-1053575. We are also thankful for the computational resources provided by the GreenPlanet and High Performance Computing cluster at UCI campus.

5.7 References

1. Nisbet, D. R. & Williams, R. J. Self-Assembled Peptides: Characterisation and In Vivo Response. *Biointerphases* **7,** 1–14 (2012).
2. Dehsorkhi, A., Castelletto, V. & Hamley, I. W. Self-assembling amphiphilic peptides. *J. Pept. Sci.* **20,** 453–467 (2014).
3. Hartgerink, J. D., Zubarev, E. R. & Stupp, S. I. Supramolecular one-dimensional objects. *Current Opinion in Solid State & Materials Science* **5,** 355–361 (2001).
4. Cui, H., Webber, M. J. & Stupp, S. I. Self-assembly of peptide amphiphiles: From molecules to nanostructures to biomaterials. *Biopolymers* **94,** 1–18 (2010).
5. Bajpai, A. K., Shukla, S. K., Bhanu, S. & Kankane, S. Responsive polymers in controlled drug delivery. *Progress in Polymer Science* **33,** 1088–1118 (2008).
6. Pettikiriarachchi, J. T. S., Parish, C. L., Shoichet, M. S., Forsythe, J. S. & Nisbet, D. R. Biomaterials for Brain Tissue Engineering. *Aust. J. Chem.* **63,** 1143 (2010).
7. Vermonden, T., Censi, R. & Hennink, W. E. Hydrogels for Protein Delivery. *Chem. Rev.* **112,** 2853–2888 (2012).
8. Guo, H. *et al.* The Robust Hydrogel Hierarchically Assembled from a pH Sensitive Peptide Amphiphile Based on Silk Fibroin. *Biomacromolecules* **14,** 2733–2738 (2013).
9. Newcomb, C. J. *et al.* Cell death versus cell survival instructed by supramolecular cohesion of nanostructures. *Nature Communications* **5,** 1–10 (1AD).

10. Hartgerink, J. D. Self-Assembly and Mineralization of Peptide-Amphiphile Nanofibers. *Science* **294,** 1684–1688 (2001).
11. Hartgerink, J. D., Beniash, E. & Stupp, S. I. Peptide-amphiphile nanofibers: A versatile scaffold for the preparation of self-assembling materials. *Proceedings of the National Academy of Sciences* **99,** 5133–5138 (2002).
12. Matson, J. B. & Stupp, S. I. Drug release from hydrazone-containing peptide amphiphiles. *Chem. Commun.* **47,** 7962–7964 (2011).
13. Ghosh, A. *et al.* Fine-Tuning the pH Trigger of Self-Assembly. *J. Am. Chem. Soc.* **134,** 3647–3650 (2012).
14. Hosseinkhani, H., Hosseinkhani, M., Khademhosseini, A., Kobayashi, H. & Tabata, Y. Enhanced angiogenesis through controlled release of basic fibroblast growth factor from peptide amphiphile for tissue regeneration. *Biomaterials* **27,** 5836–5844 (2006).
15. Lee, S. S. *et al.* Bone regeneration with low dose BMP-2 amplified by biomimetic supramolecular nanofibers within collagen scaffolds. *Biomaterials* **34,** 452–459 (2013).
16. Woolfson, D. N. & Ryadnov, M. G. Peptide-based fibrous biomaterials: some things old, new and borrowed. *Current Opinion in Chemical Biology* **10,** 559–567 (2006).
17. Ulijn, R. V. & Smith, A. M. Designing peptide based nanomaterials. *Chem. Soc. Rev.* **37,** 664 (2008).
18. Cavalli, S., Albericio, F. & Kros, A. Amphiphilic peptides and their cross-disciplinary role as building blocks for nanoscience. *Chem. Soc. Rev.* **39,** 241 (2009).
19. Hamley, I. W. Self-assembly of amphiphilic peptides. *Soft Matter* **7,** 4122 (2011).
20. Löwik, D. W. P. M., Garcia-Hartjes, J., Meijer, J. T. & van Hest, J. C. M. Tuning Secondary Structure and Self-Assembly of Amphiphilic Peptides. *Langmuir* **21,** 524–526 (2005).
21. Shimada, T., Lee, S., Bates, F. S., Hotta, A. & Tirrell, M. Wormlike Micelle Formation in Peptide-Lipid Conjugates Driven by Secondary Structure Transformation of the Headgroups †. *J. Phys. Chem. B* **113,** 13711–13714 (2009).
22. Missirlis, D. *et al.* Effect of the Peptide Secondary Structure on the Peptide Amphiphile Supramolecular Structure and Interactions. *Langmuir* **27,** 6163–6170 (2011).
23. Zhou, X.-R., Ge, R. & Luo, S.-Z. Self-assembly of pH and calcium dual-responsive peptide-amphiphilic hydrogel. *J. Pept. Sci.* **19,** 737–744 (2013).
24. Greenfield, M. A., Hoffman, J. R., Olvera de la Cruz, M. & Stupp, S. I. Tunable Mechanics of Peptide Nanofiber Gels. *Langmuir* **26,** 3641–3647 (2010).
25. Yan, C. & Pochan, D. J. Rheological properties of peptide-based hydrogels for biomedical and other applications. *Chem. Soc. Rev.* **39,** 3528–3540 (2010).
26. Callahan, D. J. *et al.* Triple Stimulus-Responsive Polypeptide Nanoparticles That Enhance Intratumoral Spatial Distribution. **12,** 2165–2170 (2012).
27. Chien, M.-P. *et al.* Enzyme-Directed Assembly of a Nanoparticle Probe in Tumor Tissue. *Adv. Mater.* **25,** 3599–3604 (2013).
28. Goldberger, J. E., Berns, E. J., Bitton, R., Newcomb, C. J. & Stupp, S. I. Electrostatic control of bioactivity. *Angewandte Chemie (International ed. in English)* **50,** 6292–6295 (2011).
29. Xu, X. *et al.* Smart Nanovehicles Based on pH-Triggered Disassembly of Supramolecular Peptide-Amphiphiles for Efficient Intracellular Drug Delivery. *Small* **10,** 1133–1140 (2013).
30. Son, S. J. *et al.* Synthesis and Self-Assembly of a Peptide - Amphiphile as a Drug Delivery Vehicle. *Aust. J. Chem.* **66,** 23 (2013).
31. Ku, T.-H. *et al.* Controlling and Switching the Morphology of Micellar Nanoparticles with Enzymes. *J. Am. Chem. Soc.* **133,** 8392–8395 (2011).
32. Cao, C. *et al.* Redox modulated hydrogelation of a self-assembling short peptide amphiphile. *Chin. Sci. Bull.* **57,** 4296–4303 (2012).
33. Lee, O.-S., Cho, V. & Schatz, G. C. Modeling the Self-Assembly of Peptide Amphiphiles into Fibers Using Coarse-Grained Molecular Dynamics. *Nano Lett.* **12,** 4907–4913 (2012).
34. Monticelli, L. *et al.* The MARTINI Coarse-Grained Force Field: Extension to Proteins. *J. Chem. Theory Comput.* **4,** 819–834 (2008).
35. Yu, T. & Schatz, G. C. Free Energy Profile and Mechanism of Self-Assembly of Peptide Amphiphiles Based on a Collective Assembly Coordinate. *J. Phys. Chem. B* **117,** 9004–9013 (2013).
36. Yu, T., Lee, O.-S. & Schatz, G. C. Steered Molecular Dynamics Studies of the Potential of Mean Force for Peptide Amphiphile Self-Assembly into Cylindrical Nanofibers. *J. Phys. Chem. A* **117,** 7453–7460 (2013).

37. Yu, T. & Schatz, G. C. Free-Energy Landscape for Peptide Amphiphile Self-Assembly: Stepwise versus Continuous Assembly Mechanisms. *J. Phys. Chem. B* **117,** 14059–14064 (2013).
38. Fu, I. W., Markegard, C. B. & Chu, B. K. The Role of Electrostatics and Temperature on Morphological Transitions of Hydrogel Nanostructures Self-Assembled by Peptide Amphiphiles Via Molecular .... *Advanced healthcare ...* (2013). doi:10.1002/adhm.201200400
39. Cote, Y. *et al.* Mechanism of the pH-Controlled Self-Assembly of Nanofibers from Peptide Amphiphiles. *J. Phys. Chem. C* **118,** 16272–16278 (2014).
40. Pashuck, E. T., Cui, H. & Stupp, S. I. Tuning Supramolecular Rigidity of Peptide Fibers through Molecular Structure. *J. Am. Chem. Soc.* **132,** 6041–6046 (2010).
41. Wesson, L. & Eisenberg, D. Atomic solvation parameters applied to molecular dynamics of proteins in solution. *Protein Science* **1,** 227–235 (1992).
42. Gu, W., Rahi, S. J. & Helms, V. Solvation Free Energies and Transfer Free Energies for Amino Acids from Hydrophobic Solution to Water Solution from a Very Simple Residue Model. *J. Phys. Chem. B* **108,** 5806–5814 (2004).
43. Korevaar, P. A., Newcomb, C. J., Meijer, E. W. & Stupp, S. I. Pathway Selection in Peptide Amphiphile Assembly. *J. Am. Chem. Soc.* **136,** 8540–8543 (2014).
44. Davis-Searles, P. R., Saunders, A. J., Erie, D. A., Winzor, D. J. & Pielak, G. J. Interpreting the effects of small uncharged solutes on protein-folding equilibria. *Annual Review of Biophysics and Biomolecular Structure* **30,** 271–306 (2001).
45. Nguyen, H. D., Marchut, A. J. & Hall, C. K. Solvent effects on the conformational transition of a model polyalanine peptide. *Protein Science* **13,** 2909–2924 (2004).
46. Wallqvist, A. & Ullner, M. A simplified amino acid potential for use in structure predictions of proteins. *Proteins: Structure, Function, and Bioinformatics* **18,** 267–280 (1994).
47. Fu, I. W., Markegard, C. B., Chu, B. K. & Nguyen, H. D. Role of Hydrophobicity on Self-Assembly by Peptide Amphiphiles via Molecular Dynamics Simulations. *Langmuir* **30,** 7745–7754 (2014).
48. Andersen, H. C. Molecular dynamics simulations at constant pressure and/or temperature. *J. Chem. Phys.* **72,** 2384 (1980).
49. Frishman, D., Frishman, D., Argos, P. & Argos, P. Knowledge-based protein secondary structure assignment. *Proteins: Structure, Function, and Bioinformatics* **23,** 566–579 (1995).
50. Nguyen, H. D. & Hall, C. K. Molecular dynamics simulations of spontaneous fibril formation by random-coil peptides. *Proceedings of the National Academy of Sciences* **101,** 16180–16185 (2004).
51. Humphrey, W., Dalke, A. & Schulten, K. VMD: visual molecular dynamics. *Journal of molecular graphics* **14,** 33–38 (1996).
52. Vymětal, J. & Vondrášek, J. Gyration- and Inertia-Tensor-Based Collective Coordinates for Metadynamics. Application on the Conformational Behavior of Polyalanine Peptides and Trp-Cage Folding. *J. Phys. Chem. A* **115,** 11455–11465 (2011).
53. Dima, R. I. & Thirumalai, D. Asymmetry in the Shapes of Folded and Denatured States of Proteins †. *J. Phys. Chem. B* **108,** 6564–6570 (2004).
54. Thota, N., Luo, Z., Hu, Z. & Jiang, J. Self-Assembly of Amphiphilic Peptide (AF) 6H 5K 15: Coarse-Grained Molecular Dynamics Simulation. *J. Phys. Chem. B* **117,** 9690–9698 (2013).
55. Thota, N. & Jiang, J. Self-Assembly of Amphiphilic Peptide (AF) 6H 5K 15Derivatives: Roles of Hydrophilic and Hydrophobic Residues. *J. Phys. Chem. B* **118,** 2683–2692 (2014).
56. Velinova, M., Sengupta, D., Tadjer, A. V. & Marrink, S.-J. Sphere-to-Rod Transitions of Nonionic Surfactant Micelles in Aqueous Solution Modeled by Molecular Dynamics Simulations. *Langmuir* **27,** 14071–14077 (2011).
57. Mu, Y. & Yu, M. Effects of hydrophobic interaction strength on the self-assembled structures of model peptides. *Soft Matter* **10,** 4956 (2014).
58. Alder, B. J. & Wainwright, T. E. Studies in molecular dynamics. I. General method. *J. Chem. Phys.* **31,** 459 (1959).
59. Shu, J. Y. *et al.* Amphiphilic Peptide–Polymer Conjugates Based on the Coiled-Coil Helix Bundle. *Biomacromolecules* **11,** 1443–1452 (2010).
60. Jain, A. & Ashbaugh, H. S. Helix Stabilization of Poly(ethylene glycol)–Peptide Conjugates. *Biomacromolecules* **12,** 2729–2734 (2011).
61. Gore, T., Dori, Y., Talmon, Y., Tirrell, M. & Bianco-Peled, H. Self-Assembly of Model Collagen Peptide Amphiphiles. *Langmuir* **17,** 5352–5360 (2001).

62. Dube, N. *et al.* Effect of Alkyl Length of Peptide–Polymer Amphiphile on Cargo Encapsulation Stability and Pharmacokinetics of 3-Helix Micelles. *Biomacromolecules* **15,** 2963–2970 (2014).
63. Xu, X.-D., Jin, Y., Liu, Y., Zhang, X.-Z. & Zhuo, R.-X. Self-assembly behavior of peptide amphiphiles (PAs) with different length of hydrophobic alkyl tails. *Colloids and Surfaces B: Biointerfaces* **81,** 329–335 (2010).
64. Do, T. D. *et al.* Factors That Drive Peptide Assembly and Fibril Formation: Experimental and Theoretical Analysis of Sup35 NNQQNY Mutants. *J. Phys. Chem. B* **117,** 8436–8446 (2013).
65. Paramonov, S. E., Jun, H.-W. & Hartgerink, J. D. Self-Assembly of Peptide–Amphiphile Nanofibers: The Roles of Hydrogen Bonding and Amphiphilic Packing. *J. Am. Chem. Soc.* **128,** 7291–7298 (2006).
66. Ortony, J. H. *et al.* Internal dynamics of a supramolecular nanofibre. *Nat Mater* **13,** 812–816 (2014).
67. Bulut, S. *et al.* Slow Release and Delivery of Antisense Oligonucleotide Drug by Self-Assembled Peptide Amphiphile Nanofibers. *Biomacromolecules* **12,** 3007–3014 (2011).
68. Nguyen, H. D., Nguyen, H. D., Hall, C. K. & Hall, C. K. Spontaneous Fibril Formation by Polyalanines; Discontinuous Molecular Dynamics Simulations. *J. Am. Chem. Soc.* **128,** 1890–1901 (2006).
69. Dill, K. A., Alonso, D. O. V. & Hutchinson, K. Thermal stabilities of globular proteins. *Biochemistry* **28,** 5439–5449 (1989).
70. Shimizu, S. & Chan, H. S. Temperature dependence of hydrophobic interactions: A mean force perspective, effects of water density, and nonadditivity of thermodynamic signatures. *J. Chem. Phys.* **113,** 4683–4700 (2000).
71. Lee, O.-S., Stupp, S. I. & Schatz, G. C. Atomistic Molecular Dynamics Simulations of Peptide Amphiphile Self-Assembly into Cylindrical Nanofibers. *J. Am. Chem. Soc.* **133,** 3677–3683 (2011).

CHAPTER 6 The Tail of Two Peptide Amphiphiles: Effect of Conjugation with Hydrophobic Polymer on Folding of Peptide Sequences

6.1 Abstract

Peptide amphiphiles (PA) offer the potential of incorporating biological function into synthetic materials for tissue engineering in regenerative medicine. These hybrid conjugates are known to undergo self-assembly starting from single molecules to nanofibers before turning into hydrogel scaffolds; such a process involves conformational changes in secondary structures of peptides. Therefore, insights on the ability of peptide amphiphiles to form secondary structure as single molecules are useful for understanding self-assembly behavior. We report here a molecular simulation study of peptide folding by two PA sequences, each contains an alkyl tail and short peptide segment. The alkyl tail is observed to play two opposing roles in modulating sequence-dependent folding kinetics and thermodynamics. On one hand, it restricts conformational freedom reducing the entropic cost of folding, which is thus promoted. On the other hand, it acts as an interaction site with nonpolar peptide residues, blocking the peptide from helix nucleation, which reduces folding.

6.2 Introduction

Hydrogels, which belong to class of biomaterial defined by its 3-dimensional cross-linked polymer networks and its ability to absorb liquid,[1] can be potentially used in a variety of applications including diagnostic medicine, drug delivery, and tissue engineering.[2-5] Peptide-polymer conjugates, called peptide amphiphiles (PA), have been

shown to undergo a molecular self-assembly process with precise control in fabricating nanostructures as hydrogels.[6-10] The basic molecular structure of peptide amphiphiles is composed of two major constituents: a hydrophobic alkyl tail and a hydrophilic peptide sequence that is conjugated at the N-terminus. The alkyl tail length and peptide sequence are important parameters that affect self-assembly and control the macroscopic properties of the gel.[11-13]

In PA self-assembly, the formation of aggregates containing multiple PA monomers is driven by the hydrophobic collapse of the alkyl tails, which bury in the interior. The peptides on the surface form inter-peptide interactions[14] such as hydrogen bonding[13,15] and electrostatic interaction,[16] which control the shape and stability of aggregates as well as macroscopic properties of hydrogels. Specifically, the formation of β-sheets via intermolecular hydrogen bonding drives the morphology of aggregates to long structures that are often called cylindrical nanofibers.[17] Moreover, the mechanical properties of hydrogels are directly related to the nature and degree of β-sheet formation.[18,19] Therefore, it is important to examine the ability of peptide amphiphiles to form secondary structures through not only intermolecular interactions but also intramolecular interactions since the competition of these two types of interactions affects self-assembly in peptide-based systems.[18,19]

Conjugation of peptides to monoalkyl hydrocarbon chains has been shown to stabilize helix formation of a short peptide segment by Forns *et al*.[20] They showed that the 16-residue peptide alone does not form a distinct structure in solution, whereas the peptide adopts predominantly a α-helical structure in solution when a C_6 or C_{16} monoalkyl hydrocarbon chain is N-terminally acetylated. Moreover, the thermal stability of the α-helix

is greater upon addition of the C_{16} compared with the C_6 chain. Conjugation of less nonpolar polymers than the alkyl chain such as poly(ethylene glycol) can increase helix formation as demonstrated by Jain *et al.,* who reported that favorable peptide-polymer interactions, such as hydrogen bonding and electrostatic attraction, enhance helix formation.[21] In contrast, conjugation of more nonpolar polymers than the alkyl chain such as polystyrene induces helix destabilization near the peptide-polymer interface through favorable hydrophobic interactions between polystyrene and the adjacent residues as reported by Shu *et al*.[22] Furthermore, the unfolding effect by hydrophobic interactions is also observed in side-conjugation of polystyrene to the peptide (i.e., attachment of polymeric chain to the middle of peptide),[23] which induces a helix-to-sheet transition. These studies demonstrate that the effect of conjugation depends on three factors: (1) polymer type, (2) peptide sequence, and (3) placement of conjugation.

In this study, we aim to elucidate the role of conjugation by a nonpolar polymer to a peptide on helix stability and its dependency on peptide sequence via atomistic molecular dynamics (MD) simulations. To do so, we study two model peptide-polymer conjugates, which are hereafter named PA1 and PA2 whose sequences are palmitoyl-$Val_3Ala_3Glu_3$ and palmitoyl-$Ala_3Val_3Glu_3$, respectively (**Fig. 4.1a-b**). Even though they are comprised of the same amino acids, reversing the positions of alanine and valine residues results in different arrangements of secondary structures, which causes PA1 to create a stiffer gel than PA2 as demonstrated by Pashuck *et al*.[12]. First, we performed replica exchange molecular dynamics over a wide temperature range from 260 K to 550 K on both conjugated and unconjugated sequences to analyze the free energy landscapes and compare the thermodynamically favorable structures at equilibrium. Then, we performed constant-

temperature MD simulations at 298 K to elucidate the kinetics details of folding, including conformational change, nucleation, hydrogen bonding, and secondary structure dynamics.

6.3 Simulation Methods

To examine folding kinetics, twenty molecular dynamic simulations for each molecule of PA1 and PA2 that are conjugated (full PA sequence), unconjugated (alkyl-tail-free peptide sequence) and truncated (peptide sequence conjugated to a shortened alkyl tail of 4 carbon groups) starting as random coils. These simulations were performed for 200 ns at a temperature of 298 K using NAMD,[24] a parallel molecular dynamics code for high performance simulations. To examine folding thermodynamics, replica-exchange molecular dynamic simulations[25] were performed for 16 replicas starting as random coils over a range of 16 temperatures from 260 K to 550 K using NAMD.[24] Each replicate was simulated for 4 ps before attempting an exchange yielding a total simulation time of 400 ns per replica. These replica-exchange simulations were conducted for 100,000 exchanges with an acceptance rate of approximately 70%. All PA sequences were modeled using the CHARMM 27 forcefield[26-28] unless otherwise specified. The interaction energy cutoff parameter was set to 18Å.[24] The solvent was modeled using the generalized Born implicit solvent model.[29] Free energy calculations were performed using the MBAR program developed by the Chodera and coworkers.[30] Secondary structure and hydrogen bond analysis were obtained from the STRIDE standalone program.[31] Center of mass distance calculations between peptide and alkyl tail selections were performed with the Tk Console extension tool in VMD (Visual Molecular Dynamics),[32] which was also used for image rendering of PA conformations.

For the constant-temperature MD simulations, the last 10% conformations of each simulation over a period of 20 ns were used as the final structures; however, the whole trajectory was used to extract kinetics information. For the replica-exchange simulations, which reached equilibrium after 280 ns, the last 10% conformations over 40 ns were used as the equilibrium structures which we used to calculate thermodynamics properties.

6.4 Results and Discussion

6.4.1 Equilibrium conformations of PA1 are more helical than PA2

At equilibrium, the propensity to form alpha helical structure is similar for both sequences as seen in **Figure 6.1c-d,** which shows the percentage of secondary structures as a function of the temperature averaged from the last 40 ns from two separate replica-exchange simulations on conjugated PA sequences. These sequences become predominantly α-helical at low temperatures and random coils at high temperatures. The transition from α-helix to random coil is relatively sharp without an intermediate state. Interestingly, the most common type of secondary structures (i.e., β-structure) is absent at all temperatures. Since the peptide sequences contain only nine residues, they are too short to either form a complete β-strand or β-hairpin that is thermodynamically more stable than a α-helical structure. Also, they contain six strong α-helix-forming residues of alanine and glutamic acids and only three β-structure-forming residues of valines,[33,34] α-helix is thus preferred over β-structure.

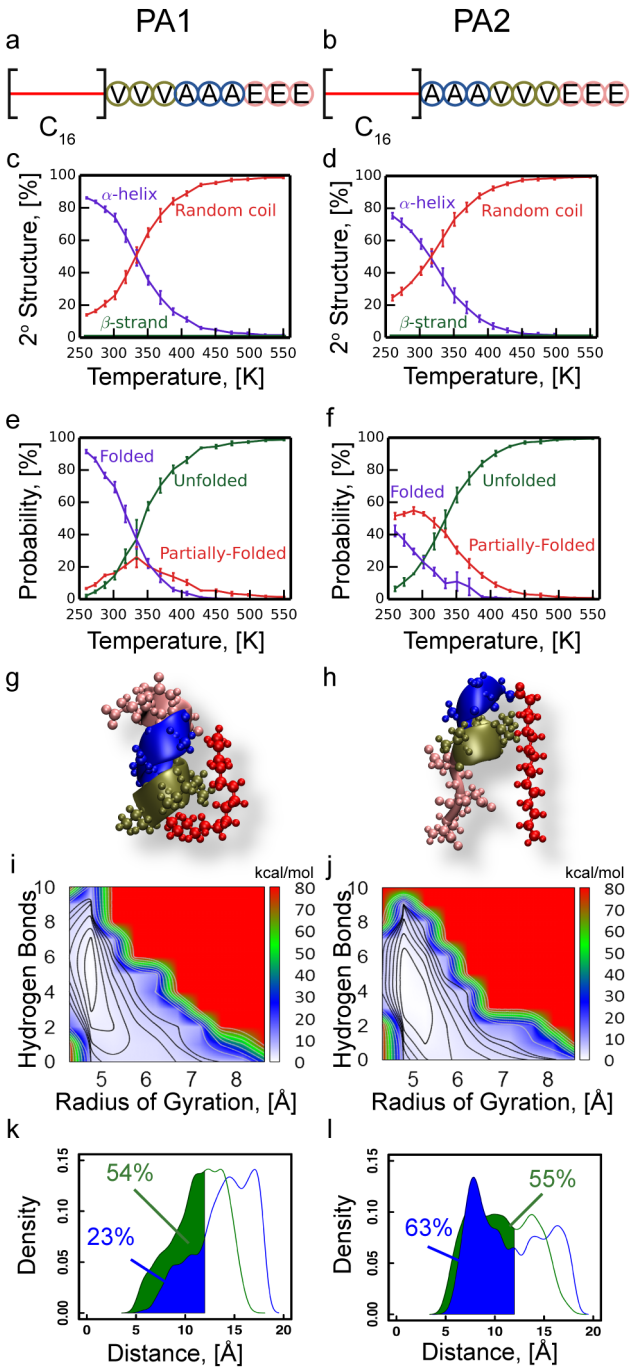

Figure 6.1. (a)-(b) PA1 and PA2 sequences: numerical order from residue #1 to residue #9 goes from the first amino acid that is adjacent to the alkyl tail. **(c)-(d)** Plots of the percentage of secondary structure formation as a function of temperature obtained from replica-exchange simulations. Data is averaged from the last 10% of equilibrium data. **(e)-(f)** Distributions of conformations in various structural states as a function of temperature. **(g)-(h)** Equilibrium conformations obtained from replica-exchange temperature simulation at T = 260 K showing a folded structure for PA1 and a partially-folded structure for PA2. Color scheme for the molecule by using VMD: hydrophobic polymeric tail (red), valine (green), alanine (blue), and glutamic acid (pink). **(i)-(j)** 2D PMF contour plots of conjugated sequences at T=298 K showing the free energy as a function of the number of hydrogen bonds and radius of gyration. Black contours are drawn every

1 kcal/mol, beginning at 1 kcal/mol. Grey contours are drawn every 10 kcal/mol, beginning 10 kcal/mol after the final black contour. **(k)-(l)** Density curves of the distance between the first half of the alkyl tail and alanine (blue) and valine (green) residues at 298 K. Data for PA1 is in the left column and PA2 is in the right column.

However, classifying conformations into three structural states based on helical content (less than 20% of residues that are helical for the unfolded state, between 20% and 80% for the partially-folded state, and greater than 80% for the folded state[35]) shows that PA1 has a higher probability than PA2 of being in the folded state at low temperatures as seen in **Figure 6.1e-f**, which shows the distribution of three structural states as a function of temperature. Indeed, PA1 forms nearly two times as many folded structures than PA2 at the lowest temperature of 260 K. Moreover, PA2 has equal probabilities of being in either the folded or partially folded states. As the temperature increases to room temperature of 298 K, PA2 is more likely in the partially folded state compared to PA1, which remains highly in the folded state. Representative conformations for the folded state by PA1 and the partially-folded state for PA2 are shown in **Figure 6.1g-h.** The same conclusion is reached using different definitions (in percentage of helical content) of the unfolded, partially folded and folded states based on raw distribution data (**Figure 6.6)**.

The 2D potential of mean force (PMF) as a function the number of hydrogen bonds and radius of gyration, which is calculated from the replica exchange data at a temperature of 298 K, confirms greater folding propensity of PA1 compared to PA2 (**Figure 6.1i-j**). The basin of the folded state in PA1, which is enclosed by a 1 kcal/mol contour, is localized in a region where PA1 can form 3-7 hydrogen bonds with a radius of gyration less than 5 Å, corresponding to the folded state. However, the basin of the folded state in PA2 encompasses a larger region by which PA2 can form 1-6 hydrogen bonds with a radius of

gyration greater than 5 Å. This means that PA2 is more flexible fluctuating between the folded and partially-folded states.

Competitive interactions with the alkyl tail possibly discourage α-helical folding as seen in **Figure 6.1k-l**, which shows the distribution of conformations as a function of the distance between the centers of mass from the first half of the alkyl tail to either three alanine residues (blue) or three valine residues (green) for both sequences. Although the cutoff distance for van der Waal interaction is at 18 Å, the hydrophobic interaction strength is strongest below 12 Å; therefore, the critical distance used for comparison is 12 Å. The percentages of conformations wherein the alkyl tail is within 12 Å of the three valine residues are similar for both sequences. However, the percentage of conformations wherein the alkyl tail is within 12 Å of the three alanine residues is at 63% for PA2 compared to 23% for PA1. This indicates that the alkyl tail might reduce folding of PA2 by binding strongly to the alanine residues. In subsequent sections, helix propensity of both sequences and the role of the alkyl tail are investigated via constant temperature simulations at 298 K, where folding kinetics can be explored in greater detail.

6.4.2 Removal of alkyl tail results in all unfolded conformations

To elucidate the role of the alkyl tail in folding, twenty constant-temperature MD simulations at 298 K were performed for each sequence without the alkyl tail for 200 ns. These simulations using the CHARMM 27 force field[26,27] produce solely unfolded conformations. Ten additional constant-temperature simulations using the CHARMM 36 force field[36] also yield only structures in the unfolded state.

To confirm that equilibrium conformations of tail-free sequences are truly unfolded, replica exchange simulations were performed over a temperature range of 260 K to 550 K

over 400 ns per replica. The 2D potential of mean force as a function the number of hydrogen bonds and radius of gyration is calculated from the replica exchange data at a temperature of 298 K. These contour plots for both tail-free sequences in **Figure 6.2** show that the global minimum is located at a radius of gyration of 7.5 Å and 0 hydrogen bond corresponding to the unfolded state. Indeed, analysis of the percentage of secondary structures as a function of the temperature indicates that all residues of the last 40 ns from replica-exchange simulations are random coil over the whole temperature range (**Figure 6.7)**. In contrast, the contour plots for conjugated sequences in **Figure 6.1g-h** show that the global minimum free energy is located at a radius of gyration of 4.75 Å and 5 hydrogen bonds for PA1 corresponding to the folded state. Based on these results, the alkyl tail is a necessary component to produce folded structures.

Unconjugated molecules prefer to be in the unfolded state (**Figure 6.2**) while conjugated molecules prefer to be in the folded or partially folded state (**Figure 6.1g-h**). This is due to the freedom of unconjugated molecules that are more flexible than conjugated molecules to sample more conformations at the unfolded state as indicated by the high probability of being in the unfolded state compared to the folded state for unconjugated sequences (**Figure 6.8**). Therefore, entropic cost of folding or the loss of conformational entropy of main chain and side chain atoms is larger for unconjugated molecules than that for conjugated molecules. In other words, secondary structure induction by conjugation is attributed to a reduced conformational freedom of the peptide segment; thus its entropic cost to folding becomes smaller than those in unconjugated peptides. Similarly in an experimental setting, Forns *et al*. [20] observed the induction of helical structures after conjugation of an alkyl tail of either 6 or 16 carbons to a 16 residue

peptide whose sequence is KAEIEALKAEIEALKA. They showed that the peptide alone does not form a distinct structure in solution whereas the peptide adopts predominantly α-helical structures when a C_6 or C_{16} monoalkyl hydrocarbon chain is N-terminally acetylated. Moreover, the thermal stability of α-helix is greater when the peptide is conjugated to a C_{16} tail than to a C_6 tail indicating that the longer tail is more effective in restricting conformational freedom of the peptide.

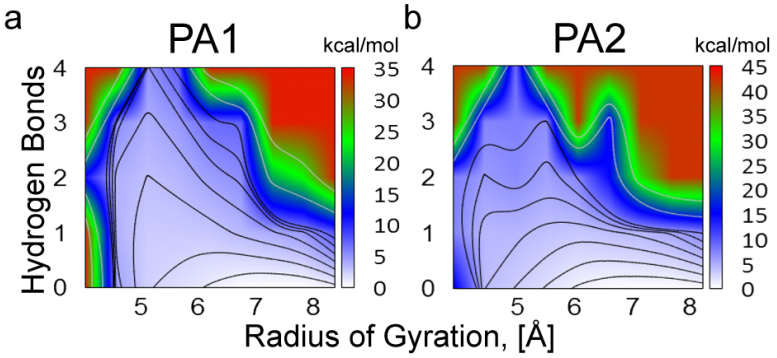

Figure 6.2. 2D PMF contour plots of tail-free sequences at T=298 K showing the free energy as a function of the number of hydrogen bonds and radius of gyration. Global minimum for tail-free sequences is at 0 hydrogen bond and 7.5 Å. Black contours are drawn every 1 kcal/mol, beginning at 1 kcal/mol. Grey contours are drawn every 10 kcal/mol, beginning 10 kcal/mol after the final black contour.

6.4.3 PA2 exhibit increased unfolded conformations as compared to PA1 from constant-temperature simulations

Table 6.1. Distribution of conformations exhibited by PA1 and PA2 at 298 K showing the percentage of simulations result in conformations of a certain state from constant-temperature simulations.

Sequence	Unfolded, %	Partially-Folded, %	Folded, %
PA1	40	50	10
PA2	60	35	5

Twenty additional MD simulations were run for 200 ns for each full PA sequence at a constant temperature of 298 K. The final structures are grouped by their average helical content from the last 20 ns. The results show that PA1 forms unfolded structures in 40% of

total simulations while PA2 forms unfolded structures in 60% of total simulations (**Table 6.1**). Inversely, PA1 forms more partially-folded structures by 15% and more folded structures by 5% compared to PA2. The average helical content for PA1 partially-folded structures is about 10% higher than that of PA2 partially-folded structures (data not shown). Since the temperature of 298K at which these constant-temperature simulations were conducted is significantly lower than the melting point (that can be extracted at 50% of helicity from **Figure 6.1c-d**), both PA molecules are expected to get kinetically trapped at local minima resulting in large percentages of unfolded or partially folded structures and small percentages of folded structures at 5-10% (**Table 6.1**). Therefore, it's important to decipher detailed kinetics pathways including kinetically trapped events as discussed below.

Analysis of the probability of forming α-helical hydrogen bonds throughout every simulation reveals some degree of difficulty by certain hydrogen acceptor-donor groups (**Figure 6.3**). For PA2, the pairwise hydrogen bond acceptor-donor residues 3 & 7, 4 & 8, and 5 & 9 have a lower probability of forming α-helical hydrogen bonds compared to their positional counterparts in PA1. Likewise, residues 1 & 5 and residues 2 & 6 in PA1 have a lesser propensity to form hydrogen bonds compared to their positional counterparts in PA2. The failure to form these bonds results in unfolded structures, where parts of the sequence are random coils.

It is well-known that alanine and glutamic acids have a strong preference for forming α-helices while valine has the highest propensity over other natural amino acids to form β-sheet than other secondary structures.[33,34] Therefore, it is not a surprise that PA1, which has six strong α-helix-forming residues of alanine and glutamic acids in a contiguous

segment, has high probabilities along those residues at positions 4-9 (AAAEEE) and low probabilities along valine residues at positions 1-3 (VVV) (**Figure 6.3**). However, it is a surprise that PA2 can form α-helical hydrogen bonds even with high probability at positions 1-3 (AAA) since its six strong α-helix-forming residues of alanine and glutamic acids are disrupted by three intervening weak α-helix-forming residues of valines at positions 4-6 (VVV). Moreover, PA2 has a higher probability at the hydrogen bond group 1-5 compared to his positional counterpart in PA1. This can be explained the examining the presence of intervening valine residues.

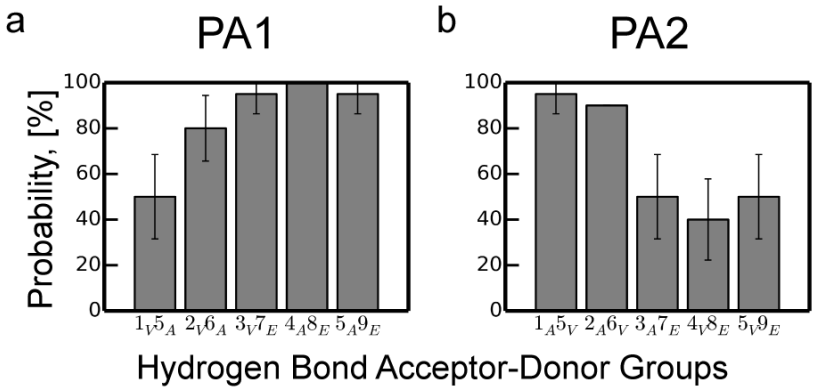

Figure 6.3. Probability of forming a α-helical hydrogen bond by all possible hydrogen acceptor-donor groups of (a) PA1 and (b) PA2. The label on the x-axis shows residue positions (as numbers) and amino acid identity (as letters).

The presence of valines as intervening residues of any hydrogen bond group decreases the probability of forming α-helical hydrogen bonds. This is exemplified in the formation of the terminal hydrogen bond involving residues 1 & 5. The hydrogen bond group 1_V5_A of sequence PA1 contains two valine and one alanine residues in between while the hydrogen bond group 1_A5_V of sequence PA2 contains two alanine and one valine residues in between. Even though both groups have the same types of end residues, the

presence of one additional intervening valine residue causes 1_A5_V of PA2 to form nearly twice the number of α-hydrogen bonds compared to 1_V5_A of PA1 (**Figure 6.3**). A comparison of other hydrogen bond groups amongst PA1 and PA2 reveals similar results except the hydrogen bond involving residues 2 & 6 whose hydrogen-bonding probabilities are similar around 80%. Overall, PA1 exhibits a greater likelihood to form hydrogen bonds than PA2, which correlates to its higher probability of reaching the folded state.

6.4.4 Preferred nucleation site is a 3_{10}-helical turn with alanine residues before transitioning into a α-helical conformation

We observed that the first critical event of successful folding by PA molecules into α-helical structures requires the creation of a helical turn. However, this turn is different than a typical α-helical conformation, which involves one hydrogen bond to make a complete turn of 5 residues.[37,38] It turns out that this turn resembles a $\mathbf{3_{10}}$-helical conformation, which requires two hydrogen bonds to make a complete turn of three residues.[37,38] For example, a 3_{10}-helical turn on site 4, 5, 6 of PA1 is shown in **Figure 6.4a** forming a pair of hydrogen bonds between residues 3 and 6 and between residues 4 and 7. Later, this 3_{10}-helical turn transitions into a α-helical turn which spans from residues 3 through 7 with a hydrogen bond between residues 3 and 7 as shown in **Figure 6.4b**.

The formation of a $\mathbf{3_{10}}$-helical turn, which is identified as a nucleation site since it is critically created first, is observed in most constant-temperature simulations. In fact, 100% of PA1 simulations form 3_{10} helical turns while 90% of PA2 simulations form 3_{10} helical turns as nucleation sites (10% did not proceed to form any helices). As seen in **Figure 6.4c-d**, there are five possible sites of forming $\mathbf{3_{10}}$-helical hydrogen bonds, beginning at the second residue and ending at the eighth residue. The site with the greatest probability of

forming the first 3_{10}-helical turn in PA1 involves residues 4, 5, and 6 as seen in **Figure 6.4c**. This site has the greatest possible number of alanine residues in a sequential order (AAA). However, the positional counterpart at positions 4, 5, and 6 (VVV) in PA2 has a zero probability of forming due to the lack of alanine residues (**Figure 6.4d**). For PA2, the site with the most alanines at positions 2, 3 and 4 (AAV) has the greatest probability of forming the first 3_{10} helical turn (**Figure 6.4d**). The positional counterpart in PA1, with a total of one alanine residue, has a zero probability of forming due to a difference of just one alanine residue. Based on these results, it can be concluded that nucleation preferably occurs on sites containing more alanine residues than other hydrophobic amino acids. Even though site 2-3-4 in PA1 and site 4-5-6 have zero probability of forming the first 3_{10}-helical turn as shown in **Figure 6.4c-d,** they still have an opportunity to form 3_{10} helical turns later after other nucleating sites have formed 3_{10} helical turns elsewhere.

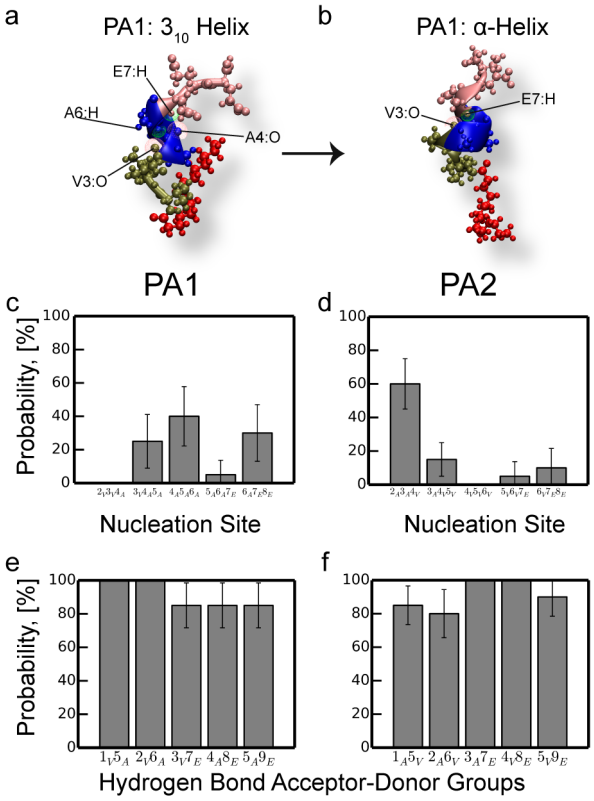

Figure 6.4. (a)-(b) Snapshots showing a 3_{10}-helical turn formed on residues 4, 5, and 6 of PA1 at t=24 ns involving two hydrogen bonds between residues 3 and 6 and between residues 4 and 7. At t=36 ns, a α-helical turn on residue 3, 4, 5, 6, and 7 is transitioned from the former 3_{10}-helical turn by forming one hydrogen bond between residues 3 and 7. **(c)-(d)** The probability of forming a 3_{10}-helical turn as a nucleation site by all three-residue groups. **(e)-(f)** The probability of an α-helical hydrogen bond transitioning from its complementary pair of 3_{10}-helical hydrogen bonds. The label on the x-axis shows residue positions (as numbers) and amino acid identity (as letters).

Once 3_{10}-helical turns are formed, PA molecules proceed to fold into α-helical structures by transitioning 3_{10}-helical turns into α-helical turns as shown in **Figure 6.4a-b**. Such transitions are relatively frequent as seen in **Figure 6.4e-f**, which shows the probability that a α-helical hydrogen bond is formed by transitioning a 3_{10}-helical turn to a α-helical conformation. A transition is tabulated if a complementary pair of 3_{10} helical hydrogen bonds is formed before its corresponding α-helical hydrogen bond. The results indicate that it is highly probable (77% to 100%) that the complementary pair of 3_{10}-helical hydrogen bonds form first since they have shorter spacing than the α-helical

hydrogen bond by definition. Transitions from other secondary elements to α-helices have been previously observed by Colombo *et al.*,[39] who examined 200 nucleation events using MD simulations and found that α-helix nucleation events were preceded by formation of β-turns and 3_{10} helices whose frequencies depend upon the sequence. Although the lifetimes of these structures were short, they acted as important precursors to the formation of α-helices.

6.4.5 Interactions with alkyl tail are disruptive preventing folding

Favorable hydrophobic interactions between the alkyl tail and the first six residues that are nonpolar of the peptide segment drive conformations to the unfolded state by preventing helical hydrogen bonds from being formed in constant temperature simulations. This can be seen in **Figure 6.5a**, which plots the number of the hydrogen bonds, the average distances between the first half the alkyl tail and the first three or the middle three residues as a function of time for a constant temperature simulation of PA2 at 298 K. A dashed red line is drawn at 12 Å to clearly show the interacting phases between tail and peptide segment. From 0-84 ns, the molecule remains in an unfolded conformation due to the strong hydrophobic interactions between the alkyl tail and peptide segment being formed as shown by the long durations of tail-peptide contact in the **Figure 6.5a**. When the alkyl tail ceases to interact with the peptide, 3_{10}-helical bonds (green) begin to form with the nucleation of a 3_{10}-helical turn at residues 2, 3, and 4 (AAV) occurring at 84 ns as shown in **Figure 6.5b**. Another 3_{10}-helical turn forms at residues 6, 7 and 8 (VEE) at 111 ns. Subsequently, these 3_{10}-helical turns transition into a α-helical turn at residues 4 through 8 (VVVEE) at 117 ns. A complete helix forms at t~185 ns. Once a helix is completely formed, the alkyl tail comes back and becomes more stably attached to the

peptide segment. Moreover, when the alkyl tail binds tightly and continuously with the peptide especially alanine residues (**Figure 6.9**), the peptide struggles to form even just one hydrogen bond; therefore, the peptide remains as an unfolded structure throughout the whole simulation.

The disruptive nature of the alkyl tail that prevents peptide folding when it forms favorable hydrophobic interactions with the first six nonpolar residues is also observed in PA1. Even when the peptide has already folded into a partial helix, the alkyl tail can still prevent it from further folding by forming hydrophobic interactions and ultimately cause the peptide to unfold (**Figure 6.10**).

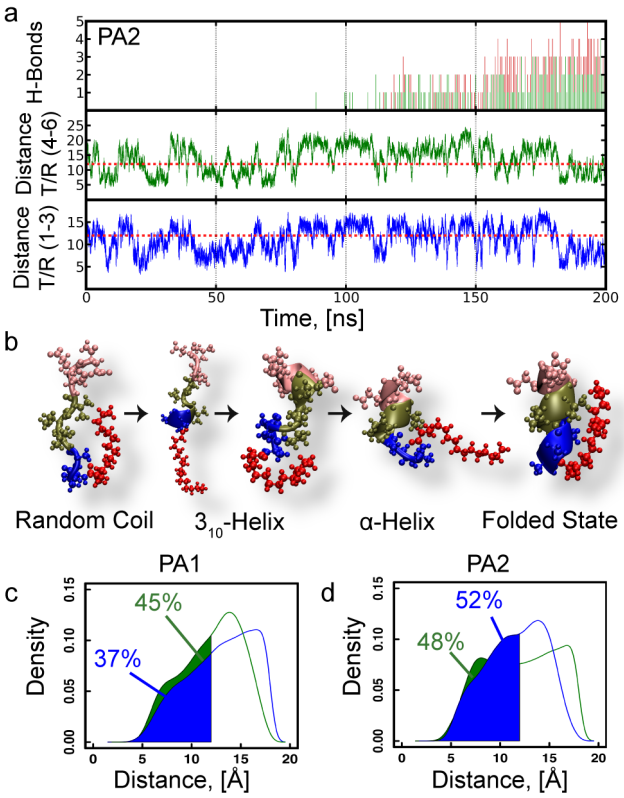

Figure 6.5. (a) For the PA2 sequence: (top panel) a plot of the number of α-helical hydrogen bonds (red), 3_{10} helical hydrogen bonds (green); (middle panel) distance between the center of masses of the first half of the alkyl tail and valine residues 4-6 (green); (bottom panel) distance between the center of masses of the first half of the alkyl tail and alanine residues 1-3 (blue) as a function of time (ns). A dashed red line is drawn at 12 Å showing the interacting phases between alkyl tail and peptide segment. **(b)** Snapshots of PA2 showing a

3_{10}-helical turn formed on residues 2, 3 and 4 (AAV) at 84 ns and another 3_{10}-helical turn formed on residues 6,7 and 8 (VVE) at 111 ns before transitioning to α-helical turn on residues 4-8 (VVVEE). **(c)-(d)** density curves of the distance between the first half of the alkyl tail and alanines (blue) and valines (green) for PA1 and PA2. Percentage of hydrophobic contacts at 12Å and below is shaded.

The higher rate of unfolding in PA2 compared to PA1 can be explained by the frequency of disruptive interactions between the alkyl tail and alanines, which has been previously shown to be the preferred site for nucleation. According to **Figure 6.5c-d**, PA2 alanines have approximately 1.4 times the probability (52%) of forming interactions with the alkyl tail compared to PA1 alanines (37%). Since PA2 alanines are positioned closer to the alklyl tail, hydrophobic interactions occur more frequently causing the prevention of nucleation of forming 3_{10} helices by alanine sites. The nucleation of PA1 is affected to a lesser degree by interactions with the alkyl tail since alanine residues in PA1 are positioned further away and experiences fewer hydrophobic interactions with the alkyl tail.

Based on this data, the kinetic pathway to an unfolded structure is followed when favorable interactions between nearby nonpolar residues and conjugated polymer inhibit helical nucleation. Such disruptive nature of hydrophobic conjugated polymer has also been observed by Shu *et al.*[22] In their experimental study, polystyrene, which a hydrophobic polymer, is covalently attached to a protein that is capable of folding into a coiled-coil helix bundle. Strong hydrophobic interactions between polystyrene and the nearby hydrophobic residues caused partial unfolding of the helix at the peptide-polymer interface. When unconjugated peptides were mixed in thin films containing free hydrophobic polymers, less disruption of helix formation was observed relative to conjugation of the polymer. Hence, this is similar to our results that the closeness of PA2

alanines induces a stronger affinity to the alkyl tail relative to the farther position of PA1 alanines.

6.4.6 Minimizing alkyl tail interactions results in higher folding

Table 6.2. Distribution of conformations exhibited by PA2 with the alkyls tail shortened to 4 carbons at 298 K from constant-temperature simulations.

Sequence	Unfolded, %	Partially-Folded, %	Folded, %
Truncated PA2	45	50	5

To examine the effect of the alkyl tail length on peptide folding, 20 additional constant temperature simulations at 298 K on PA2 with a tail length of 4 carbons were conducted. Even though this truncated alkyl tail can reduce hydrophobic interactions with the peptide segment, it is too short to decrease the flexibility of the peptide tail and thus to reduce the entropy cost of folding, two end carbons of the alkyl tail were held fixed. Previously, constant temperature simulations on PA2 (with a full alkyl tail) exhibit an unfolding rate at 60% (**Table 6.1**). With the alkyl tail length reduced, the unfolding rate drops to 45% (**Table 6.2**). With the main driving force to folding maintained and disruptive forces reduced, higher rates of folding are observed by a 15% increase in the percentage of simulations that results in the partially-folded state while the percentage of simulations that results in the folded state remains the same at 5%.

6.5 Conclusions

The alkyl tail plays two opposing roles in the folding kinetics of the two peptide amphiphiles under consideration. On one hand, the alkyl tail acts as a stabilizing force that induces conformational restriction resulting in decreasing the entropic cost of folding based on the comparison of free energy profiles of conjugated and unconjugated PA

molecules from replica exchange simulations. In this case, it is observed that conjugated molecules prefer to be in the folded or partially folded state whereas unconjugated sequences adopt virtually no helical structures due to their inherent high conformational freedom of being short and flexible peptide sequences. On the other hand, the alkyl tail acts as a disruptive force that prevents helical folding by blocking nucleating site especially when such site is adjacent to the alkyl tail. This is based on constant-temperature simulations at 298 K, which were performed to analyze the kinetic folding pathways and elucidate the precise role of the alkyl tail. In this case, it is identified that the first critical event of folding kinetics requires creating a 3_{10}-helical turn, which involves alanine residues and later switches into a α-helical turn. This indicates the critical role of alanine residues that can influence the overall folding. To compare the amount of interactions between the alkyl tail and alanine residues of each sequence, the distance between the centers of masses of the first half of the alkyl tail to the alanine residues were calculated. PA2 alanines experience 1.4 times as many interactions relative to PA1 alanines (52% to 37%) since they are closer to the alkyl tail. The high frequency of tail-peptide interactions prevents the peptide from folding in PA2 relative to PA1. When the alkyl tail is truncated to four carbon groups and the end carbons are immobile, the main driving force to folding is maintained and disruptive forces are reduced, higher rates of folding are observed.

We have elucidated the role of the alkyl tail on the folding of two peptide amphiphiles at infinitely diluted conditions, open questions remain on the ability of these PA molecules to form intermolecular interactions at concentrated conditions during self-assembly. The answers to these questions are starting to emerge in understanding the role of secondary-structure formation on the self-assembly of hydrogel nanostructures that are

responsive to external stimuli.[40-43] For instance, a recent work examined the general role of hydrophobicity (which is affected by the choice of solvent, polymer type or peptide sequence) on PA self-assembly.[43] During the early stage of self-assembly when PA molecules are still isolated from one another, it was found that intramolecular hydrophobic interactions between the alkyl tail and non-polar peptide side chains cause individual PA molecules to collapse into condensed conformations, which interfere with the formation of intermolecular hydrogen bonds between peptide molecules. This results in the formation of cylindrical structures that contain peptides in just random-coil conformations. In contrast, when intramolecular hydrophobic interactions between non-polar polymer and peptide side chains are low, intermolecular hydrophobic interactions between non-polar polymers drive the formation of spherical micelles while intermolecular hydrogen bonds between peptide segments facilitate the merging of multiple spherical micelles into cylindrical nanofibers that contain a high amount of β-sheets. Further simulation studies on the role of peptide sequence and conjugation on PA self-assembly will provide valuable information in aiding the design of functional hydrogel biomaterials.

6.6 Acknowledgements

This work was originally published in Biomacromolecules, 2014 © American Chemical Society. Co-authors include Brian K Chu, Cade B Markegard, Seong E Choi, and Hung D Nguyen. HDN acknowledges financial support from UC Irvine. IWF acknowledges support from a Graduate Research Fellowship from the National Science Foundation (DGE-1321846). This work used the Extreme Science and Engineering Discovery Environment (XSEDE), which is supported by National Science Foundation grant number OCI-1053575.

We are also thankful for the computational resources provided by the GreenPlanet and High Performance Computing clusters at UCI campus.

6.7 Supplementary Information

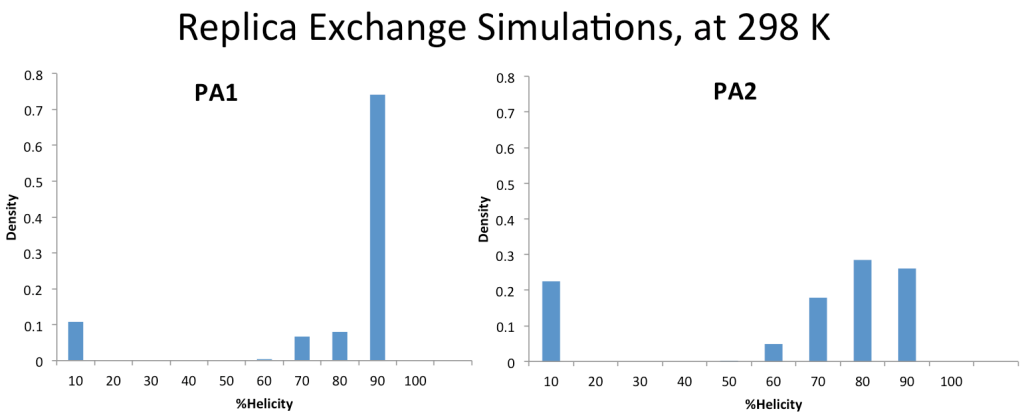

Figure 6.6. Distributions of helical conformations from replica-exchange simulations at 298K by the full PA1 and PA2 sequences.

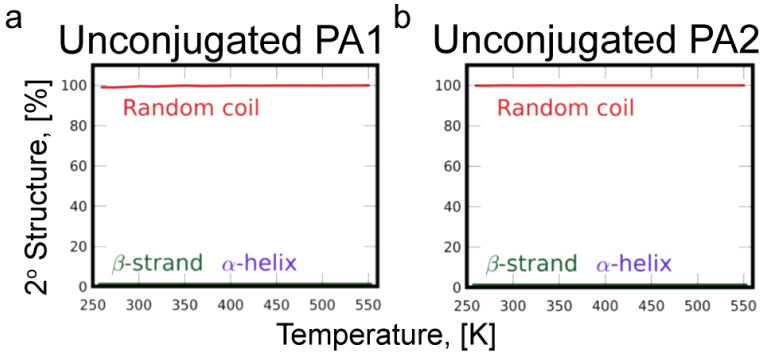

Figure 6.7. The percentage of secondary structure formation as a function of temperature obtained from replica-exchange simulations for the (a) PA1 and (b) PA2 unconjugated sequences.

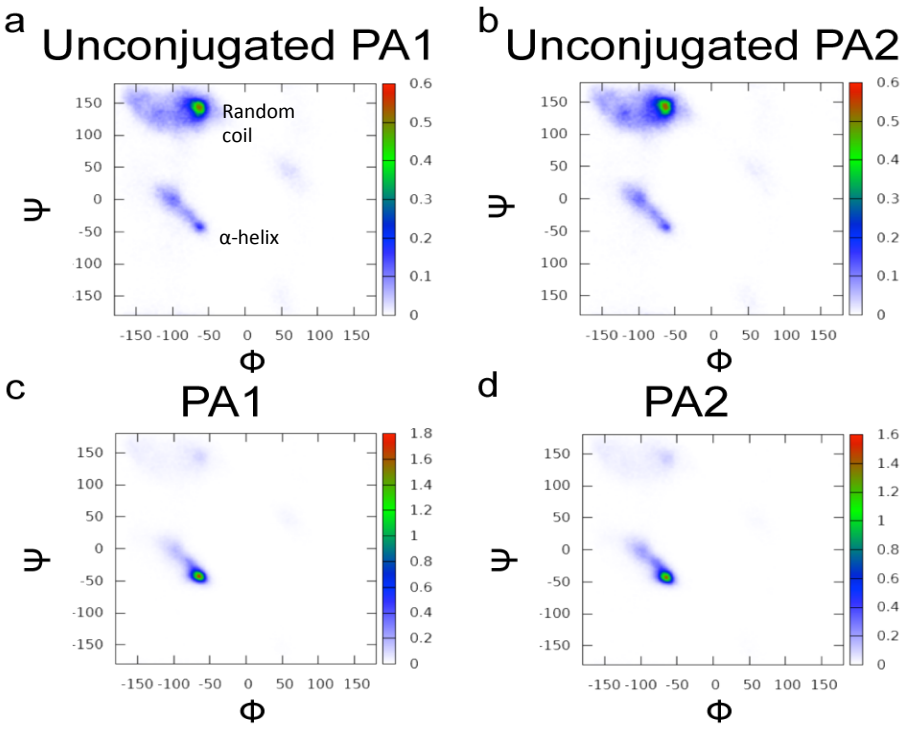

Figure 6.8. Probability as a function of psi-phi angles from replica-exchange simulations at all temperatures (260-550 K) for (a) unconjugated PA1, (b) unconjugated PA2, (c) conjugated PA1, (d) conjugated PA2. High probability at the unfolded state (being a random coil) over the folded state (being a α-helix) for both unconjugated sequences; the reverse is true for conjugated sequences.

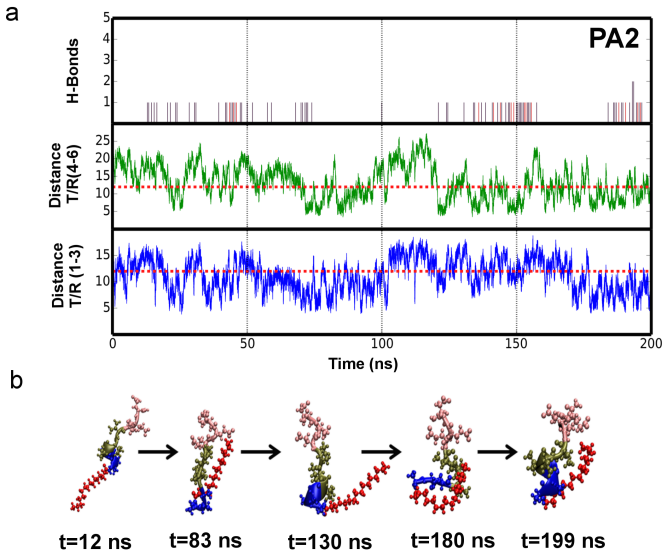

Figure 6.9. For the PA2 sequence: **(a)** A plot of the number of alpha helical hydrogen bonds (red), 3_{10} helical hydrogen bonds (dark purple), distance between the center of masses of the first half of the alkyl tail and residues 1-3 (blue) and 4-6 (green) vs. Time (ns) **(b)** Snapshots of folding and unfolding at different time frames with continuous alkyl tail interactions throughout the whole simulation.

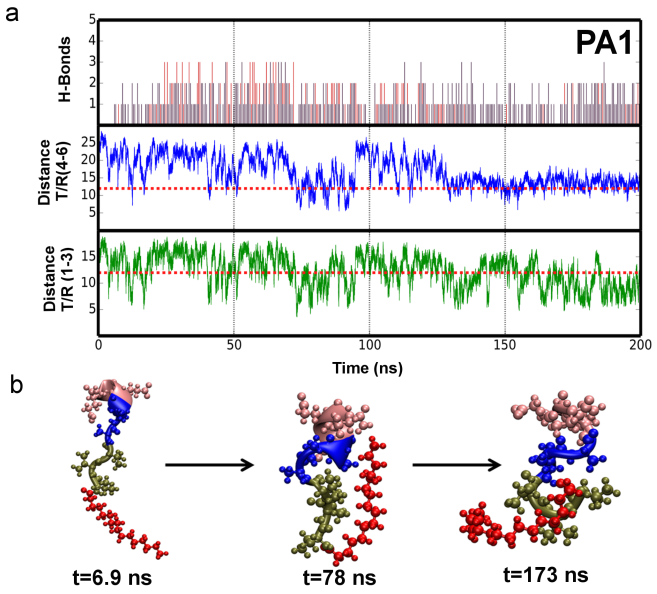

Figure 6.10. For the PA1 sequence: **(a)** A plot of the number of alpha helical hydrogen bonds (red), 3_{10} helical hydrogen bonds (dark purple), distance between the center of masses of the first half of the alkyl tail and residues 1-3 (green) and 4-6 (blue) vs. Time (ns). **(b)** Snapshots: 310 helix nucleation at t=6.9 ns, interacting alkyl tail at t=78 ns, unfolded structure at t=173 ns

6.8 References

1. Drury, J. L. & Mooney, D. J. Hydrogels for tissue engineering: scaffold design variables and applications. *Biomaterials* **24,** 4337–4351 (2003).
2. Peppas, N. A., Hilt, J. Z., Khademhosseini, A. & Langer, R. Hydrogels in Biology and Medicine: From Molecular Principles to Bionanotechnology. *Adv. Mater.* **18,** 1345–1360 (2006).
3. Chow, D., Nunalee, M. L., Lim, D. W., Simnick, A. J. & Chilkoti, A. Peptide-based biopolymers in biomedicine and biotechnology. *Materials Science and Engineering: R: Reports* **62,** 125–155 (2008).
4. Vermonden, T., Censi, R. & Hennink, W. E. Hydrogels for Protein Delivery. *Chem. Rev.* **112,** 2853–2888 (2012).
5. Khademhosseini, A. & Langer, R. Microengineered hydrogels for tissue engineering. *Biomaterials* **28,** 5087–5092 (2007).
6. Yu, Y.-C. *et al.* Structure and Dynamics of Peptide–Amphiphiles Incorporating Triple-Helical Proteinlike Molecular Architecture †. *Biochemistry* **38,** 1659–1668 (1999).
7. Hartgerink, J. D. Self-Assembly and Mineralization of Peptide-Amphiphile Nanofibers. *Science* **294,** 1684–1688 (2001).
8. Luo, J. & Tong, Y. W. Self-assembly of collagen-mimetic peptide amphiphiles into biofunctional nanofiber. *ACS Nano* **5,** 7739–7747 (2011).
9. Jonker, A. M., Löwik, D. W. P. M. & van Hest, J. C. M. Peptide- and Protein-Based Hydrogels. **24,** 759–

773 (2012).
10. Jones, R. R. *et al.* Collagen stimulating effect of peptide amphiphile C16-KTTKS on human fibroblasts. *Mol. Pharmaceutics* **10,** 1063–1069 (2013).
11. Hartgerink, J. D., Beniash, E. & Stupp, S. I. Peptide-amphiphile nanofibers: A versatile scaffold for the preparation of self-assembling materials. *Proceedings of the National Academy of Sciences* **99,** 5133–5138 (2002).
12. Pashuck, E. T., Cui, H. & Stupp, S. I. Tuning Supramolecular Rigidity of Peptide Fibers through Molecular Structure. *J. Am. Chem. Soc.* **132,** 6041–6046 (2010).
13. Missirlis, D. *et al.* Effect of the Peptide Secondary Structure on the Peptide Amphiphile Supramolecular Structure and Interactions. *Langmuir* **27,** 6163–6170 (2011).
14. Missirlis, D. *et al.* Linker Chemistry Determines Secondary Structure of p5314-29 in Peptide Amphiphile Micelles. *Bioconjugate Chem.* **21,** 465–475 (2010).
15. Shimada, T., Lee, S., Bates, F. S., Hotta, A. & Tirrell, M. Wormlike Micelle Formation in Peptide-Lipid Conjugates Driven by Secondary Structure Transformation of the Headgroups †. *J. Phys. Chem. B* **113,** 13711–13714 (2009).
16. Krista L Niece, Jeffrey D Hartgerink, Jack J J M Donners, A. & Stupp, S. I. Self-Assembly Combining Two Bioactive Peptide-Amphiphile Molecules into Nanofibers by Electrostatic Attraction. **125,** 7146–7147 (2003).
17. Velichko, Y. S., Stupp, S. I. & la Cruz, de, M. O. Molecular Simulation Study of Peptide Amphiphile Self-Assembly. *J. Phys. Chem. B* **112,** 2326–2334 (2008).
18. Tysseling, V. M. *et al.* Self-assembling peptide amphiphile promotes plasticity of serotonergic fibers following spinal cord injury. *J. Neurosci. Res.* **88,** 3161–3170 (2010).
19. Paramonov, S. E., Jun, H.-W. & Hartgerink, J. D. Self-Assembly of Peptide–Amphiphile Nanofibers: The Roles of Hydrogen Bonding and Amphiphilic Packing. *J. Am. Chem. Soc.* **128,** 7291–7298 (2006).
20. Forns, P., Lauer-Fields, J. L., Gao, S. & Fields, G. B. Induction of protein-like molecular architecture by monoalkyl hydrocarbon chains. *Biopolymers* **54,** 531–546 (2000).
21. Jain, A. & Ashbaugh, H. S. Helix Stabilization of Poly(ethylene glycol)–Peptide Conjugates. *Biomacromolecules* **12,** 2729–2734 (2011).
22. Shu, J. Y. *et al.* Amphiphilic Peptide–Polymer Conjugates Based on the Coiled-Coil Helix Bundle. *Biomacromolecules* **11,** 1443–1452 (2010).
23. Dube, N., Presley, A. D., Shu, J. Y. & Xu, T. Amphiphilic Peptide-Polymer Conjugates with Side-Conjugation. *Macromol. Rapid Commun.* **32,** 344–353 (2011).
24. Phillips, J. C. *et al.* Scalable molecular dynamics with NAMD. *J. Comput. Chem.* **26,** 1781–1802 (2005).
25. Sugita, Y. & Okamoto, Y. Replica-exchange molecular dynamics method for protein folding. *Chemical Physics Letters* **314,** 141–151 (1999).
26. MacKerell, A. D., Jr *et al.* All-atom empirical potential for molecular modeling and dynamics studies of proteins. *J. Phys. Chem. B* **102,** 3586–3616 (1998).
27. Mackerell, A. D., Jr., Feig, M. & Brooks, C. L., III. Extending the treatment of backbone energetics in protein force fields: Limitations of gas-phase quantum mechanics in reproducing protein conformational distributions in molecular dynamics simulations. *J. Comput. Chem.* **25,** 1400–1415 (2004).
28. Brooks, B. R. *et al.* CHARMM: The biomolecular simulation program. *J. Comput. Chem.* **30,** 1545–1614 (2009).
29. Still, W. C. *et al.* Semianalytical treatment of solvation for molecular mechanics and dynamics. *J. Am. Chem. Soc.* **112,** 6127–6129 (1990).
30. Shirts, M. R. & Chodera, J. D. Statistically optimal analysis of samples from multiple equilibrium states. *J. Chem. Phys.* **129,** 124105 (2008).
31. Frishman, D. & Argos, P. Knowledge-based protein secondary structure assignment. *Proteins: Structure, Function, and Bioinformatics* **23,** 566–579 (1995).
32. Humphrey, W., Dalke, A. & Schulten, K. VMD: visual molecular dynamics. *Journal of molecular graphics* **14,** 33–38 (1996).
33. Chou, P. Y. & Fasman, G. D. Prediction of protein conformation. *Biochemistry* **13,** 222–245 (1974).
34. Levitt, M. Conformational Preferences of Amino-Acids in Globular Proteins. *Biochemistry* **17,** 4277–4284 (1978).
35. Clementi, C., Nymeyer, H. & Onuchic, J. N. Topological and energetic factors: what determines the

structural details of the transition state ensemble and 'en-route' intermediates for protein folding? an investigation for small globular proteins. *Journal of Molecular Biology* **298,** 937–953 (2000).
36. Best, R. B. *et al.* Optimization of the Additive CHARMM All-Atom Protein Force Field Targeting Improved Sampling of the Backbone ϕ, ψ and Side-Chain χ1 and χ2 Dihedral Angles. **8,** 3257–3273 (2012).
37. Kabsch, W., Kabsch, W., Sander, C. & Sander, C. Dictionary of protein secondary structure: pattern recognition of hydrogen-bonded and geometrical features. *Biopolymers* **22,** 2577–2637 (1983).
38. Enkhbayar, P., Hikichi, K., Osaki, M., Kretsinger, R. H. & Matsushima, N. 310-helices in proteins are parahelices. *Proteins: Structure, Function, and Bioinformatics* **64,** 691–699 (2006).
39. Monticelli, L., Tieleman, D. P. & Colombo, G. Mechanism of Helix Nucleation and Propagation: Microscopic View from Microsecond Time Scale MD Simulations. *J. Phys. Chem. B* **109,** 20064–20067 (2005).
40. Lee, O.-S., Liu, Y. & Schatz, G. C. Molecular dynamics simulation of β-sheet formation in self-assembled peptide amphiphile fibers. *J Nanopart Res* **14,** 1–7 (2012).
41. Lee, O.-S., Cho, V. & Schatz, G. C. Modeling the Self-Assembly of Peptide Amphiphiles into Fibers Using Coarse-Grained Molecular Dynamics. *Nano Lett.* **12,** 4907–4913 (2012).
42. Fu, I. W., Markegard, C. B., Chu, B. K. & Nguyen, H. D. The Role of Electrostatics and Temperature on Morphological Transitions of Hydrogel Nanostructures Self-Assembled by Peptide Amphiphiles Via Molecular Dynamics Simulations. *Advanced Healthcare Materials* **2,** 1388–1400 (2013).
43. Fu, I. W., Markegard, C. B., Chu, B. K. & Nguyen, H. D. Role of Hydrophobicity on Self-Assembly by Peptide Amphiphiles via Molecular Dynamics Simulations. *Langmuir* **30,** 7745–7754 (2014).

CHAPTER 7 Sequence-Dependent Structural Stability of Self-Assembled Cylindrical Nanofibers by Peptide Amphiphiles

7.1 Abstract

Three-dimensional networks of nanofibers, which are formed through self-assembly of peptide amphiphiles, serve as a biomimetic hydrogel scaffold for tissue engineering. With an emphasis to improve hydrogel properties for cell-specific behavior, a better understanding between structural characteristics and physical properties of the macroscopic gel is sought. Large-scale molecular dynamics simulations were performed on two PA sequences with identical composition (palmitoyl-$V_3A_3E_3$ and palmitoyl-$A_3V_3E_3$) showing different self-assembly kinetic mechanisms. While both sequences yielded cylindrical nanofibers, these structures have contrasting internal arrangement with respect to the hydrophobic core; the former is continuous with predominately alkyl tails whereas the latter is disjointed with interconnecting micelles. Two additional sequences (palmitoyl-V_6E_3 and palmitoyl-A_6E_3) were examined to determine the effects of a homogenous β-sheet forming segment that is either strongly or mildly hydrophobic on self-assembly. Results from this study indicate that internal structural arrangement of nanofibers can provide a correlation with structural stability and mechanical behavior of hydrogel nanostructures.

7.2 Introduction

Design strategies for self-assembling amphiphilic peptides have embraced a modular approach that yields nanostructures with highly specific structural properties[1-3] and biofunctionalities.[4-6] As surfactant-like peptides, peptide amphiphiles (PA) are an

emerging class of biomaterials that are able to undergo spontaneous conformational transitions as a result of local environmental changes.[7-10] These molecules primarily encompass two fundamental elements to promote gelation and self-assembly: a relatively short hydrophilic peptide sequence that is attached to a synthetic hydrophobic group.[11-13] From this template, numerous variations have been made including the use of multiple hydrophobic fatty acid attachment,[14-16] modification of peptide sequence,[17,18] and incorporation of site-specific bioactive epitope[19-21] for a broad range of applications such as diagnostic medicine, controlled and targeted drug delivery, tissue engineering, and nanofabrication.[22-25] However, while it is known that certain desired characteristics are attributed to specific non-covalent interactions through structural modifications, rational design and systematic understanding remains incomplete.

The self-assembly of a network of fibrillar nanostructures from PA molecules has been shown to be a promising biomimetic hydrogel scaffold.[24,26] Individual fibrillar nanostructures are characterized by cylindrical nanofibers that exhibit β-sheet elements on the surface with a hydrophobic core.[2,11] Early design principles of PA molecules have primarily emphasized structural modifications to improve biocompatibility or to minimize immunogenic properties;[11,27] however, with the aims to use PA self-assembled nanostructures as a synthetic hydrogel scaffold that mimics extracellular matrix, consideration is also placed on the relationship between structural characteristics and mechanical behavior. For example, modifying the mechanical rigidity of hydrogels serving as extracellular matrix results in different cell adhesion and cell differentiation behaviors.[28-30] To incorporate this additional design parameter for PA molecules, experimental studies have found that the stiffness of the gel can be correlated with the

presence of secondary structure β-sheet elements, which is attributed to increased intermolecular hydrogen bonding and structural stability.[17,31] Similar trends have also been observed for amphiphilic peptide systems to relate secondary structure formation to mechanical strength and subsequent molecular arrangement properties.[20,32-37] Consequently, the ability to exert control and influence the morphological outcome of PA self-assembled nanostructures provides a platform to study in-depth the relationship between structural features and bulk material properties.

The particular choice and arrangement of hydrophobic residues have been shown to affect not only the supramolecular architecture[38,39] but also the corresponding gel stiffness.[40,41] For PA molecules that have a palmitic alkyl tail ($C_{16}H_{31}O$- or palmitoyl), sequence patterns have been designed to manipulate the hydrophobic-to-hydrophilic ratio to determine the impact on self-assembly behavior. Using a systematic approach and keeping the number of residues constant in the β-sheet forming region, Pashuck *et al.* designed three PA sequences, $V_4A_2E_3$, $V_3A_3E_3$, and $V_2A_4E_3$ to examine the effect of decreasing the number of strong β-sheet formers.[17] As the number of strong β-sheet formers is decreased, rheological measurement of the storage modulus shows a decreasing trend indicative of weaker gel formation. This effect corroborates with the lowered propensity to form intermolecular hydrogen bonds, which can contribute to minimizing the rigidity of the nanostructure. Similar decreases in gel stiffness are also observed when the total number of hydrophobic residues is reduced proportionally using $V_4A_4E_3$, $V_3A_3E_3$, and $V_2A_2E_3$. In the same study, Pashuck *et al.* examined the effect of strong β-sheet former placement with respect to the position of the alkyl tail.[17] For two PA sequences with identical composition, $V_3A_3E_3$ and $A_3V_3E_3$, placement of the strong β-sheet former, valine,

further away from the alkyl tail decreased the gel stiffness by a surprising one order-of-magnitude. Although both sequences formed characteristic nanofibril structure with comparable β-sheet formation, it was hypothesized that the difference in mechanical property was attributed to twistedness from misaligned and hyperextended hydrogen bonding. Although the aforementioned studies suggest that selective placement of individual residues can provide an additional strategy to influence self-assembly behavior, the weighted contribution from different non-covalent interactions (e.g., hydrophobic interaction, hydrogen bond, electrostatic repulsion) is difficult to evaluate, prompting for more studies to elucidate such effects at a molecular level.

In this article, we perform molecular dynamics simulations using our coarse-grained ePRIME model,[42] which permits spontaneous formation of hydrogen bonds and secondary structures. These simulations are truly large-scale on multiple systems that contain 800 PA molecules, which is at least 10 times larger than a typical simulation involving short peptides using other coarse-grained models.[43] By interchanging blocks of hydrophobic residues with one another with respect to the position of the palmitic alkyl tail, our studies showcases the subtle differences in the molecular arrangement to correlate with the experimental differences observed in mechanical properties. The sequences (**Table 7.1**) examined in this work, **PA1**: palmitoyl-$V_3A_3E_3$ and **PA2:** palmitoyl-$A_3V_3E_3$, are based on prior experimental work by Pashuck *et al*.[17] From our simulation studies, we found that the difference between the two sequences is attributed to the packing geometry as a result of the increased hydrophobic interaction between the peptide sequence and the alkyl tail. The core of the nanofibril structure is found to be less continuous when the strong hydrophobic block (valine) is placed further away from the alkyl tail. Two additional

sequences, **PA3:** palmitoyl-V_6E_3 and **PA4:** palmitoyl-A_6E_3 (**Table 7.1**) were also examined to determine the effects of using a homogenous β-sheet forming segment that is either strongly or mildly hydrophobic. From these four PA sequence variants and their influence on the corresponding self-assembly behavior, a better understanding can be gained regarding the role of the β-sheet forming region. We aim to provide further insight and intuition to customize sequences with desired structure and functionality. Having previously examined the effects of pH-dependent electrostatics[10,42] and solvent-dependent hydrophobicity[44,45] on the formation of hydrogel nanostructures, this study of sequence effects adds a more comprehensive understanding of PA self-assembly.

7.3 Methods

Two short peptide amphiphile (PA) sequences (**Table 7.1**) represented as **PA1**: palmitoyl-$V_3A_3E_3$ and **PA2:** palmitoyl-$A_3V_3E_3$, are examined in which the chemical identity and composition remains identical with the exception of the sequence pattern arrangement within the β-sheet forming segment. These two sequences was chosen based on previous experimental work by Pashuck *et al*.[17] Two additional sequences, **PA3:** palmitoyl-V_6E_3 and **PA4:** palmitoyl-A_6E_3, are considered to determine the effects of using a homogenous β-sheet forming segment by extending the length of a single hydrophobic residue that is either strongly or mildly hydrophobic. Each PA molecule is represented using a coarse-grained model ePRIME,[42] an extension of the Protein Intermediate Resolution Model (PRIME),[46-48] that accounts for all twenty naturally occurring amino acids. For the peptide residues, three spheres are used to represent the backbone atoms: amide, α carbon, and carbonyl groups (NH, $C_\alpha H$, and CO, respectively). The corresponding amino acid sidechains is either represented with either one or two spheres based on the length of the side chain

based on the scheme originally developed by Wallqvist and Ullner.[49] The size of a sidechain sphere is derived from the solvent accessible area experimentally determined by Wesson and Eisenberg.[50] For the hydrophobic palmitoyl tail, each CH_2 group is represented as a single sphere whose bond distance and fluctuation are extracted from available atomistic parameters.[42]

For the system of interest, an implicit solvent model is implemented to reduce the system's size to allow for tractable simulations in order to capture the spontaneous self-assembly process. The solvent effect is incorporated into the effective residue-residue potential based on the hydrophobic character of the corresponding peptide residue or alkyl group. Representation of this behavior is either through a square-well or square-shoulder potential that approximates an attractive or repulsive continuous potential, respectively. For example, square-well potential is used for attractive interactions between hydrophobic side chains and/or polymeric segments, whereas square-shoulder potential is used for repulsive interactions between hydrophilic side chains or polymeric segments. The strength of the interaction between two groups is $\varepsilon_{HP} = R(\Delta G_i + \Delta G_j)$[50,51], where ΔG is the free energy of transferring each group from water to octanol, and R is a measure of the strength of the hydrophobic interaction. In this study, the value for R, which is interpreted as the degree of hydrophobicity between nonpolar groups and is governed by the particular solvent choice, is kept constant at $R = 1/3$ based on prior work in our group that has established this reference condition for the formation of prototypical cylindrical nanofibers.[42,44,52]

Hydrogen bonding is represented by a directionally dependent square-well attraction of strength ε_{HB} = 12 kJ/mol between NH and CO united atoms. Electrostatic

interactions, which are treated at the level of Debye–Huckel theory, are implemented using three-step attractive square-well or repulsive shoulder-well potentials with a 12-Å cutoff. In this study, the strength of an electrostatic repulsion between two charges on the glutamic acids, ε_{ES}, is the same as that of the hydrogen bond, ε_{HB}, as it is the optimal condition where cylindrical nanofibers were observed in our previous study.[42]

In conjunction with the coarse-grained representation of the system, discontinuous molecular dynamics (DMD) is utilized to enable simulations of large system sizes and extended time scales. As an alternative to standard molecular dynamics, DMD models bonded and nonbonded interactions through discontinuous potentials, e.g., hard- sphere and square-well potentials. Unlike soft potentials, such as the Lennard–Jones potential, discontinuous potentials exert forces only when particles collide, enabling the exact (as opposed to numerical) solution of the collision dynamics. DMD simulations proceed by locating the next collision, advancing the system to that collision, and then calculating the collision dynamics. By reducing the interaction details that is needed by being an event-driven process as opposed to time-driven process, this type of simulation allows for greater time scales on large systems. Simulations are performed in the canonical ensemble (NVT) with periodic boundary conditions imposed to eliminate artifacts due to box walls. Constant temperature is achieved by implementing the Andersen thermostat method.[53] In this case, all beads are subjected to random, infrequent collisions with ghost particles whose velocities are chosen randomly from a Maxwell Boltzmann distribution centered at the system temperature. Simulation temperature is expressed in terms of the reduced temperature, $T^* = k_BT/\varepsilon_{HB}$, where k_B is Boltzmann's constant and T is the temperature. Reduced time is defined to be $t^* = t/\sigma(k_BT/ m)^{1/2}$, where t is the simulation time and σ and

m are the average bead diameter and mass, respectively. While the use of reduced quantities *in silico* poses difficulty in achieving an experimental analogue, qualitative correlations can be extracted. From earlier work examining single- molecule behavior using both atomistic and coarse-grained models,[42,54] a qualitative frame of reference can be identified correlating the melting temperature of T* = 0.085T to 320 K.

The initial configuration of each simulation contains 800 PA molecules (44 000 particles) in a cubic box whose dimension is 250 Å. This initial configuration was randomized to remove any bias conformation by heating the system at a high temperature (T* = 5.0) for a short amount of time (<1% of production run) to mimic experimental conditions. Afterward, the system was quickly quenched to T* = 0.11, which is the final temperature for the production run for around 200 time units until reaching equilibrium. The criteria for equilibrium is that each simulation was conducted for a long period of time until the ensemble averages of the system's total potential energy varied by no more than 2.5% during the last three-quarters of each simulation run. The sudden change in temperature should have negligible effects on the system properties, as the randomization is used only for the purpose of removing any computational bias due to the technique of populating the system with PA molecules. From our previous study on the effects of temperature,[42] we found that below and at the melting point of T* = 0.085 PAs formed kinetically trapped aggregates that are amorphous. At higher temperatures, T* = 0.10–0.11, cylindrical nanofibers can be formed when R = 1/3. Similarly, Lee *et al.*[55] conducted their simulations observing the formation of nanofibers at 330 K, which is slightly higher than the melting point. In this study, the temperature is constant at T* = 0.11.

Quantitative analysis in this paper is performed on the data collected during the production period. Average properties at equilibrium are computed from the last 10% of simulation data with error bars taken from the standard deviation of at least 5 independent simulations for **PA1** and **PA2**, and at least 2 independent simulations for **PA3** and **PA4**. Multiple independent simulations were performed considering the stochastic nature of self-assembly; however, results indicate variability in the data is relatively minimal. Calculation of the secondary structure present in the system is through the implementation of STRIDE,[56] with primary focus on α-helix, β-strand/sheet, and random coil that also contains turn structures. To identify an aggregate formed during the trajectory of the simulation, individual PA molecules of a cluster must form at least two interpeptide hydrogen bonds or four hydrophobic interactions with a neighboring PA molecule in the same group.[47] This criterion ensures that an aggregate is defined by at least two or more PA molecules to form enough stable interactions.

Calculation of the PA molecule's velocity is reported based on the 13 individual regions of the molecule itself. The 16-hydrocarbon alkyl tail is parsed into 4 equal regions with the remaining 9 regions corresponding to each of the peptide residue. The velocity was calculated for the entire 800-PA molecule system and averaged over the independent simulations. Lindemann criterion was calculated as a function of the z-direction for a representative aggregate identified in the 800-PA molecule system. A total of 25 regions were chosen along the fiber axis of the nanostructure to compute the Lindemann criterion to obtain information in localized regions. The evaluation of the Lindemann criterion is determined by using equation 1.

$$\Delta_L = \frac{\sqrt{\sum_i (\boldsymbol{r_i} - \langle \boldsymbol{r_i} \rangle)^2 / N}}{a'} \quad (1)$$

The total number of atoms is represented by N and a' is the most probable non-bonded near neighbor distance, $\mathbf{r_i}$ is the position of atom *i*, and $\langle \boldsymbol{r_i} \rangle$ denotes configurational average. The value of 4.5 is used for *a'* and is obtained from established simulation work that determined that this parameter is relatively independent of temperature and different proteins.[57] Determination of the Lindemann criterion provides a basis as to whether systems exhibit either solid-like or liquid-like properties. From previous simulation data, solid-like behavior is observed at $\Delta_L < 0.14$, and liquid-like characteristics is observed at $\Delta_L > 0.14$.[57] Although the range of values calculated from our studies is within solid-like behavior, our interpretation of the data is based on the relative values considering that the parameter is dependent on the total number of atoms, which may affect the actual magnitude.

7.4 Results and Discussion

Table 7.1. Four PA sequence variants are investigated. The color scheme shown is to highlight distinct amino acid residues for easier differentiation.

PA molecule	Sequence alkyl tail - β-sheet region - charged region
PA 1	$C_{16}H_{31}O$-VVVAAA-EEE
PA 2	$C_{16}H_{31}O$-AAAVVV-EEE
PA 3	$C_{16}H_{31}O$-VVVVVV-EEE
PA 4	$C_{16}H_{31}O$-AAAAAA-EEE

The chemical sequence of the four PA molecules is shown in **Table 7.1** with three distinct regions: a hydrophobic palmitic alkyl tail, six-residue β-sheet forming region of

valines and/or alanines, and a negatively charged group of three glutamic acids. **PA1** and **PA2** have identical chemical composition but different position of the hydrophobic residues, valine and alanine, in the β-sheet forming region. **PA3** and **PA4** are complementary sequences designed to examine the effects of using a homogenous β-sheet forming segment that is either strongly or mildly hydrophobic. For the purpose of this paper, **PA1** and **PA2** will be primarily discussed in more details than **PA3** and **PA4** whose additional data and analysis are presented as Supplementary Information.

Our coarse-grained ePRIME model has been previously validated for use in self-assembly study on **PA1**.[42] We performed replica-exchange simulations using both atomistic CHARMM 27 force field[58-60] and ePRIME models to examine the effect of temperature on the folding process of a single **PA1** molecule. Equilibrium results showed that our coarse-grained or all-atom models produce similar conformations over a wide range of temperatures.[42] For this paper, we have performed an additional validation study on **PA2** obtaining high agreement between ePRIME and CHARMM results on not only the secondary structure formed by the peptide segment as a function of temperature but also the interactions between the alkyl tail and the peptide segment (**Figure 7.7**).

In addition, we have performed a more detailed study previously on peptide folding by **PA1** and **PA2** using the atomistic CHARMM model.[58-60] The alkyl tail was observed to play two opposing roles in modulating sequence-dependent folding kinetics and thermodynamics. On one hand, it restricts conformational freedom reducing the entropic cost of folding, which is thus promoted. On the other hand, it acts as an interaction site with nonpolar peptide residues, blocking the peptide from helix nucleation, which reduces folding. It was identified that the first critical event of folding kinetics requires creating a

3_{10}-helical turn, which involves alanine residues and later switches into a α-helical turn. PA2 alanines experience 1.4 times as many van der Waals interactions with the alkyl tail compared to PA1 alanines since they are closer to the alkyl tail. The high frequency of tail-peptide interactions prevents the peptide from folding in PA2 relative to PA1. When the alkyl tail was truncated to four immobile carbon groups, disruptive hydrophobic interactions are reduced to enable higher rates of folding.

7.4.1 Switching placement of hydrophobic peptide residue blocks yield nanostructures with contrasting structural arrangements

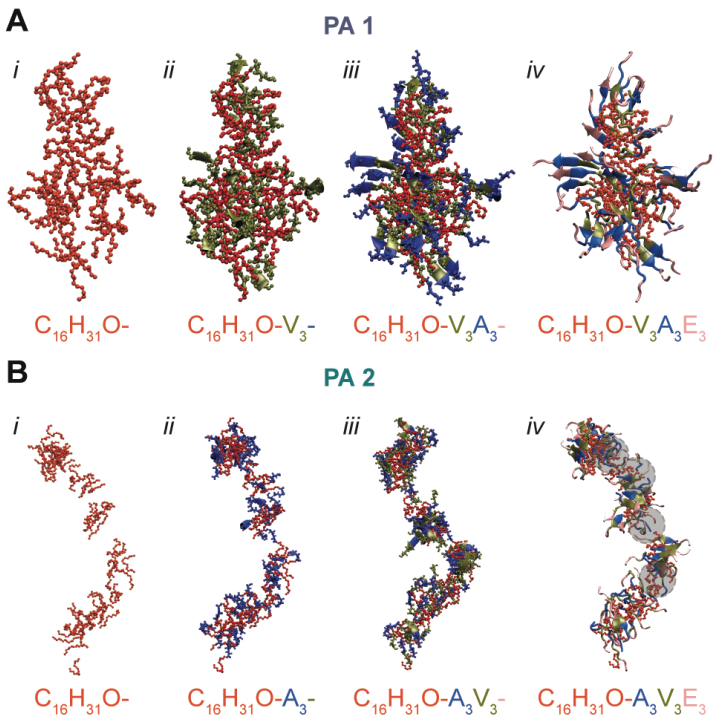

Figure 7.1. Representative equilibrium structure of cylindrical nanofibers showcasing (i) only the alkyl tails, (ii) plus the next three residues, (iii) plus another three residues, and (iv) the whole sequence of (A) PA1 and (B) PA2. Color scheme using VMD[61]: alkyl tail (red), valine (green), alanine (blue), and glutamic acid (pink).

Starting from initial configurations containing 800 PA molecules in random coil conformations at a moderate temperature of T* = 0.11, spontaneous self-assembly occurs

resulting in the formation of nanofiber structures with an elongated, high-aspect ratio geometric profile by both sequences **PA1** and **PA2**. Representative equilibrium self-assembled structures of **PA1** and **PA2** are shown in **Figure 7.1A** and **6.1B**, respectively. Both structures are comprised primarily of hydrophobic alkyl tails shielded by charged peptide segments. Formation of β-sheet secondary structure is evident along the surface of each nanostructure. However, upon detailed inspection, the internal spatial arrangement of these two structural analogues with identical chemical composition is noticeably different. By visually isolating the alky tails, the local organization of the collected assembly is highlighted to showcase that the interior hydrophobic core of PA1 cylindrical nanofiber is contiguous **(Figure 7.1Ai).** In contrast, the interior hydrophobic core of PA2 cylindrical nanofiber has multiple discontinuous junctions **(Figure 7.1Bi)**.

For **PA1**, a contiguous inner hydrophobic core comprises predominantly of alkyl tails are arranged in a compact form to maximize alkyl-alkyl interactions. In addition, adjacent hydrophobic residues, valine residues, are intertwined with the alkyl tails to strengthen the hydrophobic interactions (**Figure 7.1Aii** and **Figure 7.1Aiii**). This can be seen by the relatively high number of intermolecular hydrophobic interactions between the alkyl tail on each PA molecule and the first three peptide residues (i.e., valines for **PA1**) on nearby PA molecules as shown in **Figure 7.2A**.

In contrast, **PA2** cylindrical nanofiber contain multiple micelles that are interconnected at discontinuous junctions **(Figure 7.1B)**. The inner hydrophobic core of each micelle is comprised of only alkyl tails without pulling the first three peptide residues (i.e., mildly hydrophobic alanines for **PA2**) into the interior. This results in the relatively low number of intermolecular hydrophobic interactions between the alkyl tail on each PA

molecule and alanines on nearby PA molecules as shown in **Figure 7.2A.** Moreover, about 15% molecules in **PA2** cylindrical nanofibers adopt an opposite orientation in which the charged segment is located within the inner core to form hydrophobic interactions between valine residues with other alkyl tails in the interior. In this case, the alkyl tails of these inverted molecules form hydrophobic interactions with alanine and valine residues on other molecules to connect multiple micelles at discontinuous junctions. Furthermore, alanine and valine residues form hydrogen bonds between micelles as shown in **Figure 7.1Bii** and **6.1Biii**. Therefore, multiple micelles are held together by a combination of hydrophobic interactions between nonpolar peptide residues and additional hydrogen bonds by those residues.

The large number of interactions between the alkyl tail and adjacent valine residues works together in **PA1** to condense and bind together creating a hydrophobic core that is not only composed of the alkyl tails but also strongly hydrophobic valine residues (**Figure 7.2B**). Since the strong hydrophobic residue group, valines, is placed farther away from the alkyl tail in **PA2**, alkyl tails form only a few intermolecular hydrophobic interactions with weakly hydrophobic alanine residues (**Figure 7.2A**). Therefore, the hydrophobic core is less compact since each alkyl tail would have to twist and extend itself to form interactions with valine residues (**Figure 7.2C**). By having a more porous hydrophobic core, the ability to form β-sheets diminishes since the peptide residues are no longer within optimal distance to promote intermolecular hydrogen bonding while minimizing charge-charge repulsion. This can be attributed to the observed difference in the macroscopic gel stiffness as discussed in subsequent sections.

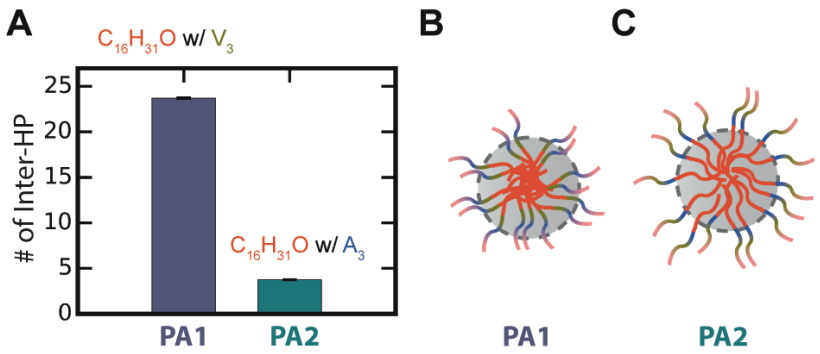

Figure 7.2. (A) Average number of intermolecular hydrophobic interactions between the alkyl tail of each PA molecule and the first three residues adjacent to the alkyl tail of a neighboring PA molecule within the interior of cylindrical nanofibers in PA1 and PA2 systems. Schematic diagram showing a cross-sectional view of typical cylindrical nanofibers (perpendicular to the elongated direction) illustrating the data shown in (A) for (B) PA1 and (C) PA2.

7.4.2 Sequence-dependent structural difference is caused by dynamic assembly mechanisms

Through a series of micelle merging events, spontaneous self-assembly of PA molecules into a cylindrical nanofiber are shown in **Figure 7.3** for **PA1** and **PA2**. For **PA1**, initial clusters of PA molecules adopt a spherical micelle configuration (**Figures 6.3A**) such that the charged glutamic acid residues are distributed uniformly to minimize electrostatic repulsions. The inner core is comprised of alkyl tails that are sequestered away from the surface. Upon the formation of intermolecular hydrogen bonds by the hydrophobic valine and alanine residues, the peptide segments on the surface of each micelle undergo an ordering process by forming multiple separate β-sheets. As a result, the hydrophobic core is exposed to the surface or solvent, which promotes merging with nearby micelles to grow into a cylindrical nanostructure. A schematic diagram in **Figure 7.3B** is shown to generalize a self-assembly kinetic mechanism for **PA1** from multiple simulations. The assembly mechanism can be interpreted from the plot shown in **Figure 7.3C** in which the average number of PAs increases in a stepwise process whereas the total number of

aggregates decreases in a reciprocating fashion. At each merging step, structural reorganization occurs allowing for maximizing the number of hydrophobic interactions within the core along the length of each elongated nanostructure, which grows into a longer nanofiber by adding more micelles at its two ends. Lateral growth of the nanofibril structure is limited due to the majority of charged glutamic acid segments residing on the side surface compared to its ends. Several key characteristics of the final structure (**Figure 7.3A)** are identified: alkyl tails with a large degree of entanglement are predominantly residing in the interior of the nanofiber, β-sheet forming perpendicular to the elongated core, and charged segments are scattered on the surface.

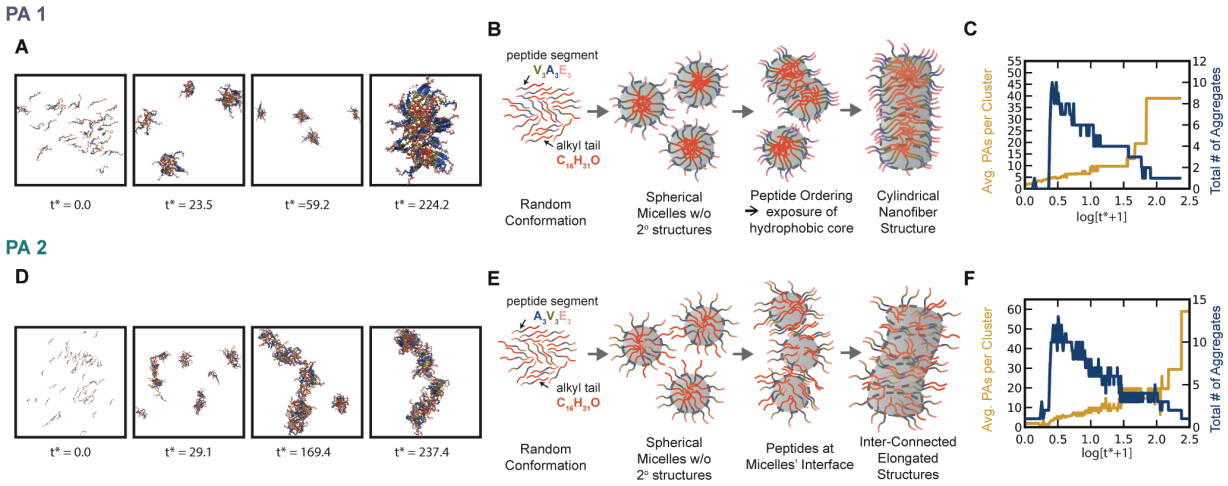

Figure 7.3. For PA1: (A) Snapshots showing dynamic self-assembly process at different times starting from random configurations; (B) Schematic diagram generalizing a self-assembly kinetic mechanism for PA1 from multiple simulations; (C) Time-dependent data are plotted on a logarithmic scale for the average number of PA molecules per aggregate and total number of aggregates. Similarly for PA2: (D) Snapshots; (E) Schematic diagram; and (F) Quantitative data.

The early stage of **PA2** self-assembly process is similar to that of **PA1** self-assembly (**Figure 7.3D** and **Figure 7.3E)**. Starting from isolated molecules, **PA2** molecules quickly condense into small aggregates driven by hydrophobic collapse. As these small aggregates

reach a size that is limited by the number of charged groups, subsequent steps for **PA2** aggregates to increase in size diverge from the already described **PA1** mechanism. In addition to micelle merging events that occur through the exposure of the hydrophobic core due to β-sheet formation, hydrophobic interactions between non-polar groups on the surface of different micelles become more prominent. Since the strongly hydrophobic residue group of valine residues is placed farther away from the alkyl tail, the hydrophobic core of each micelle becomes less compact considering that the alkyl tail would have to twist and extend itself to form interactions with valine. Consequently, the inner core of each micelle adopts a different structural arrangement in which a few **PA2** molecules position in an opposite orientation with the charged segment located within the inner core while their alkyl tails are exposed to the surface. This allows connection between two nearby micelles by forming not only by hydrophobic alkyl-alkyl interaction but also by hydrophobic alkyl – side chain interaction and side chain – side chain interaction in addition to hydrogen bonds. This suggests that **PA2**'s discontinuous structure is seemingly held together through a combination of intermolecular hydrogen bonds and hydrophobic interactions at the interface of multiple smaller aggregates (**Figure 7.3E**). Subsequently, structural reorganization is less favored as indicated by absence of large plateaus in the plot of assembly kintiecs (**Figure 7.3F)**.

7.4.3 Molecular arrangement of the local environment influences the internal dynamics of the nanostructure

Calculation of the amount of β-sheets (**Figure 7.4A**) shows that both **PA1** and **PA2** cylindrical nanofibers exhibit significantly large β-sheet formation at 24-30%, which is comparable to experimental results by Niece *et al.*,[12] who found the β-sheet population of

similar PAs at ~25 ± 20%. Moreover, **PA1** has a slightly higher propensity to form β-sheets than **PA2** (**Figure 7.4A**). The significance of **PA2** having a weaker propensity to form β-sheet compared to **PA1** may suggest a correlation to the one order of magnitude difference in bulk material properties as observed by Pashuck *et al*.[17] This has also been seen by other investigators who found the formation of rod-like nanostructures is associated with the presence of hydrophobic residues with a strong propensity to form β-sheet structure; in addition, high amount of β-sheets correlates with stiffer hydrogel properties.[12,31,62]

However, the experimental study by Pashuck *et al*.[17] suggested that the β-sheet misalignment or twisting, instead of the amount of β-sheets, plays an important role in influencing the stiffness of the gel. In this case, each cylindrical nanofiber structure was assumed to contain multiple large β-sheets that are infinitely long, running continuously along the fiber axis. But prior experimental studies with similar PAs have quantified the amount of β-sheets to be approximately ~25 ± 20%,[12] which is in agreement with a modeling simulation study using atomistic models by Lee *et al*. who found the presence of sparsely distributed small β-sheets along the surface.[63] Nevertheless, we attempted to determine the degree of β-sheet twistedness by calculating the angles between one hydrogen bond to other hydrogen bonds within each β-sheet using PyMOL.[64] We found no significant difference of such angle distributions by β-sheets between **PA1** and **PA2** nanofibers (**Figure 7.8**). Perhaps the slightly lower β-sheet formation for **PA2** than **PA1** might be a potential factor for the experimental observation of a tremendous difference in mechanical property between **PA1** and **PA2**. Based on the structures shown, **PA2** is unable to maximize the formation of intermolecular hydrogen bonds due to the presence of 15%

PA molecules in an inverted orientation. Considering the increased propensity for peptide residues to form hydrophobic interactions at discontinuous junctions, the ability to form secondary structures is thereby inhibited. These factors not only result in a reduced amount of β-sheet structure, but also lead to a discontinuous hydrophobic core. Consequently, it is believed that the amount of β-sheets and the structural integrity of the hydrophobic core influence the mechanical property of the self-assembled nanofiber structure. To compare with this experimental speculation, we measured individual peptide residues likelihood to form β-sheet elements and this is shown in **Figure 7.4B**. For **PA1**, residues 3-6 (-VAAA-) are shown to have a higher propensity to form β-sheets as compared to **PA2** for the residues in the same position (-AVVV-). This suggests that the ability for β-sheets for **PA2** is inhibited or unfavorable and could be related to the placement of the hydrophobic residues with respect to the alkyl tail.

In an attempt to provide a more quantitative and concrete correlation between the subtle difference between the arrangement of the inner core of **PA1** and **PA2** and their structural stability, we also calculated the Lindemann criterion. The dimensionless parameter can be interpreted as a value to represent the geometric packing or porosity of a structure. If the Lindemann value is large, it represents that the structure exhibits more liquid-like properties whereas if the number is small, it exhibits more solid-like dynamics. From a previous simulation study, solid-like behavior is observed at $\Delta_L < 0.14$, and liquid-like characteristics is observed at $\Delta_L > 0.14$.[57] Although the range of Lindemann values calculated from our studies is within solid-like behavior, our interpretation of the data is based on the relative values considering that the parameter is dependent on the total number of atoms, which varies from one position to another and thereby may affect the

actual magnitude. In **Figure 7.4C**, the Lindemann values are plotted as a function of position along the fiber axis (or elongated dimension) of a representative nanostructure of **PA1** and **PA2**. Since the end groups are more flexible, comparison should be made between the two sequences at the central part of the nanostructures. In this case, a noticeable difference exists in the Lindemann values of **PA1** and **PA2**. Unlike **PA1** in which the structure shows increasingly more solid-like dynamics towards the core the structure, **PA2** shows an inverse trend: the core exhibit more liquid-like dynamics. This suggests that **PA1** structure becomes more condense and tighter corroborating with previous speculation due to the added hydrophobic interactions between the entangled alky tails and alkyl tail – valine interaction. Moreover, **PA2** experiences several large spikes that correlate with discontinuities observed along the inner hydrophobic core of a more porous structure.

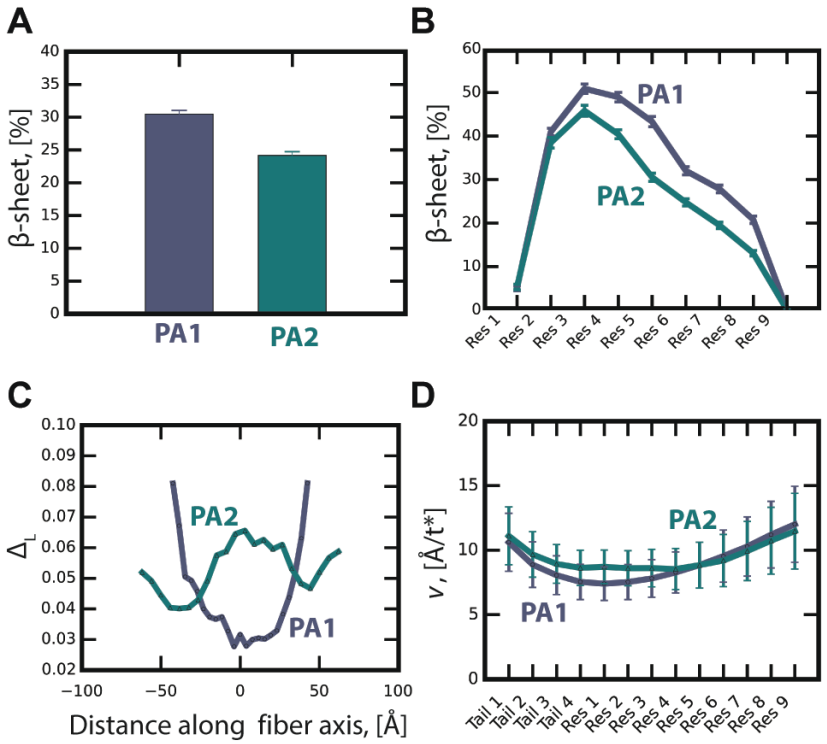

Figure 7.4. For both PA1 and PA2 cylindrical nanofibers at equilibrium: (A) Average amount of β-sheets. (B) The β-sheet propensity is plotted as a function of the peptide residue. (C) The Lindemann value at different

points along the fiber axis. (D) Average velocity of individual regions of each molecule. The first 4 regions correspond to the alkyl tail and remaining 9 regions correspond to 9 peptide residues.

To gain further insight and to account for the experimentally observed drastic difference in gel stiffness, dynamics of individual molecules of the collective assemblies are monitored. For **PA1** and **PA2**, each molecule is subdivided into a total of 13 sections with the first 4 sections representing four quarters of the alkyl tail and the remaining 9 sections corresponding to each amino acid. For each of the aggregates in the system, the velocity was calculated for each section as shown in **Figure 7.4D**. The local molecular motion is largest at the ends of the alkyl tail (Tail 1-2) and at the negatively charged glutamic residues (Res 7-9) for both **PA1** and **PA2**. The increased molecular motion of the glutamic acid residues can be attributed to the added flexibility as a result of their peripheral location on the surface. While the ends of the alkyl tails are buried within and shielded from the aqueous medium, they exhibit increased molecular motion due to their nature of hydrophobic interactions, which are isotropic and thus easily broken up and reformed constantly. This allows them to move around without overcoming any energetic barrier. In contrast, a slight decrease in the calculated velocity is observed at positions Tail 3-4 and Residue 1-3, indicating that these groups of molecules are more restricted and experience less movement due to their non-isotropic interactions (i.e., hydrogen bonding) by the β-sheet-forming peptide residues. The aforementioned trends in the velocity are comparable to experimental findings by Ortony *et al*. using electron paramagnetic resonance spectroscopy to probe the internal dynamics of a nanofiber structure.[65] On one hand, solid-like dynamics were observed at the middle peptide region due to the significant amount of β-sheet formation that imposes structural order through directional dependent hydrogen bonding. On the other hand, fluid-like dynamics were observed at the surface and the core

where alkyl tails exist. Faster dynamics at the periphery near the charged residues due to the reduced amount of hydrogen bonds, which decreases the rigidity of the architecture. Increased motion at the core is attributed to the flexibility of the end segment of the alkyl tails and their location that is a large distance away from the peptide residues.

7.4.4 Dissociative properties of assembled aggregates suggest a correlation between structural stability and mechanical property

Assembled nanostructures that are strongly held together are expected to maintain their structural stability by resisting morphological changes even at high temperatures. Therefore, successive constant temperature simulations at increasing temperature were performed to investigate if the structural differences between PA1 and PA2 have any direct influence on the mechanical properties of the collective assembly. Starting at the moderate temperature of T* = 0.11, each system was subjected a temperature increase by an increment of T* = 0.01 for about 30 reduced time units until the final temperature of T* = 0.15 was reached. The time interval was chosen to provide a reasonable amount of time for the system to reach an equilibrated state before raising the temperature again. As seen in **Figure 7.5A** and **6.5B**, the same structures from earlier PA1 and PA2 analysis is selected for continuity. In **Figure 7.5A,** snapshots of the equilibrated structure for **PA1** at the end of each heating interval is shown. For the selected structure, its ability to retain its structural framework over the course of the successive heating stages is noteworthy. Up to T*=0.14, the structure seems to stretch out due to the added kinetic energy such that the hydrophobic core becomes less entangled and more relaxed. Gradually, more hydrogen bonds are broken resulting in the dissociation of β-sheets as temperature increases;

therefore, peptide segments switch from β-strand to random-coil conformation. However, the structure remains as an elongated micelle since the alkyl tails can still maintain their hydrophobic interactions. When the temperature is finally reached at T* = 0.15, the structure is observed to undergo dissociation into smaller aggregates.

Unlike the nanostructure for **PA1**, the **PA2** nanostructure is more susceptible to dissociation even when the temperature is only slightly increased. From the snapshots shown in **Figure 7.5B**, at T*=0.12 the cylindrical nanofiber quickly dissociates into clusters that break into smaller aggregates. When the temperature reaches T* = 0.15, the nanostructure has fully disintegrated into isolated random molecules. By plotting the average PAs per cluster as shown in **Figure 7.5C**, the aforementioned process for **PA1** and **PA2** can be differentiated by the rate at which the average number of PAs decreases over time. Throughout the heating process, **PA1** structure is relatively stable without losing its structure until an extremely high temperature is reached. In contrast, the plot for **PA2** shows sharp decreases indicating the structure is rapidly dissociating. The total number of aggregates is also monitored (**Figure 7.5D**) as a function of time and supports previous findings by mirroring the data shown in **Figure 7.5C**. As the temperature increases, the rate at which the total number of aggregates increases is much faster than **PA1**. These results confirm our finding based on the Lindemann criterion that structural stability of **PA1** nanofibers is higher than that of the **PA2** counterpart.

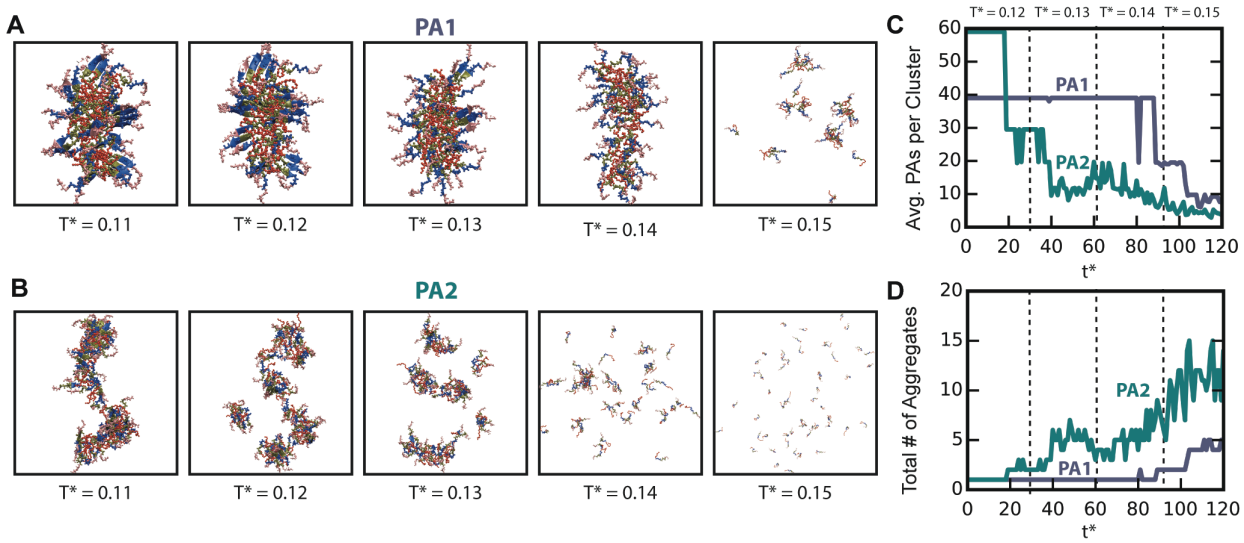

Figure 7.5. Snapshots of the equilibrated structure at the end of each temperature (T*=0.12 – 0.15) during the heating process for (A) PA1 and (B) PA2 starting from cylindrical nanofiber structures assembled at T*=0.11. (C) Plot of the average number of PA molecules per cluster as a function of time for PA1 and PA2. (D) Plot of the total number of aggregates as a function of time for PA1 and PA2. For (C) and (D), heating intervals and heating temperatures are indicated by the dashed lines.

7.4.5 Composition and residue order of PA sequence affect PA self-assembly and structural stability

In addition to examining positional influence on the self-assembly behavior of PA molecules, the effect of increasing the length of a single peptide residue that is either strongly or mildly hydrophobic to yield a homogenous β-sheet forming segment was also studied for a more comprehensive understanding. **PA3** and **PA4** contain the same number of residues as **PA1** and **PA2**; however, instead of having two different residues in the β-sheet forming region, the β-sheet forming segment has been replaced to contain only either valine or alanine residues. **PA3** assembly results in the formation of cylindrical nanofibers. From **Figure 7.6A** and **Figure 7.9A**, the equilibrated structure for **PA3** resembles **PA1** in adopting an elongated shape with a continuous hydrophobic core comprise of alkyl tails. While valine residues are known for high propensity for β-sheet formation,[66] the percentage of β-sheets of **PA3** is 8% lower than that that of **PA1 (Figure 7.10A-B)**. As observed from its structure (**Figure 7.6A** and **Figure 7.9A)**, the increased

hydrophobic interaction between the alkyl tail and the valine side chain takes precedence over the likelihood to form hydrogen bonds since valine residues are strongly hydrophobic. Consequently, the structure is observed to be more compact with the valine residues being withdrawn into the hydrophobic core.

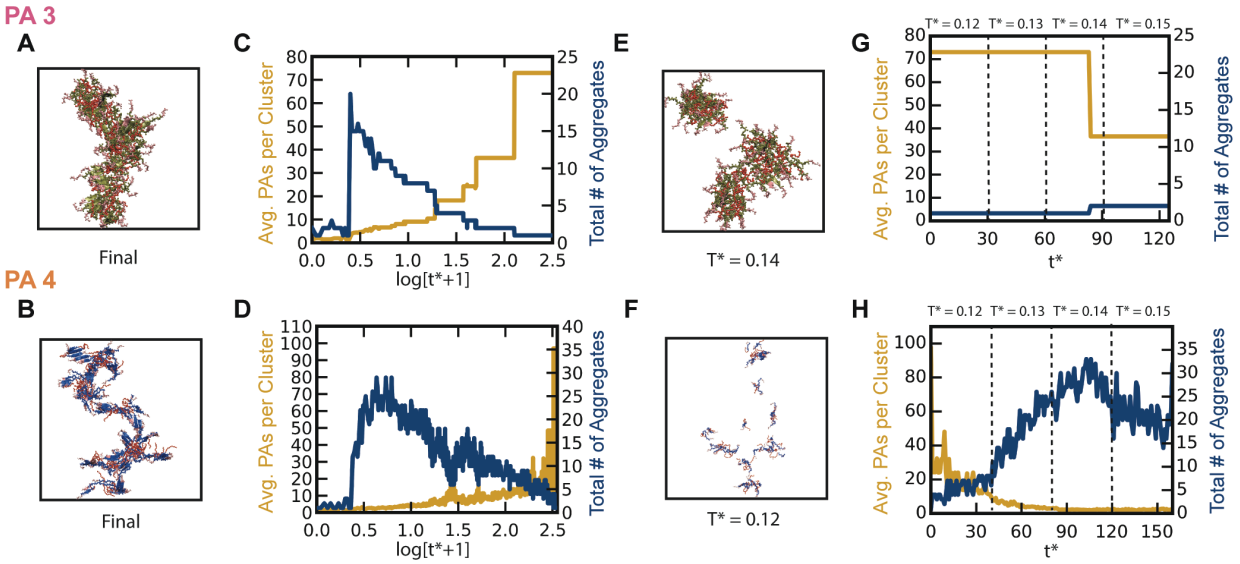

Figure 7.6. Snapshot of the equilibrated structure for (A) PA3 and (B) PA4 cylindrical nanofibers. Assembly kinetics with respect to the average number of PAs per cluster and total number of aggregates is plotted as a function of time for (C) PA3 and (D) PA4. Snapshot of (E) PA3 and (F) PA4 nanostructure at the temperature at which the structure starts to dissociate. Dissociation kinetics with respect to the average number of PAs per cluster and total number of aggregates is plotted as a function of time for (G) PA3 and (H) PA4 during the heating process. The heating intervals and temperature are indicated by dashed lines.

When the β-sheet forming region is only of alanine residues for **PA4**, the self-assembled nanostructure resembles **PA2** cylindrical structure with the exception of added junctions and more discontinuities along the inner core (**Figure 7.6B** and **Figure 7.9B)**. Since alanine is known as weakly hydrophobic, the hydrophobic core is even less compact than that of PA2 cylindrical nanofibers since the alkyl tail form less hydrophobic interactions with alanine residues. Consequently, alanine residues are not withdrawn into the hydrophobic core. Instead they form the most amount of hydrogen bonds and thus β-sheets **(Figure 7.10A-B)** over the other three sequences as expected.[66] Moreover, the

increased propensity for intermolecular hydrogen bonds for **PA4** facilitate aggregate growth through added intermolecular hydrogen bonds creating more branched or disjointed junctions between micelles.

The assembly kinetics of **PA3** and **PA4** are shown in **Figure 7.6C** and **6.6D**, respectively; details of the entire assembly mechanism are shown in **Figure 7.11**. The self-assembly mechanism of PA3 is similar to that of **PA1** while the self-assembly mechanism of PA4 is similar to that of **PA2.**

Upon performing a heated simulation these two systems, mechanical features can also be extrapolated based on their dissociation mechanism (**Figure 7.12**). **Figure 7.6E** and **6.6F** show snapshots of **PA3** and **PA4** nanostructures at the temperatures where they start to disintegrate. Unlike **PA4** that immediately starts to dissociate into small clusters and individual molecules at T*=0.12, **PA3** nanostructure is much more robust and does not dissociate until higher temperatures of T*=0.14 (**Figure 7.12**). As shown in **Figure 7.6G**, **PA3** structure is considerably stable throughout the heating simulation. The stability is most likely attributed to the added hydrophobic interactions due to the presence of only valine residues that strengthen the core and outweighing the charge-charge repulsion from the glutamic acid residues. However, **PA4** is observed to be much more dynamic with the total number of aggregates quickly increasing indicative of the formation of small clusters (**Figure 7.6H**). Since disjointed micelles are weakly interconnected at multiple junctions, **PA4** nanostructure is more susceptible to disruptions by a slight temperature increase. Indeed, **PA4** nanostructures exhibit the most liquid-like dynamics while **PA3** nanostructures exhibit the most solid-like dynamics even when being compared with **PA1**

and **PA2** nanostructures based on the Lindemann parameter (**Figure 7.13A**) and motion velocity (**Figure 7.13B**).

7.5 Conclusions

By simply interchanging the position of two blocks of hydrophobic residues (**PA1**: palmitoyl-$V_3A_3E_3$ and **PA2:** palmitoyl-$A_3V_3E_3$) within the β-sheet forming region of a model PA molecule, rod-like structures with distinctive internal structural arrangements were self-assembled. Characteristics of a prototypical cylindrical nanofiber structure of **PA1** is identified by the ability of the alkyl tails to pull the valine residues into the interior of the nanostructure to promote intermolecular hydrophobic interactions between the alkyl tail of a PA molecule with the first three peptide residues (i.e., valines) on nearby PA molecules. The hydrophobic core of **PA1** cylindrical nanofibers is therefore dense and contiguous containing not only the alkyl tails but also of valine residues. In contrast, the alkyl tails of **PA2** molecules form significantly less intermolecular hydrophobic interactions between the alkyl tail of a PA molecule and the first three peptide residues (i.e., weakly hydrophobic alanines) of nearby PA molecules. Therefore, the hydrophobic core of **PA2** cylindrical nanofibers contains only the alkyl tails. Moreover, there are additional hydrophobic interactions between the alkyl tail of inverted molecules and valine residues, and hydrogen bonds that bridge the interface between micelles along **PA2** fiber axis. Since the peptide residues of **PA2** form an increased number of hydrophobic interactions at the interface, the total number of hydrogen bonds that can be formed is subsequently reduced resulting in a lower propensity of β-sheet formation. While **PA1** and **PA2** forms sufficient β-sheet structures to promote one-dimensional self-assembled structures, calculation of the Lindemann parameter indicate that **PA2** nanofibers are structurally less stable than **PA1** counterparts. Both **PA1** and **PA2**

nanofibers were then subjected to temperature increases during a heating process showing that as the temperature increased from T* = 0.12 to 0.15, the rate at which **PA2** dissociated into isolated random coil is much faster than **PA1**. These findings demonstrate a strong correlation with previous experimental work showing **PA2** exhibiting weaker mechanical properties than **PA1**.[17]

Compared to the experimental speculation that **PA2** forms an increased amount of misaligned hydrogen bonds and twisted β-sheets, our simulation results suggest that the reduced amount of β-sheets and the arrangement of hydrophobic core are mainly responsible for the observed decrease in macroscopic bulk material property. This observation is comparable to previous simulation results by Lee *et al.*,[67] who demonstrated that the difference in mechanical property between palmitoyl-$V_2A_4E_3$ and palmitoyl-$V_4A_2E_3$ is not β-sheet twistedness since each β-sheet is not infinitely continuous along the fiber axis as proposed by Stupp and coworkers[17] but rather small in size containing 2-5 peptides as similarly observed in our simulations. Additional study on two more sequences (**PA3:** palmitoyl-V_6E_3 and **PA4:** palmitoyl-A_6E_3) to examine the effect of having a homogenous sequence that is either strongly or mildly hydrophobic for the β-sheet forming region was performed in this study. Our results indicate the formation of two unique self-assembled nanostructures: elongated micelles and disjointed cylindrical micelles. Comparing all four sequences, it is shown that the balance between noncovalent interactions is immensely significant. As the β-sheet forming peptide region become less hydrophobic as in the case of **PA4**, the ability to form stable one-dimensional nanofiborus structure with contiguous hydrophobic core is limited. This agrees with our previous studies that examine the effects of solvent-dependent hydrophobicity[44,45] and to some extent pH-dependent

electrostatics[10,42] on PA self-assembly. Through this study, adjusting the position of individual residues may provide an alterative pathway to achieve desirable structural and functional characteristics for the development of innovative biomaterials in a more fine-tuning manner. This would allow using molecular simulations to aid in the design and development of bio-inspired materials for the fields of drug delivery, diagnostic medicine, tissue engineering, and regenerative medicine

7.6 Acknowledgements

This work is accepted for publication with minor revision in Biomacromolecules, 2015 © American Chemical Society. Co-authors include: Hung D. Nguyen. HDN acknowledges financial support from UC Irvine. IWF acknowledges support from a Graduate Research Fellowship from the National Science Foundation (DGE-1321846). This work used the Extreme Science and Engineering Discovery Environment (XSEDE), which is supported by National Science Foundation grant number OCI-1053575. We are also thankful for the computational resources provided by the GreenPlanet and High Performance Computing clusters at UCI campus.

7.7 Supplementary Information

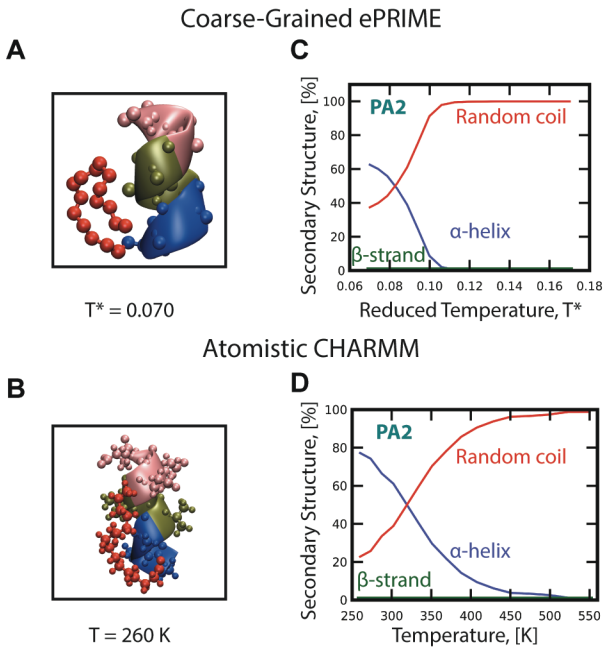

Figure 7.7. Snapshots of equilibrium structures of a singe PA2 molecule at the lowest temperature from replica-exchange simulations using (A) coarse-grained ePRIME model and (B) atomistic CHARMM model. The color scheme is: hydrophobic alkyl tail (red), valine (green), alanine (blue), and glutamic acid (pink). Plot of the percentage of secondary structure formation as a function of temperature for a singe PA2 molecule from replica-exchange simulations using (C) coarse-grained ePRIME model and (D) atomistic CHARMM model. Data shown is taken from the average of the last 10% of equilibrium data and standard deviation is ±20%.

At the lowest temperature of T∗ = 0.07, the peptide folds into a α-helical conformation (**Figure 7.7A**) using our coarse-grained ePRIME model.[42] Comparing this structure to the final conformation obtained at T = 260K using atomistic CHARMM 27 force field[58-60] model (**Figure 7.7B**) shows a high resemblance in the folded conformation of the peptide segment, and the interactions between the alkyl tail and the peptide segment from the coarse-grained and all-atom simulations. In both simulations, the peptide segment folds into an α-helical conformation, with favorable hydrophobic interactions present between the flexible hydrophobic tail and the sidechains of the corresponding hydrophobic residues.

Equilibrium results obtained from replica-exchange simulations using either our coarse-grained ePRIME or all-atom CHARMM 27 force field models produce similar structures over a wide range of temperatures as shown in **Figure 7.7C** and **Figure 7.7D**,

which plot the percentage of secondary structures created by the peptide segment as a function of temperature. Both show the transition between α-helical conformation at low temperatures and random coil at high temperatures. This indicates that our coarse-grained model of the chosen PA molecule has a remarkable ability to predict not only the secondary structure created by the peptide segment as a function of temperature but also the interactions between the alkyl tail and the peptide segment.

For the replica-exchange MD simulation using our coarse-grained ePRIME model, each simulation contains 16 replicas distributed over a broad interval of temperature ranging from T* = 0.07 to T* = 0.17. Exchange attempts occur every t* = 5.0 reduced time units. This corresponds to a replica-exchange attempt after ~6 000 000 collisions at each temperature. Approximately 29 700 replica-exchange attempts are made before equilibrium is reached. The criteria for equilibrium is that the ensemble average of the system's total potential energy, which is collected at the end of each DMD run, should vary by no more than 2.5% during the second half of all DMD runs at each temperature. Once equilibrium is reached, the data collection phase begins in which 3300 extra replica-exchange attempts are made.

All-atom replica-exchange simulation is also performed using NAMD[68] for a single PA chain to serve as a validation of our coarse-grained model. The simulation has 16 replicas over a wide range of temperatures ranging from T = 260 K to T = 550 K using the CHARMM 27 force field. A replica-exchange attempt is made at every 2000 steps, which corresponds to 4 ps for each temperature, and an approximate 85 000 replica-exchange attempts were made.

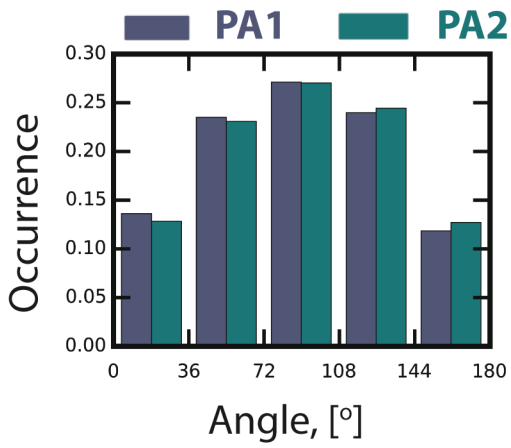

Figure 7.8. The probability of β-sheet twisting at a certain angle is plotted for PA1 and PA2 cylindrical nanofibers. Angles are determined using PyMOL[64] implementing the "angle_between_helices.py" open source script by Thomas Holder. The values are obtained from all simulations for PA1 and PA2.

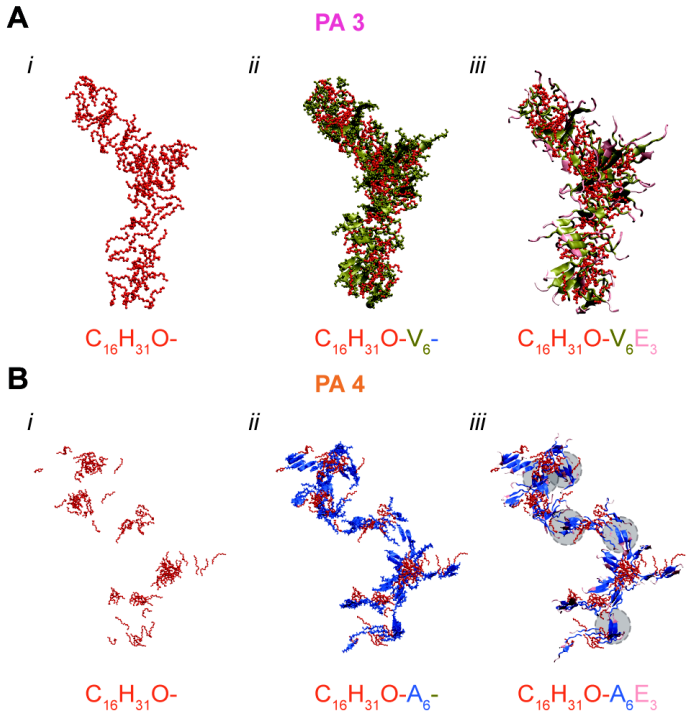

Figure 7.9. Representative equilibrium structure of cylindrical nanofibers showcasing (i) only the alkyl tails, (ii) plus the six β-forming residues, and (iii) the whole sequence of (A) PA3 and (B) PA4. Color scheme using VMD[61]: alkyl tail (red), valine (green), alanine (blue), and glutamic acid (pink).

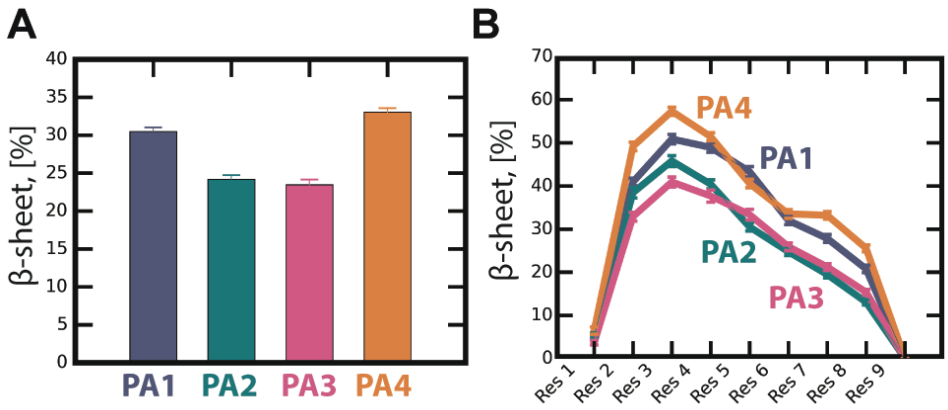

Figure 7.10. For four sequences: (A) Average amount of β-sheets on cylindrical nanofibers at equilibrium and (B) the β-sheet propensity is plotted as a function of the peptide residue.

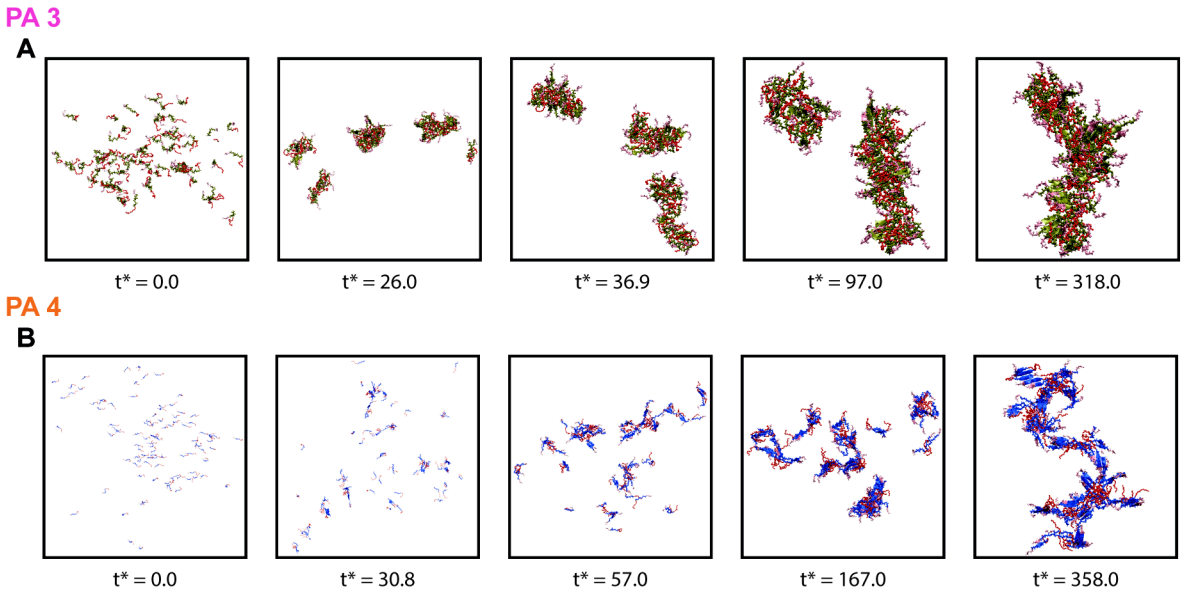

Figure 7.11. Snapshots showing a dynamic self-assembly process at different times for (A) PA3 and (B) PA4 starting from random configurations.

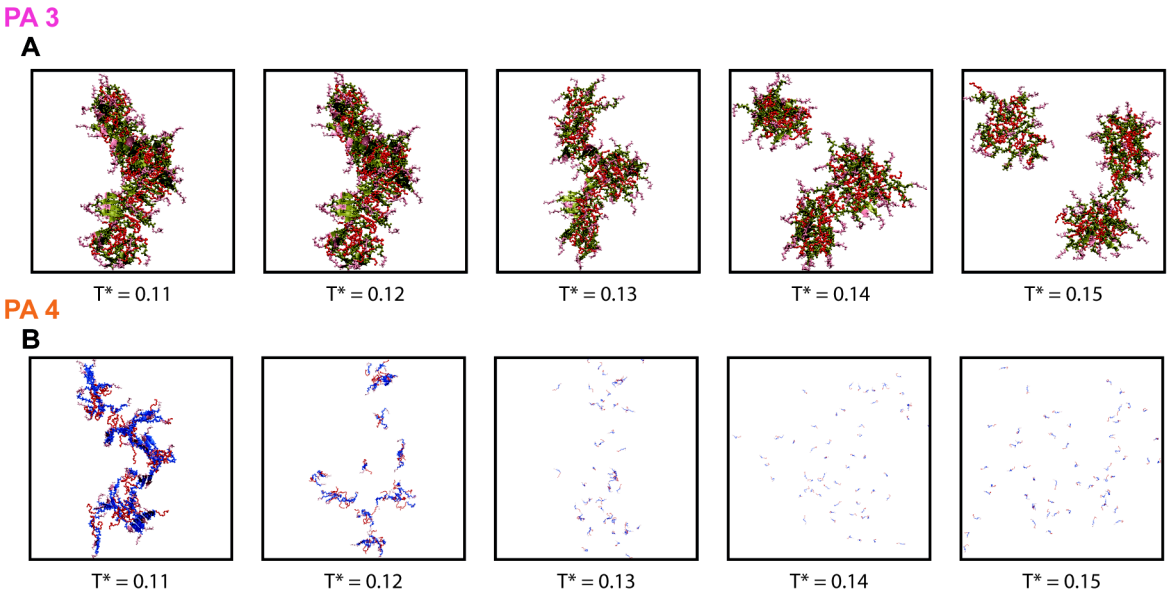

Figure 7.12. Snapshots of the equilibrated structure at the end of each increasing temperature (T*=0.12 – 0.15) during the heating process for (A) PA3 and (B) PA4 starting from cylindrical nanofiber structures assembled at T*=0.11.

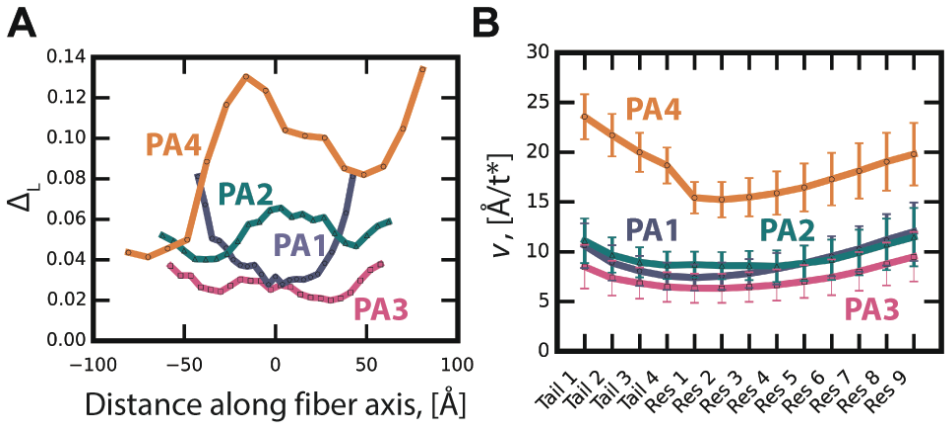

Figure 7.13. For four sequences: (A) the Lindemann value at different points along the fiber axis of cylindrical nanofibers and (B) the velocity of individual regions of each molecule. The first 4 regions correspond to the alkyl tail and remaining 9 regions correspond to 9 peptide residues.

7.8 References

1. Dirks, A. T. J., Nolte, R. J. M. & Cornelissen, J. J. L. M. Protein-Polymer Hybrid Amphiphiles. *Adv. Mater.* **20,** 3953–3957 (2008).
2. Hartgerink, J. D. Self-Assembly and Mineralization of Peptide-Amphiphile Nanofibers. *Science* **294,** 1684–1688 (2001).
3. Trent, A., Marullo, R., Lin, B., Black, M. & Tirrell, M. Structural properties of soluble peptide amphiphile micelles. *Soft Matter* **7,** 9572–9582 (2011).
4. Tysseling-Mattiace, V. M. *et al.* Self-Assembling Nanofibers Inhibit Glial Scar Formation and Promote Axon Elongation after Spinal Cord Injury. *Journal of Neuroscience* **28,** 3814–3823 (2008).
5. Sohdi, A., Campbell, D. & Topham, P. Polymer-peptide conjugate hydrogels: towards controlled drug

delivery. *Chiang Mai journal of science* (2012).
6. Pettikiriarachchi, J. T. S., Parish, C. L., Shoichet, M. S., Forsythe, J. S. & Nisbet, D. R. Biomaterials for Brain Tissue Engineering. *Aust. J. Chem.* **63,** 1143 (2010).
7. Ghosh, A. *et al.* Fine-Tuning the pH Trigger of Self-Assembly. *J. Am. Chem. Soc.* **134,** 3647–3650 (2012).
8. Ghosh, A., Dobson, E. T., Buettner, C. J., Nicholl, M. J. & Goldberger, J. E. Programming pH-Triggered Self-Assembly Transitions via Isomerization of Peptide Sequence. *Langmuir* **30,** 15383–15387 (2014).
9. Frisch, H. & Besenius, P. pH-Switchable Self-Assembled Materials. *Macromol. Rapid Commun.* **36,** 346–363 (2014).
10. Cote, Y. *et al.* Mechanism of the pH-Controlled Self-Assembly of Nanofibers from Peptide Amphiphiles. *J. Phys. Chem. C* **118,** 16272–16278 (2014).
11. Hartgerink, J. D., Beniash, E. & Stupp, S. I. Peptide-amphiphile nanofibers: A versatile scaffold for the preparation of self-assembling materials. *Proceedings of the National Academy of Sciences* **99,** 5133–5138 (2002).
12. Niece, K. L. *et al.* Modification of gelation kinetics in bioactive peptide amphiphiles. *Biomaterials* **29,** 4501–4509 (2008).
13. Toksoz, S., Mammadov, R., Tekinay, A. B. & Guler, M. O. Electrostatic effects on nanofiber formation of self-assembling peptide amphiphiles. *Journal of Colloid And Interface Science* **356,** 131–137 (2011).
14. Yu, Y.-C., Berndt, P., Tirrell, M. & Fields, G. B. Self-assembling amphiphiles for construction of protein molecular architecture. *J. Am. Chem. Soc.* **118,** 12515–12520 (1996).
15. Black, M. *et al.* Self-Assembled Peptide Amphiphile Micelles Containing a Cytotoxic T-Cell Epitope Promote a Protective Immune Response In Vivo. *Adv. Mater.* **24,** 3845–3849 (2012).
16. He, C., Han, Y., Fan, Y., Deng, M. & Wang, Y. Self-Assembly of Aβ-Based Peptide Amphiphiles with Double Hydrophobic Chains. *Langmuir* **28,** 3391–3396 (2012).
17. Pashuck, E. T., Cui, H. & Stupp, S. I. Tuning Supramolecular Rigidity of Peptide Fibers through Molecular Structure. *J. Am. Chem. Soc.* **132,** 6041–6046 (2010).
18. Cui, H., Cheetham, A. G., Pashuck, E. T. & Stupp, S. I. Amino Acid Sequence in Constitutionally Isomeric Tetrapeptide Amphiphiles Dictates Architecture of One-Dimensional Nanostructures. *J. Am. Chem. Soc.* **136,** 12461–12468 (2014).
19. Storrie, H. *et al.* Supramolecular crafting of cell adhesion. *Biomaterials* **28,** 4608–4618 (2007).
20. Dagdas, Y. S., Tombuloglu, A., Tekinay, A. B., Dana, A. & Guler, M. O. Interfiber interactions alter the stiffness of gels formed by supramolecular self-assembled nanofibers. *Soft Matter* **7,** 3524–3532 (2011).
21. Ghanaati, S. *et al.* Dynamic in vivo biocompatibility of angiogenic peptide amphiphile nanofibers. *Biomaterials* **30,** 6202–6212 (2009).
22. Dehsorkhi, A., Castelletto, V. & Hamley, I. W. Self-assembling amphiphilic peptides. *J. Pept. Sci.* **20,** 453–467 (2014).
23. Cui, H., Webber, M. J. & Stupp, S. I. Self-assembly of peptide amphiphiles: From molecules to nanostructures to biomaterials. *Biopolymers* **94,** 1–18 (2010).
24. Jun, H.-W. *et al.* Tuning the mechanical and bioresponsive properties of peptide-amphiphile nanofiber networks. *Journal of Biomaterials Science, Polymer Edition* **19,** 665–676 (2008).
25. Kim, J.-K., Anderson, J., Jun, H.-W., Repka, M. A. & Jo, S. Self-Assembling Peptide Amphiphile-Based Nanofiber Gel for Bioresponsive Cisplatin Delivery. *Mol. Pharmaceutics* **6,** 978–985 (2009).
26. Khan, S., Sur, S., Newcomb, C. J., Appelt, E. A. & Stupp, S. I. Acta Biomaterialia. *Acta Biomaterialia* **8,** 1685–1692 (2012).
27. Klok, H.-A. Biological-synthetic hybrid block copolymers: Combining the best from two worlds. *J. Polym. Sci. A Polym. Chem.* **43,** 1–17 (2004).
28. Engler, A. J., Sen, S., Sweeney, H. L. & Discher, D. E. Matrix Elasticity Directs Stem Cell Lineage Specification. *Cell* **126,** 677–689 (2006).
29. Tse, J. R. & Engler, A. J. *Preparation of Hydrogel Substrates with Tunable Mechanical Properties*. (John Wiley & Sons, Inc., 2001). doi:10.1002/0471143030.cb1016s47
30. Discher, D. E. Tissue Cells Feel and Respond to the Stiffness of Their Substrate. *Science* **310,** 1139–1143 (2005).
31. Paramonov, S. E., Jun, H.-W. & Hartgerink, J. D. Self-Assembly of Peptide–Amphiphile Nanofibers: The Roles of Hydrogen Bonding and Amphiphilic Packing. *J. Am. Chem. Soc.* **128,** 7291–7298 (2006).
32. Yan, C. & Pochan, D. J. Rheological properties of peptide-based hydrogels for biomedical and other

applications. *Chem. Soc. Rev.* **39,** 3528–3540 (2010).
33. Schneider, J. P. *et al.* Responsive Hydrogels from the Intramolecular Folding and Self-Assembly of a Designed Peptide. *J. Am. Chem. Soc.* **124,** 15030–15037 (2002).
34. Roberts, D., Rochas, C., Saiani, A. & Miller, A. F. Effect of Peptide and Guest Charge on the Structural, Mechanical and Release Properties of β-Sheet Forming Peptides. *Langmuir* **28,** 16196–16206 (2012).
35. Ramachandran, S., Trewhella, J., Tseng, Y. & Yu, Y. B. Coassembling Peptide-Based Biomaterials: Effects of Pairing Equal and Unequal Chain Length Oligopeptides. *Chem. Mater.* **18,** 6157–6162 (2006).
36. Ramachandran, S. & Yu, Y. B. Peptide-based viscoelastic matrices for drug delivery and tissue repair. *BioDrugs* **20,** 263–269 (2006).
37. Ramachandran, S., Tseng, Y. & Yu, Y. B. Repeated Rapid Shear-Responsiveness of Peptide Hydrogels with Tunable Shear Modulus. *Biomacromolecules* **6,** 1316–1321 (2005).
38. Meng, Q. *et al.* Tunable Self-Assembled Peptide Amphiphile Nanostructures. *Langmuir* **28,** 5017–5022 (2012).
39. Yuwono, V. M. & Hartgerink, J. D. Peptide Amphiphile Nanofibers Template and Catalyze Silica Nanotube Formation. *Langmuir* **23,** 5033–5038 (2007).
40. Wang, J. *et al.* Dynamic self-assembly of surfactant-like peptides A6K and A9K. *Soft Matter* **5,** 3870 (2009).
41. Missirlis, D. *et al.* Effect of the Peptide Secondary Structure on the Peptide Amphiphile Supramolecular Structure and Interactions. *Langmuir* **27,** 6163–6170 (2011).
42. Fu, I. W., Markegard, C. B., Chu, B. K. & Nguyen, H. D. The Role of Electrostatics and Temperature on Morphological Transitions of Hydrogel Nanostructures Self-Assembled by Peptide Amphiphiles Via Molecular Dynamics Simulations. *Advanced Healthcare Materials* **2,** 1388–1400 (2013).
43. Morriss-Andrews, A. & Shea, J.-E. Computational Studies of Protein Aggregation: Methods and Applications. *Annu. Rev. Phys. Chem.* **66,** 643–666 (2015).
44. Fu, I. W., Markegard, C. B., Chu, B. K. & Nguyen, H. D. Role of Hydrophobicity on Self-Assembly by Peptide Amphiphiles via Molecular Dynamics Simulations. *Langmuir* **30,** 7745–7754 (2014).
45. Fu, I. W., Markegard, C. B. & Nguyen, H. D. Solvent Effects on Kinetic Mechanisms of Self-Assembly by Peptide Amphiphiles via Molecular Dynamics Simulations. *Langmuir* **31,** 315–324 (2015).
46. Voegler Smith, A. & Hall, C. K. α-Helix formation: Discontinuous molecular dynamics on an intermediate-resolution protein model. *Proteins: Structure, Function, and Bioinformatics* **44,** 344–360 (2001).
47. Nguyen, H. D. & Hall, C. K. Molecular dynamics simulations of spontaneous fibril formation by random-coil peptides. *Proceedings of the National Academy of Sciences* **101,** 16180–16185 (2004).
48. Nguyen, H. D., Marchut, A. J. & Hall, C. K. Solvent effects on the conformational transition of a model polyalanine peptide. *Protein Science* **13,** 2909–2924 (2004).
49. Wallqvist, A. & Ullner, M. A simplified amino acid potential for use in structure predictions of proteins. *Proteins: Structure, Function, and Bioinformatics* **18,** 267–280 (1994).
50. Wesson, L. & Eisenberg, D. Atomic solvation parameters applied to molecular dynamics of proteins in solution. *Protein Science* **1,** 227–235 (1992).
51. Gu, W., Rahi, S. J. & Helms, V. Solvation Free Energies and Transfer Free Energies for Amino Acids from Hydrophobic Solution to Water Solution from a Very Simple Residue Model. *J. Phys. Chem. B* **108,** 5806–5814 (2004).
52. Fu, I. W., Markegard, C. B. & Nguyen, H. D. Solvent Effects on Kinetic Mechanisms of Self-Assembly by Peptide Amphiphiles via Molecular Dynamics Simulations. *Langmuir* **31,** 315–324 (2015).
53. Andersen, H. C. Molecular dynamics simulations at constant pressure and/or temperature. *J. Chem. Phys.* **72,** 2384 (1980).
54. Chu, B. K., Fu, I. W., Markegard, C. B., Choi, S. E. & Nguyen, H. D. A Tail of Two Peptide Amphiphiles: Effect of Conjugation with Hydrophobic Polymer on Folding of Peptide Sequences. *Biomacromolecules* 140808081703004 (2014). doi:10.1021/bm500733h
55. Lee, O.-S., Cho, V. & Schatz, G. C. Modeling the Self-Assembly of Peptide Amphiphiles into Fibers Using Coarse-Grained Molecular Dynamics. *Nano Lett.* **12,** 4907–4913 (2012).
56. Frishman, D. & Argos, P. Knowledge-based protein secondary structure assignment. *Proteins: Structure, Function, and Bioinformatics* **23,** 566–579 (1995).
57. Zhou, Y. *et al.* Native proteins are surface-molten solids: application of the Lindemann criterion for the

solid versus liquid state. *Journal of Molecular Biology* **285,** 1371–1375 (1999).
58. MacKerell, A. D., Jr *et al.* All-atom empirical potential for molecular modeling and dynamics studies of proteins. *J. Phys. Chem. B* **102,** 3586–3616 (1998).
59. Mackerell, A. D., Jr., Feig, M. & Brooks, C. L., III. Extending the treatment of backbone energetics in protein force fields: Limitations of gas-phase quantum mechanics in reproducing protein conformational distributions in molecular dynamics simulations. *J. Comput. Chem.* **25,** 1400–1415 (2004).
60. Brooks, B. R. *et al.* CHARMM: The biomolecular simulation program. *J. Comput. Chem.* **30,** 1545–1614 (2009).
61. Humphrey, W., Dalke, A. & Schulten, K. VMD: visual molecular dynamics. *Journal of molecular graphics* **14,** 33–38 (1996).
62. Stendahl, J. C., Rao, M. S., Guler, M. O. & Stupp, S. I. Intermolecular Forces in the Self-Assembly of Peptide Amphiphile Nanofibers. *Adv. Funct. Mater.* **16,** 499–508 (2006).
63. Lee, O.-S., Stupp, S. I. & Schatz, G. C. Atomistic Molecular Dynamics Simulations of Peptide Amphiphile Self-Assembly into Cylindrical Nanofibers. *J. Am. Chem. Soc.* **133,** 3677–3683 (2011).
64. The PyMOL Molecular Graphics System, Version 1.7.4 Schrödinger, LLC.
65. Ortony, J. H. *et al.* Internal dynamics of a supramolecular nanofibre. *Nat Mater* **13,** 812–816 (2014).
66. Chou, P. Y. & Fasman, G. D. Prediction of protein conformation. *Biochemistry* **13,** 222–245 (1974).
67. Lee, O.-S., Liu, Y. & Schatz, G. C. Molecular dynamics simulation of β-sheet formation in self-assembled peptide amphiphile fibers. *J Nanopart Res* **14,** 1–7 (2012).
68. Phillips, J. C. *et al.* Scalable molecular dynamics with NAMD. *J. Comput. Chem.* **26,** 1781–1802 (2005).

CHAPTER 8 Toward Self-Assembly of Nonviral Gene Delivery Complexes via Molecular Dynamics Simulations

8.1 Abstract

Coarse-grained, ePRIME model has been further developed into BioModi (Biomolecular Multiscale Models at UC Irvine) to incorporate and adequately model the biological behavior of nucleic acids and polyethylene glycol units. Physiologically relevant behavior is captured from performing atomistic simulations to determine the dynamics of individual PEGylated-polypeptide and double stranded siRNA molecules. siRNA is modeled with sequence specificity instead of a simple flexible polymer to account for sequence-dependent interactions (e.g. base-stacking, electrostatic interactions, solvent-induced interactions). From performing simulations with large number of PEGylated cationic polymer (PEG_{5000}-LYS_n; n = 9,27,50) and $siRNA_{21}$ (5′-CAAGCUGACCCUGAAGUUCdTdT-3′), complexation is observed between these two species. In particular, shorter cationic polymer length leads to formation of larger aggregate size and a greater cationic polymer to siRNA ratio. In accordance with experimental results, longer cationic polymer length at a higher N/P ratio can yield predominant formation of larger aggregate size. Understanding the role of the electrostatic interaction in the self- assembly process aids in characterizing structural and behavior properties of the system for the rational design of a targeted delivery system for nucleic acids.

8.2 Introduction

The discovery of RNA interference[1,2] as a post-transcription mechanism for gene silencing has been rapidly developed as a therapeutic approach for infectious diseases,

cancer treatment, genetic disorders.[3] Through the use of sequence-specific small interfering RNA (siRNA), the approach surpasses other conventional drug therapies (e.g. small molecule protein therapeutics) in that it offers an enticing ability to virtually silence any gene.[4,5] However, the greatest challenge in utilizing siRNA rests upon achieving effective systemic delivery. Naked siRNA injected intravenously is subjected to nuclease degradation and rapid renal excretion in addition to having non-specific interactions with serum proteins.[6] Both viral and non-viral vectors have been designed to be successful gene carriers; however, due to low cost of production and increased biocompatibility, non-viral vectors have been considered to be more preferable. General design characteristics of non-viral vectors are typically cationic in nature to promote complexation with anionic nucleic acids through attractive electrostatic interactions. In particular, focus will be placed on using peptide-polymer conjugates that can form polyionic complex micelles to effectively shield siRNA to improve therapeutic delivery.

The use of small interfering RNAs (siRNA) to correct the over- or under expression of genes have been shown to be a promising approach for the treatment of diseases.[7] Beginning with either a long double-stranded RNA that can be separated into fragments by the enzyme Dicer or produced synthetically as a sequence of 21-25 base pairs, siRNA can be directly introduced into the cell. Next, siRNA is incorporated into the RNA- induced silencing complex, RISC, which separates the siRNA into two single strands and discards one of them. The strand that is left behind, antisense strand, directs the RISC to mRNA molecules and through complementary base pairing, the siRNA can selectively target and bind to a selected region. Consequently, that specific region is degraded resulting in the absent expression of a certain gene. Although this method has been shown to be effective,

the issue rests upon having a delivery system that can ensure the delivery of siRNA molecules to target cells.[8]

Peptide-polymer conjugate molecules are desirable non-viral vectors because they are less cytotoxic and offer more flexibility in terms of structural and chemical properties in comparison with viral-vectors. The peptide-polymer conjugate of interest is comprised of a PEGylated polymer attached to a cationic polypeptide. The benefits of using a PEGylated-cationic peptide as opposed to a simple cationic polypeptide that can already neutralize the anionic charges on siRNA for easier cellular internalization, the positive surface charge can still lead to non-specific interactions with other macromolecules or that the interaction can be so strong that it does not facilitate an effective dissociation. With PEGylated species, there is more steric stabilization and can form a protective outer shell to better encapsulate the gene from physiological surroundings.[9]

The structural versatility of peptide-polymer conjugates can be further modified to serve as a non-viral vector specifically as a gene delivery system. The use of small interfering RNAs (siRNA) to correct over- or under- expression of genes has been shown to be a promising approach for the treatment of diseases. However, it faces many in-vivo barriers such as lacking an efficient carrier to reach target cells, avoiding enzymatic degradation, and ultimately achieve an effective dissociation for gene transfer.[7] Experimental work have previously examined the use of PEGylated polyplex micelles that are comprised of a PEGylated polymer attached to a cationic polypeptide chain as viable gene vectors.[10] The choice of using non-viral vectors as opposed to viral vectors parallels that of selecting biohybrid synthetic polymer in that they offer increased steric stabilization and less cytotoxicity while offering ability to fine-tune specific properties to enable

effective transfection and release of nucleic acids. Simple cationic polymers without PEGylated species provides a mean for enhanced cellular internalization by neutralizing positive charges of siRNA however a net surface charge can yield non- specific interactions with other macromolecules deterring from effective dissociation of the gene. Through the combination of the PEGylated species, a protective layer owing to the core-shell model can better encapsulate and shield the gene from the physical environment.

With consideration to rationally design a non-viral vector, previous biological experiments have shown that multitude of factors can influence the efficacy of a gene delivery system. These factors include structural arrangement of the carriers, molecular weight, size, charge density between gene and carrier, and etc. However, comparing between different common carriers to extrapolate behavioral trends has led to some contradictory results. For PLL-DNA system, short PLL lengths resulted in more condensed DNA structures whereas for PAMAM-RNA, increased branching due to additional surface amines leads to more stable complexes.[11]

The effect of the cationic polymers' architecture on complexation has been examined by Smith et al.,[12] using atomistic MD simulations for six cationic polymers of varying structures (i.e. PLL vs. PAMAM, as dendritic and linear forms) with siRNA. Through the use of MD simulations, the intricate process of gene/carrier binding occurs can be quantified through the binding free energy to provide insight on the disassembly mechanism. While polymers with greater charge can form stronger complexes, they may be problematic while accounting for dissociation and delivery of the gene. In a related study to examine PAMAM-RNA complex at different pH environment to model the late endosome

stage, complexes at low pH were observed to form more compact structures than at neutral pH.[13]

Modification of the polycation architecture in addition to changing the charge density between the gene and carrier has been shown to affect the complex stability. In an attempt to adequately model the *in-vitro* system that would typically contain more than a single carrier or a single siRNA molecule, multiple carriers and/or genes were examined to look at the underlying interaction necessary for complexation.[14,15] Comparison between branched PEIs and linear PEIs indicated that linear PEIs are more flexible allowing for better surface coverage between DNA and PEI and consequently more stable structures. For a system that has excess of PEI to fully neutralize DNA, stable aggregates are also more likely to form.

Atomistic MD simulations have shown to be a technique that can provide the means to examine the detailed binding process as well as investigating the role of certain factors that can affect the stability of the resulting complex. However, previous simulation studies have only examined small systems of several siRNA molecules and/or carriers due to computational constraints. A recent study using coarse-grained molecular dynamics has examined how the architecture and flexibility of the polycations can affect the structure of the polyionic complexes.[16] The ability to examine the formation and subsequently characterize the interactions of the resulting polyionic complex would be difficult in atomistic simulations due to the limited timescale. From their simulation studies, Elder and Jayaraman[16] indicated that the charge ratio, as defined by the number of positive to negatively charged groups, largely determines the polyionic complex structure. At charge neutrality (CR=1) for a fully flexible polyanion, the polyionic complex adopts a globular

conformation that is smaller in size and more compact due to elimination of excess charges. On the other hand, when the charge ratio is greater than one, the polyionic complex is much larger and anisotropic. At CR>1, changing the architecture of the polycation (e.g. graft length or graft spacing) suggests that the surface charge of the polyionic complex can be modified accordingly. Since these molecules are relevant for gene delivery, the need to possess a net surface charge is important for effective transfection consideration.

For our system, we conjugate PEG onto poly(lysine) and use siRNA with 21 base pairs. Poly-L-Lysine is commonly used as a non-viral DNA condensing agent and is attractive because it is readily biodegradable and PEG is added to increase circulation half-life. Through mainly electrostatic interactions, we expect to form a polyionic complex with a core-shell architecture.[17] The outer shell will consist of the PEG that will enhance circulation time and the inner core will be of the siRNA with the cationic lysine. The inner core can also be used as a potential reservoir for drug loading as well. The overall size will be less than 150 nm clearance value in which the positive charged complex can attach to the negative charge on cell surface to be endocytosed. In particular, effective complexation will be characterized and determined as a function of modifying the length of the lysine segment and the nitrogen to phosphate ratio of the system.

8.3 Methods

8.3.1 Atomistic Models

Double stranded, α-siRNA (5'-CAAGCUGACCCUGAAGUUCdTdT-3') was built using AMBER ff12SB[18] by first building the structure as if it was an α-DNA molecule and then converting back to α-RNA. To attain the structure with sticky ends, the complementing

nucleotide of the sticky ends were removed. After the structure is minimized and heated to the desired temperature, constant temperature simulation is performed using SANDER at T = 270K and T= 300K at an ion concentration of 0.001 M.

Single molecule PEGylated-poly(L-Lysine) ($PEG_{44}LYS_{18}$) was built using MATCH[19], a Multipurpose Atom-Typer for CHARMM, using the CHARMM 22 force field. The PEG length is equivalent to ~PEG2000 and is considered to be a smaller representation of the experimental molecule of PEG5000. Although the length is reduced due to the software limitation, the resulting dynamic behavior of the polymer is believed to be an adequate representation for the larger scaled-up molecule. Constant temperature simulations were performed using NAMD[20] at an ion concentration of 0.001 M and T = 298 K to be comparable with experimental conditions. A total of 50 ns was simulated with a 2 fs timestep and outputs were written every 1 ps. End-to-end distance and radius of gyration for the molecule was calculated using analysis scripts from Visual Molecular Dynamics (VMD).[21]

8.3.2 Coarse-grained siRNA and PEGylated-poly(L-lysine) Model

Development of a coarse-grained model for siRNA has been built upon prior existing model in our laboratory, BioModi (Biomolecular Multiscale Models at UC Irvine).[22] This simulation package incorporates the new model for DNA, with the peptides and polymers model, ePRIME.[23-25] Similar to DNA, a 3-site-per-nucleotide model was chosen to represent siRNA as "bead-on-a-string" following the success of other theoretical groups in accurately representing nucleic acids with the least number of particles.[26,27] A total of 3 coarse-grained beads were used: phosphate (P), sugar (S), and base (B) (**Figure 8.1**).

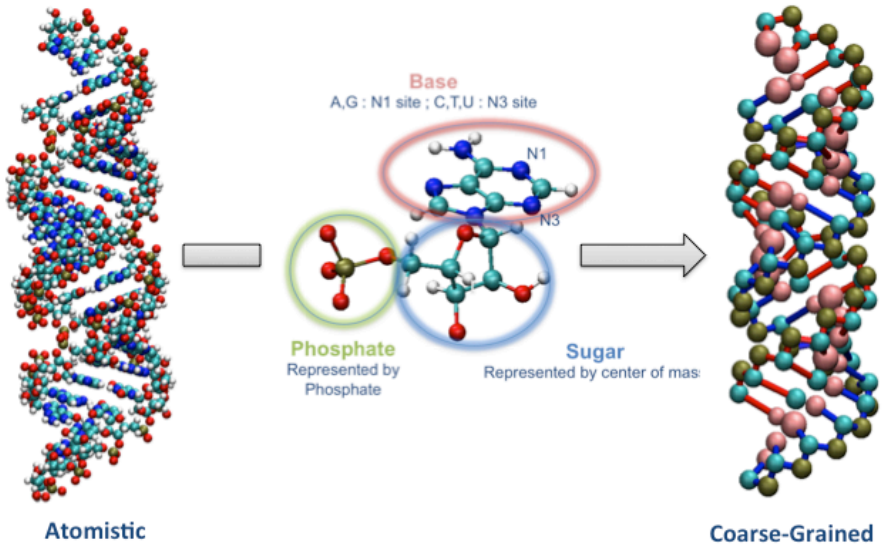

Figure 8.1. Coarse-grained representation for siRNA with a 3-site-per-nucleotide from atomistic representation. One bead particle is used to represent each chemical moiety for phosphate, sugar, and base group.

For the phosphate and sugar moiety, an effective, united-atom interaction site is obtained by using the coordinates of the phosphate atom, and the center of mass of the five-atom ring sugar, respectively. The representation for the base unit is determined at the N1 site for purine bases (adenine and guanine) and the N3 position for pyrimidine (thymine, cytosine, and uracil). Bead sizes are given in **Table 8.1**.

Table 8.1. United atom sizes for nucleic acid beads in BioModi.

Particle	Bead Diameter (Å)
Phosphate, P	5
Sugar, S	5
ADE, B	2.63
GUA, B	2.67
CYT, B	2.67
THY, B	2.63
URA, B	2.63
dCYT, B	2.67
dTHY, B	2.63

Besides covalent bonds, neighboring beads are constrained by imposing pseudo-bonds to mimic the chain connectivity and the local geometry such as bond angles and dihedrals (**Figure 8.2**).

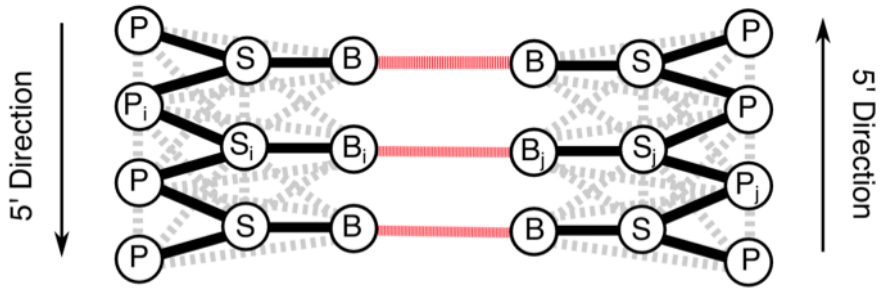

Figure 8.2 Covalent bonds are schematically shown as dark black lines connecting united atoms. Pseudo-bonds are schematically shown as dashed blacks lines and are used to maintain bond angles and dihedrals. Base-pair interactions (red lines) are directional in orientation.

A total of 31 covalent bonds and pseudo bonds (**Table 8.2**) were extracted from atomistic molecular dynamics simulation of duplex siRNA with 19 nucleotide (5'-CAAGCUGACCCUGAAGUUC-3'). The simulation was conducted using NAMD 2.8 with implicit solvent and the CHARMM 27 force field. After minimizing and heating to 298 K at an ion concentration of 0.001M, the data was collected over a 50 ns equilibration run.

Table 8.2. Average distances and standard deviation of 31 covalent bond and pseudo-bonds for double stranded siRNA.

Bond Type	**Average (Å)**	**Standard Deviation**	**Bond Type**	**Average (Å)**	**Standard Deviation**
S_i-S_i+1	6.12	0.34	P_i+1-B_i	9.08	1.19
P_i-P_i+1	6.36	0.38	P_i+1-B_i	9.54	0.93
P_i-S_i	3.49	0.07	P_i+1-B_i	7.18	0.86
S_i-P_i+1	4.36	0.14	S_i+1-B_i	8.27	1.33
S_i-B_i	6.78	0.13	S_i+1-B_i	8.17	1.85
S_i-B_i	6.71	0.14	S_i+1-B_i	8.38	1.48
S_i-B_i	5.29	0.11	S_i+1-B_i	7.60	1.67
S_i-B_i	5.37	0.12	S_i+1-B_i	8.12	1.72
S_i-B_i	8.57	0.59	S_i-B_i+1	8.97	0.39
P_i-B_i	8.40	0.58	S_i-B_i+1	9.29	1.02
P_i-B_i	7.20	0.34	S_i-B_i+1	5.25	0.10

P_i-B_i	7.67	0.48	S_i-B_i+1	7.20	0.31
P_i-B_i	9.15	0.52	S_i-B_i+1	7.59	0.37
P_i-B_i	9.18	0.48	P_i-S_i+1	7.60	0.94
P_i+1-B_i	7.58	0.37	S_i-P_i+1	7.58	1.66
P_i+1-B_i	7.51	0.51			

Interactions between nucleotides are modeled by discrete potentials as discussed in prior simulation work (e.g. hydrogen bonding, base-stacking, electrostatic interaction, and solvent induced). For more information on the model, please refer to reference by Markegard et al.[22]

PEGylated-poly(L-lysine) is modeled using ePRIME[23-25]. The PEG polymer is represented with 2 coarse-grained beads: one-bead for the terminal methyl group and another bead for the repeating (-OCH_2CH_2) group. Bond fluctuations are obtained from atomistic simulations performed using NAMD with the CHARMM 22 force field. After minimizing and heating to 298 K at an ion concentration of 0.001M, the data was collected over a 50 ns equilibration run.

Table 8.3. Average distances and standard deviation of covalent and pseudo-bonds for PEG.

Bond Type	Average (Å)	Standard Deviation
PEG_i-PEG_{i+1}	3.57	0.15
PEG_i-PEG_{i+2}	6.94	0.45
PEG_i-PEG_{i+3}	10.14	0.83

Lysine is modeled with a 3 coarse-grain bead backbone for the amide, alpha carbon, and carbonyl groups (NH, CαH, and CO). Adapting a model by Wallqvist and Ullner,[28] the side chains are represented by one or two spheres based on the length of the side chain. The size of the side chain is derived from the experimentally determined solvent-accessible

area obtained by Eisenberg and co-workers.[29] Individual parameters for peptide residue, lysine are shown in **Table 8.4.**

Table 8.4. ePRIME parameters for peptide residue, Lysine.

Amino Acid	Sidechain Atom	Character	ΔG Free Energy (kJ/mol)	Radius (Å)	Charge
Lysine	— $(CH_2)_3$- —(CH_2)-NH_3^+	Hydrophobic Hydrophilic	3.49 -5.15	2.17 2.80	Positive

For the system of interest, an implicit solvent model is implemented to reduce the system's size for tractable simulations that can still capture the underlying physics of the system. The solvent effect is incorporated into the effective residue-residue potential due to the hydrophobic or hydrophilic character of each peptide residue or PEGylated monomer. Representation of this behavior is either through a square-well or square-shoulder potential that approximates an attractive or repulsive continuous potential, respectively. For example, square-well potential is used for attractive interactions between hydrophobic side chains and/or polymeric segments, whereas square-shoulder potential is used for repulsive interactions between hydrophilic side chains or polymeric segments. The strength of the interaction between two groups is $\varepsilon_{HP} = R(\Delta Gi + \Delta Gj)$, where ΔG is the free energy of transferring each group from water to octanol and R is a measure of the strength of the hydrophobic interaction ranging from 1/6 to 1.3. For this system, R = 1/3. Coarse-grained representation for the PEGylated-Lysine molecule is shown in **Figure 8.3**.

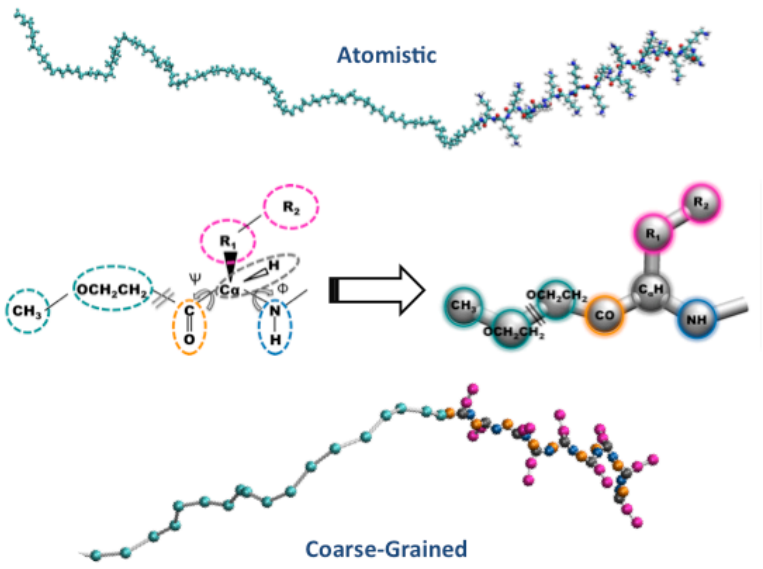

Figure 8.3. Coarse-grained model of PEGylated-lysine molecule from atomistic representation. Each repeating unit of the PEG monomer is represented as one bead and another bead for the terminal methyl group. For the peptide, 3 coarse grain beads represent the backbone for NH, $C_\alpha H$, and CO and the sidechain is represented by 2 coarse grain beads based on the size and bulkiness of lysine residues.

8.3.3 Complexation of siRNA with PEGylated poly(L-lysine)

A total of three PEGylated poly(L-lysine)$_x$ (x = 9, 27, 50) sequences at two different charge densities (i.e., N/P = 1 and N/P = 10) at a constant reduced temperature of T*=1.0 and 0.001 M salt concentration were examined using BioModi, a coarse grained model for siRNA, peptides, and polymers. **Table 8.5** lists out the simulation parameters used for each system. A total of at least three simulations at each condition were used in the analysis, as it was determined that the standard deviations were sufficiently low. The simulation data analyzed for steady state is the last 10% of the simulation.

Table 8.5. Parameters listed for the systems of interests to examine the complexation behavior of PEGylated poly(L-lysine) and siRNA.

N/P=1	**PEG_{5000}-LYS_9**	**PEG_{5000}-LYS_{27}**	**PEG_{5000}-LYS_{50}**
Box size (Å)	841	847	1308
Concentration (M)	1.00E-03	1.00E-03	2.73E-04

Total number of united-atoms	46696	52772	55781
Number of siRNA strands	108	206	258
Number of siRNA duplex	54	103	129
Number of Peptide-Polymer molecules	250	160	109
N/P=2	**PEG_{5000}-LYS_9**	**PEG_{5000}-LYS_{27}**	**PEG_{5000}-LYS_{50}**
Box size (Å)	N/A	N/A	1.02E+03
Concentration (M)	N/A	N/A	3.71E-04
Total number of united-atoms	46696	52772	55781
Number of siRNA strands	108	206	258
Number of siRNA duplex	54	103	129
Number of Peptide-Polymer molecules	250	160	109
N/P=4	**PEG_{5000}-LYS_9**	**PEG_{5000}-LYS_{27}**	**PEG_{5000}-LYS_{50}**
Box size (Å)	N/A	N/A	797
Concentration (M)	N/A	N/A	5.68E-04
Total number of united-atoms	46696	52772	55781
Number of siRNA strands	108	206	258
Number of siRNA duplex	54	103	129
Number of Peptide-Polymer molecules	250	160	109
N/P=10	**PEG_{5000}-LYS_9**	**PEG_{5000}-LYS_{27}**	**PEG_{5000}-LYS_{50}**
Box size (Å)	389	395	575

Concentration (M)	7.31E-03	4.86E-03	1.16E-03
Total number of united-atoms	46696	52772	55781
Number of siRNA strands	108	206	258
Number of siRNA duplex	54	103	129
Number of Peptide-Polymer molecules	250	160	109

8.4 Results and Discussions

8.4.1 Dynamic All-Atomistic Behavior of PEGylated Cationic Polymer and siRNA can be captured using Coarse-Grained Model

Atomistic topology and parameter files are obtained for PEGylated-poly(L-Lysine) using MATCH,[19] a Multipurpose Atom-Typer for CHARMM. The initial 3D structure and connectivity of the atoms is determined from ChemDoodle and Maestro software. As compared to experimental studies, a smaller scale PEGylated-poly(L-Lysine) molecule, $PEG_{44}LYS_{18}$, is used for atomistic studies as a result of computational power and time limits. Even though experimental studies examines the behavior of a bulkier PEG tail of ~5kDa versus ~2kDa with $PEG_{44}LYS_{18}$, and different sequence lengths of lysine, the current molecule is believed to be an adequate and reasonable approximation. For $PEG_{44}LYS_{18}$, this molecule was parameterized using MATCH with the CHARMM 22 force field, and constant temperature simulations were performed using NAMD[20] at physiological conditions, [ion] = 0.001M and T = 298K. To determine the dynamics of the cationic polymer including its size, length, and flexibility, the end-to-end distance and radius of gyration for the molecule was calculated. The end-to-end distance values are shown in **Figure 8.4A** with the values being normalized by the maximum length of the $PEG_{44}LYS_{18}$ during the trajectory. The ability for

the molecule to attain a broad range of end-to-end distance suggests that the overall molecule can either be arranged in a close- or an extended- configuration. Considering that the simulation is performed at physiological conditions, this indicates that the current environmental conditions does not restrict the conformations of $PEG_{44}LYS_{18}$ and instead promote favorable interaction between $PEG_{44}LYS_{18}$ and other species in the system. Further calculations of the radius of gyration by separating the PEG tail and the positively charged lysine segment indicate that the PEG tail is much more flexible than the lysine counterpart (**Figure 8.4B)**. Throughout the trajectory of the simulation, PEG tail exhibits larger fluctuations indicating that the overall size of the PEG tail changes substantially from an extended chain to a coiled chain. In contrast, the lysine segment is relatively stable with minimal fluctuations suggesting that this domain is much more rigid.

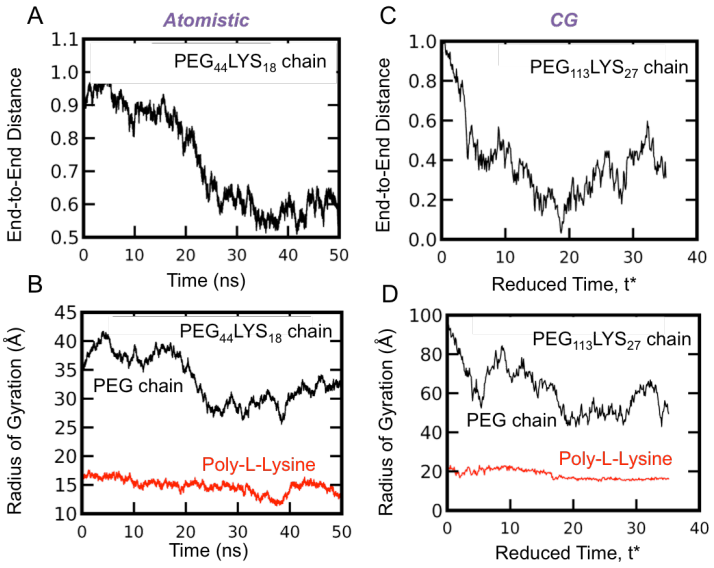

Figure 8.4. (A) Calculated end-to-end distance, normalized by the maximum value, for $PEG_{44}LYS_{18}$ using atomistic simulation, and (B) radius of gyration for the individual domains: PEG_{44} (PEG2000) and LYS18. (C) Calculated end-to-end distance, normalized by the maximum value for $PEG_{113}LYS_{27}$ using coarse-grained simulation, and (B) radius of gyration for the individual domains: PEG_{113} (PEG5000) and LYS27.

Unlike the atomistic model, the coarse grained model is able to provide a more direct comparison with experimental studies even though some details are sacrificed to increase computational power and time. The PEGylated-poly(L-Lysine) molecule is represented by 113 repeating units (ie. each bead represents -OCH_2CH_2-) corresponding to a 5kDa PEG tail. Longer lysine lengths can also be modeled using ePRIME: the protein backbone is modeled by 3 beads corresponding to α-Carbon, carbonyl, and amine group, and the positively charged sidechains is represented by 2 beads. By measuring the average bond distance fluctuations along the PEG tail and of the lysine segment, our coarse-grained model can capture the dynamic atomistic behavior exhibited by this molecule. As shown in **Figure 8.4C**, the end-to-end distance of coarse-grained $PEG_{113}LYS_{27}$ can span a similar range as compared to atomistic $PEG_{44}LYS_{18}$. Although the coarse-grained model can adopt more compact conformations compared to atomistic model, the overall behavior of the molecule is retained as demonstrated by similar trends. Calculating the radius of gyration for the coarse-grained model also provides a qualitative validation (**Figure 8.4D**). Considering that the molecules used are different between the atomistic and coarse-grained model, actual quantitative comparisons are difficult; hence the difference in the axis range. However, comparing the range of motion exhibited by the molecule, subtle differences exhibited by the individual domains are kept in the coarse-grained model.

Similar procedure is followed to determine the structural dynamics of siRNA. The siRNA sequence of interest is 5'-CAAGCUGACCCUGAAGUUCdTdT-3'. This 19 nucleotide sequence with 2 nucleotide overhangs on the 3' end is built using AMBER ff12SB.[18] Constant temperature simulation is performed using SANDER at T = 270K and T= 300K at an ion concentration of 0.001 M. Minimal structural variation is observed for the α-siRNA

sequence at either T= 270K or T= 300K by calculating the major groove width as determined by the distance between phosphate groups (**Figure 8.5A**). The calculated major groove width does not include the van der Waals radii of the phosphate group. Taking the latter into account shows a good correspondence with experimental values of ~ 13Å. Overall, structural integrity is preserved with explicit hydrogen bond for base pairing and base stacking interactions to maintain duplex but helicity is lost. From the bond fluctuations of the siRNA, coarse-grained model for siRNA is built and is tested across 5 different temperatures (T* = 0.7 – 1.1). From the plot shown in **Figure 8.5B**, at T*=1.1, the siRNA is shown to denature indicating that the melting temperature has been reached at T* > 1.0. For the rest of the coarse-grained simulations, the temperature chosen to correspond with physiological condition is T* = 1.0.

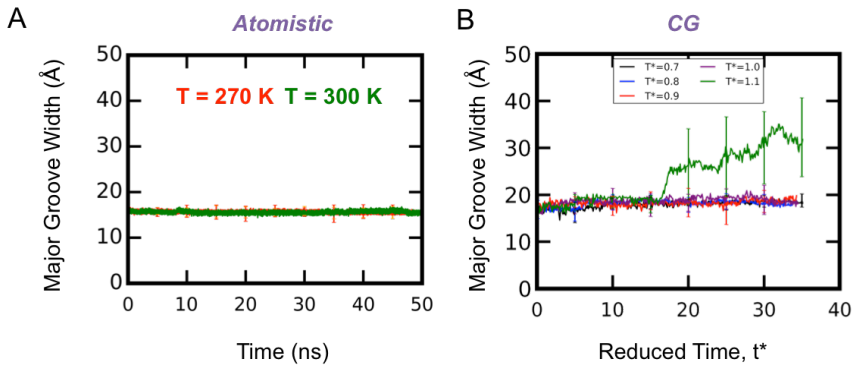

Figure 8.5. Calculated major groove width for α-siRNA structure at different temperatures for (A) atomistic and (B) coarse-grained model. The major groove width shown includes the 5.8Å VDW radii of phosphate group so shown values are larger than the experimentally reported value of ~11 – 13Å.[30]

8.4.2 Short cationic polymers can form large condensed complexes

By modifying the cationic polymer length, $PEG_{113}LYS_n$ (n = 9, 27, 50), it was observed that all three sequence variants yielded complexes with one or more siRNA duplex. In particular, larger condensed complexes, as defined by the total number of siRNA

and PEGylated-polymer chains, were formed by $PEG_{113}LYS_9$ at low and high N/P ratio of 1 and 10, respectively (**Figure 8.6A**). The ability for shorter cationic polymer lengths to form larger aggregates with siRNA may be attributed to the difference in size between the two species. The primary interaction driving the formation of these aggregates is favorable attractive electrostatic interaction between the negatively charged siRNA duplex and the positively charged lysine residues. Accounting for a total of 21 possible charges on the siRNA, and 9 charges on the peptide segment, interactions between several PEGylated-polymers and siRNA would be promoted to increase enthalpic energy (**Figure 8.6B**). However, experimental data shows preference for longer cationic polymers to be more therapeutically effective for sustained circulation time to improve bioavailability.[31]

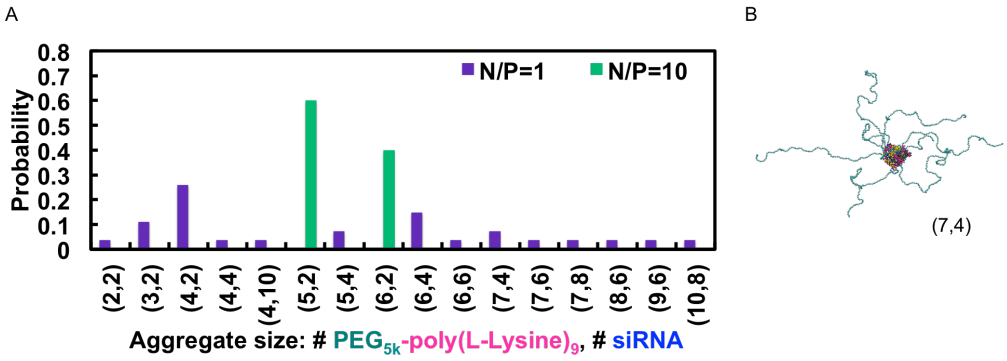

Figure 8.6. (A) Propensity to form aggregates at N/P = 1 and N/P = 10 for $PEG_{5k}LYS_9$ or $PEG_{113}LYS_9$. Aggregate composition is denoted as follows: (Number of PEGylated polymer chains, Number of siRNA chain). (B) An example of an aggregate with 2 double stranded siRNA shielded by 7 PEGylated polymer chains.

8.4.3 Long cationic polymers form effective complexes at high N/P ratios

Increasing the charge density, N/P ratio was found to yield comparable aggregate size for longer cationic polymer length similar to the ones formed with shorter cationic polymer lengths (**Figure 8.7A**). While a broad range of aggregate sizes can be formed with

$PEG_{113}LYS_{27}$ at N/P = 1, the likelihood for these aggregate formation is relatively low. Not until did the charge density increase to N/P = 10 for $PEG_{113}LYS_{27}$, did the probability for larger aggregate formation increases substantially. Moreover, this also suggest that $PEG_{113}LYS_{27}$ is able to form interactions with multiple duplexes at once which aids in the promotion of forming larger aggregates. Considering that the size ratio between siRNA and LYS_{27} is slightly lower than LYS_9, in order to increase the number of favorable interactions for lysine, multiple siRNA duplexes would be needed. To compensate for multiple siRNA, more cationic polymer would be needed as well resulting in a positive feedback loop. The latter effect seems to be viable since snapshots of these aggregates (**Figure 8.7B and 8.7C**) shows exposed area that can facilitate and accommodate increased number of both siRNA and $PEG_{113}LYS_{27}$ chains.

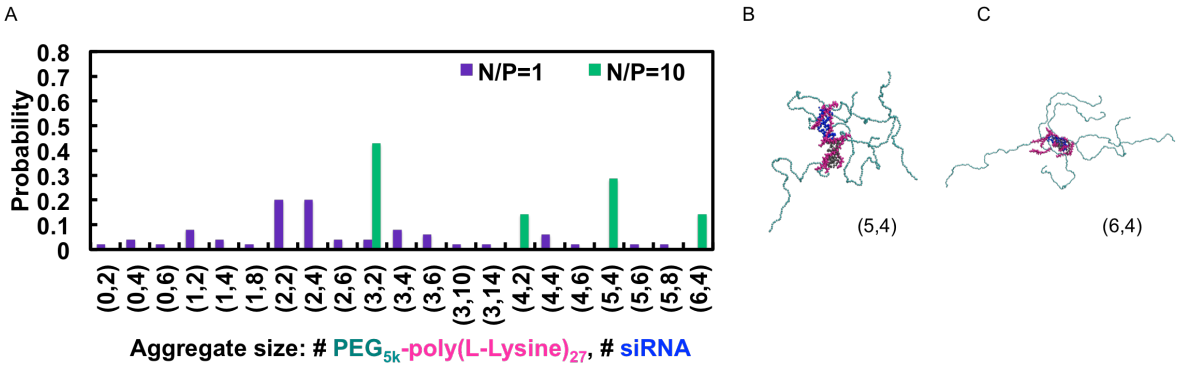

Figure 8.7. (A) Propensity to form aggregates at N/P = 1 and N/P = 10 for $PEG_{5k}LYS_{27}$ or $PEG_{113}LYS_{27}$. Aggregate composition is denoted as follows: (Number of PEGylated polymer chains, Number of siRNA chain). (B) An example of an aggregate with 2 double stranded siRNA shielded by 5 PEGylated polymer chains and (C) an example of an aggregate with 2 double stranded siRNA shielded by 6 PEGylated polymer chains.

In contrast, for cationic polymer that contains an extremely long peptide segment such as $PEG_{113}LYS_{50}$, the ability to form effective complexes is lowered. Since the size ratio between siRNA and LYS_{50} is smaller, it indicates that one LYS_{50} would be sufficient to interact with siRNA completely, thereby reducing the total size of an aggregate. From

Figure 8.8, although increasing the charge density ratio can form larger aggregates with multiple siRNA duplex, the most probable complex is formed by 2 $PEG_{113}LYS_{50}$ chains with a single siRNA duplex. In other words, while the number of interactions are maximized between cationic polymer and siRNA, the siRNA remains exposed to the surrounding environment.

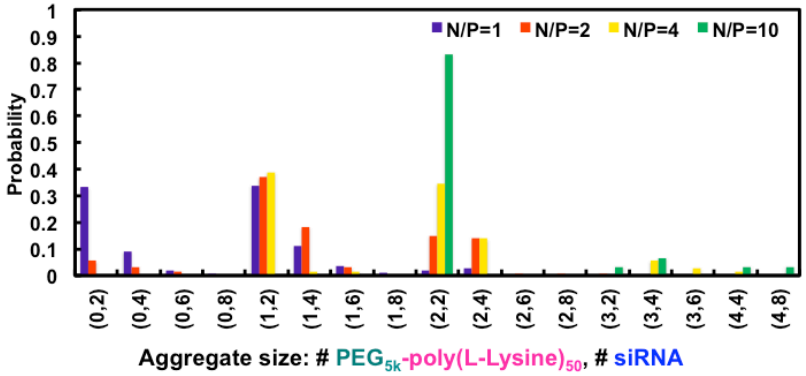

Figure 8.8. Propensity to form aggregates at N/P = 1, 2, 4, and 10 for $PEG_{5k}LYS_{50}$ or $PEG_{113}LYS_{50}$. Aggregate composition is denoted as follows: (Number of PEGylated polymer chains, Number of siRNA chain)

8.4.4 Decreasing cationic polymer length can improve siRNA shielding

To achieve an effective complex between siRNA and cationic polymer, several parameters must be attained. First, an effective complex would contain at least one or more siRNA duplexes to promote transfection efficiency. Second, siRNA should be well sequestered away from the aqueous medium with adequate number of bulky PEGylated tails shielding the siRNA to enhance cellular uptake. Comparing the three different sequence variants, $PEG_{113}LYS_{27}$ is best able to meet those requirements (**Figure 8.9A**). At a high charge density ratio of N/P = 10 in which formation of large aggregates are more likely for longer cationic polymer lengths, larger aggregates are typically formed by $PEG_{113}LYS_{9}$. However, upon examining the ratio of the cationic polymer to siRNA chains,

the ability to form complexes with two or more siRNA duplex is not as prevalent compared to $PEG_{113}LYS_{27}$ (**Figure 8.9B and 8.9C**). When complexes are formed between the two species, since $PEG_{113}LYS_{9}$ has a short peptide segment, multiples of the cationic polymers versus siRNA would be needed to form optimum number of electrostatic interactions. Consequently, $PEG_{113}LYS_{27}$ being on the approximate same length scale as siRNA becomes more favorable to form complexes that are comparable in size with $PEG_{113}LYS_{9}$ while ensuring siRNA is protected with adequate PEGylated tails. On the other hand, even though $PEG_{113}LYS_{50}$ is able to form large complexes, the likelihood is significantly reduced and at the same time, siRNA is much more exposed limited by the number of PEGylated tails that can form interactions with siRNA (**Figure 8.9D**).

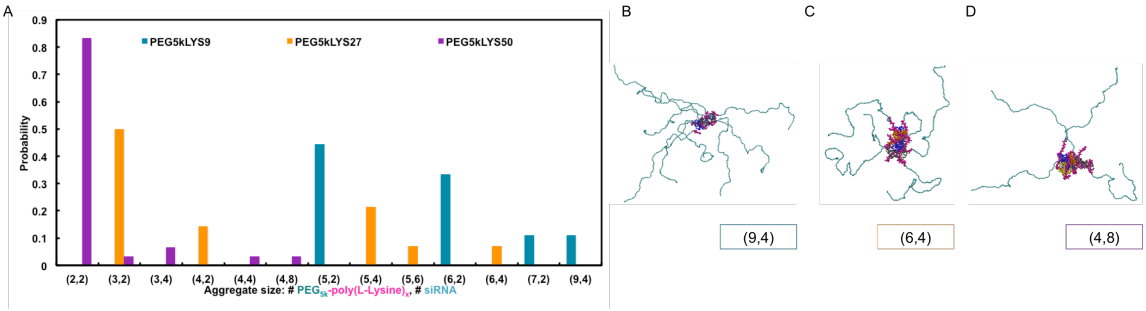

Figure 8.9. (A) Propensity to form aggregates at N/P = 10 for $PEG_{5k}LYS_{x}$ (x= 9, 27, and 50) or $PEG_{113}LYS_{x}$ (x= 9, 27, and 50). Aggregate composition is denoted as follows: (Number of PEGylated polymer chains, Number of siRNA chain). (B) Represented aggregates for (B) $PEG_{5k}LYS_{9}$; (C) $PEG_{5k}LYS_{27}$; and (D) $PEG_{5k}LYS_{50}$ indicating that effective complexation can be achieved with $PEG_{5k}LYS_{27}$, a cationic polymer that is sufficiently long to increase bioavailability while being able to shield and complex with large number of siRNA molecules.

8.5 Conclusions

Current coarse-grained model, BioModi, has been developed and extended to incorporate and adequately model the biological behavior of peptide residues, nucleic acids and polyethylene glycol units. Physiologically relevant behavior is captured from performing atomistic simulations to determine the dynamics of individual PEGylated-

polypeptide and double stranded siRNA molecules. Interest is focused on examining the interactions and complexation between cationic polymers with siRNA. Four systems were examined to study the effects of the length of the cationic polypeptide ($PEG_{5k}LYS_x$; x = 9, 27, or 50) and changing the charge density of the system (Nitrogen to Phosphate ratio of either N/P=1 or N/P=10). The molecular weight of the PEG chain was kept constant at 5000Da. Concentrations simulated were modeled after experimental conditions.

Factors such as length of PLL and charge density between the gene and carrier are observed to influence the behavior of these molecules in a large system representative of experimental studies. Complexation of siRNA and cationic polymer is observed using coarse-grained model. Shorter cationic polymer length led to formation of larger aggregate size; in particular with higher cationic polymer to siRNA ratio indicating better shielding of siRNA to increase its bioavailability. However, since experimental results shows preference for longer cationic polymer length for increased stability, it was found that similar aggregate sizes can be observed by increasing the N/P ratio. Future work will incorporate other sequences to examine the disassembly event. Extension of this model can be used toward developing more sophisticated system such as larger molecules with more complex architectures.

8.6 Acknowledgements

This work has not been published yet and is in preparation for submission. Co-authors include Cade B. Markegard, Gwendolen Chu, and Hung D. Nguyen.

8.7 References

1. Fire, A. *et al.* Potent and specific genetic interference by double-stranded RNA in Caenorhabditis

elegans. *Nature* **391,** 806–811 (1998).
2. Montgomery, M. K., Xu, S. & Fire, A. RNA as a target of double-stranded RNA-mediated genetic interference in Caenorhabditis elegans. *Proceedings of the National Academy of Sciences* **95,** 15502–15507 (1998).
3. Nikitenko, N. A. & Prassolov, V. S. Non-Viral Delivery and Therapeutic Application of Small Interfering RNAs. *Acta naturae* **5,** 35–53 (2013).
4. Kanasty, R., Dorkin, J. R., Vegas, A. & Anderson, D. Delivery materials for siRNA therapeutics. *Nat Mater* **12,** 967–977 (2013).
5. Vaishnaw, A. K. *et al.* A status report on RNAi therapeutics. *Silence* **1,** 14 (2010).
6. Deng, Y. *et al.* Therapeutic potentials of gene silencing by RNA interference: principles, challenges, and new strategies. *Gene* **538,** 217–227 (2014).
7. Whitehead, K. A., Langer, R. & Anderson, D. G. Knocking down barriers: advances in siRNA delivery. *Nat Rev Drug Discov* **8,** 129–138 (2009).
8. Han, S.-O., Mahato, R. I., Sung, Y. K. & Kim, S. W. Development of Biomaterials for Gene Therapy. *Molecular Therapy* **2,** 302–317 (2000).
9. Park, T., Jeong, J. & Kim, S. Current status of polymeric gene delivery systems ☆ . *Advanced Drug Delivery Reviews* **58,** 467–486 (2006).
10. Jeong, J. H., Park, T. G. & Kim, S. H. Self-Assembled and Nanostructured siRNA Delivery Systems. *Pharm Res* **28,** 2072–2085 (2011).
11. Mann, A., Richa, R. & Ganguli, M. DNA condensation by poly-l-lysine at the single molecule level: Role of DNA concentration and polymer length. *Journal of Controlled Release* **125,** 252–262 (2008).
12. Ouyang, D., Zhang, H., Herten, D.-P., Parekh, H. S. & Smith, S. C. Structure, Dynamics, and Energetics of siRNA−Cationic Vector Complexation: A Molecular Dynamics Study. *J. Phys. Chem. B* **114,** 9220–9230 (2010).
13. Ouyang, D., Zhang, H., Parekh, H. S. & Smith, S. C. The effect of pH on PAMAM dendrimer–siRNA complexation — Endosomal considerations as determined by molecular dynamics simulation. *Biophysical Chemistry* **158,** 126–133 (2011).
14. Sun, C., Tang, T. & Uludag, H. Molecular Dynamics Simulations for Complexation of DNA with 2 kDa PEI Reveal Profound Effect of PEI Architecture on Complexation. *J. Phys. Chem. B* **116,** 2405–2413 (2012).
15. Sun, C., Tang, T. & Uludag, H. Biomaterials. *Biomaterials* **34,** 2822–2833 (2013).
16. Elder, R. M. & Jayaraman, A. Coarse-Grained Simulation Studies of Effects of Polycation Architecture on Structure of the Polycation and Polycation–Polyanion Complexes. *Macromolecules* **45,** 8083–8096 (2012).
17. Shim, M. S. & Kwon, Y. J. Acid-transforming polypeptide micelles for targeted nonviral gene delivery. *Biomaterials* **31,** 3404–3413 (2010).
18. DA, C. *et al.* AMBER 12.
19. Yesselman, J. D., Price, D. J., Knight, J. L. & Brooks, C. L., III. MATCH: An atom-typing toolset for molecular mechanics force fields. *J. Comput. Chem.* **33,** 189–202 (2011).
20. Phillips, J. C. *et al.* Scalable molecular dynamics with NAMD. *J. Comput. Chem.* **26,** 1781–1802 (2005).
21. Humphrey, W., Dalke, A. & Schulten, K. VMD: visual molecular dynamics. *Journal of molecular graphics* **14,** 33–38 (1996).
22. Markegard, C. B., Fu, I. W., Reddy, K. A. & Nguyen, H. D. Coarse-Grained Simulation Study of Sequence Effects on DNA Hybridization in a Concentrated Environment. *J. Phys. Chem. B* 150126153442009 (2015). doi:10.1021/jp509857k
23. Fu, I. W., Markegard, C. B., Chu, B. K. & Nguyen, H. D. The Role of Electrostatics and Temperature on Morphological Transitions of Hydrogel Nanostructures Self-Assembled by Peptide Amphiphiles Via Molecular Dynamics Simulations. *Advanced Healthcare Materials* **2,** 1388–1400 (2013).
24. Voegler Smith, A. & Hall, C. K. α-Helix formation: Discontinuous molecular dynamics on an intermediate-resolution protein model. *Proteins: Structure, Function, and Bioinformatics* **44,** 344–360 (2001).
25. Nguyen, H. D., Marchut, A. J. & Hall, C. K. Solvent effects on the conformational transition of a model polyalanine peptide. *Protein Science* **13,** 2909–2924 (2004).
26. Knotts, T. A., Rathore, N., Schwartz, D. C. & de Pablo, J. J. A coarse grain model for DNA. *J. Chem. Phys.* **126,** 084901 (2007).
27. Ding, F. *et al.* Ab initio RNA folding by discrete molecular dynamics: From structure prediction to

folding mechanisms. *RNA* **14,** 1164–1173 (2008).
28. Wallqvist, A. & Ullner, M. A simplified amino acid potential for use in structure predictions of proteins. *Proteins: Structure, Function, and Bioinformatics* **18,** 267–280 (1994).
29. Wesson, L. & Eisenberg, D. Atomic solvation parameters applied to molecular dynamics of proteins in solution. *Protein Science* **1,** 227–235 (1992).
30. Tolbert, B. S. *et al.* Major groove width variations in RNA structures determined by NMR and impact of 13C residual chemical shift anisotropy and 1H–13C residual dipolar coupling on refinement. *J Biomol NMR* **47,** 205–219 (2010).
31. Ward, C. M., Read, M. L. & Seymour, L. W. Systemic circulation of poly (L-lysine)/DNA vectors is influenced by polycation molecular weight and type of DNA: differential circulation in mice and rats and the implications for human gene therapy. *Blood* **97,** 2221–2229 (2001).

CHAPTER 9 Summary and Future Directions

9.1 Summary

In this dissertation, self-assembly behavior of peptide-polymer conjugates was studied using our newly developed coarse-grained, ePRIME, model. In Chapter 2, formation of a cylinder nanofiber structure from a large spontaneous self-assembly event was observed. The characteristics of the structure shared similarities with experimental findings and provided further insight into developing an improved schematic representation. Corroborating with experimental studies, at strong electrostatic interaction strength (i.e., high pH, low salt concentration) and at high temperatures, cylindrical nanofiber exhibits a morphological transition into spherical micelles and random coil of single molecules. In Chapter 3, a quantitative view of the pH-dependent self-assembly of nanofibers is provided through a multiresolution approach by implementing both all-atom constant pH and coarse-grained molecular dynamics simulations. With the use of both of these methods, the transition between a cylindrical nanofiber and spherical micelle is captured and is shown to correlate with experimental data. The kinetic pathway by which nanostructures are formed are characterized and specific charged residues that induces secondary structure disruption are also identified.

In Chapter 4, the effect of modifying the hydrophobic interaction strength between the hydrophobic polymer and peptide residues is examined. As the hydrophobic strength is increased, morphological transitions are observed from open networks of secondary structures toward closed cylindrical nanostructures are observed. The ability to form distinctive nanostructures by varying the hydrophobic interaction strength indicates that

the particular choice of polymer type or solvent can be considered as an additional design parameter for the development of innovative biomaterials. Two-dimensional phase diagrams are delineated to illustrate the delicate interplay between these non-covalent interactions to better identify the morphological and structural transitional points. Chapter 5 presents a detailed quantitative analysis to characterize the multistep process for the formation of these nanostructures.

In Chapter 6, single molecule peptide amphiphile are examined with two sequences that share the same chemical composition but have different placement of hydrophobic residues with respect to the polymer tail. From the simulations, as the strong hydrophobic residue is placed further away from the polymer tail, propensity for the single molecule to fold is significantly decreased due to hindrance form the favorable interactions between the polymer and nonpolar peptide residues. Chapter 7 examines these two sequences in large self-assembly events and observes that the change in nonpolar residue placement can affect local structural organization of the resulting nanostructure. Results from this study provided a correlation with structural stability and mechanical behavior of hydrogel nanostructures.

In Chapter 8, our coarse-grained ePRIME model is extended into BioModi to represent a heterogeneous system of two different species. This enables simulation studies to examine the complexation behavior between siRNA and PEGylated block copolymers. Several parameters were found to influence efficient complexation including the length of the cationic polymer, and charge density between the gene and carrier.

The ability to use coarse-grained molecular dynamics to simulate peptide-polymer conjugates aims to provide a complementary understanding to experimental work. By

systematically varying the sequence and examining the role of external stimuli on these systems aid in the design and development of bioinspired materials for the fields of drug delivery, diagnostic medicine, tissue engineering, and regenerative medicine.

9.2 Future Work

The work discussed in this dissertation hopes to further the current understanding of the self-assembly behavior of peptide-polymer conjugates. However, there are still many exciting topics worthy of future explorations. Even though several distinct kinetic mechanisms (Chapter 2,4,5,7) have been identified as a function of the external stimuli for peptide amphiphiles, fundamentals of "micelle-merging" events can be examined in-depth. Our term for the morphological transition for spherical micelles to merge together to yield rod-like cylindrical nanofibers shares similarity with "symmetry-breaking" events as observed in biology[1] and nanotechnology[2] related fields. For example, the formation of anisotropic nanoparticles has been of interest since functionality is heavily corresponded to the particular shape of the nanoparticle.[2] Yet, the ability to fine-tune and control desired growth in a specific direction remains limited. As such, our model could be extended to study other systems to provide a more comprehensive understanding of the factors that contributes to structural and morphological transitions.

In Chapter 7, the placement of nonpolar residues with respect to the polymer tail was found to influence the resulting nanostructure's stability even though the chemical composition of the peptide amphiphile remained unchanged. This suggests that the positioning of hydrophobic residues can be an additional design parameter to consider in order to attain customization of desired structural and mechanical properties. Recent work

by Ghosh et al., have shown that isomerization of a peptide amphiphile molecule can promote cylindrical nanofiber formation[3] in addition to replacing peptide residues with strong hydrophobic residues[4]. Simulation studies can be performed to obtain a better understanding as to whether the hydrophobic strength of a residue predominates or if the placement of the residue governs the self-assembled nanostructures. The weighted contribution of nonconvalent interactions can be determined to provide further details of which intermolecular interaction is more significant. Other studies regarding the stability of the structure can also be examined by performing steered molecular dynamics simulations.[5]

A limitation with our current coarse-grained model is the use of reduced quantities to represent variables for experimental conditions. While a direct correspondence to experimental or physiological values is difficult, a reference condition is currently obtained by identifying the melting temperature between our coarse-grained model and atomistic model. Although qualitative understandings provide benchmarks for experimentalists, the goal is to eventually achieve a direct correspondence between simulation and experimental parameters without sacrificing computational power. Future work will be to implement a method to the current ePRIME model to represent pH dependence behavior. This model he model will be based upon work previously developed by Tieleman's group[6] that has performed constant pH simulation using coarse-grained MARTINI model to examine the aggregation behavior of oleic acid.

While ePRIME has been extended to model siRNA and block copolymers, the current system is considered to be a test model to indicate that the model is able to represent a heterogeneous system showcasing complexation to occur between the two species. Further

work can be placed to examine an alternative cationic polymer that incorporates histidine residues[7,8] to leverage its ability to undergo deprotonation at physiological pH. The incorporation of a "molecular-switch" with the use of histidine residues will enable an understanding of the disassembly mechanism involved in efficient gene transfection. Other more sophisticated systems with more complex architectures can also be used such as bolaamphiphiles, which exhibit low toxicities and high bioavailability in the blood stream making it an ideal vector for gene silencing.[9]

In general, the use of coarse-grained molecular dynamics simulations have been shown to be feasible to guide the design and development of peptide-polymer conjugates as novel biomaterial for a broad range of applications in drug and gene delivery, tissue engineering, and regenerative medicine.

9.3 References

1. Li, R. & Bowerman, B. Symmetry Breaking in Biology. *Cold Spring Harbor Perspectives in Biology* **2,** a003475–a003475 (2010).
2. Walsh, M. J., Barrow, S. J., Tong, W., Funston, A. M. & Etheridge, J. Symmetry Breaking and Silver in Gold Nanorod Growth. *ACS Nano* **9,** 715–724 (2015).
3. Ghosh, A., Dobson, E. T., Buettner, C. J., Nicholl, M. J. & Goldberger, J. E. Programming pH-Triggered Self-Assembly Transitions via Isomerization of Peptide Sequence. *Langmuir* **30,** 15383–15387 (2014).
4. Ghosh, A. *et al.* Fine-Tuning the pH Trigger of Self-Assembly. *J. Am. Chem. Soc.* **134,** 3647–3650 (2012).
5. Yu, T., Lee, O.-S. & Schatz, G. C. Steered Molecular Dynamics Studies of the Potential of Mean Force for Peptide Amphiphile Self-Assembly into Cylindrical Nanofibers. *J. Phys. Chem. A* **117,** 7453–7460 (2013).
6. Bennett, W. F. D., Chen, A. W., Donnini, S., Groenhof, G. & Tieleman, D. P. Constant pH simulations with the coarse-grained MARTINI model — Application to oleic acid aggregates. *Can. J. Chem.* **91,** 839–846 (2013).
7. Midoux, P., Pichon, C., Yaouanc, J.-J. & Jaffrès, P.-A. Chemical vectors for gene delivery: a current review on polymers, peptides and lipids containing histidine or imidazole as nucleic acids carriers. *British Journal of Pharmacology* **157,** 166–178 (2009).
8. Chou, S.-T. *et al.* Enhanced silencing and stabilization of siRNA polyplexes by histidine-mediated hydrogen bonds. *Biomaterials* **35,** 846–855 (2014).
9. Kim, T. *et al.* In Silico, In Vitro, and In Vivo Studies Indicate the Potential Use of Bolaamphiphiles for Therapeutic siRNAs Delivery. *Mol Ther Nucleic Acids* **2,** e80 (2013).